Coordination networks based on carboxylate and beta-diketonate ligands

Cassar, Kevin

Award date:
2007

Awarding institution:
University of Bath

Coordination networks based on carboxylate and β-diketonate ligands

by Kevin Cassar

A thesis submitted for the degree of Doctor of Philosophy
University of Bath
Department of chemistry
June 2007

Acknowledgments

Many people have participated both directly and indirectly in the realisation of this work by offering all sorts of support, ranging from financial, moral and scientific.

I first start by thanking my three supervisors, Andy Burrows, Mary Mahon and Sean Rigby for their help in the scientific field and for their immense patience especially during frustrating and hard times. I would also like to thank Alan Carver and Fernando Acosta for their technical help.

I also would like to thank past and present members from the Burrows group for making the lab a home rather than a working place.

Acknowledgments go to my friends Stuart McDonalds, Mike Bonne, Andy Kirk, Zena Hughes, Jason Aquilina, Noel Vella and my family for lending me a shoulder to lean on during hard times.

Last but not least I would like to thank EPSRC for the financial support, Tim Prior and John Warren from Daresbury labs for time at the Synchrotron Radiation.

Abstract

In recent years there has been an increasing interest in metal organic frameworks (MOFs). These compounds consist of metal centres linked together by organic linkers to form 1-, 2- or 3 dimensional networks. During the course of this work, various new materials were synthesised and characterised.

The first chapter of this work highlights some of the MOFs reported in the literature. Networks containing pyridyl, nitrile and carboxylates, are discussed, as are the applications of MOFs.

In Chapter 2 the sensitivity of the reaction between $Zn(NO_3)_2 \cdot 6H_2O$ and 1,4-benzenedicarboxylic acid towards variations in the reaction conditions is described. The thermal stabilities of appropriate networks are also considered.

The reaction between $Cd(NO_3)_2 \cdot 4H_2O$ and 1,4-benzenedicarboxylic acid was studied and the results are reported in Chapter 3. The thermal stabilities of selected novel networks are also analysed and the Lewis-acid catalytic properties of two MOFs were also studied. The gas adsorption/desorption properties of these two networks are reported in Chapter 4.

One aim of this project was to find an alternative to carboxylate ligands that can form neutral networks. In Chapter 5 the synthesis and use of various bis-β-diketonate ligands in network formation is reported. These ligands were also found to have the ability to form Secondary Building Units (SBUs).

The discussion in Chapter 6 focuses on mixed metal networks obtained from functionalised β-diketonate ligands. New MOFs assembled from copper or iron and silver linked together by a cyano-functionalised β-diketonate ligand are reported in the penultimate chapter. The concluding chapter contains experimental data.

List of contents

Chapter 1 Introduction

Chapter 2 Zinc dicarboxylate networks

Chapter 3 Cadmium dicarboxylate networks

Chapter 4 Gas adsorption properties of $\{[Cd_3(tph)_3]\}_\infty$ and $\{[Cd_3(bpdc)_3]\}_\infty$

Chapter 5 Networks from bis-β-diketonate ligands

Chapter 6 Functionalised β-diketonate ligands

List of abbreviations

Terms

Secondary Building Unit	SBU
Thermogravimetric analysis	TGA

Chemicals

N,N-dipropylformamide	DPF
N,N-diethylformamide	DEF
di-2-pyridylamine	dpa
Sodium acetylacetonate	Na[acac]
N,N'-dimethylformamide	DMF
Dimethylsulfoxide	DMSO
Silver triflate	AgOTF

Ligands

acetate	OAc
1,3-benzenedicarboxylic acid	1,3-H_2bdc
1,2-benzenedicarboxylic acid	1,2-H_2bdc
pyridine	py
2,2'-bipyridine	bpy
4,4'-bipyridine	4,4'-bipy
1,3,5-tri(4-ethynylbenzonitrile)benzene	4-teb
1,3,5-tri(3-ethynylbenzonitrile)benzene	3-teb
4,4',4'',4'''-tetracyanotetraphenylmethane	tctpm
1,4-benzenedicarboxylic acid	H_2tph
4,4'-biphenyldicarboxylic acid	H_2bpdc
2,4-pentanedione	Hacac
3,4-diacetyl-2,5-dioxohexane	H_2tae
3,3'-(1,4-phenylenedimethylene)di-2,4-pentanedione	H_2pdp
3,3'-dithio-di-2,4-pentanedione	H_2dtp
1,3,5-benzenetricarboxylic acid	H_3btc
2,4,6-tris(4-pyridyl)-1,3,5-triazine	tpt
5-(4-pyridyl)-4,6-dipyrrinate	4-Hpyrdpm
5-(4'-cyanophenyl)dipyrromethene	4-cydpm
1,3,5-tri(benzoic acid)benzene	H_3btb
3,3',5,5'-biphenyltetracarboxylic acid	H_4bptc
3-(4-pyridyl)-2,4-pentanedione	Hppd
1,1,5,5-hexafluoroacetylacetone	Hhfacac
1,3,5-benzenetricarboxylic acid tris [N-(4-pyridyl)amide]	4-btapa
pyridinedicarboxylic acid	H_2pydc
Fumaric acid	Hfma
trans-bis(4-pyridyl)ethylene	bpe
2,6-naphthalenedicarboxylic acid	H_2ndc
3-(4-pyridylethylene)-2,4-pentanedione	Hpep
1-(4-pyridyl)-1,3-butanedione	Hpdd
1,1'-(1,4-phenyl)bisbutane-1,3-dione	H_2pbd

1,1'-(1,3-phenylene)-bis(4,4-dimethylpentane-1,3-dione)	H_2pdmp

List of compounds synthesised

Molecular formula	Number/abbreviation of compound
$\{[Zn(tph)(H_2O)]\cdot DMF\}_\infty$	**1**
$\{[Zn_3(tph)_3(H_2O)_3]\cdot 4DMF\}_\infty$	**2**
$\{[Zn(tph)(DMF)]\}_\infty$	**3**
$\{(Me_2NH_2)_2[Zn_3(tph)_4]\cdot DMF\cdot H_2O\}_\infty$	**4**
$\{[Me_2NH_2)_2[Zn(DMF)_4(OH_2)_2][Zn_6(tph)_8]\cdot 6DMF\}_\infty$	**5**
$\{[Zn_4(\mu_4\text{-}O)(tph)_3]\cdot 3DEF\}_\infty$	MOF-5
$\{(Et_2NH_2)_2[Zn_3(tph)_4]\cdot 2.5DEF\}_\infty$	**6**
$\{[Zn(bpdc)(DMF)]\cdot 2DMF\}_\infty$	**7**
$\{[Zn_3(bpdc)_3(DMF)_2]\cdot 3DMF\cdot H_2O\}_\infty$	**8**
$\{[Cd(tph)(DMF)]\}_\infty$	**9**
$\{[Cd(tph)(DMF)_{0.5}]\}_\infty$	**9a**
$\{[Cd(tph)]\}_\infty$	**9b**
$\{[Cd_3(tph)_3(DMF)_4]\}_\infty$	**10**
$\{[Cd_3(tph)_3(DMF)_4]\}_\infty$	**11**
$\{(Me_2NH_2)_2[Cd(tph)_2]\cdot 2DMF\}_\infty$	**12**
$\{[Cd_3(tph)_3(DEF)_2]\}_\infty$	**13**
$\{[Cd_3(tph)_3(DEF)]\}_\infty$	**13a**
$\{[Cd(tph)]\}_\infty$	**13b**
$\{[Cd_3(bpdc)_3(DMF)_2]\}_\infty$	**14**
$\{[Cd(bpdc)]\}_\infty$	**14b**
3,4-diacetyl-2,5-dioxohexane	H_2tae
$\{[Zn(tae)(DMF)]\cdot 0.6CHCl_3\cdot 0.4DMF\}_\infty$	**15**
$\{[Zn_3(tae)_3(MeOH)(DMSO)_{4.2}]0.8DMSO\}_\infty$	**16**
$\{[Zn_2(\mu\text{-}tae)_2(OH_2)_2]\}_\infty$	**17**
$\{[Zn_2(\mu\text{-}tae)_2(MeOH)_2]\cdot 2MeOH\}_\infty$	**18**
$\{[Cd_2(\mu\text{-}tae)_2(OH_2)_2]\cdot 2.5H_2O\}_\infty$	**19**
3,3'-(1,4-phenylenedimethylene)di-2,4-pentanedione	H_2pdp
3,3'-dithio-di-2,4-pentanedione	H_2dtp
$[Fe_3(dtp)_3(OMe)_3(MeOH)_3]$	**20**
3-cyano-2,4-pentanedione	Hcpd
$[Cu(cpd)_2]$	**21**
$[Cu_6(\mu_3\text{-}OMe)_4(\mu\text{-}OMe)_2(cpd)_6]$	**22**
$[Fe(cpd)_3]$	**23**
$[Al(cpd)_3]$	**24**
$\{Ag[Cu(cpd)_2]NO_3\}_\infty$	**25**
$\{Ag_2[Fe_2(\mu\text{-}OMe)_2(cpd)_4](NO_3)_2\cdot C(CH_3)_2O\}_\infty$	**26**
$\{Ag[Fe_2(\mu\text{-}OMe)_2(cpd)_4]NO_3\}_\infty$	**27**
$\{Ag[Fe(cpd)_3]NO_3\}_\infty$	**28**
$\{Ag[Fe_2(\mu\text{-}OMe)_2(cpd)_4](OH)\cdot 0.4H_2O\}_\infty$	**29**
$\{[Ag(cpd)]\}_\infty$	**30**

Chapter 1 Introduction

1.1 General introduction

One aspect of supramolecular chemistry that has attracted significant attention in recent years is the synthesis of metal organic frameworks. These compounds consist of metal centres, most commonly transition metals, linked together by organic ligands to form 1-, 2- or 3-D networks.[1] A particular feature of some of these networks is the presence of empty spaces which are occupied by solvent molecules. These spaces (or pores) give these compounds potential useful applications such as reversible gas storage[2-5] and catalytic properties.[6]

The architecture of the metal organic frameworks and the pores can be engineered by altering the configuration, shape and size of the connector, as well as by changing the coordination around the metal centre.[7-10] In many cases, the properties of the subsequent networks depend on the shape and size of the pores. Since the dimensionality of the pores is dependent on the architecture of the networks, any modifications in the latter can bring about a change in the properties of the material.

Three common types of organic ligands that have been used in the synthesis of networks are *N*-heterocycles,[11-13] nitriles[14-16] and carboxylates.[4,5,17-20] A flavour of the wide range of chemistry in this area will be given in this chapter.

1.1.1 Network nomenclature

The nomenclature developed by A.F.Wells,[21] will be used to describe the architecture of the networks in this work.

Using this system, networks can be described by two numbers. The numbers are enclosed in brackets and separated by a comma in the form of (n,p). p represents the connectivity. This denotes the number of ligands extended from a metal centre. For example, if a metal centre is connected to three ligands that extend the network in three

directions, p will be 3. Note that terminal ligands do not extend the network thus do not contribute to the value of p.

The remaining number, n, describes the shortest pathway in a network. Thus for example in a honeycomb architecture (Figure 1.1), the network consist of hexagons and the shortest pathway starting from a point and ending in the same location consists of six sides, hence in this case n will be 6. This network is therefore described as (6,3).

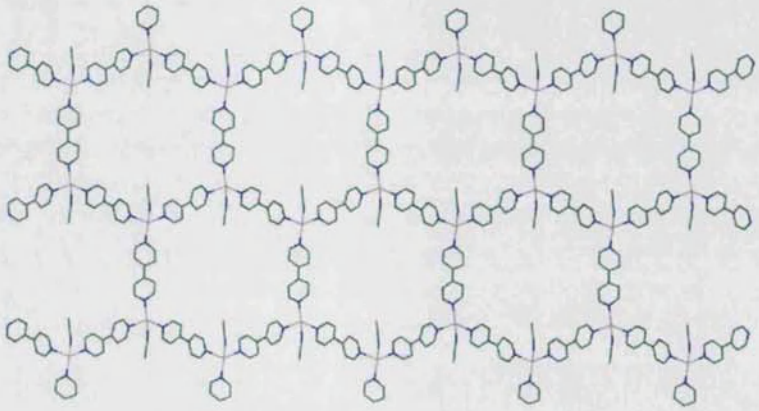

Figure 1.1. The honeycomb network of $\{[Ag(4,4'\text{-bipyridine})_{1.5}(CH_3CN)]SbF_6\}_\infty$[22] The silver metal centres (grey colour) are coordinated to 3 ligands and the shortest pathway consists of 6 sides. Green atoms represent carbon while blue colour represent nitrogen.

1.2 Networks from *N*-heterocyclic ligands

Early metal organic frameworks were formed from *N*-heterocyclic ligands such as 4,4'-bipyridine. The lone pair on the nitrogen atom is orthogonal to the π-system of each aromatic ring and thus is available to form a dative covalent bond to metal centres.[23] Due to the geometry of these ligands, they behave as linear rigid linkers. As will be demonstrated, various network geometries can be obtained from this class of linkers.

1.2.1 Networks with square grid shapes

One type of network configuration that is frequently encountered is the square grid motif (Figure 1.2).[7] Compounds having this particular architecture have a metal to ligand ratio of 1:2 with the metals usually adopting octahedral geometry. Two terminal ligands occupy the axial positions on the metal centre while the remaining four ligands connect the metal centres together into a 2-D net.

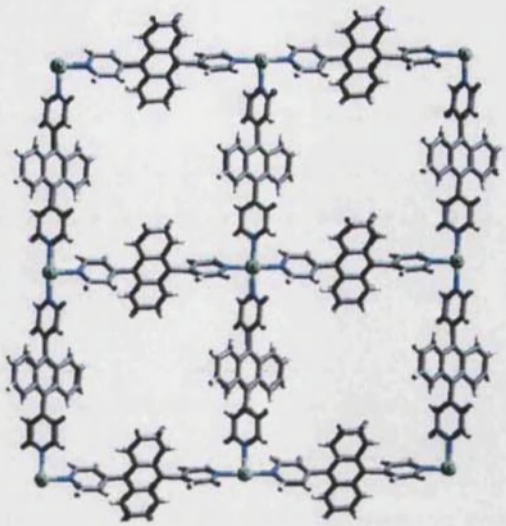

Figure1.2. The square grid motif of $\{[Ni(9,10\text{-bis}[4\text{-pyridyl}]anthracene)_2(H_2O)_2]\cdot 2NO_3\}_\infty$[12] The water ligands are directed in and out of the plane of the paper. The green, blue and grey coloured spheres represent nickel, nitrogen and carbon atoms respectively.

$\{[Ni(9,10\text{-bis}[4\text{-pyridyl}]anthracene)_2(H_2O)_2]\cdot 2NO_3\}_\infty$[12] (Figure 1.2) is one example of a square grid network. In this complex the nickel centres adopt an octahedral geometry with two water ligands acting as terminal points. When nickel was reacted with 1,2-bis(4-pyridyl)ethane,[24] an isostructural network was obtained, but with smaller pores. In contrast, a network with larger pores was obtained by using a longer ligand such as 4,4'-bis(4-pyridyl)biphenyl.[11] This comparison shows that the size of the pores can be modified by varying the length of the organic connector.

The structure of $\{[Fe(2,5\text{-dicarboxypyridine})(4,4'\text{-bipyridine})]\cdot H_2O\}_\infty$[13] also consists of a 2-D square grid. This particular compound exhibits guest exchange behaviour whereby the water molecules can be replaced by methanol and ethanol.[13]

1.2.2 Honeycomb networks

Another network configuration that can be obtained from *N*-heterocyclic ligands and metal centres includes the hexagonal shaped honeycomb network or, as sometimes referred to as, the (6,3) network.

The structure of the honeycomb net consists of 3-connecting metal centres joined together by linear bidentate ligands. In this case the metals and the linkers form a network that consists of 6-sided polygons (Figure 1.1), hence the (6,3) nomenclature.[21]

Honeycomb networks with trigonal ligands acting as the 3-connecting centres are relatively common. In contrast, networks having the metals as the 3-connecting centres are rare.[22] An example of the latter type is $\{[Ag(4,4'\text{-bipy})_{1.5}(CH_3CN)]SbF_6\}_\infty$ (4,4'-bipy = 4,4'-bipyridine),[22] with the silver centres adopting a distorted tetrahedral geometry. The coordination sphere of silver is populated by three 4,4'-bipyridyl ligands and a terminal acetonitrile molecule.

Other possible 2-D architectures that can be obtained from *N*-heterocyclic ligands and metal salts include the herringbone, brick wall and bilayer networks (Figure 1.3).[8] These three networks consist of metal centres having a T-shaped geometry. This building unit can be obtained from an octahedral metal centre by including terminal ligands that prevent the network from growing in the other directions. For example, the nitrate ligands in $\{[Ni(4,4'\text{-azopyridine})_{1.5}(NO_3)_2]\}_\infty$ act as capping agents and thus the nickel centre is extended in a T-shaped fashion.[25]

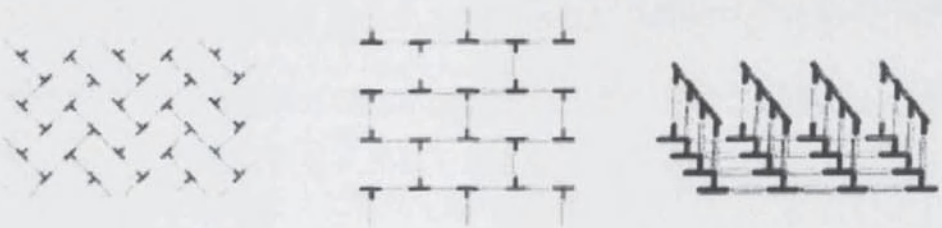

Figure 1.3. From left to right, diagrammatical representations of the herringbone, brick wall and bilayer motifs.

1.2.3 *N*-heterocyclic ligands acting as pillars

Bidentate *N*-heterocyclic ligands with *para*-nitrogen atoms can bind to vacant metal coordination sites of existing 2-D networks. The *N*-heterocyclic ligands act as pillars and consequently link the 2-D networks together into a 3-D architecture as shown in Figure 1.4.

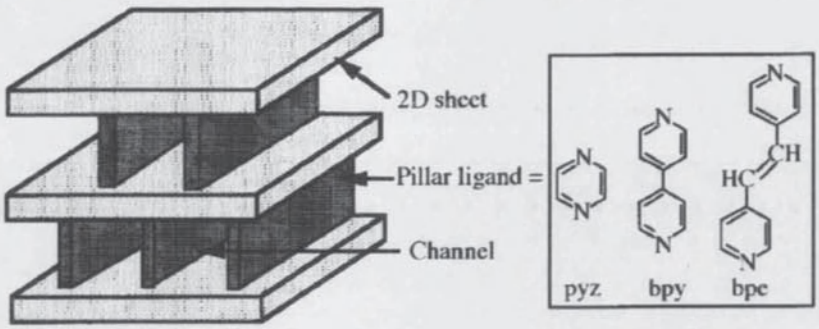

Figure 1.4. Schematic representation of the pillar effect of bidentate *N*-heterocyclic ligands.[26]

One such example containing a pillar ligand is $\{[Ni_6(btc)_4(4,4'\text{-bipy})_6(MeOH)_3(H_2O)_9]\cdot guest\}$[27] ($btc^{3-}$ = 1,3,5-benzenetricarboxylate). 4,4'-bipy coordinates to the vacant sites on the nickel centres thus joining the 2-D honeycomb layers of $\{[Ni_3(btc)_2]\}_\infty$ together to form the 3-D structure of $\{[Ni_6(btc)_4(4,4'\text{-bipy})_6(MeOH)_3(H_2O)_9]\cdot guest\}$.

1.2.4 Diamondoid networks

The diamondoid network is another frequently encountered topology.[8, 10] This particular motif consists of tetrahedral metal centres joined together by linear linkers.

$\{[Cu(4,4'\text{-bipy})_2]PF_6\}_\infty$ has been shown to adopt the diamondoid topology.[28] The copper(I) centres adopt tetrahedral geometry and the metal centres are joined together by the linear 4,4'-bipy ligands. $\{[Cu(4,4'\text{-bipy})_2]PF_6\}_\infty$ consists of four independent interpenetrated networks (Figures 1.5a and 1.5b respectively).

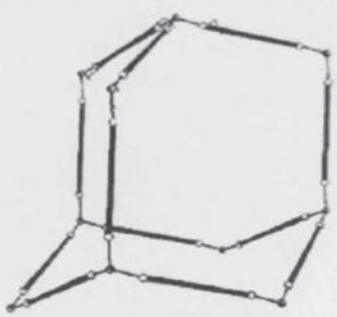

Figure 1.5a. The diamondoid network.

Figure 1.5b. The four fold interpenetrated network of $\{[Cu(4,4'\text{-bipy})_2]PF_6\}_\infty$

$\{[Ag(4,4'\text{-bipy})_2](CF_3SO_3)\}_\infty$ also has a diamondoid network.[29] Like $\{[Cu(4,4'\text{-bipy})_2]PF_6\}_\infty$, the metal centres of $\{[Ag(4,4'\text{-bipy})_2](CF_3SO_3)\}_\infty$ adopt a distorted tetrahedral geometry with the linear bidentate ligand connecting the metal centres together.

1.2.5 (10,3) nets

The (10,3) type net represents another way in which metals and bidentate *N*-heterocyclic ligands can be joined together. A (10,3) net can be assembled in seven different ways and each member of this family is assigned a letter.

The most symmetric and commonly reported member of the (10,3) series is (10,3)-a (Figure 1.6). Due to the helical nature of the (10,3)-a, this network has an inherent chirality. Compounds having this particular architecture, such as $\{[Cu(3,5\text{-pyridinedicarboxylate})(DMF)(py)]\}_\infty$ have been used as chiral catalysts.[30]

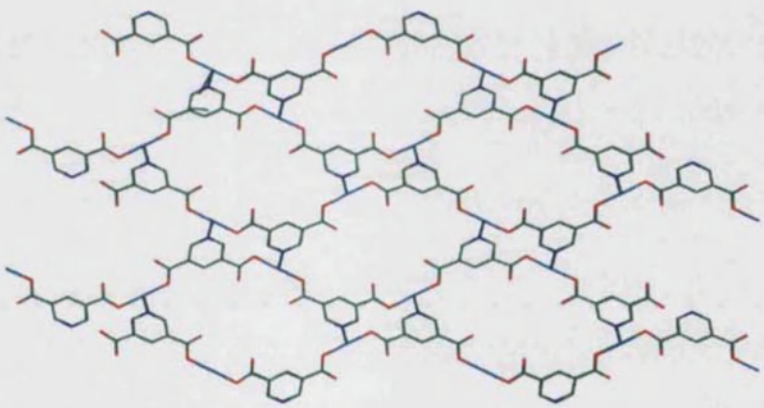

Figure 1.6. The (10,3)-a network of $\{[Cu(3,5\text{-pyridinedicarboxylate})(DMF)(py)]\}_\infty$ viewed down the *a* axis. Helices are in the plane of the paper. Blue, red green and turquoise atoms represent nitrogen, oxygen, carbon and copper atoms respectively.

(10,3)-a racemates are also possible. These compounds often consist of one chiral net interpenetrated by the opposite handed net. One such example is $\{[Zn(tpt)_{2/3}(SiF_6)(H_2O)_2(MeOH)]\}_\infty$[31] (tpt = 2,4,6-tris(4-pyridyl)-1,3,5-triazine) which consists of eight independent helices with four helices having one optical configuration and the other four adopting the opposite configuration.

1.2.6 Multidentate *N*-heterocyclic ligands

When the connectors consist of three or more functional groups, the ligands are no longer linear. This alteration is reflected in the final topology of the network. This section will consider networks formed from multidentate *N*-heterocyclic ligands such as 2,4,6-tris(4-pyridyl)-1,3,5-triazine (tpt) (Figure 1.7) and 5-(4-pyridyl)-4,6-dipyrrinate (4-pyrdpm) (Figure 1.8)

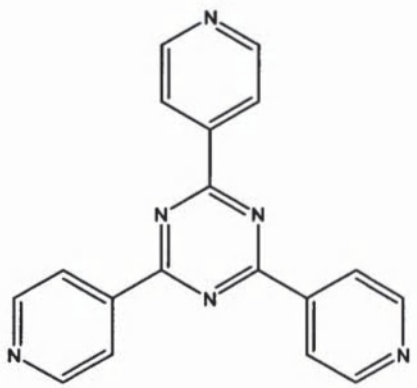

Figure 1.7. Diagrammatical representation of 2,4,6-tris(4-pyridyl)-1,3,5-triazine (tpt).

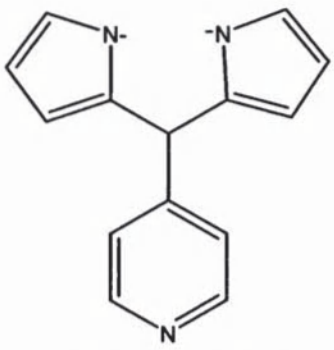

Figure 1.8. Diagrammatical representation of 5-(4-pyridyl)-4,6-dipyrrinate (4-pyrdpm).

In tpt, the pyridyl groups are situated at angles of 120° with respect to each other. This ligand can act as a three way connector and because it can extend the network in three different directions, tpt has the potential to form (n,3) type nets such as the honeycomb (6,3) or the chiral (10,3) and (12,3) nets. Examples of (10,3) and (12,3) compounds obtained from tpt are the aforementioned $\{[Zn(tpt)_{2/3}(SiF_6)(H_2O)_2(MeOH)]\}_\infty$[31] and $\{[Ni(tpt)(NO_3)]\cdot guest\}_\infty$[32] respectively.

5-(4-pyridyl)-4,6-dipyrrinato (4-pyrdpm)[33] (Figure 1.8) has two different binding sites, which are the pyrrinato and the pyridyl rings. The presence of two different functional groups allowed the formation of bimetallic networks in separate steps. The pyrrinato rings were coordinated to either cobalt(III) or iron(III) to form discrete M(4-pyrdpm)$_3$ molecules (Figure 1.9).[33] The discrete M(4-pyrdpm)$_3$ units were coordinated to silver salts through the pyridyl moities. When reacted with AgOTf, Co(4-pyrdpm)$_3$ formed $\{[Co(4\text{-}pyrdpm)_3Ag_3](OTf)_3\}_\infty$ while when Fe(4-pyrdpm)$_3$ was reacted with $AgBF_4$, $\{[Fe(4\text{-}pyrdpm)_3Ag_3](BF_4)_3\}_\infty$ resulted. $\{[Co(4\text{-}pyrdpm)_3Ag_3](OTf)_3\}_\infty$ and $\{[Fe(4\text{-}pyrdpm)_3Ag_3](BF_4)_3\}_\infty$ adopt the (10,3)-b (Figure 1.10a). On the other hand {[Fe(4-

pyrdpm)$_3$Ag$_3$](OTf)$_3$}$_\infty$ has (10,3)-d topology (Figure 1.10b). When the OTf$^-$ or BF_4^- counter ions were substituted by PF_6^- or SbF_6^-, both Co(4-pyrdpm)$_3$ and Fe(4-pyrdpm)$_3$ formed 2-D honeycomb networks.[34] This illustrates the dependency of this particular system on the counter ion.

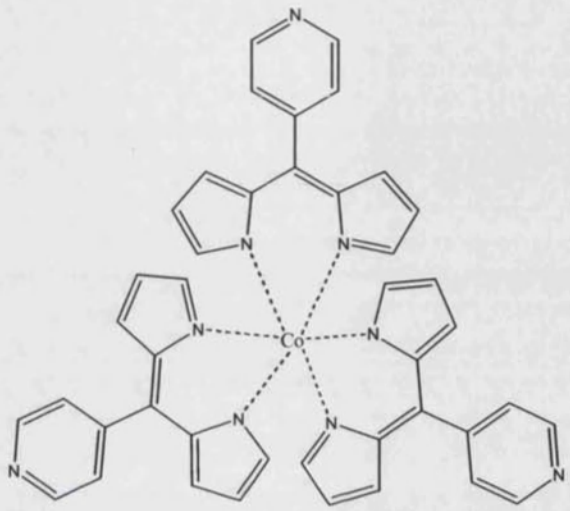

Figure 1.9. Diagrammatical representation of the discrete Co(4-pyrdpm)$_3$ units.

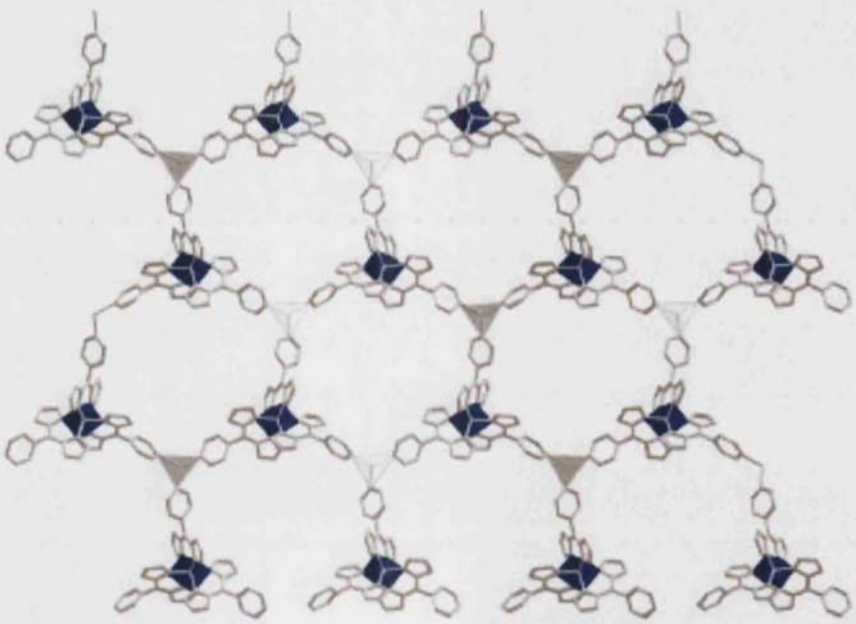

Figure 1.10a. The (10,3)-b net of {[Fe(4-pyrdpm)$_3$Ag$_3$](BF$_4$)$_3$}$_\infty$ viewed down the *c* axis.

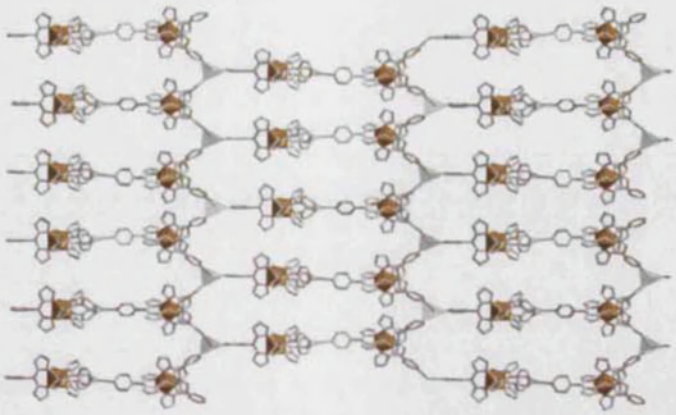

Figure 1.10b. The (10,3)-d net of $\{[Fe(4\text{-pyrdpm})_3Ag_3](OTf)_3\}_\infty$ viewed down the *c* axis.

1.3 Networks containing nitrile functional groups

Ligands containing nitrile groups have also been used in the formation of metal organic frameworks. The nitrile group is polarizable so it is considered to be a soft ligand.[35, 36] Due to its soft nature, this linker tends to form strong bonds with soft metals such as silver(I), copper(I) and cadmium(II).[35, 36] As will be highlighted in the coming paragraphs, silver is the metal of choice by many authors.

1.3.1 Networks from silver and nitrile ligands

One of the first reported networks formed from nitrile connectors was $\{[Ag(C(CN)_3)]\}_\infty$[15, 37] This compound consists of double interpenetrated (6,3) honeycomb networks with the silver centres being three coordinated. When the network of $\{[Ag(C(CN)_3)]\}_\infty$ was reacted further with phenazine, $\{[Ag(C(CN)_3)(phenazine)]\}_\infty$ was formed.[37] Thus the *N*-heterocyclic phenazine ligand acted as a pillar to link the already formed networks of $\{[Ag(C(CN)_3)]\}_\infty$together.

Other compounds incorporating nitrile groups were formed from the ligands 1,3,5-tri(4-ethynylbenzonitrile)benzene (4-teb)[16, 38] and 1,3,5-tri(3-ethynyl benzonitrile)benzene (3-teb) (Figures 1.11a and 1.11b respectively).[39]

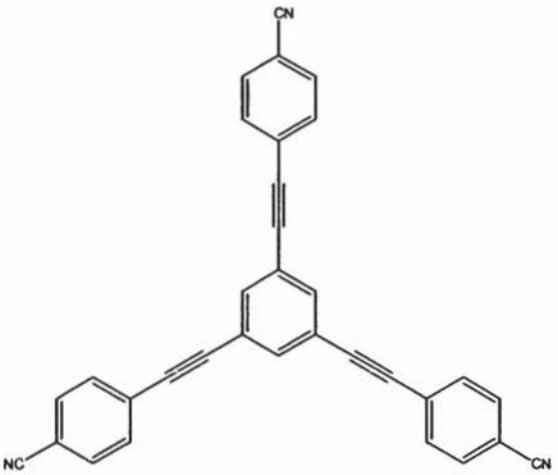

Figure 1.11a. 1,3,5-tri(4-ethynylbenzonitrile)benzene. (4-teb)

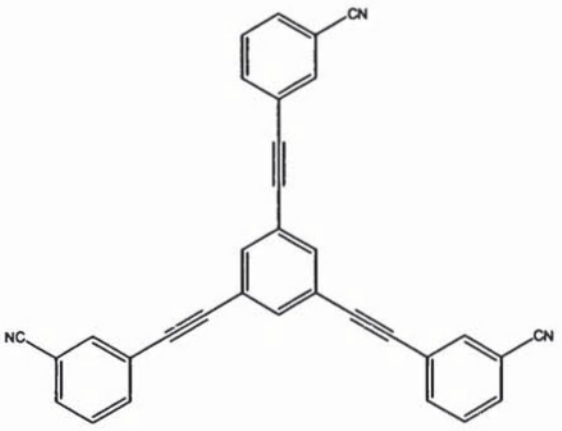

Figure 1.11b. 1,3,5tri(3ethynylbenzonitrile)benzene (3-teb).

4-teb is a tritopic ligand thus it has the potential to form (6,3), (10,3) or (12,3) architectures. When reacted with AgOTf, 4-teb formed $\{[Ag(4\text{-teb})(OTf)]\cdot benzene\}_{\infty}$[16] which is of the (6,3) type. Longer analogous connectors, such as 1,3,5-tri(4-butadiynylbenzonitrile)benzene[16] and 1,3,5-tri(4-(4-ethynylbenzonitrile)pheynylbenzene[16] reacted with AgOTf to form (6,3) type networks. The hexagonal spaces of the latter two compounds are larger than in $\{[Ag(4\text{-teb})(OTf)]\cdot benzene\}_{\infty}$

1.3.2 Zn, Cd and Cu nitrile networks

Apart from silver (I), other soft metals such as zinc(II), cadmium(II) and copper(I) have also been coordinated to nitrile containing ligands.[40, 41] These three metals have d^{10} configurations and, like silver(I), have the flexibility to adopt different geometries.

One example of a network having copper(I) as the metal centre is $\{[Cu(tctpm)]BF_4\cdot nitrobenzene\}_{\infty}$ (tctpm = 4,4',4'',4'''-tetracyanotetraphenylmethane).[40] The copper adopts a tetrahedral geometry and the ligands have tetrahedral symmetry around the methane carbon. The resulting network has an adamantanoid architecture.

1.3.3 Mixed metal frameworks

Heterobimetallic networks containing nitrile ligands have also been reported.[41, 42] A recent example of a mixed metal network is $\{[Co(4\text{-cydpm})_3]AgOTf\}_{\infty}$[42] (4-cydpm = 5-(4'-cyanophenyl)dipyrromethene). As in the case of $\{[Co(4\text{-pyrdpm})_3AgOTf\}_{\infty}$ (Section 1.2.6), the network was built in separate steps. Cobalt(III) was reacted with 4-cydpm to

form discrete $Co(4\text{-cydpm})_3$ units (Figure 1.12). These building blocks were then reacted with AgOTf to form $\{[Co(4\text{-cydpm})_3]AgOTf\}_\infty$ $\{[Co(4\text{-cydpm})_3]AgOTf\}_\infty$ belongs to the (10,3)-a family.

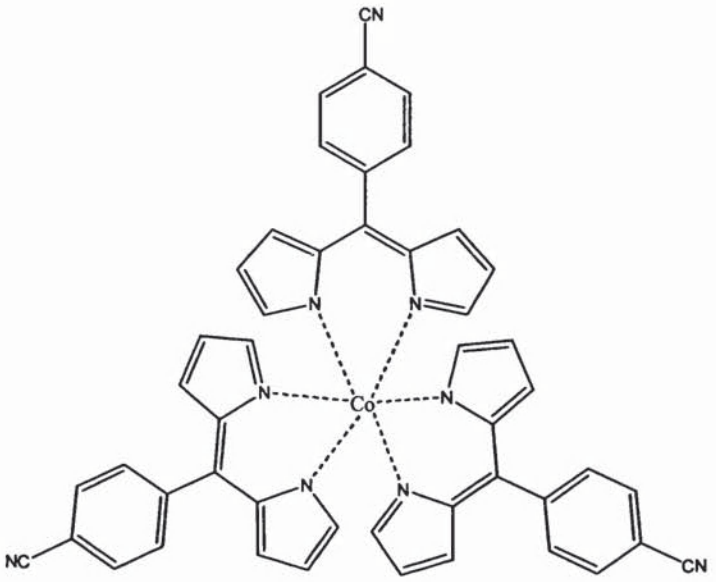

Figure 1.12. Diagrammatical representation of $[Co(4\text{-cydpm})_3]$.

1.3.4 Limitations of *N*-heterocyclic and nitrile ligands

Although ligands containing *N*-heterocyclic and nitrile groups have been used to produce a wide selection of metal organic networks, these ligands have limitations.

Networks formed from *N*-heterocyclic and nitrile ligands have residual cationic charges that arise due to the inability of the mentioned ligands to neutralise the charges of the metal centres. Thus the networks inevitably include counter ions. Such anionic guest inclusion is not a desirable feature because the ions take up pore space.

Another problem encountered in the synthesis of metal organic frameworks is interpenetration. The term interpenetration has been used to refer to the phenomenon when the free spaces of a network are filled by an independent network to which it is not bonded. Interpenetration offers enhanced stability to the networks and it is more likely to be found in compounds containing big pores. Interpenetration is often not a desirable feature because in such cases, the space inside the pores is not accessible for other applications.

1.3.5 Overcoming the limitations of *N*-heterocyclic and nitrile networks

Another way of forming more robust networks is by using secondary building units (SBUs).[24] SBUs offer enhanced stability to the networks and frameworks incorporating these units are less likely to be interpenetrated. SBUs consist of two or more metal centres that are bridged together through M-O-C units which act as building nodes.

One example of an SBU is the 'paddle-wheel' motif (Figure 1.13).[20] In this particular building block, two metal centres are bridged together by the carboxylate group to form $[M_2(CO_2)_4]$ units. This cluster acts as the building block for the network. As will be demonstrated, carboxylate ligands can form a wide variety of SBUs.

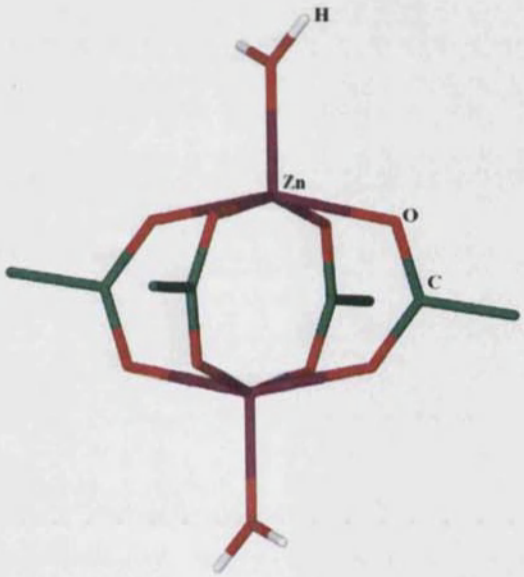

Figure 1.13. The 'paddle-wheel' SBU.

Carboxylates are negatively charged and thus the networks formed between metals and ligands containing these functional groups tend to be neutral overall. This eliminates the need for inclusion of counter ions and thus provides more free space inside the pores.

1.4 The chemistry of carboxylates

In order to coordinate to metals, carboxylic acids have to be converted to carboxylate groups. Carboxylic acids are deprotonated by a variety of organic and inorganic bases such as triethylamine,[43] pyridine[44] and sodium hydroxide.[45]

The carboxylate functional group is considered to be a hard ligand,[35, 36, 46] thus it typically forms strong bonds with hard metals. The carbon-oxygen bonds of this group are polar with a negative charge residing on the oxygen atoms. The choice of metals in the construction of carboxylate based networks are usually transition metals.[46] This group of metals adopt a wide range of geometries and this can manifest itself in the formation of networks with different architectures.[8]

1.4.1 Different binding modes of carboxylates

Carboxylate groups can form covalent or dative bonds to one or more metal centres. The ligating group can coordinate via either one or both oxygen atoms through a variety of binding modes. [47, 48]

1.4.1.1 Binding of the carboxylate to a single metal centre

The carboxylate group can be found coordinated to one metal centre only.[49,50, 51] This can occur through either one or both oxygen atoms. In the former case the binding is referred to as the monodentate binding mode (Figure 1.14a).[49] When the metal is coordinated to both oxygen atoms, the functional group acts as a bidentate ligand and this type of bonding has been named as the chelating bidentate mode (Figure 1.14b).[49]

Figures 14.a and 14.b. From left to right, diagrammatical representation of the monodentate and chelating bidentate binding modes of a carboxylate.

1.4.1.2 Binding of the carboxylate to two metal centres

Binding to two different metal centres is also possible and this can occur through one[52] or both oxygen atoms[4] of the carboxylate group. In the former case, the ligating atom bridges between two different metal centres (Figure 1.14c). This mode is referred to as the monodentate bridging mode. When both oxygen atoms take part in coordination, the binding mode is called bridging bidentate (Figure 1.14d).[49]

Figure 1.14c and 1.14d. From left to right, diagrammatical representation of the monodentate bridging and bridging bidentate binding modes of a carboxylate.

1.4.1.3 Binding of the carboxylate to three metal centres

Carboxylates groups also have the potential to bind to more than two metal centres. The most encountered case is the coordination of the functional group to three metal centres. In this case, one oxygen atom binds to one metal while the other part coordinates to two metal centres.[53] This method of binding is termed chelating bridging bidentate (Figure 1.14e).[49]

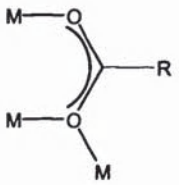

Figure 1.14e. Diagrammatical representation of the chelating bridging bidentate binding mode.

1.4.2 The ability of the carboxylate group to bind to different metal centres

As has been stated previously, the metals of choice for the assembly of networks are transition metals. Some *d*-block metals can adopt more than one geometry. For example, d^{10} metals such as zinc(II) and cadmium(II) have no ligand field stabilisation energy and hence different metal geometries are possible.[54] This can manifest itself in networks having metal centres with two different metal geometries within the same network. Examples of such cases are the 3-metal centre SBU type networks that will be discussed later in chapters 2 and 3.

1.4.3 The ability of carboxylates to form Secondary Building Units (SBUs)

As already described, SBUs tend to give enhanced stability to networks and also prevent interpenetration.[20] Reported SBUs relevant to this thesis will be discussed in the coming section.

1.4.3.1 'Paddle-wheel' type SBUs

One of the most recurring SBUs is based on the $Zn_2(OAc)_4$ (OAc = acetate) 'paddle-wheel' structure. The 'paddle-wheel' motif (Figure 1.15) consists of two metal centres and four carboxylate groups that coordinate in a bridging bidentate manner.

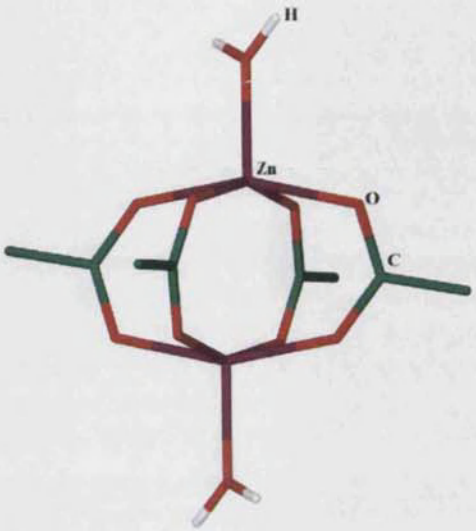

Figure 1.15. The 'paddle-wheel' type SBU present in $\{[Zn(tph)(H_2O)]\cdot(DMF)\}_\infty$ [20]

$\{[Zn(tph)(H_2O)]\cdot(DMF)\}_\infty$[20] (Figure 1.16) is based on the $Zn_2(OAc)_4$ SBU. The axial positions on the zinc centres are occupied by terminal aqua ligands thus preventing the network growing in the third dimension. On joining these SBUs together by benzene rings, a 2-D network is formed (Figure 1.16). Each building unit is connected to four other SBUs and the shortest pathway in the network consists of four ligands. Thus the network of $\{[Zn(tph)(H_2O)]\cdot(DMF)\}_\infty$ can be represented as (4,4).[21]

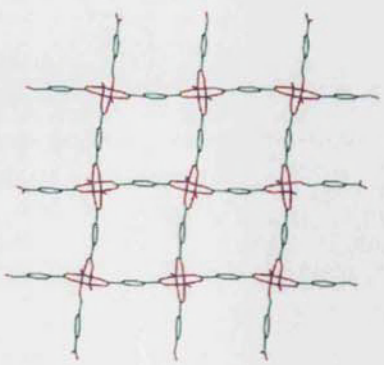

Figure 1.16. The structure of $\{[Zn(tph)(H_2O)]\cdot DMF\}_\infty$ The DMF guest molecules and hydrogen atoms have been removed for clarity.

The 2-D sheets of $\{[Zn(tph)(H_2O)]\cdot(DMF)\}_\infty$ stack in 'registry', with the voids of the network being occupied by guest DMF molecules. The coordinated water molecules were lost on heating, thus leaving behind vacant coordination sites on the zinc centres. These sites are then occupied by the oxygen atoms of the carboxylate groups from adjacent sheets. This effect changes the network architecture from 2-D to 3-D. [20]

Other networks containing 'paddle-wheel' SBUs include $\{[Fe_2(bpdc)_2(DMF)_2]\cdot(H_2O)_{0.4}(DMF)_{3.6}\}_\infty$ ($bpdc^{2-}$ = 4,4'-biphenyldicarboxylate),[55] and $\{[Cu_2(1,5\text{-dichloroterephthalate})_2(DMF)_2]\cdot(H_2O)(DMF)_{3.5}\}_\infty$[55]

1.4.3.2 Supertetrahedron ($[M_4(\mu_4\text{-}O)(O_2CR)_6]$) SBUs

Another SBU that received a lot of attention is the tetrahedral $[M_4(\mu_4\text{-}O)(O_2CR)_6]$ motif which was named by Yaghi et *al* as the supertetrahedron.[4] This consists of a tetrahedral oxide ion coordinated to 4 tetrahedral metal atoms. The carboxylate groups of this building unit coordinate to the metal centres in a bridging bidentate manner (Figure 1.17). When the SBUs are linked together by linear ligands, a cubic 3-D architecture is obtained (Figure 1.17).

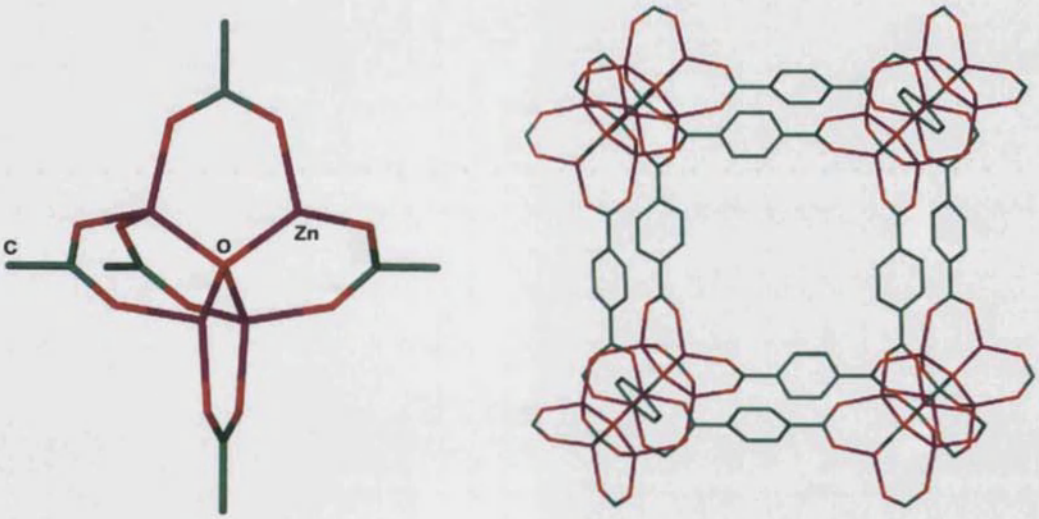

Figure 1.17. The supertetrahedron cluster SBU and the 3-D cubic network of $\{[Zn_4(\mu_4\text{-}O)(tph)_3]\cdot(DMF)_8(C_6H_5Cl)\}_\infty$

One network that is built from $[M_4(\mu_4\text{-}O)(O_2CR)_6]$ units is $\{[Zn_4(\mu_4\text{-}O)(tph)_3]\cdot(DMF)_8(C_6H_5Cl)\}_\infty$[4] This compound was first synthesised from $Zn(NO_3)_2\cdot6H_2O$ and H_2tph using a mixture of DMF/chlorobenzene in the presence of small amounts of

H_2O_2.[4] Et_3N was allowed to diffuse into the solution slowly so as to deprotonate the ligand and thus initiate network formation. Other synthetic pathways for the formation of this compound have since been reported by other authors.[6]

1.4.3.3 Three metal centre SBUs

SBUs consisting of metals having two different geometries are also possible.[56-61] The most common types of these consist of an octahedral unit sandwiched between two tetrahedral or trigonal bipyramidal metal centres. Examples of networks built from 3-metal centre units are $\{[Zn_3(tph)_3(MeOH)_2]\cdot 4MeOH\}_\infty$[61] and $\{[Zn_3(tph)_3(DEF)_2]\cdot DEF\}_\infty$[56]

In the structure of $\{[Zn_3(tph)_3(MeOH)_2]\cdot 4MeOH\}_\infty$[61] the SBUs consist of an octahedral metal sandwiched between two trigonal bipyramidal zinc centres (Figure 1.18). The terminal methanol molecules are coordinated to each of the trigonal bipyramidal zinc centres thus halting the network growth in these directions.[61]

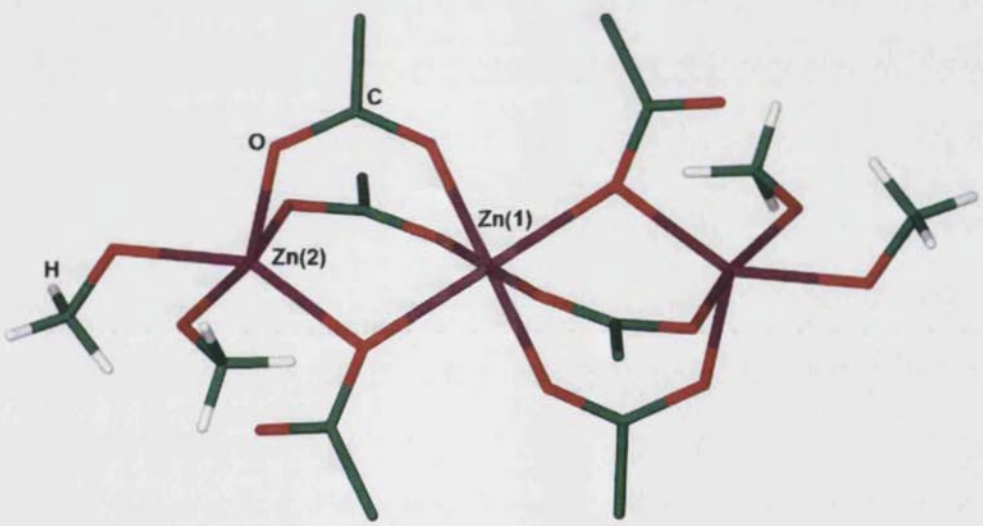

Figure 1.18.[61] The three metal centre SBU of $\{[Zn_3(tph)_3(MeOH)_2]\cdot 4MeOH\}_\infty$

The network of $\{[Zn_3(tph)_3(DEF)_2]\cdot DEF\}_\infty$[56] is also based on a octahedral zinc unit in between two trigonal bipyramidal metal centres. This network has a (3,6) topology that consists of triangular shaped pores (Figure 1.19).

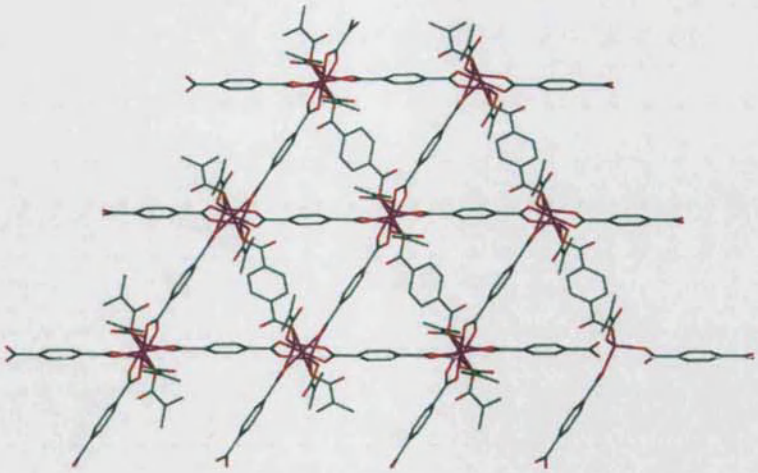

Figure 1.19.[56] The (3,6) network of $\{[Zn_3(tph)_3(DEF)_2]\cdot DEF\}_\infty$ as viewed down the *a* axis.

A similar type of 3-metal centre SBU consists of two tetrahedral and one octahedral metal units. This type of building block can be observed in the networks of $\{[Zn_3(tph)_3(H_2O)_3]\cdot 4DMF\}_\infty$[57] $\{[Zn_3(OH)_2(tph)_2]\cdot 2DEF\}_\infty$[58] and $\{[Zn_5(OH)_4(tph)_3]\cdot 2DMF\}_\infty$[60]

$\{[Zn_3(OH)_2(tph)_2]\cdot 2DEF\}_\infty$[58] was obtained from the reaction between $Zn(NO_3)_2\cdot 6H_2O$ and H_2tph in *N,N*-diethylformamide (DEF). The structure of $\{[Zn_3(OH)_2(tph)_2]\cdot 2DEF\}_\infty$ consists of $[Zn_3O_8(OH)_2]_n$ infinite chains of alternating tetrahedral-octahedral-tetrahedral metal centres (Figure 1.20). The zinc atoms of the SBU are linked together by μ_3-hydroxyl groups and bridging bidentate carboxylate moieties.

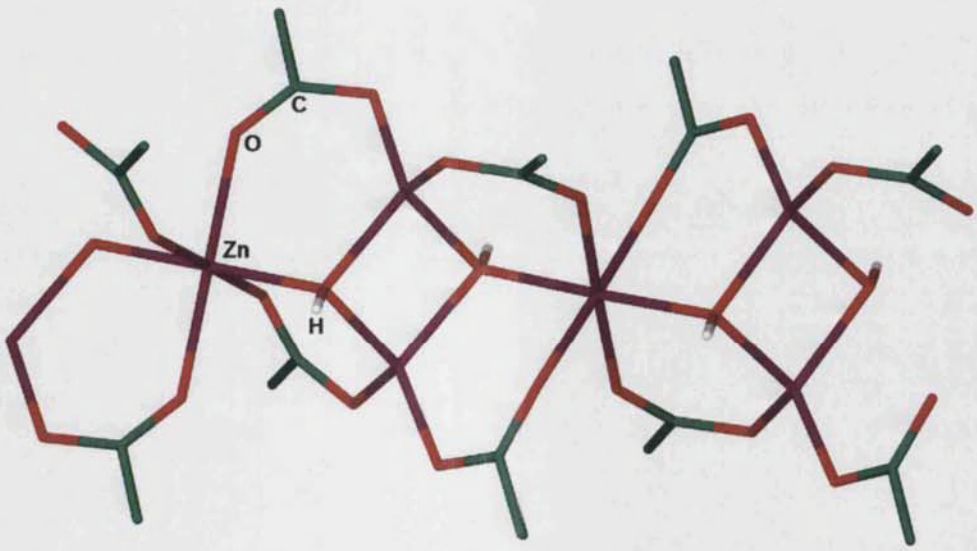

Figure 1.20. The 1-D infinite chain SBU of $\{[Zn_3(OH)_2(tph)_2]\cdot 2DEF\}_\infty$

The 1-D $[Zn_3O_8(OH)_2]_n$ chains are bridged into a 3-D network by the tph^{2-} ligands (Figure 1.21). The network has rhombic shaped pores which are filled by guest DEF molecules.

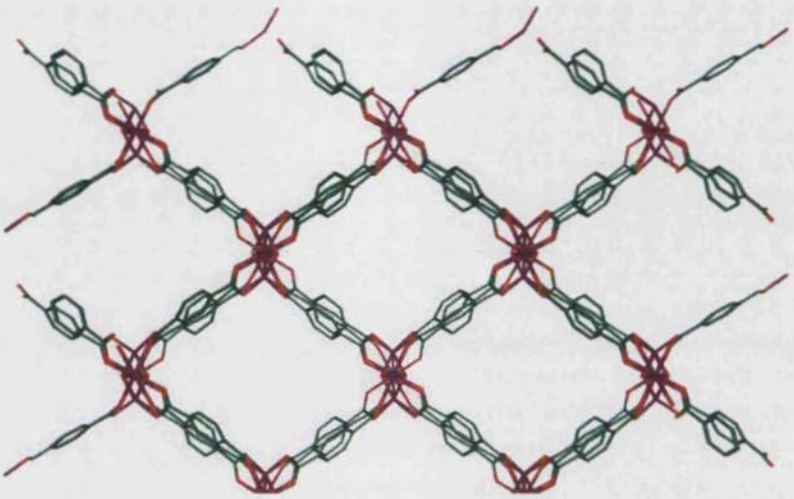

Figure 1.21.[58] The 3-D network of $\{[Zn_3(OH)_2(tph)_2]\cdot 2DEF\}_\infty$ The DEF guest molecules and hydrogen atoms are removed for clarity.

$\{[Zn_5(OH)_4(tph)_3]\cdot 2DMF\}_\infty$[60] is also based on the 3-metal centre tetrahedral-octahedral-tetrahedral unit. The zinc centres are linked together by μ_3-hydroxyl and carboxylate groups into 1-D infinite chains. The chains are in turn connected together by the benzene rings of tph^{2-} ligands to form a 3-D network (Figures 1.22a and 1.22b respectively).

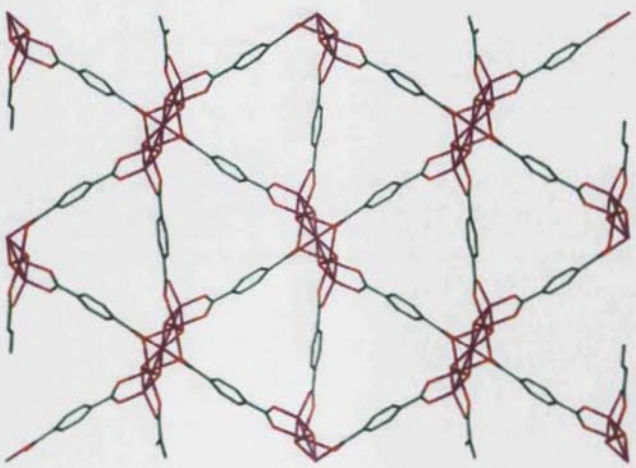

Figure 1.22a.[60] The (3,6) sheets of $\{[Zn_5(OH)_4(tph)_3]\cdot 2DMF\}_\infty$ Hydrogen atoms and guest DMF molecules are removed for clarity.

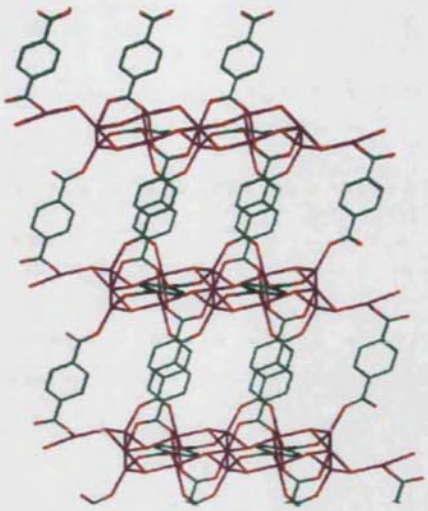

Figure 1.22b. The network of $\{[Zn_5(OH)_4(tph)_3]\cdot 2DMF\}_\infty$

$\{[Zn_5(OH)_4(tph)_3]\cdot 2DMF\}_\infty$ has triangular shaped pores which are of comparable shape to the voids of $\{[Zn_3(tph)_3(DEF)_2]\cdot DEF\}_\infty$ (Figure 1.19) with the difference that the former network is 3-D while the latter is 2-D. The main reason for this difference lies in the composition of the SBUs. The terminal methanol molecules in the SBU of $\{[Zn_3(tph)_3(DEF)_2]\cdot DEF\}_\infty$ (Figure 1.18) halts the growth of the network in the third dimension.

1.4.4 Linear dicarboxylate ligands other than 1,4-benzenedicarboxylate

Another linear dicarboxylate ligand that has received considerable attention is 4,4'-biphenyldicarboxylate ($bpdc^{2-}$).[62] In general, long linkers tend to form interpenetrated networks but, on the inclusion of SBUs, $bpdc^{2-}$ can also form non-interpenetrated networks.

Some networks having $bpdc^{2-}$ as the organic ligand include the 'paddle-wheel' type $\{[Fe_2(bpdc)_2(DMF)_2]\cdot(H_2O)_{0.4}(DMF)_{3.6}\}_\infty$,[55] $\{[Zn_3(OH)_2(bpdc)_2]\cdot 4DEF\cdot 2H_2O\}_\infty$ which has an isostructural network to that of $\{[Zn_5(OH)_4(tph)_3]\cdot 2DMF\}_\infty$[60] described in Section 1.4.3.3 and $\{[Zn_3(bpdc)_3(DMF)_2]\cdot 4DMF\}_\infty$ reported by Brammer and co-workers.[63] The latter structure will be described in more detail in Chapter 2.

1.4.5 Networks from non linear dicarboxylate ligands

The discussions about dicarboxylates were centred on linear linkers. Carboxylate linkers having the functional groups oriented at any angle rather than 180° can also be used to generate networks. Examples include 1,2- and 1,3-bdc^{2-} (bdc^{2-} =

benzenedicarboxylate),[53] 1,3,5-benzenetricarboxylate,[52, 61, 64-66] 1,3,5-tri(4-benzoate)benzene[2] and 3,3',5,5'-biphenyltetracarboxylate.[17, 18] The change in orientation of the functional groups with respect to each other causes the formation of networks with different topologies.

1.4.5.1 Structural isomers of 1,4-benzenedicarboxylate

1,2-benzenedicarboxylate (1,2-bdc^{2-}) and 1,3-benzenedicarboxylate (1,3-bdc^{2-}) are positional isomers of tph^{2-} (tph^{2-} = 1,4-benzenedicarboxylate). The carboxylate functional groups in the two isomers are placed on the benzene ring at 60° and 120° angles respectively (Figure 1.23). When 1,2-bdc^{2-} and 1,3-bdc^{2-} were coordinated to metal centres, the alteration of the position of the carboxylate groups manifested itself in the geometry of the networks.

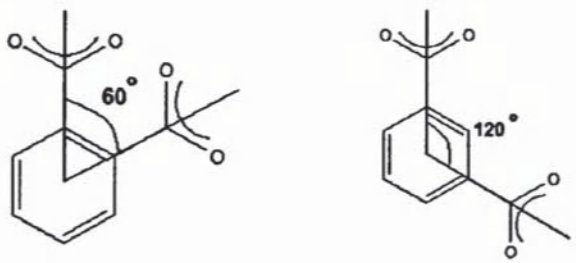

Figure 1.23. From left to right, diagrammatical representation of 1,2-benzenedicarboxylate (1,2-bdc^{2-}) and 1,3-benzenedicarboxylate (1,3-bdc^{2-}) showing the 60° and 120° angles between the functional groups respectively.

For example, when 1,2-bdc^{2-} was reacted with $Cd(Ac)_2 \cdot 2H_2O$ in the presence of 4,4'-bipyridine (4,4'-bipy), a helical structure with the formula $\{[Cd(H_2O)(1,2\text{-bdc})(4,4'\text{-bipy})]\}_\infty$ was obtained (Figure 1.24).[53]

When a similar reaction was carried out using the isomeric 1,3-bdc^{2-}, $\{[Cd(1,3\text{-bdc})(4,4\text{-bipy}]\}_\infty$ was formed.[53] This compound has a structure that consists of ribbon-like chains.

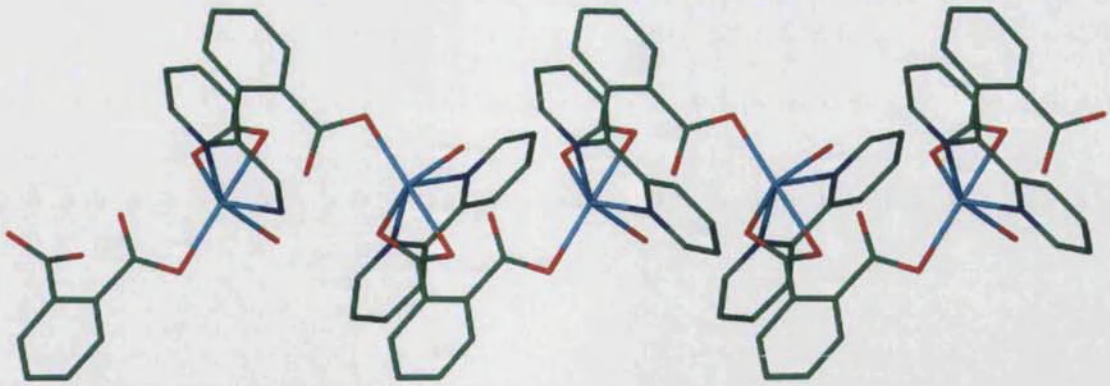

Figure 1.24. The helical network structure observed in $\{[Cd(H_2O)(1,2\text{-bdc})(4,4'\text{-bipy})]\}_\infty$

1.4.5.2 Networks from 1,3,5-benzenetricarboxylate (btc^{3-})

The carboxylate groups of 1,3,5-benzenetricarboxylate (btc^{3-}) are positioned at 120° on the benzene ring. Due to this, btc^{2-} can be considered to be analogous to 2,4,6-tris(4-pyridyl)-1,3,5-triazine, 1,3,5-tri(4-ethynylbenzonitrile)benzene and the nuclear complexes of $[M(4\text{-pyrdpm})_3]$ and $[M\text{-}(4\text{-cydpm})_3]$ (M = Fe or Co) which were described in sections 1.2.6 and 1.3.3 respectively.

Yaghi and coworkers reported a series of networks using zinc and btc^{3-}. The topology of these network was dependent on the reaction conditions, such as the solvent and the strength of the base.[66] For example, with acetate as the conjugate base and water as the solvent, a 1-D network was obtained. When the reaction was conducted in ethanol using pyridine as the base, the network formed was 2-D. A 3-D network with the formula $\{[Zn_2(btc)(NO_3)(EtOH)_3]\cdot(H_2O)(EtOH)_2\}_\infty$ resulted when pyridine was substituted by triethylamine.[66]

Another network containing btc^{3-} as the organic unit is $\{[Co(btc)(py)_2]\cdot py_{2/3}\}_\infty$ (py = pyridine) (Figure 1.25).[65] The compound has a structure that consists of 2-D sheets which are held together by $\pi\cdots\pi$ stacking between the pyridine ligands.

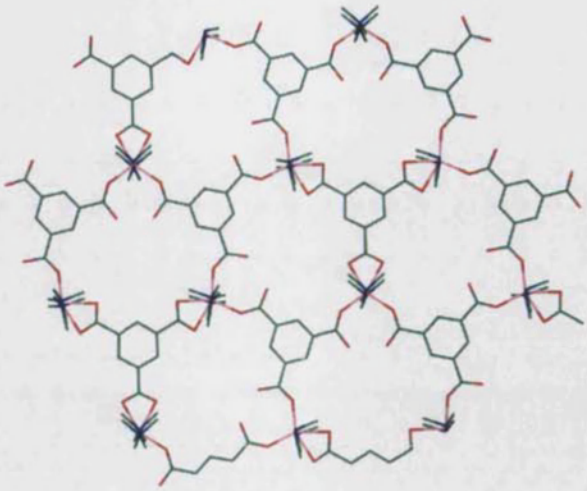

Figure 1.25. The 2-D sheets of $\{[Co(btc)(pyridine)_2]\}_\infty$

1.4.5.3 Networks from 1,3,5-tri(4-benzoate)benzene (btb^{3-})

1,3,5-tri(4-benzoate)benzene (btb^{3-}) (Figure 1.26) also has 3 carboxylate functional groups positioned at 120° with respect to one another. Therefore btb^{3-} can be regarded as an enlarged analogue of btc^{3-}.

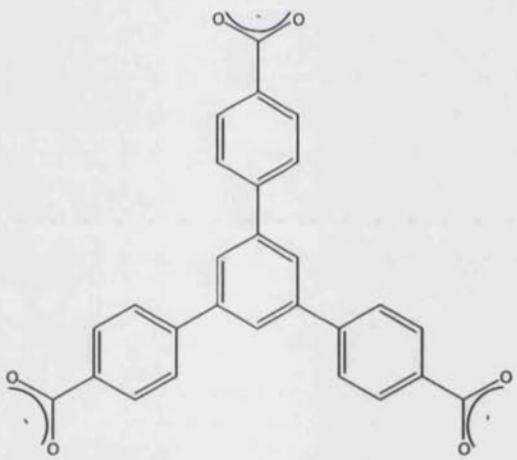

Figure 1.26. Diagrammatic representation of 1,3,5-tri(4-benzoate)benzene.

When H_3btb was reacted with $Zn(NO_3)_2 \cdot 6H_2O$, $\{[Zn_4(\mu_4\text{-}O)(btb)_2] \cdot (DEF)_{15}(H_2O)_3]\}_\infty$ was obtained (Figure 1.27).[4] This network consists of $[M_4(\mu_4\text{-}O)(O_2CR)_6]$ type SBUs but the overall topology of $\{[Zn_4(\mu_4\text{-}O)(btb)_2] \cdot (DEF)_{15}(H_2O)_3]\}_\infty$ varies from the cubic net formed by linking the tetrahedron SBUs by linear connectors (Section 1.4.3.2).

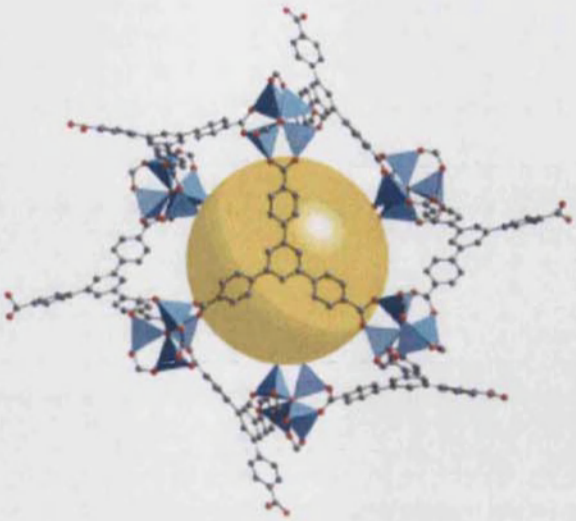

Figure 1.27.[2] The 3-D network of $\{[Zn_4(\mu_4\text{-}O)(btb)_2]\cdot(DEF)_{15}(H_2O)_3]\}_\infty$ The SBUs are represented as a collection of blue triangular pyramids while the space inside the pore is represented as a yellow sphere.

1.4.5.4 Networks built from tetracarboxylates

Ligands containing four carboxylate functional groups have also been as building blocks. 3,3',5,5'-biphenyltetracarboxylate[17] (Figure 1.28) and 1,3,5,7-adamantanetetracarboxylate[20] are two examples.

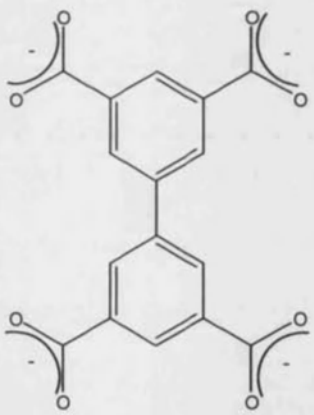

Figure 1.28. Diagrammatical representations of 3,3',5,5'-biphenyltetracarboxylate.

When reacted with $Co(NO_3)_2\cdot 6H_2O$ at 75°C for two days, 3,3',5,5'-biphenyldicarboxylate ($bptc^{4-}$) formed a mixture of $\{[Co_2(bptc)(H_2O)_5]\cdot(DMF)_3(EtOH)(H_2O)_4\}_\infty$ and $\{[Co_2(bptc)(H_2O)(DMF)_2]\cdot(DMF)(H_2O)_{1.5}\}_\infty$ (Figures 1.29a and 1.30a respectively).[17] However, the latter could be obtained in a pure form by heating the reaction mixture for a longer period.

$\{[Co_2(bptc)(H_2O)_5]\cdot(DMF)_3(EtOH)(H_2O)_4\}_\infty$ consists of two distinct SBUs that have square and rectangular shapes. The $bptc^{4-}$ connectors link the SBUs together into a NbO type structure (Figure 1.29b).

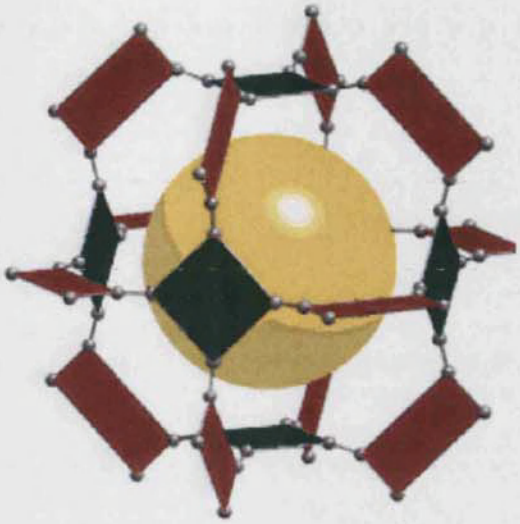

Figure 1.29a. The network of $\{[Co_2(bptc)(H_2O)_5]\cdot(DMF)_3(EtOH)(H_2O)_4\}_\infty$ The SBUs are coloured red and green while the empty space inside the pore is represented as yellow sphere.

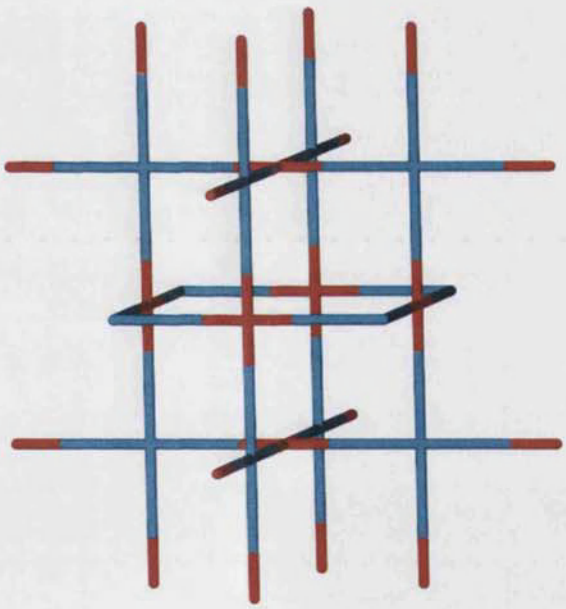

Figure 1.29b. The NbO structure. Red and blue sticks represent oxygen and niobium atoms respectively.

On the other hand, the network of $\{[Co_2(bptc)(H_2O)(DMF)_2]\cdot(DMF)(H_2O)_{1.5}\}_\infty$ is based on tetrahedral- and rectangular-shaped SBUs that are linked together into a 3-D PtS type net (Figure 1.30b).

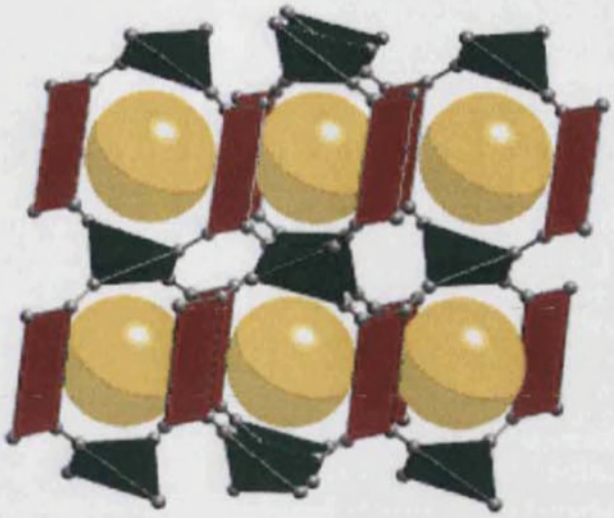

Figure 1.30a. The network of $\{[Co_2(bptc)(H_2O)(DMF)_2]\cdot(DMF)(H_2O)_{1.5}\}$ consisting of rectangular and tetrahedral shaped SBUs. The free space inside the pores is represented as yellow spheres.

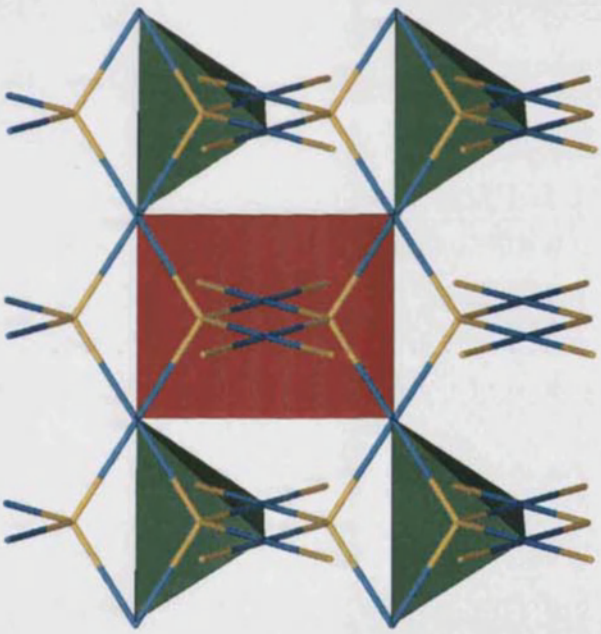

Figure 1.30b. The PtS structure. Yellow and blue sticks represent sulphur and platinum respectively. Green tetrahedra and a red square were added in the picture to aid comparison with Figure 1.30a.

When $Cu(NO_3)_2\cdot 2.5H_2O$ was used instead of $Co(NO_3)_2\cdot 6H_2O$, the network obtained, $\{[Cu_2(bptc)(H_2O)_2]\cdot(DMF)_3(H_2O)\}_\infty$[18] consisted of 'paddle-wheel' type SBUs. Due to the geometry of the ligand, the SBUs were linked together into a NbO type net (Figure 1.31).

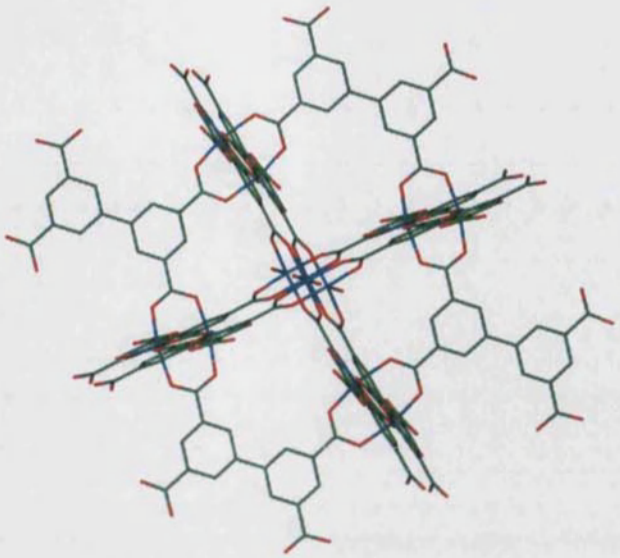

Figure 1.31. The NbO type net of $\{[Cu_2(bptc)(H_2O)_2]\cdot(DMF)_3(H_2O)\}_\infty$

1.4.6 Properties of metal organic frameworks

Apart from the diverse network topologies, metal organic frameworks have attracted attention for their intrinsic properties. Catalytic functions, gas adsorption [2-5, 18 6, 7, 67] and optical properties [47, 51, 52, 68, 69] are some of the potential applications demonstrated by these materials.

1.4.6.1 Network catalytic properties

Several metal organic frameworks have been reported to show catalytic properties. The catalytic centre in a metal-organic framework is confined within the architecture of the network and this can produce enhanced stability,[70] a feature that is not observed in molecular catalysts.

The previously discussed 'paddle-wheel' networks reported by Yaghi and co workers[20] have been found to possess catalytic properties. For example, $\{[Zn(tph)(H_2O)]\cdot DMF\}_\infty$[20] catalysed the esterification reaction of 4-*tert*-butylbenzoic acid.[6] $\{[Zn_4(\mu_4\text{-}O)(tph)_3]\cdot(DMF)_8(C_6H_5Cl)\}_\infty$ also reported by Yaghi and coworkers,[4] was tested for esterification catalytic properties. While $\{[Zn_4(\mu_4\text{-}O)(tph)_3]\cdot(DMF)_8(C_6H_5Cl)\}_\infty$ has a tenfold larger surface area than $\{[Zn(tph)(H_2O)]\cdot DMF\}_\infty$, it showed no catalytic activity.[6] Muller and coworkers[6] suggest that the vacant sites on the zinc centres in the latter give the network catalytic properties. These vacant sites result after the removal of the coordinated water molecules.

The 1-D network of $\{[Ti(\mu_{2,7}\text{-dihydroxynaphthalene})_2(py)_2]\}_\infty$ and the 2-D network of $\{Ti(\mu_{2,7}\text{-dihydroxynaphthalene})_2(4\text{-picoline})_2]\cdot 4\text{-picoline}_{0.5}\}_\infty$ were reported to catalyse the Ziegler-Natta polymerisation of ethene or propene.[71]

When incorporated into networks, $\{Zr(O\textit{i}Bu)_2(anthracenebisresorcinol)\}_\infty$ and $\{Ti(O\textit{i}Pr)Cl(anthracenebisresorcinol)\}_\infty$ were found to catalyse the Diels-Alder addition of acrolein and 1,3-cyclohexadiene (Figure 1.32).[72, 73] The reaction proceeded to 98% completion within three hours. The observed reaction rate is much higher than that obtained when the reaction was conducted in the presence of starting materials only.

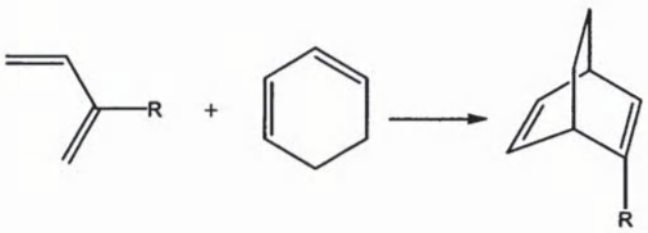

Figure 1.32. Diagrammatical representation of the Diels-Alder addition of acrolein and 1,3-cyclohexadiene.

The network of $\{[Cu_3(btc)_2]\}_\infty$ catalyses two reactions that are extensively used in industry namely, the isomerisation of α-pinene oxide into campholemic aldehyde (Figure 1.33a) and the rearrangement of the ethylene acetal of 2-bromopropiophenone into 2-chloroethyl-2-phenylpropanoate (Figure 1.33b).[74] Campholemic aldehyde is a fragrant compound while 2-chloroethyl-2-phenylpropanoate is an active anti-inflammatory agent.

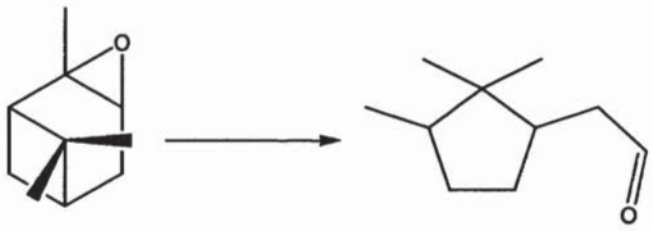

Figure 1.33a. The isomerisation of α-pinene oxide into campholemic aldehyde.

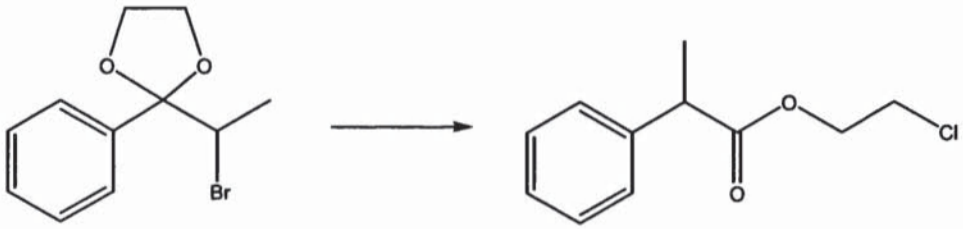

Figure 1.33b. The rearrangement of the ethylene acetal of 2-bromopropiophenone into 2-chloroethyl-2-phenylpropanoate.

Catalytic properties are not exclusive to metal organic frameworks having carboxylates as the organic linkers. For example, $\{[Cd(4\text{-btapa})_2(NO_3)_2]\cdot 6H_2O\cdot 2DMF\}_\infty$[75] (4-btapa = 1,3,5-benzenetricarboxylic acid tris [N-(4-pyridyl)amide] Figure 1.34) catalyses the condensation reaction between benzaldehyde and malonitrile.

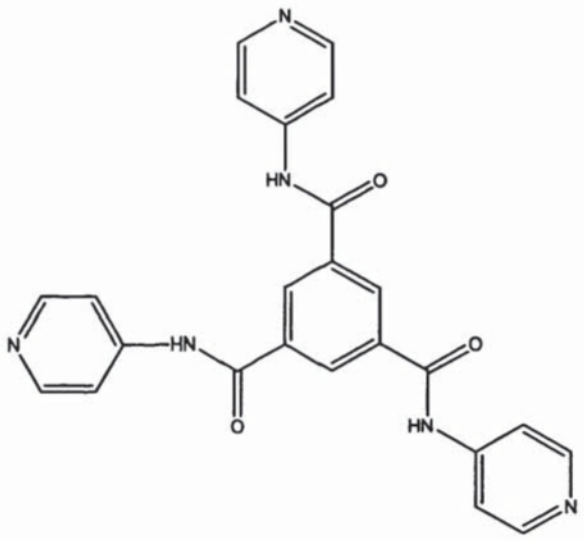

Figure 1.34. Diagrammatical representation of 1,3,5-benzenetricarboxylic acid tris [N-(4-pyridyl)amide].

1.4.6.2 Network gas storage abilities

Apart from the various possible architectures and catalytic properties, metal organic frameworks have attracted attention mostly for their ability to store gases, such as N_2, H_2 and CH_4. The ability to store hydrogen gas makes MOFs potential 'on-board' hydrogen storage materials for use in the car industry and thus make hydrogen an alternative to fossil fuels.[1, 76, 77]

Zeolites and active carbons can also store gases within their pores but metal organic frameworks are much better at doing so due to their higher surface areas and faster molecular traffic.[6]

The gas adsorption properties of the α-Po network of $\{[Zn_4(\mu_4\text{-}O)(tph)_3]\cdot(DMF)_8(C_6H_5Cl)\}_\infty$ commonly referred to as MOF-5 (Figure 1.17), have been studied extensively by various scientists.[5, 44, 78, 79] The surface area of this specific network was recorded at 3400 m^2g^{-1}, and a total of 1.13 wt% hydrogen adsorption was observed.[6] The relatively large aperture to the cavities (1.1-1.3nm^2) aids the fast movement of gases in and out of the pores (molecular traffic). A series of networks based on the $[M_4(\mu_4\text{-}O)(O_2CR)_6]$ SBU, such as $\{[Zn_4(\mu_4\text{-}O)(ndc)_3]\}_\infty$[20] ($ndc^{2-}$ = 2,6-naphthalenedicarboxylate) and $\{[Zn_4(\mu_4\text{-}O)(btb)_2]\}_\infty$[80] have also demonstrated gas storage behaviour. The surface areas of the latter two compounds are 1750 m^2g^{-1} and 4500 m^2g^{-1} respectively.

$\{[Cu_3(1,3,5\text{-}btc)_2]\}_\infty$[81] has attracted the interest of many authors.[82-84] This network consists of 'paddle-wheel' type SBUs that are linked together by 1,3,5-benzenetricarboxylate ions. Like the previous examples, this compound was found to adsorb gases into its pores. The surface area of $\{[Cu_3(1,3,5\text{-}btc)_2]\}_\infty$ was found to be 1820 m^2g^{-1}.[6] Neutron diffraction studies conducted on the gas loaded network revealed that, at low partial pressures, deuterium atoms show preferential binding to the copper centres inside the pores.[85] The reason for the preferential site packing is believed to be due to the Lewis-acidic properties of the metal centres. Mueller and co-workers have studied the use of $\{[Cu_3(1,3,5\text{-}btc)_2]\}_\infty$ for gas purification.[6] $\{[Cu_3(1,3,5\text{-}btc)_2]\}_\infty$ removes electron rich molecules such as amines, ammonia, water, alcohols and sulphur containing compounds from natural gas.

The ability of metal organic framework to selectively remove one compound from a mixture of gases gives these compounds an additional analytical application. Chen and co-workers[86] used the doubly interpenetrated network of $\{[Zn(tph)(4,4'\text{-}bipy)_{0.5}]\}_\infty$ as a gas chromatographic column, and showed that this network showed selective binding of alkanes from a mixture of gases. In another publication, Chen and co-workers[87] showed that the pore size of a specific type of metal organic network can be tapered to discriminate towards selective binding of a particular gas (Figure 1.35). This was done by varying the

length of the ligands and thus the size of the pores. The resulting networks then selectively bound molecules that fitted inside the pores. They demonstrated that $\{[Cu_2(fma)_2(bpe)_{0.5}]\}_\infty$ (fma^{2-} = fumarate, bpe = *trans*-bis(4-pyridyl)ethylene) separated hydrogen from a mixture of hydrogen/argon, and carbon dioxide from a mixture of carbon dioxide/methane.

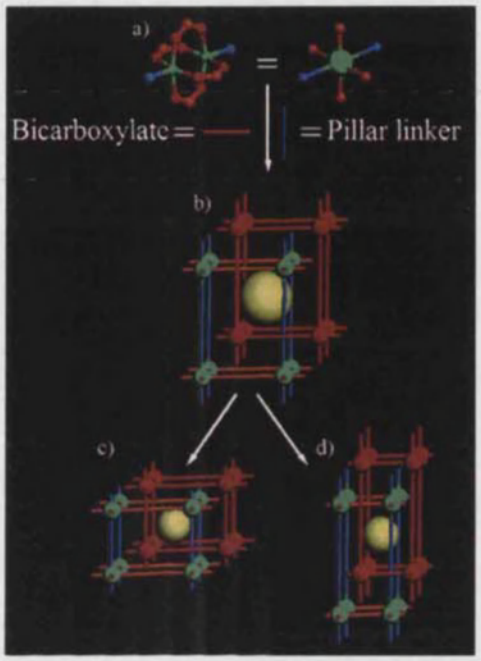

Figure 1.35. Schematic representation of the tunability of the pores as suggested by Chen and co-workers.[87]

1.4.6.3 Optical properties exhibited by metal organic frameworks

Metal organic frameworks can also be of use in non-linear optics industry[52] due to the photic properties exhibited by various networks.[47, 52, 68, 88, 89]

For example, $\{[Cd(bpy)(tph)(H_2O)]\}_\infty$[47] (bpy = 2,2'-bipyridine) consists of 2-D chains. The phenyl ring of the tph^{2-} ligand is twisted relative to the carboxylate groups, with torsion angles between two groups and the benzene ring being 5.63° and 12.58°. $\pi\cdots\pi$ stacking between the benzene groups of the tph^{2-} and bpy as well as hydrogen bonding between adjacent chains pack the 2-D networks in a 'pseudo' 3-D network. This MOF exhibited two intense adsorption bands in the UV region (253 and 301 nm) and a fluorescent emission at 379 nm.[47] The radiation emitted was several orders of magnitude greater in intensity than that exhibited by the starting materials. This emission results from π-π^* transition of the twisted benzene ring of the tph^{2-} ligand.

$\{Na_3[Cd_3(btc)_3(H_2O)_2]\cdot 6H_2O\}_\infty$[52] also showed luminescent properties. When excited at a radiation of 320 nm, the metal organic framework exhibited an intense and broad emission band with a λ_{max} at 449. The authors assigned this emission due to ligand-metal charge transfer.

He and co-workers[68] reported that when excited with a radiation of a wavelength at 318 nm, the network of $\{[ZnNa(1,2\text{-bdc})_2]\cdot NH_2(CH_3)_2\}_\infty$ showed a strong emission peak with a λ_{max} at 421 nm. This was also assigned to a ligand-metal charge transfer.

The network of $\{[Zn_4(\mu_4\text{-O})(tph)_3]\cdot(DMF)_8(C_6H_5Cl)]\}_\infty$, MOF-5, also attracted interest for its photoluminescenct properties. Civalleri and co-workers[88] have conducted *ab-initio* calculations on MOF-5 and predicted that the SBU of $[Zn_4(\mu_4\text{-O})(O_2CR)_6]$ (Section 1.4.3.2) has similar properties to ZnO nanostructures. A similar study was previously conducted by Bordiga and co-workers.[90] They predicted that, after excitation, MOF-5 emits radiation with a peak having λ_{max} at 525 nm, which is due to ligand-metal charge transfer. The intensity of the observed peak is 16 times greater than that of ZnO nanoparticles. The authors stated that the organic part of the metal-organic framework traps photons that are later transferred to the $[Zn_4(\mu_4\text{-O})(O_2CR)_6]$ cluster.

Lanthanide metals have f-orbital electrons, and electronic transitions between these orbitals give rise to luminescence. Thus metal organic frameworks consisting of lanthanides as the metal centres are more suitable for luminescent applications than transition metals. Two examples of networks consisting of lanthanides that have luminescent activity are $\{[Eu_3(\mu\text{-OH})_4(2,5\text{-pydc})_3(H_2O)_4]\}_\infty$[91] ($pydc^{2-}$ = pyridinedicarboxylate) and $\{[Eu_2(fumarate)_2(oxalate)(H_2O)_4]\cdot 4H_2O\}_\infty$[92]

1.5. Aims of thesis

Although many networks have been reported to date, there is little knowledge with regards to the sensitivity of the reactions with variations in pH, temperature, pressure and solvent composition. Thus the effects of these factors on the reaction between $Zn(NO_3)_2\cdot 6H_2O$ and H_2tph were investigated.

The metal organic frameworks formed from the reaction between $Cd(NO_3)_2 \cdot 4H_2O$ and tph^{2-}, and the influence of the factors mentioned in the previous paragraph on the outcome of this particular reaction are discussed in Chapter 3. The stability of some of the novel networks reported herein towards guest removal was investigated.

Two guest free networks, discussed in Chapter 3, were tested for potential acylation reactions of phenol. The results obtained from this study are outlined at the end of the chapter. Gas adsorption measurements for these cadmium containing networks are reported in Chapter 4.

Another project aim was to synthesise ligands that can form neutral networks consisting of SBUs in an analogous way to dicarboxylates. Chapter 5 shows that bis-β-diketonates can fulfil this role.

Several bimetallic networks containing the functionalised β-diketonato ligand, 3-cyano-2,4-pentanedionato are reported in Chapter 6. The dependency of the network topology on the starting metal salt and the solvent composition is also described.

References:

1. J.Y.Lee; J.Li; J.Jogiello, *J.Sol.State.Chem.* **2005,** 178, 2527.
2. A.R.Millward; K.S.Park; J.L.C.Rowsell; O.M.Yaghi, *J.Am.Chem.Soc.* **2004,** 126, 5666.
3. M.Eddaoudi; J.Kim; N.L.Rosi; D.T.Vodak; J.Wachter; M.O'Keeffe; O.M.Yaghi, *Science* **2002,** 295, 469.
4. M.Eddaoudi; H.Li; M.O'Keeffe; O.M.Yaghi, *Nature* **1999,** 402, 276.
5. N.L.Rosi; J.Eckert; M.Eddaoudi; D.T.Vodak; J.Kim; M.O.Keeffe; O.M.Yaghi, *Science* **2003,** 300, 1127.
6. U.Mueller; M.Schubert; F.Teich; H.Puetter; K.Schierlearndt; J.Pastre, *J.Mater.Chem.* **2006,** 16, 626.
7. S.Kitagawa; R.Kitaura; S.Noro, *Angew.Chem.Int.Ed.* **2004,** 43, 2334.
8. B.Moulton; M.J.Zaworotko, *Chem.Rev.* **2001,** 101, 1629.
9. P.J.Hagrman; D.Hagrman; J.Zubieta, *Angew.Chem.Int.Ed.* **1999,** 38, 2638.
10. R.Robson, *J.Chem.Soc.Dalton.Trans.* **2000,** 3735.
11. K.Biradha; Y.Hongo; M.Fujita, *Angew.Chem.Int.Ed.* **2000,** 39, 3843.
12. K.Biradha; M.Fujita, *J.Chem.Soc.* **2002,** 124, 2568.
13. M.Zeng; X.Feng; X.J.Chen, *J.Chem.Soc.Dalton.Trans.* **2004,** 2217.
14. K.A.Hirsch; S.R.Wilson; J.S.Moore, *Inorg.Chem.* **1997,** 36, 2960.
15. S.R.Batten; B.F.Hoskins; R.Robson, *New.J.Chem.* **1998,** 173.
16. G.B.Gardner; Y.H.Kiang; S.Lee; A.Asgaonkar; D.Venkataraman, *J.Am.Chem.Soc.* **1996,** 118, 6946.
17. B.Chen; N.W.Ockwig; F.R.Fronczek; D.S.Contreras; O.M.Yaghi, *Inorg.Chem.* **2005,** 44, 181.
18. B.Chen; N.W.Ockwig; A.R.Millward; D.S.Contreras; O.M.Yaghi, *Angew.Chem.Int.Ed.* **2005,** 44, 4745.
19. M.Eddaoudi; T.L.Groy; O.M.Yaghi; H.Li, *J.Am.Chem.Soc.* **1998,** 120, 8571.
20. M.Eddaoudi; D.B.Moler; H.Li; B.Chen; T.M.Reineke; M.O,Keeffe; O.M.Yaghi, *Acc.Chem.Res.* **2001,** 34, 319.
21. A.F.Wells, *Three-Dimensional Nets and Polyhedra.*; John Wiley and Sons.: New York., 1977.
22. J.Jiang; X.Li; X.Zhang; B.Kang; C.Su, *CrystEngComm.* **2005,** 7, 603.
23. T.W.G.Solomons, *Fundamentals of Organic chemistry.* 2nd ed.; John Wiley and Sons.: U.S.A, 1986; p 435.
24. P.Losier; M.J.Zaworotko, *Angew.Chem.Int.Ed.* **1996,** 35, 2779.
25. L.Carlucci; G.Ciani; D.M.Proserpio, *New.J.Chem.* **1998,** 22, 1319.
26. D.Li; K.Kaneko, *J.Phys.Chem.B.* **2000,** 104, 8940.
27. T.J.Prior; D.Brandshaw; S.J.Teat; M.Rosseinsky, *Chem.Commun.* **2003,** 500.
28. L.R.MacGillivray; S.Subramanian; M.J.Zaworotko, *Chem.Commun.* **1994,** 1325.
29. L.Carlucci; G.Ciani; G.M.Proserpio; A.Sironi, *Chem.Commun.* **1994,** 2755.
30. J.F.Eubank; R.D.Walsh; M.Eddaoudi, *Chem.Commun.* **2005,** 2095.
31. B.F.Abrahams; S.R.Batten; H.Hamit; B.F.Hoskins; R.Robson, *Chem.Commun.* **1996,** 1313.
32. B.F.Abrahams; S.R.Batten; M.J.Grannas; H.Hamit; B.F.Hoskins; R.Robson, *Angew.Chem.Int.Ed.* **1999,** 38, 1475.
33. S.R.Halper; S.M.Cohen, *Inorg.Chem.* **2005,** 44, 486.
34. S.R.Halper; L.Do; J.R.Stork; S.M.Cohen, *J.Am.Chem.Soc.* **2006,** 128, 15255.

35. D.F.Shriver; P.W.Atkins; C.H.Langford, *Inorganic chemistry.* 2nd. ed.; Oxford University press.: Frome, 1996; p 46-47.
36. M.J.Winter, *d-Block Chemistry.*; Oxford University Press.: Bath, 1996; p 21-22.
37. J.Konnert, *Inorg.Chem.* **1966,** 5, 1193.
38. Y.H.Kiang; G.B.Gardner; S.Lee; Z.Xu; B.Lobkovsky, *J.Am.Chem.Soc.* **1999,** 121, 8204.
39. D.Venkataraman; G.B.Gardner; S.Lee; S.J.Moore, *J.Am.Chem.Soc.* **1995,** 1995, (117), 11600.
40. B.F.Hoskins; R.Robson, *J.Am.Chem.Soc.* **1989,** 111, 5962.
41. B.F.Hoskins; R.Robson, *J.Am.Chem.Soc.* **1990,** 112, 1546.
42. D.L.Murphy; M.R.Malachowski; C.F.Campana; S.M.Cohen, *Chem.Commun.* **2005,** 550.
43. N.L.Rosi; J.Kim; M.Eddaoudi; B.Chen; M.O,Keeffe; O.M.Yaghi, *J.Am.Chem.Soc.* **2005,** 127, 1504.
44. A.C.Sudik; A.R.Millward; N.W.Ockwig; A.P.Cote; J.Kim; O.M.Yaghi, *J.Am.Chem.Soc.* **2005,** 127, 7110.
45. H.He; J.Yu; Y.Zhang; O.Pan; R.Xu, *Inorg.Chem.* **2005,** 44, 9279.
46. Q.Yue; J.Yang; G.H.Li; G.D.Li; W.Xu; J.S.Chen; S.N.Wang, *Inorg.Chem.* **2005,** 44, 5241.
47. H.B.Xu; Z.M.Su; K.Z.Shao; Y.H.Zhao; Y.Xing; Y.C.Liang; H.J.Zhang; D.X.Zhu, *Inorg.Chem.Comm.* **2004,** 7, 260.
48. C.Oldham, *Comprehensive Coordination Chemistry*; Pergamon Press.: Oxford, 1987; 'Vol.' 2.
49. J.Tao; M.L.Tong; X.M.Chen, *J.Chem.Soc.Dalton.Trans.* **2000,** 3669.
50. J.Cano; G.DeMunno; J.L.Sanz; R.Ruiz; J.Faus; F.Lloret; M.Julve; A.Canaeschi, *J.Chem.Soc.Dalton.Trans.* **1997,** 1915.
51. H.K.Fun; S.S.S.Raj; R.G.Xiong; J.L.Zuo; Z.Yu; X.Z.You, *J.Chem.Soc.Dalton.Trans.* **1999,** 1915.
52. S.Q.Xia, *Inorg.Chem.Comm.* **2004,** 7, 271.
53. A.Thirumurugan; C.N.R.Rao, *J.Mater.Chem.* **2005,** 15, 3852.
54. C.E.Housecroft; A.G.Sharpe, *Inorganic chemistry*; Pearson Education Limited: England, 2001.
55. M.Eddaoudi; J.Kim; D.Vodak; A.Sudik; J.Wachter; M.O.Keeffe; O.M.Yaghi, *P.N.A.S.* **2002,** 99, 4900.
56. A.J.Blake; P.Hubberstey; M.Schroder; C.C.Williams, *Chem.Commun.* **2005,** 5435.
57. M.Edgar; R.Mitchell; A.M.Z.Slawin; P.Lightfoot; P.A.Wright, *Chem.Eur.J.* **2001,** 7, 5168.
58. T.Loiseau; H.Muguerra; G.Ferey; M.Haouas; F.Taulelle, *J.Solid.State.Chem.* **2005,** 178, 621.
59. A.D.Burrows; K.Cassar; M.F.Mahon; J.E.Warren; S.P.Rigby, *CrystEngComm.* **2005,** 7, 548.
60. J.H.Liao; Y.J.Lee; C.T.Sue, *Inorg.Chem.Comm.* **2006,** 9, 201.
61. H.Li; C.E.Davies; T.L.Groy; D.G.Kelley; O.M.Yaghi, *J.Am.Chem.Soc.* **1998,** 120, 2186.
62. A.J.Fletcher; K.M.Thomas; M.J.Rosseinsky, *J.Solid.State.Chem.* **2005,** 178, 2491.
63. S.M.Hawxwell; H.Adams; L.Brammer, *Acta.Cryst.* **2006,** B62, 808.
64. T.L.Groy; H.Li; O.M.Yaghi, *J.Am.Chem.Soc.* **1996,** 118, 9096.
65. G.Li; H.Li; O.M.Yaghi, *Nature* **1995,** 378, 703.
66. C.E.Davies; G.Li; H.Li; O.M.Yaghi, *J.Am.Chem.Soc.* **1997,** 119, 2861.
67. J.S.Seo; D.Whang; H.Lee; S.I.Jun; Y.J.Jeon; K.Kim, *Nature* **2000,** 404, 982.

68. J.He; J.Yu; Y.Zhang; Q.Pan; R.Xu, *Inorg.Chem.* **2005,** 44, 9279.
69. W.Chen; J.Y.Wang; C.Chen; Q.Yue; H.M.Yuan; J.S.Chen; S.N.Wang, *Inorg.Chem.* **2003,** 42, 944.
70. S.H.Cho; B.Ma; S.T.Nguyen; J.T.Hupp; T.E.Albert-Schmitt, *Chem.Commun.* **2006,** 2563.
71. J.M.Tanski; P.T.Wrolczanski, *Inorg.Chem.* **2001,** 40, 2026.
72. T.Sawaki; T.Dewai, *J.Am.Chem.Soc.***1998,** 120, 8539.
73. T.Sawaki; Y.Aoyama, *J.Am.Chem.Soc.***1999,** 121, 4793.
74. L.Alaerts; E.Seguin; H.Poelman; F.Thibault-Starzyk; P.A.Jacobs; D.E.DeVos, *Chem.Eur.J.* **2006,** 12, 7353.
75. S.Hasegawa; S.Horike; R.Matsuda; S.Furukawa; K.Mochizuki; Y.Kinoshita; S.Kitagawa, *J.Am.Chem.Soc.* **2007,** 129, 2607.
76. L.Pani; M.B.Sander; X.Huang; J.Li.; M.Smith; E.Bittner; B.Backrath; J.J.Johnson, *J.Am.Chem.Soc.* **2004,** 126, 1308.
77. E.Y.Lee; M.P.Suh, *Angew.Chem.Int.Ed.* **2004,** 43, 2798.
78. T.Duren; L.Sarkisovi; O.M.Yaghi; R.Snurr, *Langmuir* **2004,** 20, 2683.
79. S.Bordiga; J.G.Vitillo; G.Ricchiardi; L.Regli; D.Cocina; A.Zecchina; B.Arstad; M.Bjorgen; J.Hafizovic; K.P.Lillerud, *J.Phys.Chem.B.* **2005,** 109, 18237.
80. H.K.Chae; D.Y.Siberio-Perez; J.Kim; Y.Go; M.Eddaoudi; A.J.Matzger; M.O'Keeffe; O.M.Yaghi, *Nature* **2004,** 427, 523.
81. S.S.Y.Chui; S.M.F.Lo; J.P.H.Charmant; A.G.Orpen; I.D.Williams, *Science* **1999,** 283, 1148.
82. J.Y.Lee; J.Li; J.Jagiello, *J.Solid State.Chem.* **2005,** 178, 2527.
83. A.Visknyakov; P.I.Ravikovitch; A.V.Neimark; M.Bulow; Q.M.Wang, *Nano Lett.* **2003,** 3, 713.
84. V.Krungleviciute; K.Lask; L.Heroux; A.D.Migone; J.Y.Lee; J.Li; A.Skoulidas, *Langmuir* **2007,** 23, 3106.
85. V.K.Peterson; Y.Liu; C.M.Brown; C.J.Kepert, *J.Am.Chem.Soc.* **2006,** 128, 15578.
86. B.Chen; C.Liang; J.Yang; D.S.Contreras; Y.L.Clancy; E.B.Lobkovsky; O.M.Yaghi; S.Dai, *Angew.Chem.Int.Ed.* **2006,** 45, 1390.
87. B.Chen; S.Ma; F.Zapata; F.R.Fronczek; E.B.Lobkovsky; H.C.Zhou, *Inorg.Chem.* **2007,** 46, 1233.
88. B.Civalleri; F.Napoli; Y.Noel; C.Roetti; R.Dovesi, *CrystEngComm.* **2006,** 8, 364.
89. M.J.Rosseinsky, *Mcroporous Mesoporous Mater.* **2004,** 73, 15.
90. S.Bordiga; C.Lamberti; G.Ricchiardi; L.Regli; F.Bonino; A.Damin; K.P.Lillerud; M.Bjorgen; A.Zecchina, *Chem.Commun.* **2004,** 2300.
91. Y.Hang; B.Wu; D.Yuan; Y.Xe; F.Jiang; M.Hong, *Inorg.Chem.* **2007,** 46, 1171.
92. W.Zhu; Z.Wang; S.Gao, *Inorg.Chem.* **2007,** 46, 1337.

Chapter 2 Zinc dicarboxylate networks

2.1 Introduction and Aims

Several networks containing zinc metal centres and dicarboxylate linkers were cited in Chapter 1. The most commonly used dicarboxylate ligands are rigid linear linkers such as 1,4-benzenedicarboxylate (tph^{2-}) and 4,4'-biphenyldicarboxylate ($bpdc^{2-}$). The configuration of the networks resulting from such linear ligands are easier to predict than the architectures obtained from flexible ligands.[1] Although such systems are widely used, at the time when this project was started there was little information with regards to the sensitivity of the reaction of $Zn(NO_3)_2 \cdot 6H_2O$ and H_2tph towards variations in the reaction conditions. Thus, the effects of pressure, temperature and changes in the solvent composition on the outcome of the reaction between $Zn(NO_3)_2 \cdot 6H_2O$ and H_2tph or H_2bpdc were investigated.

Results and discussion

2.2 Temperature effects on the reaction between $Zn(NO_3)_2 \cdot 6H_2O$ and H_2tph

A wide range of temperatures are used in the synthesis of metal organic frameworks. When this project was started, there was little information on the impact of temperature on the outcome of the reaction between $Zn(NO_3)_2 \cdot 6H_2O$ and H_2tph. Thus the role of temperature on the stated reaction using DMF as the solvent was studied and the results obtained are discussed in the following section.

Two similar reactions were carried out with the only variable being the temperature.

2.2.1 Reaction of $Zn(NO_3)_2 \cdot 6H_2O$ and H_2tph in DMF at 95°C

$Zn(NO_3)_2 \cdot 6H_2O$ and two equivalents H_2tph were dissolved in separate portions of DMF. The H_2tph solution was stirred and heated to 95°C before the addition of the $Zn(NO_3)_2 \cdot 6H_2O$ solution. The mixture was then maintained at 95°C for three hours, during which time colourless crystals formed. Analysis by single crystal X-ray crystallography

revealed the presence of $\{[Zn(tph)(H_2O)]\cdot DMF\}_\infty$ **(1)**.[2] Powder X-ray diffraction demonstrated that **1** is the only product of the reaction.

Yaghi and co-workers[3] have previously obtained **1** using a different synthetic route. They used a mixture of $Zn(NO_3)_2\cdot 6H_2O$ and H_2tph dissolved in toluene/DMF. Vapour diffusion of triethylamine (Et_3N) into the reaction mixture yielded **1**. In contrast to the published method, in this work **1** was obtained in the absence of an added base. Therefore DMF might have fulfilled a dual role of solvent and base.

$\{[Zn(tph)(H_2O)]\cdot DMF\}_\infty$ consists of zinc-acetate type 'paddle-wheel'[4] SBUs (Figure 2.1a) that are linked into a (4,4) 2-D topology by the benzene rings of the tph^{2-} ligands (Figure 2.1b). The network of **1** has already been described in Chapter 1.

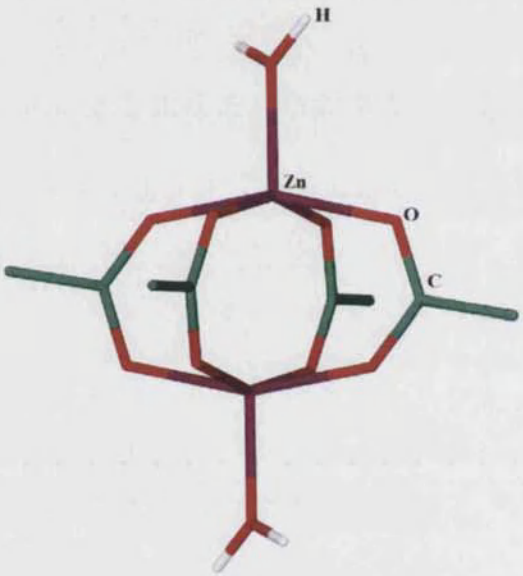

Figure 2.1a. The 'paddle-wheel' type SBU of **1**.

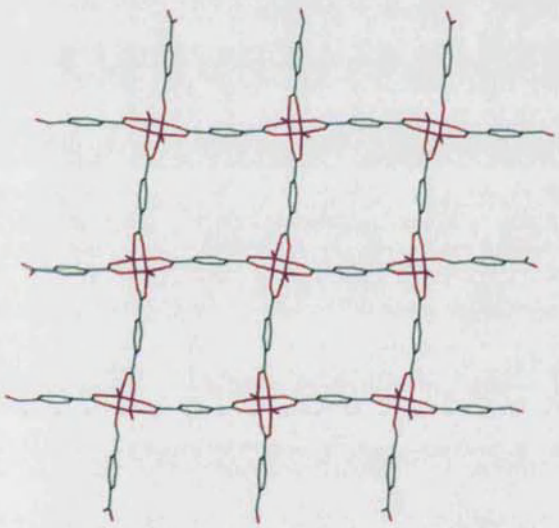

Figure 2.1b. The 2-D network of **1** viewed perpendicular to the (1 0 0) plane.

2.2.2 Reaction of $Zn(NO_3)_2\cdot 6H_2O$ and H_2tph in DMF at 115°C

When the reaction between $Zn(NO_3)_2\cdot 6H_2O$ and two equivalents H_2tph was conducted at 115°C, a mixture of $\{[Zn_3(tph)_3(H_2O)_3]\cdot 4DMF\}_\infty$ **(2)** and $\{[Zn(tph)(DMF)]\}_\infty$ **(3)** was obtained. Although both compounds have been reported previously,[3, 5] the reaction conditions by which **2** and **3** were prepared in this work are different from those reported in the literature. Edgar *et al*[5] and Yaghi *et al*[3] relied on the diffusion of Et_3N to deprotonate

the ligand while in the procedure described here, **2** and **3** were obtained in the absence of an added base.

The structures of **2** and **3** were also described in Chapter 1. **2** consists of three metal centre SBUs with the formula $M_3(O_2CR)_6$ (Figure 2.2a). The building units are connected together into a 2-D (3,6) type net (Figure 2.2b).[22] The configuration of $\{[Zn(tph)(DMF)]\}_\infty$ (**3**) consists of 'paddle-wheel' type SBUs (Figure 2.3) linked together by the benzene rings of the linkers into a 2-D (4,4) type network similar to that of **1** (Figure 2.1b).[6]

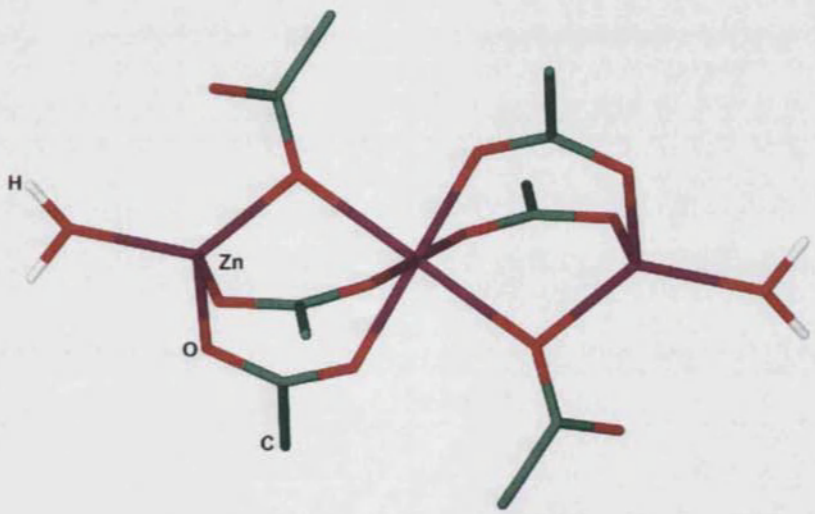

Figure 2.2a. The three metal centre SBU of **2**.

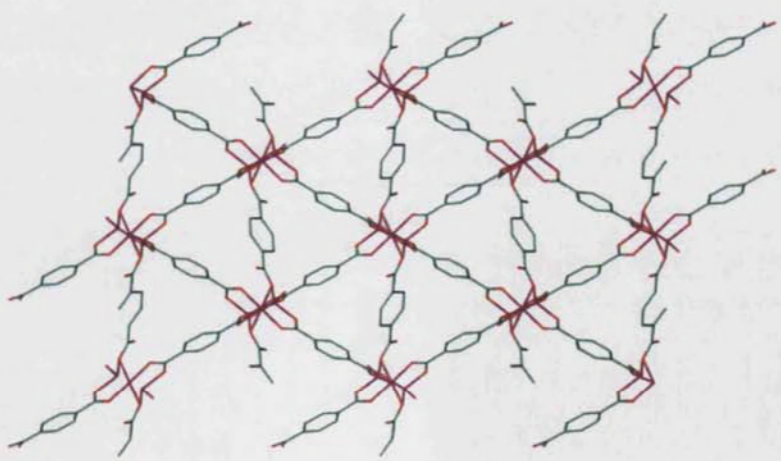

Figure 2.2b. The (3,6) type network of **2** viewed down the *a* axis.

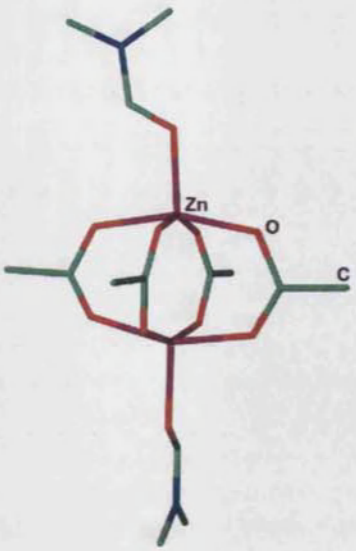

Figure 2.3. The 'paddle-wheel' SBU of **3**.

2.2.3 Network dependency on pressure

One method used in the synthesis of metal organic frameworks is solvothermal synthesis. This method involves the reaction between a metal salt and a ligand, both being dissolved in a suitable solvent, inside a sealed pressure cell. Thus, the effect that the added pressure has on the reaction between $Zn(NO_3)_2 \cdot 6H_2O$ and H_2tph was investigated.

$Zn(NO_3)_2 \cdot 6H_2O$ and two equivalents H_2tph were dissolved in separate portions of DMF and the ligand solution was transferred to a pressure cell. When the ligand solution reached 115°C, the $Zn(NO_3)_2 \cdot 6H_2O$ was added and the reaction container was sealed and pressurised with three atmospheres of nitrogen. The mixture was then heated at 115°C for three hours, during which time colourless crystals formed. X-ray powder diffraction revealed the compound to be $\{[Zn(tph)(DMF)]\}_\infty$ (**3**).

When no pressure was applied, the reaction between $Zn(NO_3)_2 \cdot 6H_2O$ and H_2tph gave a mixture of two products at 115°C (Section 2.2.2). Hence, it can be deduced that, when pressure was applied the formation of **2** was suppressed. The densities of **2** and **3** are 1.515 and 1.518[1] g cm^{-1} respectively, thus in the presence of pressure, the reaction discriminated towards the formation of the denser network.

[1] The density for **3** has been adjusted to include the extra solvent molecules present in the formula of **2**.

2.2.4 Effects of solvent purity on the reaction between $Zn(NO_3)_2 \cdot 6H_2O$ and H_2tph

X-ray powder diffraction revealed that the product from the reaction between $Zn(NO_3)_2 \cdot 6H_2O$ and H_2tph at 115°C was dependent on the age of the solvent. When an old bottle of solvent was used, X-ray powder data showed the presence of a new phase which had not been observed in the previous reactions. The new crystals were analysed further by single crystal X-ray crystallography. Two compounds, $\{(Me_2NH_2)_2[Zn_3(tph)_4] \cdot DMF \cdot H_2O\}_\infty$, (**4**) and $\{(Me_2NH_2)_2[Zn(DMF)_4(OH_2)_2][Zn_6(tph)_8] \cdot 3DMF\}_\infty$, (**5**) were identified. **4** was the predominant compound in the composition as indicated by X-ray powder data. The presence of the dimethylammonium cations in **4** and **5** instigated further investigation and, as will be discussed later, these resulted from the hydrolysis of the solvent DMF molecules.

The asymmetric unit of **4** consists of one full and one partial (half occupancy) zinc atom, one whole and two half tph^{2-} ligands, one dimethylammonium cation and partial dimethylformamide and water molecules (Figure 2.4). All the partial solvent fragments within the asymmetric unit have site occupancy factors of 0.5. The displacement ellipsoids for the atoms labelled as C(17)/C(17A) of the dimethylammonium cation represent disorder of one carbon atom over two sites. Crystallographic data for **4** are given in Table 2.1.

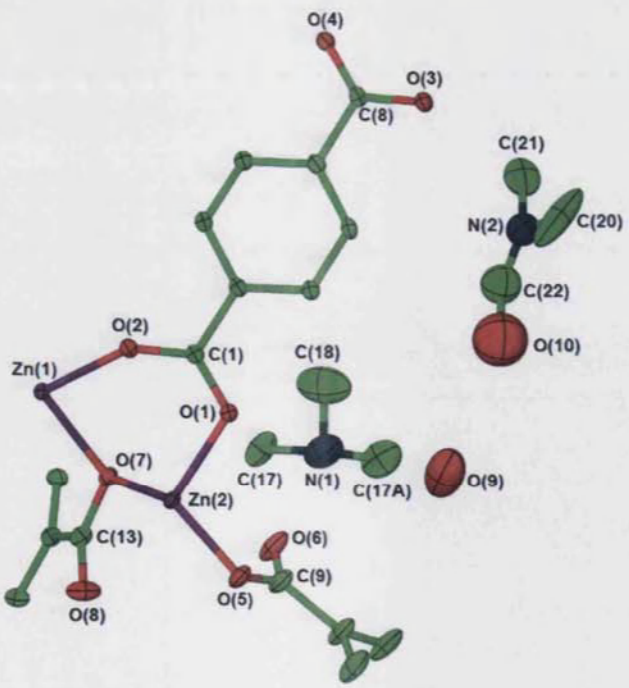

Figure 2.4. The asymmetric unit of **4** showing thermal ellipsoids at 30% probability. Hydrogen atoms are omitted for clarity.

Table 2.1. Crystallographic data for **4**.

Empirical formula	$C_{39}H_{41}N_3O_{18}Zn_3$
M	1035.86
T/ K	150(2)
Crystal system	Monoclinic
Space group, *Z*	*C2/c*, 4
a/ Å	33.1790(8)
b/ Å	9.7080(2)
c/ Å	18.2600(5)
α/ °	90
β/ °	94.422(1)
γ/ °	90
U/ Å^3	5864.1(2)
Crystal size/ mm	0.20 x 0.20 x 0.08
Wavelength/ Å	0.71073
Theta range for data collected/ °	3.67 to 27.48
Reflections collected/ observed (>2σ)	25817/ 5319
Data completeness	0.980
Max. and min. transmission	0.85 and 0.73
Goodness of fit F^2	1.079
Final *R* indices (I>2σ(I))	$R1$ = 0.0541, $wR2$ = 0.1556
R indices (all data)	$R1$ = 0.0700, $wR2$ = 0.1670
Largest diff. peak and hole eÅ^{-3}	1.131 and -0.754

The two independent metal centres of **4** have different geometries. Zn(1) has a distorted octahedral geometry with the coordination sphere being occupied by six tph^{2-} ligands, while Zn(2) adopts a tetrahedral geometry with the coordination sphere being filled by four tph^{2-} ligands. Zn(1) is located on an inversion centre. This symmetry operation gives rise to a three metal centre units, in the gross structure, that are connected together by the carboxylate groups. The functional groups coordinate to the metals in three different ways, namely the monodentate binding mode, adopted by O(5)-C(9)-O(6), the bridging bidentate mode, such as O(1)-C(1)-O(2), and the mono-bridging bidentate mode, O(7)-C(13)-O(8) (Figure 2.4).

The tetrahedral-octahedral-tetrahedral metal arrangement forms the $M_3(O_2CR)_6$ SBUs of the network (Figure 2.5). Similar networks containing three metal centre SBUs are $\{[Zn_3(tph)_3(H_2O)_3]\cdot 4DMF\}_\infty$, (**2**) and other compounds such as $\{[Zn_3(tph)_3(MeOH)_2]\cdot 4MeOH\}_\infty$ and $\{[Zn_3(tph)_3(DEF)_2]\cdot DEF\}_\infty$, reported in Chapter 1.[7, 8] The SBUs of **4** are connected together by the benzene rings in the tph^{2-} ligands to form 2-D sheets (Figure 2.6 and 2.7) having (3,6) topology.

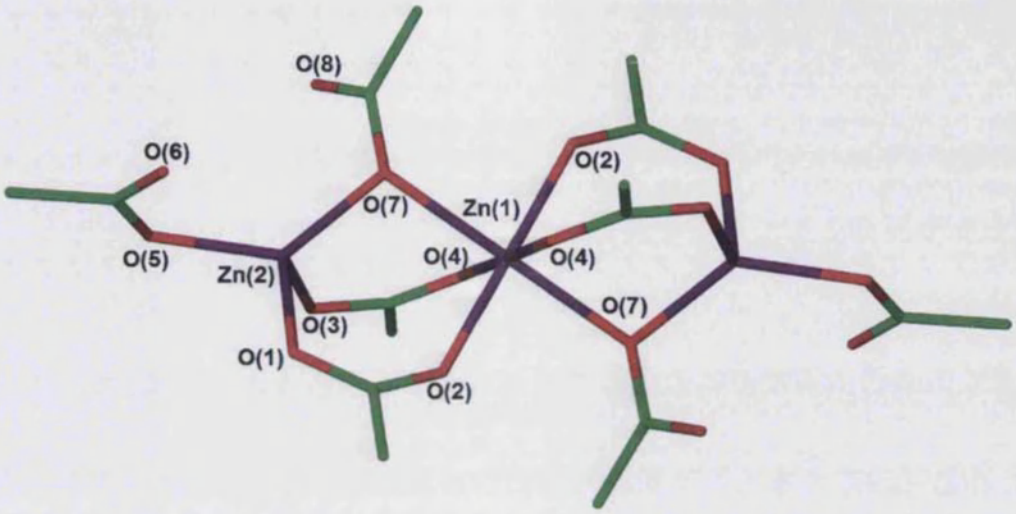

Figure 2.5. The $M_3(O_2CR)_6$ SBU of **4**.

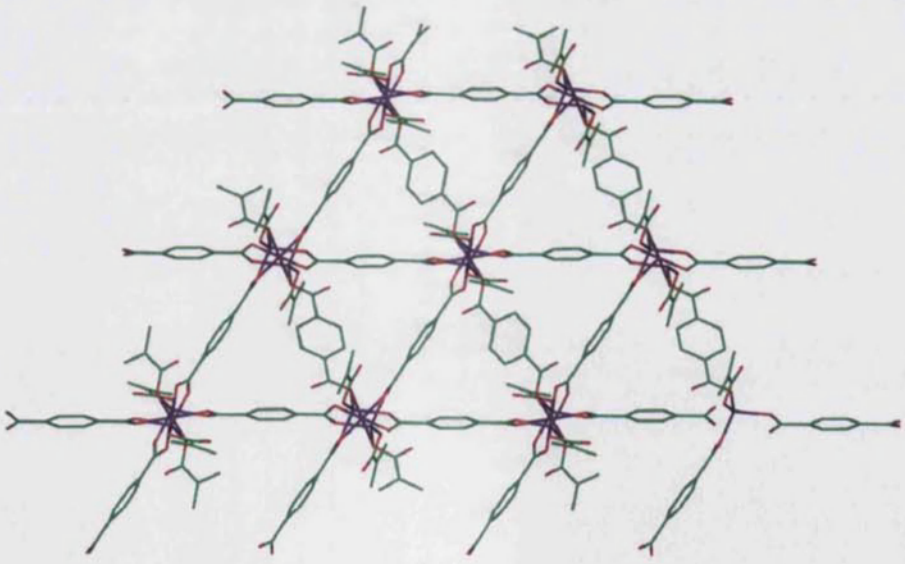

Figure 2.6. The 2-D sheet of **4** viewed down the *a* axis.

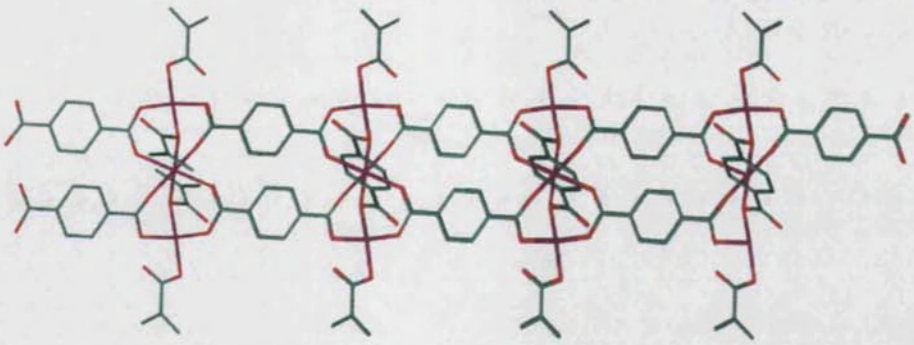

Figure 2.7. The 2-D sheet of **4** viewed down the *b* axis.

The tph^{2-} ligands with the carboxylate groups adopting the monodentate binding mode act as pillars in the structure of **4** linking the 2-D sheets together into a 3-D network (Figure 2.8).

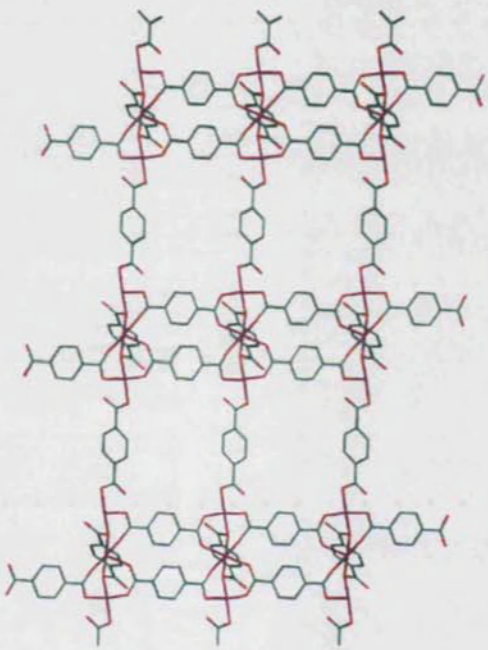

Figure 2.8. The 3-D network of **4** viewed down the *b* axis.

Lists of selected bond lengths and angles are given in Tables 2.2 and 2.3 respectively. Oxygen atoms O(6) and O(8) do not coordinate to the zinc atoms (Figure 2.5) but nevertheless O(6)-C(9) and O(8)-C(13) are still comparable in length to other oxygen-carbon bond lengths where the oxygen atoms are coordinated to metal centres (Table 2.2). Although the distances between Zn(2)···O(6) and Zn(2)···O(8) (Table 2.2 Figure 2.5) are within the sum of the van der Walls radii of zinc and oxygen (2.9 Å),[9] the mentioned atoms are too far away to be considered as covalently bonded.

Table 2.2. Selected bond lengths for **4**.[II]

Bond Atoms	Distance/ Å
Zn(1)-O(2)	2.036(2)
Zn(1)-O(4)#2	2.046(2)
Zn(1)-O(7)	2.216(2)
Zn(2)-O(1)	1.973(3)
Zn(2)-O(3)#1	1.956(3)
Zn(2)-O(5)	1.944(3)
Zn(2)-O(7)	1.985(3)
Zn(2)···O(6)	2.790(7)
Zn(2)···O(8)	2.745(6)

Bond Atoms	Distance/ Å
O(1)-C(1)	1.275(4)
O(2)-C(1)	1.250(4)
O(3)-C(8)	1.270(4)
O(4)-C(8)	1.249(4)
O(5)-C(9)	1.274(6)
O(6)-C(9)	1.240(6)
O(7)-C(13)	1.303(5)
O(8)-C(13)	1.236(5)

Table 2.3. Selected bond angles for **4**.[I]

Atoms	Angle/ °
O(2)-Zn(1)-O(7)	90.71(9)
O(2)-Zn(1)-O(4)#1	94.17(10)
O(4)#1-Zn(1)-O(7)	90.72(10)
O(5)-Zn(2)-O(1)	104.84(12)
O(5)-Zn(2)-O(7)	132.17(13)

Atoms	Angle/ °
O(1)-Zn(2)-O(7)	99.65(11)
Zn(2)-O(7)-Zn(1)	101.43(11)
O(2)-C(1)-O(1)	125.3(3)
O(4)-C(8)-O(3)	126.7(3)
O(6)-C(9)-O(5)	124.0(4)
O(8)-C(13)-O(7)	121.9(4)

The dimethylammonium cations are involved in hydrogen bonding (H(1)-N(1)···O(6) 2.71 Å, H(1)···O(6) 1.86 Å, N(1)-H(1)···O(6) 150°). Interactions between H(1) of the cations and O(6) of the tph^{2-} hold the counter ions in place.

As in the network of $\{[Zn_3(tph)_3(H_2O)_3]\cdot 4DMF\}_\infty$ (**2**) the SBUs of **4** consist of $M_3(O_2CR)_6$ motifs that are linked together by the benzene rings of the tph^{2-} ligands. Both networks have 2-D (3,6) type sheets, but while **4** is extended into a 3-D network, the terminal water ligands in **2** prevent the growth of the network in the third dimension.

[II] Symmetry transformations used to generate equivalent atoms:
#1 x,-y+1,z-1/2 #2 -x+1/2,y-1/2,-z+1/2

The second compound obtained in the reaction mixture described at the beginning of this section is $\{(Me_2NH_2)_2[Zn(DMF)_4(OH_2)_2][Zn_6(tph)_8]\cdot 6DMF\}_\infty$ (**5**). Crystallographic data for **5** are given in Table 2.4.

Table 2.4. Crystallographic data for **5**.

Empirical formula	$C_{49}H_{61}N_6O_{22}Zn_{3.5}$
M	1314.83
T/ K	150(2)
Crystal system	Triclinic
Space group, *Z*	*P*-1, 2
a/ Å	9.8266(7)
b/ Å	17.1982(12)
c/ Å	18.8302(13)
α/ °	68.785(2)
β/ °	78.445(2)
γ/ °	85.916(2)
U/ Å^3	2925.74(4)
Crystal size/ mm	0.07 x 0.07 x 0.02
Wavelength/ Å	0.67780
Theta range for data collected/ °	3.36 to 28.92
Reflections collected/ observed (>2σ)	33955/ 12297
Data completeness	0.971
Max. and min. transmission	0.980 and 0.891
Goodness of fit F^2	1.001
Final *R* indices ($I>2\sigma(I)$)	$R1 = 0.0446$, $wR2 = 0.1153$
R indices (all data)	$R1 = 0.0669$, $wR2 = 0.1232$
Largest diff. peak and hole eÅ^{-3}	0.696 and -1.173

The asymmetric unit of **5** consists of two full and three half occupancy zinc atoms, three full and two half tph^{2-} ligands, one dimethylammonium cation, three uncoordinated and two coordinated DMF molecules and a coordinated water molecule (Figure 2.9). Zn(2), Zn(4) and Zn(5) are located at inversion centres. The coordinated DMF molecules with the oxygen atoms labelled O(20)/O(20A) and O(21)/O(21A) are each located over two positions. O(20) and O(21) have site occupation factors of 0.67 each with

the minor fragments having 0.33 occupancy. Only the major parts of these two molecules are shown in Figure 2.9.

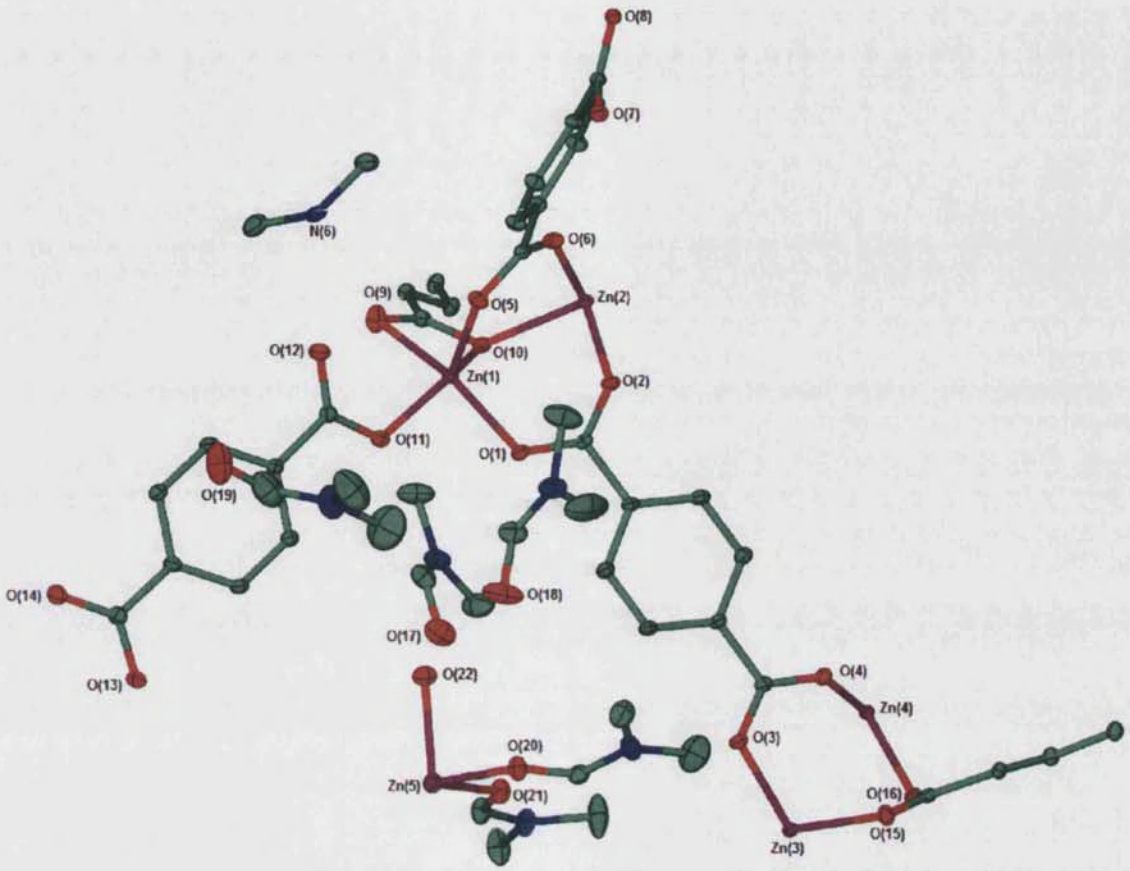

Figure 2.9 The asymmetric unit of **5** showing thermal ellipsoids at 30% probability. Hydrogen atoms are removed and only one part of the disordered DMF molecules are shown for clarity.

The zinc centres adopt three different geometries. Zn(1) is five coordinated and is connected to five oxygen atoms from four tph^{2-} ligands. As can be noted from the calculated τ value for Zn(1) (τ^{11} = 0.10), the geometry around this metal centre is best described as distorted square pyramidal.

Zn(2), Zn(4) and Zn(5) have distorted octahedral geometries but the coordination spheres of these atoms differ from each other. Zn(2) and Zn(4) are coordinated to six tph^{2-} ligands, while Zn(5) is connected to six oxygen atoms that belong to water and DMF molecules (Figure 2.9). Zn(3) adopts a distorted tetrahedral geometry.

In **5**, the carboxylate groups adopt three different binding modes, namely the bridging bidentate, the monodentate and chelating bridging bidentate modes (Figure 2.9). The carboxylates bridge three metal centres together into $M_3(O_2CR)_6$ SBUs.

There are two distinct $M_3(O_2CR)_6$ SBUs in **5**. One SBU contains one octahedral and two trigonal bipyramidal zinc centres (Figure 2.10a) while the other consist of one octahedral and two distorted tetrahedral metal centres (Figure 2.10b). Both building units involve six carboxylate groups but in one case, (Figure 2.10a), the organic ligands adopt four bridging bidentate and two chelating bridging bidentate modes, while the latter (Figure 2.10b) has all six carboxylate groups coordinated in the bridging bidentate fashion. The zinc-oxygen distances Zn(3)···O(4), Zn(3)···O(8)#1 and Zn(3)···O(16) (3.086(18) Å, 3.157(14) Å and 2.863(19) Å respectively) (Figure 2.10b, Table 2.6) show that the respective atoms are too far away for bonding to occur. These measurements further confirm that the carboxylate groups have different binding modes in the two SBUs of **5** and thus the building units are different from one another.

The different SBUs are linked in two dimensions by the phenyl rings of the tph^{2-} ligands (Figure 2.11) to form sheets of the (3,6) type. The linkers coordinating to the metal centres in a monodentate fashion bridge these sheets together to form a 3-D network (Figure 2.12). The gross architectures of **4** and **5** are similar with the main difference being that the pores of the former are occupied by guest DMF molecules, dimethylammonium counter ions and $[Zn(DMF)_4(H_2O)_2]^{2+}$ cations whereas for **4** the pores are filled by dimethylammonium cations, water and DMF molecules.

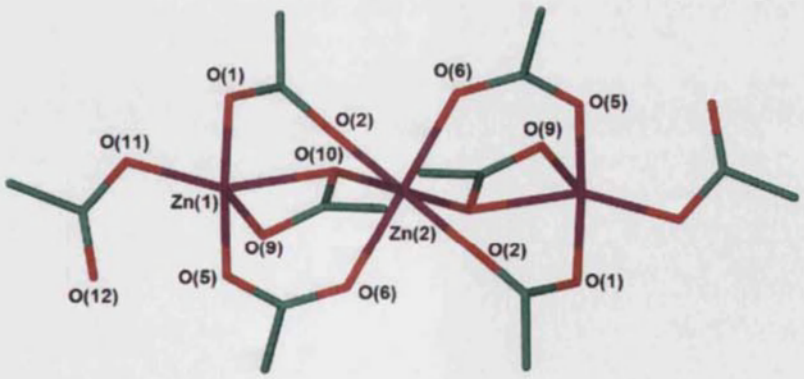

Figure 2.10a. The two trigonal bipyramidal and octahedral metal centres in one of the SBUs of **5**.

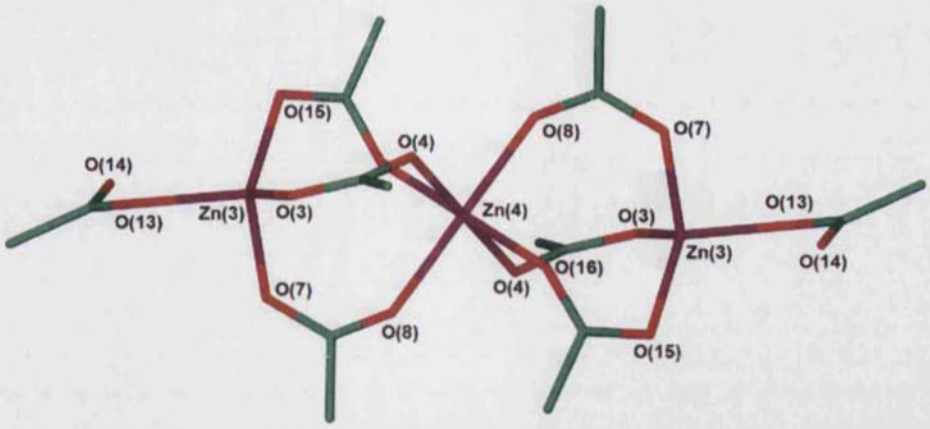

Figure 2.10b. The two tetrahedral and one octahedral metal centres in the second SBU of **5**.

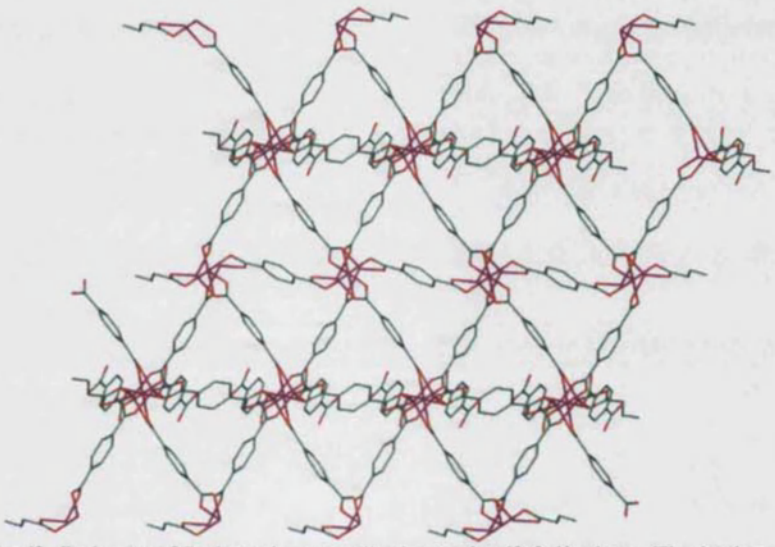

Figure 2.11. The (3,6) sheets of **5** viewed perpendicular to the (0 0 1) plane. The hydrogen atoms, guest molecules and counter ions are removed for clarity.

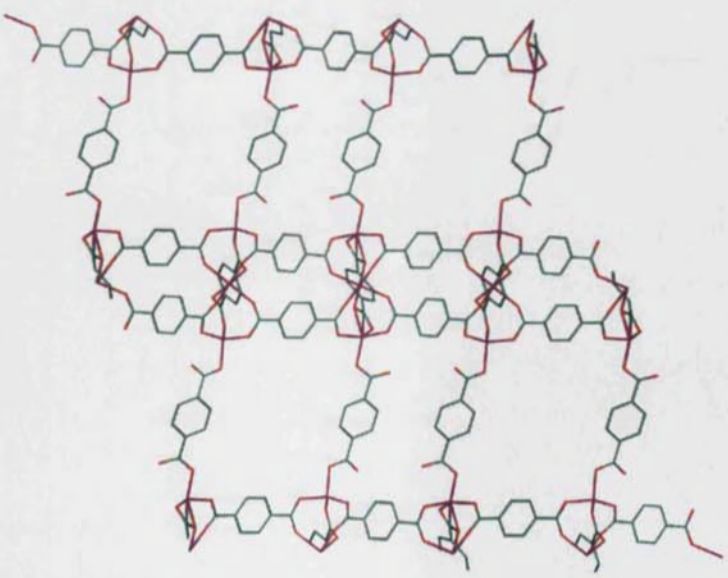

Figure 2.12. The 3-D network of **5** viewed down the *a* axis. The hydrogen atoms, guest molecules and the counter ions are removed for clarity.

Selected bond lengths and angles for **5** are given in Tables 2.5 and 2.6 respectively. The oxygen atoms O(12) and O(14) are not coordinated to the zinc centres (Figures 2.10a and 2.10b). Nevertheless the carboxylate carbon-oxygen bond lengths O(12)-C(21) and O(14)-C(28) are comparable in length to other carbon-oxygen bonds such as O(6)-C(9) and O(8)-C(16) (Table 2.5). The distances between O(12) or O(14) and the nearest zinc centres are Zn(1)···O(12) 3.063(2) Å, Figure 2.10a, Zn(3)···O(14) 2.903(2) Å, Figure 2.10b and this indicates that the respective atoms are too far apart to be considered as covalently bonded (sum of van der Walls radii 2.9 Å).

Table 2.5. Selected bond lengths for **5**.[III]

Bond Atoms	Distance/ Å
Zn(1)-O(1)	1.9897(18)
Zn(1)-O(5)	1.9402(17)
Zn(1)-O(9)	2.237(2)
Zn(1)-O(10)	2.1369(18)
Zn(1)-O(11)	1.9529(19)
Zn(2)-O(2)	2.0215(16)
Zn(2)-O(6)	2.0716(17)
Zn(2)-O(10)	2.1678(18)
Zn(3)-O(3)	1.9580(18)
Zn(3)-O(7)#1	1.9493(17)
Zn(3)-O(13)#2	1.9737(18)
Zn(3)-O(15)	1.9425(18)
Zn(4)-O(4)	2.0836(17)
Zn(4)-O(8)#1	2.0497(17)
Zn(4)-O(16)#3	2.1072(16)
Zn(5)-O(20)	2.091(4)
O(14)···Zn(3)#4	2.903(2)
O(4)···Zn(3)	3.086(18)
O(8)#1···Zn(3)	3.157(14)

Bond atoms	Distance/ Å
O(1)-C(1)	1.270(3)
O(2)-C(1)	1.252(3)
O(3)-C(8)	1.267(3)
O(4)-C(8)	1.255(3)
O(5)-C(9)	1.270(3)
O(6)-C(9)	1.244(3)
O(7)-C(16)	1.270(3)
O(8)-C(16)	1.245(3)
O(11)-C(21)	1.282(3)
O(12)-C(21)	1.245(3)
O(13)-C(28)	1.280(3)
O(14)-C(28)	1.245(3)
O(15)-C(17)	1.270(3)
O(16)-C(17)	1.254(3)
Zn(5)-O(21)	2.101(4)
Zn(5)-O(22)	2.075(2)
Zn(1)···O(12)	3.063(2)
O(16)···Zn(3)	2.863(19)

[III] Symmetry transformations used to generate equivalent atoms:
#1 x,y-1,z #2 -x+1,-y+1,-z+1
#3 -x+2,-y+1,-z #4 1-x, 1-y, 1-z

Table 2.6. Selected bond angles for **5**.[IV]

Atoms	Angle/ °
O(5)-Zn(1)-O(1)	111.95(8)
O(1)-Zn(1)-O(9)	141.71(8)
O(1)-Zn(1)-O(10)	90.31(7)
O(11)-Zn(1)-O(1)	90.85(8)
O(5)-Zn(1)-O(9)	99.74(9)
O(2)-Zn(2)-O(6)	92.73(7)
O(2)-Zn(2)-O(10)	89.26(7)
O(7)#1-Zn(3)-O(3)	108.76(8)
O(3)-Zn(3)-O(13)#2	97.88(8)
O(15)-Zn(3)-O(3)	109.03(8)
O(4)-Zn(4)-O(16)	89.62(7)
O(20)-Zn(5)-O(21)	90.64(15)
O(2)-C(1)-O(1)	125.5(2)
O(6)-C(9)-O(5)	126.5(2)
O(9)-C(29)-O(10)	119.8(2)
O(14)-C(28)-O(13)	123.7(2)

Atoms	Angle/ °
O(10)-Zn(1)-O(9)	59.84(7)
O(11)-Zn(1)-O(9)	95.01(8)
O(11)-Zn(1)-O(10)	135.65(8)
O(5)-Zn(1)-O(10)	105.73(7)
O(5)-Zn(1)-O(11)	114.74(8)
O(6)-Zn(2)-O(10)	91.29(7)
O(7)#1-Zn(3)-O(13)#2	99.44(8)
O(15)-Zn(3)-O(7)#1	122.85(8)
O(15)-Zn(3)-O(13)#2	115.84(8)
O(22)-Zn(5)-O(21)	92.16(12)
O(22)-Zn(5)-O(20)	89.71(12)
O(4)-C(8)-O(3)	125.0(2)
O(8)-C(16)-O(7)	126.3(2)
O(12)-C(21)-O(11)	125.6(2)
O(16)-C(17)-O(15)	123.7(2)

Hydrogen bond distances are given in Table 2.7 with a graphical representation of these bonds displayed in Figure 2.13. The oxygen atom O(18) of the guest DMF molecule is hydrogen bonded to H(22B) of the water molecule, H(22A)-O(22)-H(22B), that forms part of the $[Zn(DMF)_4(H_2O)_2]^{2+}$ cation. The other guest DMF molecule interacts with the same water molecule, H(22A)-O(17)-H(22B) of the $[Zn(DMF)_4(H_2O)_2]^{2+}$ to form O(17)-H(22A)··O(12) hydrogen bonds. The dimethylammonium cation is held in place through hydrogen bonds involving O(12) and O(14) from the carboxylate groups of the network. H(40B) experiences weak interactions to O(10) of the chelating bridging bidentate carboxylate (Figure 2.13).

[IV] Symmetry transformations used to generate equivalent atoms:
#1 x,y-1,z #2 -x+1,-y+1,-z+1
#3 -x+2,-y+1,-z #4 1-x, 1-y, 1-z

Table 2.7 Hydrogen bonds with H··A < r(A) + 2.000Å and <DHA > 110° for **2**.

D-H	D(D-H)	d(H··A)	<DHA	d(D··A)	A
C40-H40B	0.98	2.40	165	3.35	O10
N6-H6A	0.89	1.92	150	2.73	O12
N6-H6B	0.89	1.87	155	2.71	O14 [-x, -y+2, -z+1]
O22-H22A	0.88	1.94	142	2.70	O17
O22-H22B	0.88	1.89	159	2.74	O18

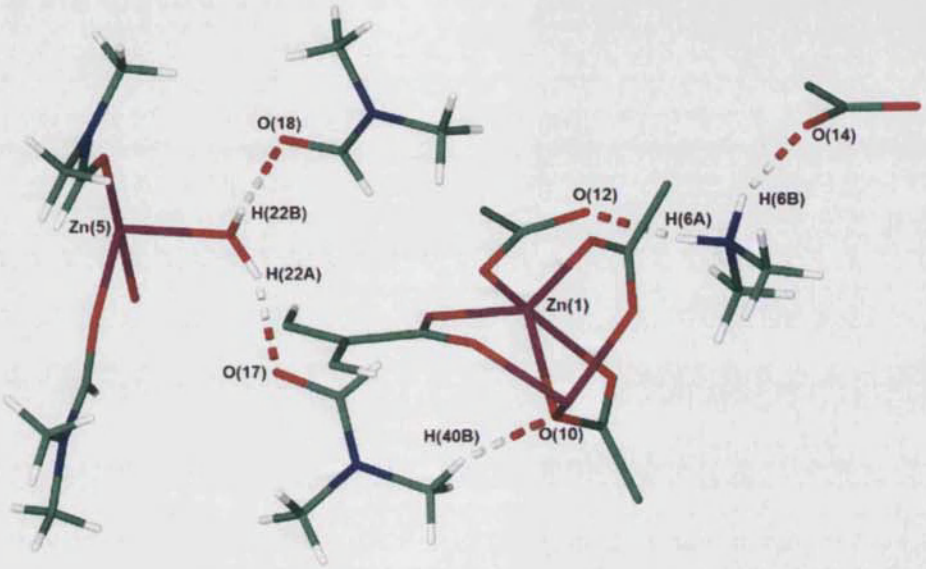

Figure 2.13. The hydrogen bonding present in **5**.

The presence of the dimethylammonium cations in **4** and **5** was unexpected. In the presence of water, DMF hydrolyses to form dimethylamine and methanoic acid (Figure 2.14).[12] The hydrolysis of the solvent was observed to occur relatively quickly, such that, when a new bottle of solvent was exposed to the moisture in the atmosphere for at least one month, the above mentioned reaction produced enough cations that the only product from the reaction between $Zn(NO_3)_2 \cdot 6H_2O$ and H_2tph at 115°C was **4** rather than **2** and **3**. Although the methanoate anions have not been observed in any of the structures reported in this work, other authors have observed the inclusion of both ions inside the voids of networks.[6]

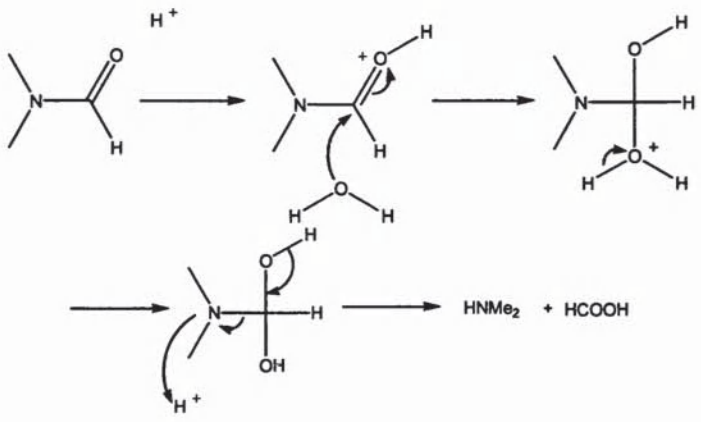

Figure 2.14. Reaction scheme showing the hydrolysis of DMF to form methanoic acid and dimethylamine.

When the reaction between $Zn(NO_3)_2 \cdot 6H_2O$ and H_2tph was carried out in the presence of dimethylammonium chloride using a fresh sample of DMF, **4** was obtained. This strongly suggests that the cations template the product of the reaction.

2.2.5 Network dependency on pH

Loiseau and coworkers[13] synthesised $\{[Zn_3(OH)_2(tph)_2] \cdot 2DEF\}_\infty$ from $Zn(NO_3)_2 \cdot 6H_2O$ and H_2tph in DEF by adjusting the pH of the reaction to 4. Hence, the pH sensitivity of the reaction between $Zn(NO_3)_2 \cdot 6H_2O$ and H_2tph in DMF was investigated. The metal salt and the ligand were dissolved in separate portions of unhydrolysed DMF and reacted following the experimental procedure outlined in Section 2.2.2, with the exception of the pH being adjusted from 5.5 to 4 by the addition of a few drops of conc HCl. After standing for three hours at 115°C, **4** was obtained as the only product. This result suggests that the acid aids the hydrolysis of the solvent molecules to form the cations required for templating the network.

Brammer and Hawxwell[14] have recently reported similar DMF hydrolysis effects using other metal nitrates and H_2tph. This observation seems to suggest that this solvent hydrolysis phenomenon is not specific to the $Zn(NO_3)_2 \cdot 6H_2O$ reactions.

N,N-diethylformamide (DEF) is another commonly used solvent. The sensitivity of the reaction between $Zn(NO_3)_2 \cdot 6H_2O$ and H_2tph to the length of the alkyl chain of the solvent was thus investigated.

2.2.6 Sensitivity of the reaction between $Zn(NO_3)_2 \cdot 6H_2O$ and H_2tph to solvent alkyl chain length

The reaction between $Zn(NO_3)_2 \cdot 6H_2O$ and H_2tph at 115°C was repeated in *N,N*-diethylformamide (DEF) rather than DMF.[15]

$Zn(NO_3)_2 \cdot 6H_2O$ and one equivalent H_2tph were dissolved in separate portions of DEF. The solution containing the ligand was stirred and heated to 115°C followed by the addition of $Zn(NO_3)_2 \cdot 6H_2O$. Stirring was stopped and the mixture was heated for three hours at 115°C during which time colourless crystals were obtained. The compound was analysed by single crystal X-ray crystallography, and found to be $\{[Zn_4(\mu_4\text{-}O)(tph)_3] \cdot 3DEF\}_\infty$. This network is analogous to MOF-5 previously reported by Yaghi et *al.*[16] A similar reaction was carried out using two equivalents of H_2tph. The only product of this reaction was MOF-5, as proven by X-ray powder crystallography, but a lower yield was obtained.

MOF-5 consists of the supertetrahedron $[Zn_4(\mu_4\text{-}O)(CO_2)_6]$ SBUs (Figure 2.15), that are connected together by the phenyl rings of tph^{2-} linkers into a 3-D cubic arrays (Figure 2.16). This SBU and the structure of MOF-5 were described in Chapter 1.

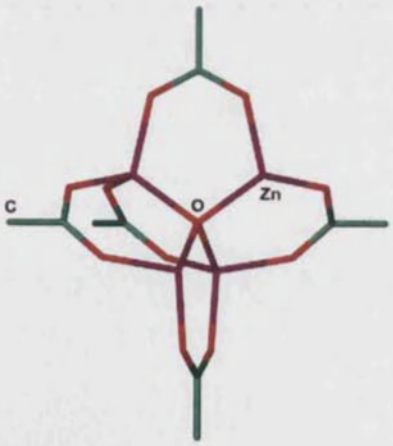

Figure 2.15. The $[Zn_4(\mu_4\text{-}O)(CO_2)_6]$ SBU of MOF-5.

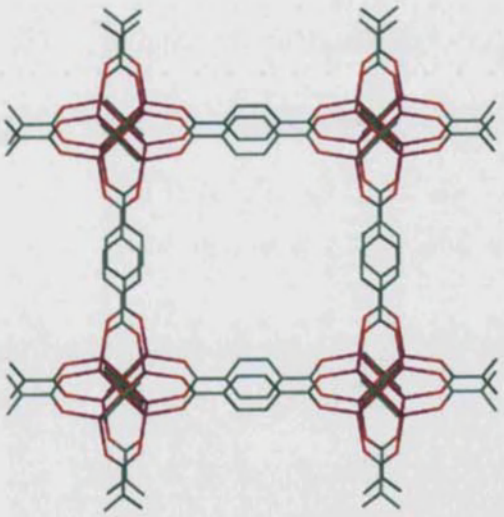

Figure 2.16. The cubic network of MOF-5 viewed along the *a* axis. The guest molecules and hydrogen atoms are removed for clarity.

On comparing the results obtained from the reaction of $Zn(NO_3)_2 \cdot 6H_2O$ and H_2tph in DMF and DEF at 115°C, it can be noted that **2** and **3** were obtained from the former solvent while MOF-5 was obtained from the latter. Also the SBU and the architecture of MOF-5 differs completely from those observed in **2** and **3**. Thus it can be stated that under the given reaction conditions, the reaction between $Zn(NO_3)_2 \cdot 6H_2O$ and H_2tph is sensitive to the length of the solvent alkyl chain.

2.2.7 Templating effect of diethylammonium cations

The templating effect of $Et_2NH_2^+$ cations on the reaction between $Zn(NO_3)_2 \cdot 6H_2O$ and H_2tph was also investigated.[15]

The reaction conditions that produced MOF-5 were used with the single difference that 0.018g (0.164 mmol) Et_2NH_2Cl were added to the solution. Orange-yellow crystals were obtained after heating the reaction mixture at 115°C for three hours. Analysis by single crystal X-ray crystallography revealed the product to be $\{(Et_2NH_2)_2[Zn_3(tph)_4] \cdot 2.5DEF\}_\infty$ (**6**). Crystallographic data for **6** are given in Table 2.8.

Table 2.8. Crystallographic data for **6**.

Empirical formula	$C_{52.5}H_{67.5}N_{4.5}O_{18.5}Zn_3$
M	1253.72
T/ K	150(2)
Crystal system	Monoclinic
Space group, *Z*	*C2/c*, 4
a/ Å	33.6075(14)
b/ Å	9.8727(4)
c/ Å	18.1642(8)
α/ °	90
β/ °	92.2260(10)
γ/ °	90
U/ Å^3	6022.3(4)
Crystal size/ mm	0.06 x 0.03 x 0.01
Wavelength/ Å	0.68680
Theta range for data collected/ °	2.08 to 26.54

Reflections collected/ observed (>2σ)	27691/ 5341
Data completeness	0.991
Goodness of fit F^2	1.033
Final R indices (I>2σ(I))	$R1$ = 0.0510, $wR2$ = 0.1458
R indices (all data)	$R1$ = 0.0674, $wR2$ = 0.1569
Largest diff. peak and hole eÅ^{-3}	0.765 and -0.494

The asymmetric unit of **6** (Figure 2.17) consists of one full and one partial zinc centres, one full and two half tph^{2-} ligands, one $Et_2NH_2^+$ cation, one full and one partial DEF guest molecules with the latter having a site occupancy factor of 0.25. The partial zinc atom, Zn(1) has a site occupation factor of 0.5 as this atom is located on an inversion centre.

The zinc centres adopt different geometries with the coordination sphere of Zn(2) being distorted tetrahedral while Zn(1) has a distorted octahedral geometry. Zn(1) is coordinated to six carboxylate groups while four tph^{2-} ligands fill the coordination sphere of Zn(2).

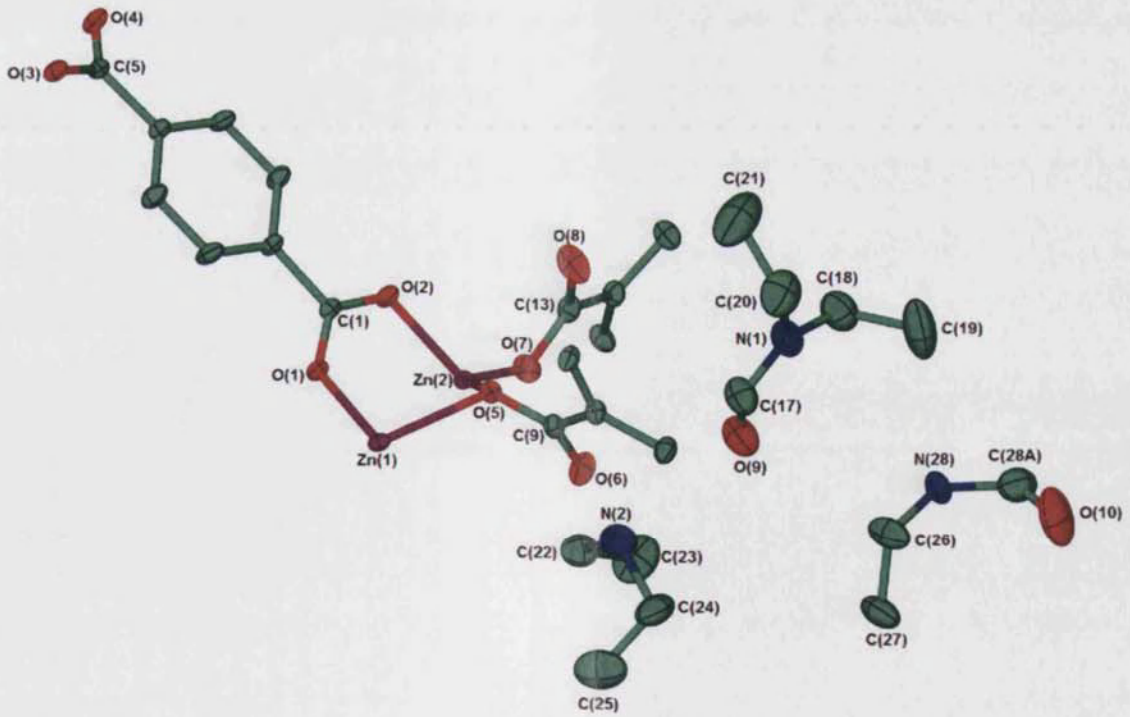

Figure 2.17. The asymmetric unit of **6** showing thermal ellipsoids at 30% probability. Hydrogen atoms are removed for clarity.

The carboxylate groups adopt three different binding modes in **6**, which are the bridging bidentate mode, O(1)-C(1)-O(2) and O(3)-C(5)-O(4), the monodentate binding mode O(7)-C(13)-O(8) and the mono-bridging bidentate mode, O(5)-C(9)-O(6) (Figure 2.17). O(1) and O(3) are more than 2.8 Å from the closest metal centre (Figure 2.18, Table 2.9) and this confirms the observation that the respective carboxylate groups bind in a bridging bidentate fashion rather than adopting the chelating bridging bidentate modes.

Zn(2) is duplicated in the SBU by the inversion symmetry at the Zn(1) position. The respective metal centres are bridged by the carboxylate groups to form a three metal centre $M_3(O_2CR)_6$ SBU (Figure 2.18). The SBUs of **6** are linked together by the tph^{2-} benzene rings to form 2-D (3,6) type sheets (Figures 2.19) while the tph^{2-} ligands that coordinate in a monodentate fashion bridges the sheets together into a 3-D network (Figure 2.20).

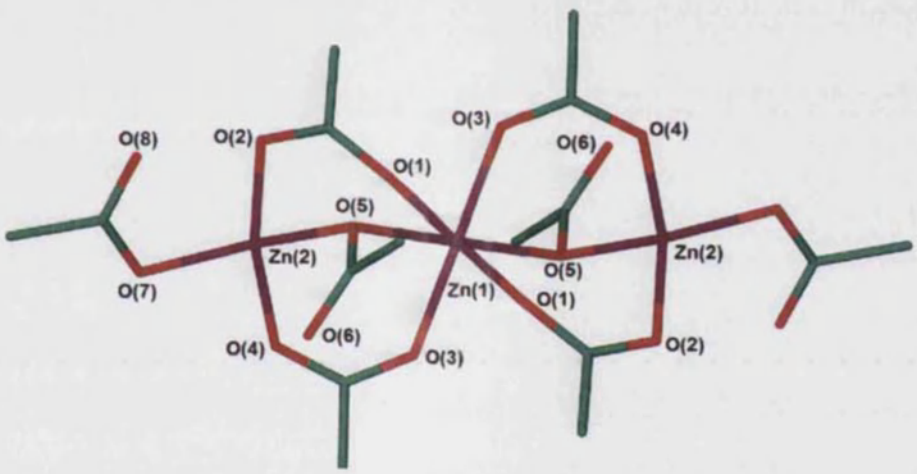

Figure 2.18. The $M_3(O_2CR)_6$ SBU of **6**.

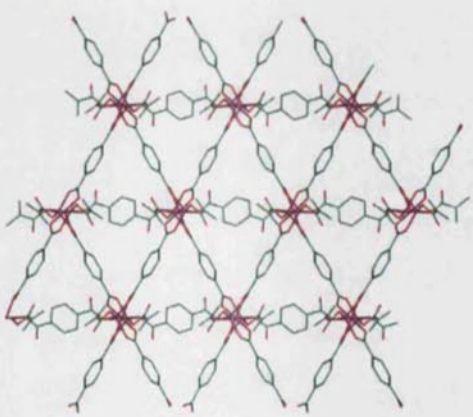

Figure 2.19. The 2-D (3,6) sheets of **6** viewed perpendicular to the (1 0 0) plane.

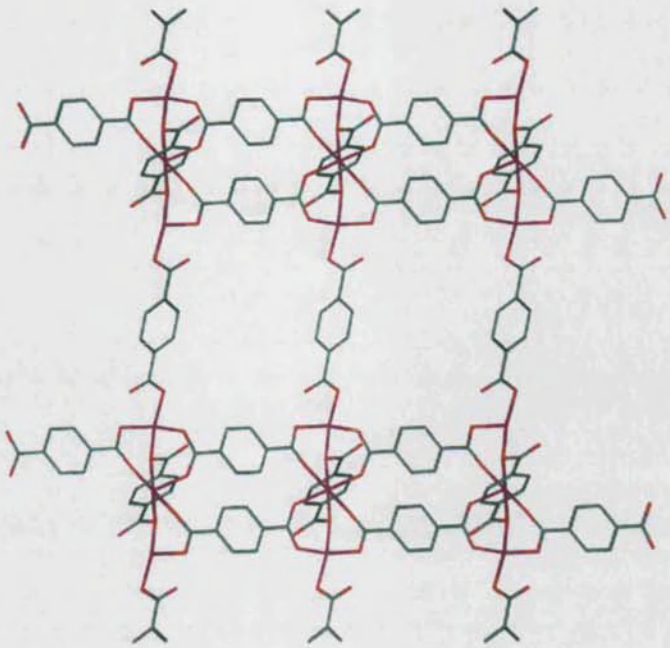

Figure 2.20. The 3-D network of **6** viewed down the *b* axis.

Tables 2.9 and 2.10 show selected bond lengths and bond angles respectively for **6**. As stated earlier, the oxygen atoms O(6) and O(8) (Figure 2.18) are not coordinated to the metal centre thus alternatively form carbon-oxygen double bonds. Nevertheless O(6)-C(9) and O(8)-C(13) are of comparable length to other carbon-oxygen bonds that have the oxygen atoms coordinated to the metal centres such as O(1)-C(1) and O(3)-C(5).

O(1) and O(3) are over 2.9 Å from the closest Zn(2) centre (Figure 2.18) thus the respective carboxylate groups labelled as O(1)-C(1)-O(2) and O(3)-C(5)-O(4) adopt the bridging bidentate mode only (Figure 2.18).

Table 2.9 Selected bond lengths for **6**.[V]

Bond Atoms	Distance/ Å
Zn(1)-O(1)	2.049(2)
Zn(1)-O(1)#3	2.049(2)
Zn(1)-O(3)#1	2.021(2)
Zn(1)-O(3)#2	2.021(2)
Zn(1)-O(5)	2.289(2)

Bond Atoms	Distance/ Å
O(1)-C(1)	1.249(4)
O(2)-C(1)	1.267(4)
O(3)-C(5)	1.245(4)
O(4)-C(5)	1.264(4)
O(5)-C(9)	1.278(4)

[V] Symmetry transformations used to generate equivalent atoms:
#1 –x+3/2,y-1/2,z+1/2 #2 x,-y+1,z-1/2
#3 –x+3/2,-y+1/2, -z

Zn(2)-O(2)	1.970(2)
Zn(2)-O(5)	2.000(2)
Zn(2)-O(4)#2	1.982(2)
Zn(2)-O(7)	1.928(2)
Zn(2)···O(8)	2.859(9)
Zn(1)···O(3)#1	3.244(6)

O(6)-C(9)	1.238(4)
O(7)-C(13)	1.271(5)
O(8)-C(13)	1.221(5)
Zn(2)···O(6)	2.887(4)
Zn(2)···O(1)	2.963(3)

Table 2.10 Selected bond angles for **6**.[VI]

Atoms	Angle/ °
O(1)-Zn(1)-O(1)#3	180.00(14)
O(3)#2-Zn(1)-O(1)#3	86.27(9)
O(3)#1-Zn(1)-O(1)	86.27(9)
O(3)#2-Zn(1)-O(1)	93.73(9)
O(1)-Zn(1)-O(5)	89.98(8)
O(1)-Zn(1)-O(5)#3	90.02(8)
O(3)#1-Zn(1)-O(3)#2	180.00(13)
O(3)#1-Zn(1)-O(5)#3	90.79(9)
O(3)#1-Zn(1)-O(5)	89.21(9)
O(3)#1-Zn(1)-O(1)#3	93.73(9)
O(3)#2-Zn(1)-O(5)#3	89.21(9)

Atoms	Angle/ °
O(1)#3-Zn(1)-O(5)#3	89.98(8)
O(3)#2-Zn(1)-O(5)	90.79(9)
O(1)#3-Zn(1)-O(5)	90.02(8)
O(5)#3-Zn(1)-O(5)	180.00(7)
O(2)-Zn(2)-O(4)#2	111.98(11)
O(4)#2-Zn(2)-O(5)	107.47(10)
O(2)-Zn(2)-O(5)	99.65(10)
O(7)-Zn(2)-O(2)	112.26(11)
O(7)-Zn(2)-O(4)#2	95.05(11)
O(7)-Zn(2)-O(5)	130.26(12)
Zn(2)-O(5)-Zn(1)	100.25(9)

H(2A) of the diethylammonium cation experiences N-H···O hydrogen bonding to O(6) (Figure 2.21) while H(2B) interacts with O(9) of the DEF molecule. Table 2.11 contains hydrogen bond details for **6**.

[VI] Symmetry transformations used to generate equivalent atoms:
#1 –x+3/2,y-1/2,z+1/2 #2 x,-y+1,z-1/2
#3 –x+3/2,-y+1/2, -z

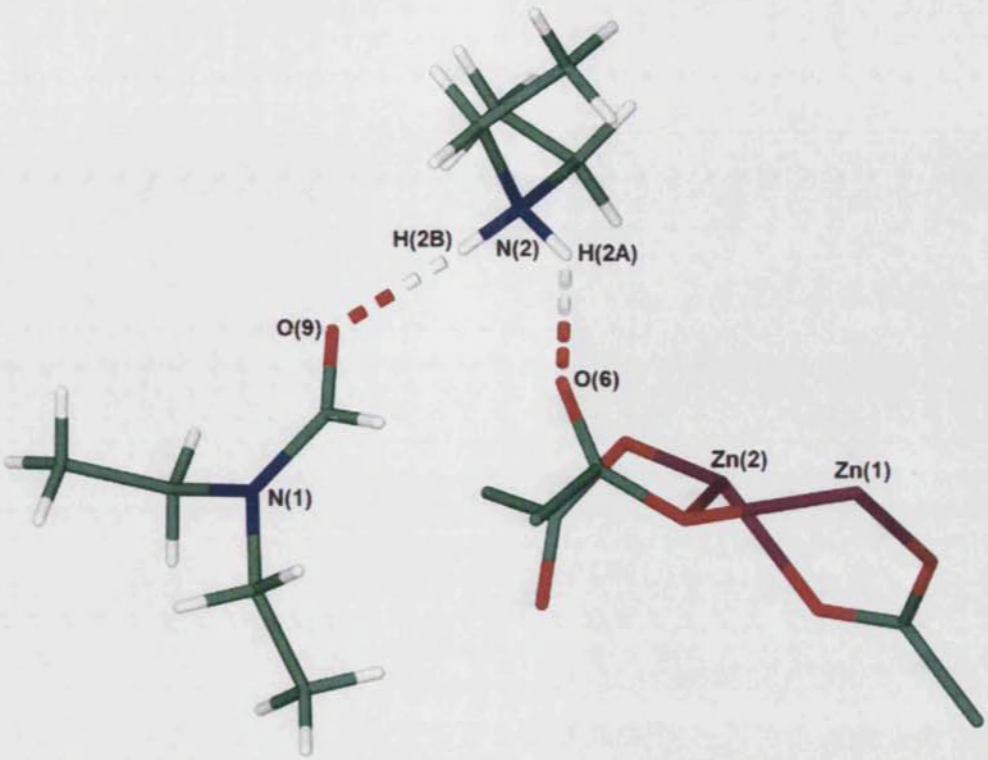

Figure 2.21. The hydrogen bonding present between $Et_2NH_2^+$, DEF and the network of **6**.

Table 2.11 Hydrogen bonds with H··A < r(A) + 2.000Å and <DHA > 110° for **6**.

D-H	d(D-H)	D(H··A)	<DHA	d(D··A)	A
N2-H2A	0.92	2.05	139	2.81	O6
N2-H2B	0.92	1.87	168	2.78	O9

2.2.8 Comparison of $\{(Me_2NH_2)_2[Zn_3(tph)_4]\cdot DMF\cdot H_2O\}_\infty$ (4) $\{(Me_2NH_2)_2[Zn(DMF)_4(OH_2)_2][Zn_6(tph)_8]\cdot 6DMF\}_\infty$ (5) and $\{(Et_2NH_2)_2[Zn_3(tph)_4]\cdot 2.5DEF\}_\infty$ (6).

The networks of **4**, **5** and **6** have many similarities. The SBUs of the three networks consist of three metal SBUs bridged by carboxylate groups with a formula $M_3(O_2CR)_6$ (Figures 2.5, 2.10a/2.10b and 2.18 respectively).

The architectures of **4**, **5** and **6** consist of (3,6) 2-D sheets linked into 3-D networks by tph^{2-} pillars. The networks in all three compounds are anionic. Charges are balanced by cations residing inside the pores. The counter ions are held in place through N-H···O hydrogen bonding to the network.

The nodes of **5** differ from those of **4** and **6**. In the latter two, the metal centres are tetra and hexacoordinated while **5** has two different $M_3(O_2CR)_6$ SBUs.

2.2.9 Increasing the length of the dicarboxylate linker

Another member of the dicarboxylate family that can act as rigid linear linker is 4,4'-biphenyldicarboxylate ($bpdc^{2-}$). Thus $bpdc^{2-}$ can be considered to be a longer analogue of tph^{2-}. Other authors[17, 18] have shown that $bpdc^{2-}$ can also react with $Zn(NO_3)_2{\cdot}6H_2O$ to form metal organic networks. Hence the reaction between $Zn(NO_3)_2{\cdot}6H_2O$ and H_2bpdc in DMF at 95°C was investigated.

$Zn(NO_3)_2{\cdot}6H_2O$ and one equivalent H_2bpdc were dissolved in separate portions of DMF. The ligand suspension was stirred and heated to 95°C, the zinc nitrate solution was then added and the reaction was left standing at 95°C. Colourless crystals formed after 3 hours. On analysis by single crystal X-ray crystallography, the crystals were revealed to be a mixture of $\{[Zn(bpdc)(DMF)]{\cdot}2DMF\}_\infty$ (**7**) and $\{[Zn_3(bpdc)_3(DMF)_2]{\cdot}3DMF{\cdot}H_2O\}_\infty$ (**8**).

The asymmetric unit of **7** consists of a zinc centre, two half $bpdc^{2-}$ ligands, one coordinated and two guest DMF molecules (Figure 2.22). The partial oxygen atoms labelled O(7)/O(7A) represent disorder over two equally occupied sites. The $bpdc^{2-}$ ligand with the carboxylate group labelled as O(3)-C(8)-O(4)/O(3A)-C(8A)-O(4A) is located over two sites and each part has an occupancy factor of 0.5. Crystallographic data for **7** are summarised in Table 2.12.

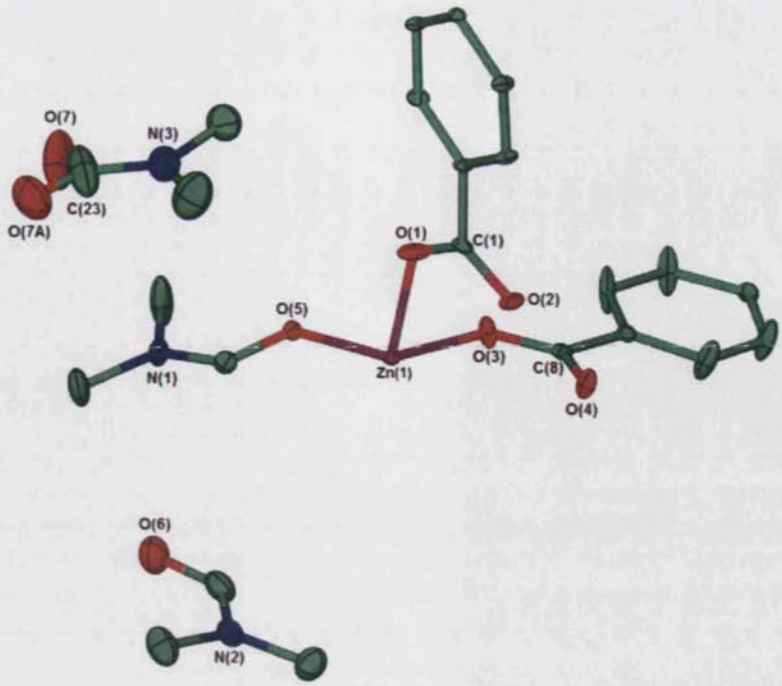

Figure 2.22. The asymmetric unit of **7** showing thermal ellipsoids at 30% probability. The hydrogen atoms are removed and only one position for the coordinated DMF and $bpdc^{2-}$ are shown for clarity.

Table 2.12. Crystallographic data for **7**.

Empirical formula	$C_{46}H_{57}N_6O_{14}Zn_2$
M	1047.71
T/ K	150(2)
Crystal system	Monoclinic
Space group, *Z*	*C*2/*c*, 4
a/ Å	26.741(5)
b/ Å	15.194(3)
c/ Å	12.224(2)
α/ °	90
β/ °	94.892(3)
γ/ °	90
U/ Å^3	4948.5(15)
Crystal size/ mm	0.07 x 0.07 x 0.02
Wavelength/ Å	0.84600
Theta range for data collected/ °	4.24 to 32.92
Reflections collected/ observed (>2σ)	18019/ 3496
Data completeness	0.965

Max. and min. transmission	0.98 and 0.92
Goodness of fit F^2	1.030
Final R indices ($I>2\sigma(I)$)	$R1$ = 0.0486, $wR2$ = 0.1265
R indices (all data)	$R1$ = 0.0787, $wR2$ = 0.1438
Largest diff. peak and hole eÅ^{-3}	0.867 and -0.678

The zinc atom adopts square pyramidal geometry with the coordination sphere being occupied by four carboxylate groups and a terminal DMF ligand (Figure 2.23).

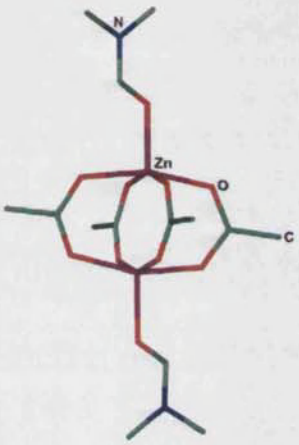

Figure 2.23. The 'paddle-wheel' type SBU of **7**.

The carboxylate groups coordinate in a bridging bidentate fashion in **7**, thus two metal centres are bridged together to form a 'paddle-wheel' type SBU (Figure 2.23). The benzene rings of the $bpdc^{2-}$ link the SBUs together into a 2-D (4,4) network (Figure 2.24). The architecture of **7** is similar to that of $\{[Zn(tph)(DMF)]\}_\infty$ (**3**), the main difference being that the former has larger pores.

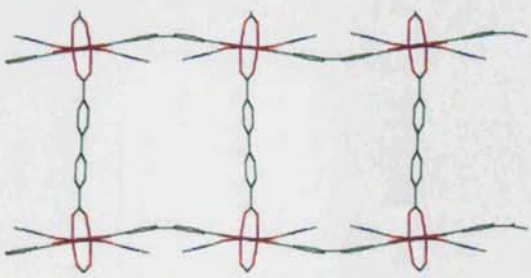

Figure 2.24. The 2-D network of **7** viewed down the *c* axis. The guest DMF molecules and hydrogen atoms are omitted for clarity.

The sheets of **7** stack parallel to one another, with the centres of adjacent sheets being offset with respect to one another. Thus the coordinated DMF molecules from one sheet lie on top of the adjacent sheet as shown in Figure 2.25.

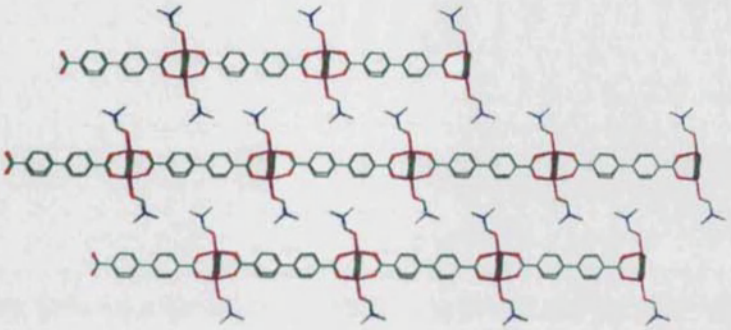

Figure 2.25. The packing of the chains of **7** viewed down the *b* axis.

As can be noted from Figure 2.26, there is a twist in the $bpdc^{2-}$ benzene rings having carbon atoms C(11), C(12) and C(13). The angle between the planes of the phenyl rings is 20°. As can be observed from Figure 2.24, the twist in the rings leads to a buckling in the network of **7**.

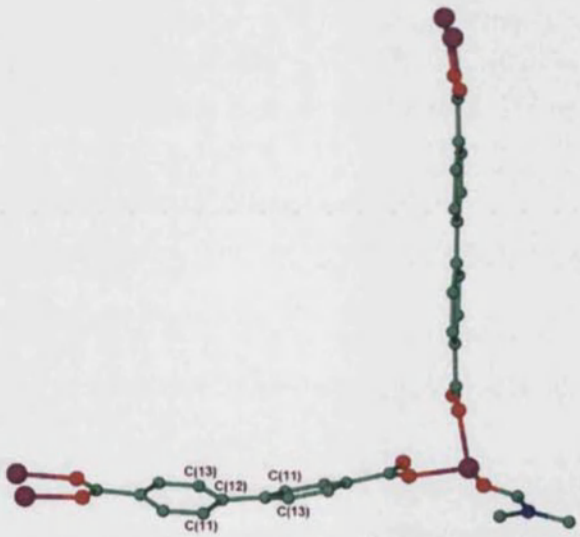

Figure 2.26. The twist in the $bpdc^{2-}$ ligands of **7**.

Selected bond lengths and bond angles for **7** are listed in Tables 2.13 and 2.14 respectively. The zinc-bpdc oxygen bond lengths vary from 2.008(2) Å to 2.061(3) Å. These values are comparable to similar zinc-oxygen bonds found in the literature.[1, 19, 20] The τ value for Zn(1) is 0, suggesting that the metal centre has a perfect square pyramidal geometry. However, as can be noted from Table 2.14, the individual oxygen-zinc-oxygen

bond angles for this metal vary from the ideal square pyramidal geometry (180°/90°) and this is due to the metal not being in the base plane.

Table 2.13. Selected bond lengths for **7**.[VII]

Bond atoms	Distance/ Å
Zn(1)-O(1)	2.008(2)
Zn(1)-O(2)#1	2.017(2)
Zn(1)-O(3)	2.040(2)
Zn(1)-O(4)#1	2.061(3)
Zn(1)-O(5)	1.987(3)
O(1)-C(1)	1.243(4)
O(2)-C(1)	1.256(4)
O(3)-C(8)	1.248(4)
O(4)-C(8)	1.243(4)

Table 2.14. Selected bond angles for **7**.[VI]

Atoms	Angle/ °
O(1)-Zn(1)-O(2)#1	159.50(12)
O(1)-Zn(1)-O(3)	88.42(11)
O(5)-Zn(1)-O(1)	103.10(10)
O(3)-Zn(1)-O(4)#1	159.52(11)
O(5)-Zn(1)-O(3)	105.58(10)
O(5)-Zn(1)-O(2)#1	97.31(10)
O(5)-Zn(1)-O(4)#1	94.89(10)
O(1)-C(1)-O(2)	125.6(3)
O(4)-C(8)-O(3)	125.1(3)

A 2-D 'paddle-wheel' network similar to **7**, has been reported by Tao et *al.*[21] The authors used Et_3N as a base to deprotonate the ligand, while the solvent was DMSO. This system yielded the network of $\{[Zn(bpdc)(DMSO)]\cdot 2DMSO\}_\infty$ which has the same topology as **7**. Apart from Zn(1)-O(1), the zinc-bpdc oxygen bond lengths of **7** (2.008(2)-2.061(3) Å) are comparable to those of $\{[Zn(bpdc)(DMSO)]\cdot 2DMSO\}_\infty$ (2.026(3)-2.064(3) Å). Tao and co-workers[21] did not report any buckling in the structure.

The second compound obtained from the reaction of $bpdc^{2-}$ and $Zn(NO_3)_2\cdot 6H_2O$ was identified as $\{[Zn_3(bpdc)_3(DMF)_2]\cdot 3DMF\cdot H_2O\}_\infty$ (**8**). The asymmetric unit of **8** consists of one full and one partial zinc, one and a half $bpdc^{2-}$ ligands, one coordinated DMF ligand, a water guest and both a full and a partial DMF molecules (Figure 2.27).

The $bpdc^{2-}$ ligands and the coordinated DMF are disordered over two equal sites. The guest DMF molecule with the nitrogen atom labelled as N(3) is located over two positions with site occupation factors of 0.6 and 0.4 respectively. The remaining DMF and water molecules each have half occupancy. Only the major disordered components of the

[VII] Symmetry transformations used to generate equivalent atoms:
#1 -x+1/2,-y+1/2,-z

asymmetric unit are shown in Figure 2.27. Crystallographic data for **8** are summarised in Table 2.15.

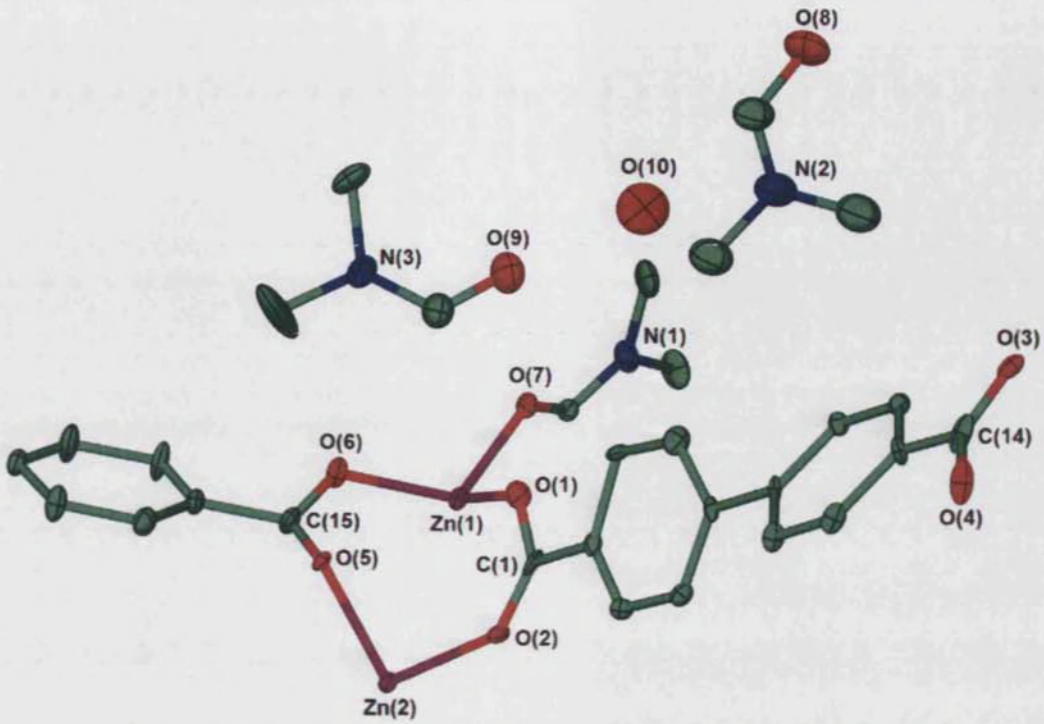

Figure 2.27. The asymmetric unit of **8** showing thermal ellipsoids at 30% probability. Hydrogen atoms are removed and only the major components of the disordered parts are shown for clarity.

Table 2.15. Crystallographic data for **8**.

Empirical formula	$C_{28.5}H_{30}N_{2.5}O_9Zn_{1.5}$
M	649.61
T/ K	150(2)
Crystal system	Monoclinic
Space group, *Z*	$P2_1/n$, 4
a/ Å	11.4740(2)
b/ Å	14.8760(2)
c/ Å	19.1300(3)
α/ °	90
β/ °	102.837(1)
γ/ °	90
U/ Å^3	3183.63(9)
Crystal size/ mm	0.40 x 0.30 x 0.06
Wavelength/ Å	0.71073

Theta range for data collected/ °	3.55 to 37.46
Reflections collected/ observed (>2σ)	52765/ 5529
Data completeness	0.993
Max. and min. transmission	0.94 and 0.68
Goodness of fit F^2	1.090
Final R indices (I>2σ(I))	$R1$ = 0.0669, $wR2$ = 0.1765
R indices (all data)	$R1$ = 0.0920, $wR2$ = 0.1920
Largest diff. peak and hole eÅ^{-3}	1.146 and -0.546

The zinc centres in **8** adopt different coordination geometries. Zn(1) has a distorted tetrahedral geometry and the coordination sphere is populated by a terminal DMF ligand and three carboxylate groups. Zn(2) adopts a distorted octahedral geometry and is coordinated to six bpdc^{2-} ligands.

The carboxylate groups adopt the bridging bidentate binding mode only in **8**. Other zinc···oxygen bond distances (Table 2.16) further confirm that the carboxylate groups adopt the above mentioned coordination mode only. The functional groups link the three metal centres together to form an octahedral and two tetrahedral $M_3(O_2CR)_6$ SBU. The coordinated DMF molecules prevent the network growth in the third dimension.

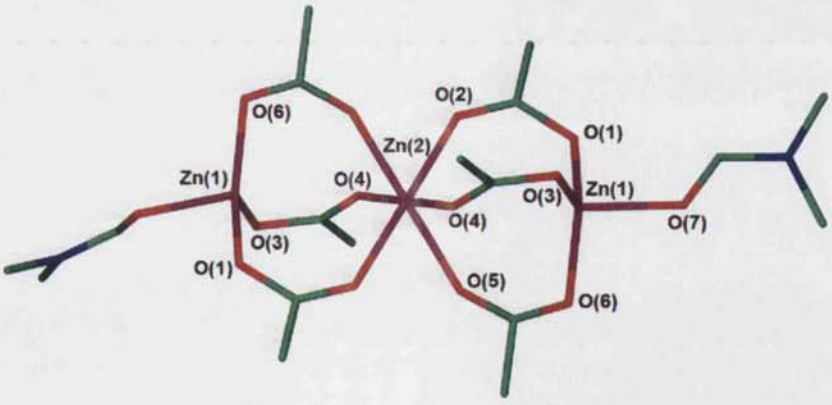

Figure 2.28. The $M_3(O_2CR)_6$ SBU of **8**. Only one part of the disordered fragments are shown for clarity.

The SBUs are connected together by the benzene rings of the bpdc^{2-} ligands to form a 2-D (3,6) type network (Figure 2.29). The sheets pack parallel to one another as shown in Figure 2.30. The centres of the individual networks are shifted with respect to one

another and thus the coordinated DMF molecules from one sheet point towards the voids of the adjacent sheets.

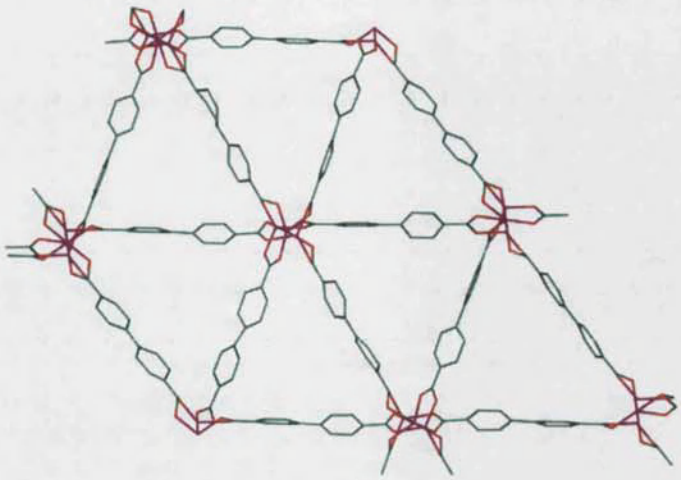

Figure 2.29. The 2-D network of **8** viewed down the *a* axis.

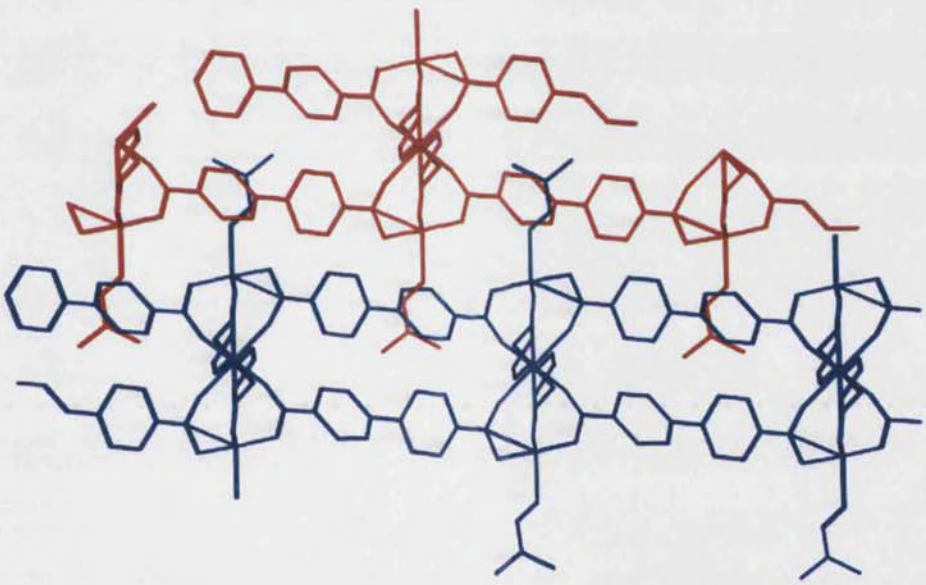

Figure 2.30. The 2-D sheets of **8** viewed down the *b* axis. The sheets are coloured red and blue for clarity.

Selected lists of bond lengths and bond angles for **8** are displayed in Tables 2.16 and 2.17 respectively. As can be noted from Table 2.16, with the exception of Zn(1)-O(3)#1, the oxygen atoms form longer bonds to the metal centres than Zn(1)-O(1) and Zn(1)-O(6). This difference in bond lengths might be a result of the undulation within the $bpdc^{2-}$ ligand.

As can be noted from Table 2.17, the oxygen-zinc-oxygen bond angles for of Zn(1) are distorted significantly from the ideal 109.5°.

Table 2.16. Selected bond lengths for **8**.[VIII]

Bond atoms	Distance/ Å	Bond atoms	Distance/ Å
Zn(1)-O(1)	1.928(4)	O(1)-C(1)	1.381(14)
Zn(1)-O(3)#1	1.911(15)	O(2)-C(1)	1.230(16)
Zn(1)-O(3A)#1	2.027(15)	O(4)-C(14)	1.27(2)
Zn(1)-O(6)	1.931(3)	O(5)-C(15)	1.373(9)
Zn(1)-O(7)	2.031(8)	O(6)-C(15)	1.231(7)
Zn(2)-O(2)	2.012(6)	O(3A)-C(14A)	1.25(2)
Zn(2)-O(5A)	2.101(7)	O(4A)-C(14A)	1.270(18)
Zn(2)-O(2A)	2.042(7)	Zn(1)···O(2)	3.093(7)
Zn(2)-O(4)#1	2.073(7)	Zn(1)···O(4)#1	2.584(9)
Zn(2)-O(4A)#1	2.076(7)	Zn(1)···O(4A)#1	2.875(7)
Zn(2)-O(5)	2.135(5)	Zn(1)···O(5A)	2.927(6)

Table 2.17. Selected bond angles for **8**.[VII]

Atoms	Angle/ °	Atoms	Angle/ °
O(3)#1-Zn(1)-O(1)	115.3(5)	O(2)-Zn(2)-O(4)#3	86.3(4)
O(1)-Zn(1)-O(6)	119.08(16)	O(2)-Zn(2)-O(5)	94.6(2)
O(1)-Zn(1)-O(7)	98.3(3)	O(4)#3-Zn(2)-O(5)	89.3(3)
O(3)#1-Zn(1)-O(6)	121.2(4)	O(5)-Zn(2)-O(5)#2	180.0(3)
O(6)-Zn(1)-O(7)	110.7(3)	O(2)-C(1)-O(1)	123.9(11)
O(2)#2-Zn(2)-O(2)	180.0(4)	O(4)-C(14)-O(3)	123(2)
		O(6)-C(15)-O(5)	120.1(5)

Very recently the network of **8** was reported by Brammer and co-workers.[22] The associated formula for the reported structure is $\{[Zn_3(bpdc)_3(DMF)_2]\cdot 4DMF\}_\infty$ This network is isostructural to that for **8** but the compounds differ in the incorporated guest solvent molecules. The compound reported by Brammer and co-workers includes 4 DMF guest molecules while the pores of **8** are filled by 3 DMF and 1 water molecule.

[VIII] Symmetry transformations used to generate equivalent atoms:
#1 x+1/2,-y+1/2,z-1/2 #2 -x,-y+1,-z
#3 -x-1/2,y+1/2,-z+1/2

2.2.10 Comparison of $\{[Zn_3(tph)_3(H_2O)_3]\cdot 4DMF\}_\infty$ (2) $\{[Zn(tph)(DMF)]\}_\infty$ (3) $\{[Zn(bpdc)(DMF)]\cdot 2DMF\}_\infty$ (7) and $\{[Zn_3(bpdc)_3(DMF)_2]\cdot 3DMF\cdot H_2O\}_\infty$ (8)

The two networks obtained from $bpdc^{2-}$ share similarities with networks obtained from tph^{2-} reported in this chapter.

Both $\{[Zn_3(tph)_3(H_2O)_3]\cdot 4DMF\}_\infty$ (**2**) and **8** are built from $M_3(O_2CR)_6$ SBUs (Figures 2.2a and 2.28 respectively). The building units of both structures have a terminal ligand coordinated to the metal centres. The architecture of both compounds consists of 2-D (3,6) type sheets.

The network of $\{[Zn(bpdc)(DMF)]\cdot 2DMF\}_\infty$ **7** shares many features with that of $\{[Zn(tph)(DMF)]\}_\infty$ (**3**). In both cases the SBUs are of the 'paddle-wheel' type with the benzene rings linking the SBUs into a (4,4) 2-D type net.

The terminal ligands of **2** and **8** differ. Water acts as a terminating point in **2** while DMF fulfils this function in **8**. The carboxylate groups of **2** adopt two different binding modes, namely the monodentate and bridging bidentate forms while only the latter is found in **8**.

The networks obtained from $bpdc^{2-}$ have bigger pores than similar network topologies having tph^{2-} as the organic linker. This is due to the longer separation of the carboxylate groups on $bpdc^{2-}$ (~10.0Å) as opposed to tph^{2-} (~5.8Å).

2.3 Properties of the networks

As mentioned in Chapter 1, metal organic frameworks can store gases or act as catalysts. For example, after the loss of the guest DMF molecules $\{[Zn(tph)(OH_2)]\cdot DMF\}_\infty$ (**1**) gave a compound with the formula $\{[Zn(tph)(OH_2)]\}_\infty$ This material was reported to possess gas storage abilities. Yaghi and co-workers[3] have reported that $\{[Zn(tph)(OH_2)]\}_\infty$ has micropores and also quantified the amount of gases adsorbed into the voids of the network.

The network of $\{[Zn_4(\mu_4\text{-}O)(tph)_3]\cdot 3DEF\}_\infty$ (**MOF-5**) which has been reported also by Yaghi and co-workers,[16] was found to be stable towards the removal of guest molecules. The guest free network attracted attention for its gas storage abilities.[16]

$\{(Me_2NH_2)_2[Zn_3(tph)_4]\cdot DMF\cdot H_2O\}_\infty$ (**4**) and its analogue $\{(Et_2NH_2)_2[Zn_3(tph)_4]\cdot 2.5DEF\}_\infty$ (**6**) have guest solvent molecules within the pores. Experimental procedures to attempt to obtain solvent-free networks were carried out. The results obtained from these experiments will be discussed below.

2.4 Guest removal experiments for $\{(Me_2NH_2)_2[Zn_3(tph)_4]\cdot DMF\cdot H_2O\}_\infty$ (4) and $\{(Et_2NH_2)_2[Zn_3(tph)_4]\cdot 2.5DEF\}_\infty$ (6)

Information about the thermal stability of the networks was obtained through thermogravimetric analysis (TGA). These experiments provided information on the temperatures at which the solvent molecules can be removed from within the pores. The guest molecules were subsequently removed by heating the networks at the temperature suggested from the TGA plot.

X-ray powder data collected for the heat-treated samples were compared to the X-ray powder patterns for the samples prior to heating. This comparison gave an indication of the stability of the network towards heating.

Other authors such as Zou and co-workers[23] used a similar method to obtain information about the thermal behaviour and stability of the networks.

2.4.1 Thermal characteristics of $\{(Me_2NH_2)_2[Zn_3(tph)_4]\cdot DMF\cdot H_2O\}_\infty$ (4)

A sample of **4** was heated from 30°C to 600°C at a rate of 10°C/s. The thermogravimetric data of **4** (Figure 2.31) show three mass losses before a plateau is reached, and above 470°C the network shows signs of decomposition. The three mass losses labelled as a, b and c account for approximately 35% of the total mass. Regions a to c could not be explained in terms of the guest molecules and thus more experiments were carried out to aid the interpretation of the data acquired from the TGA.

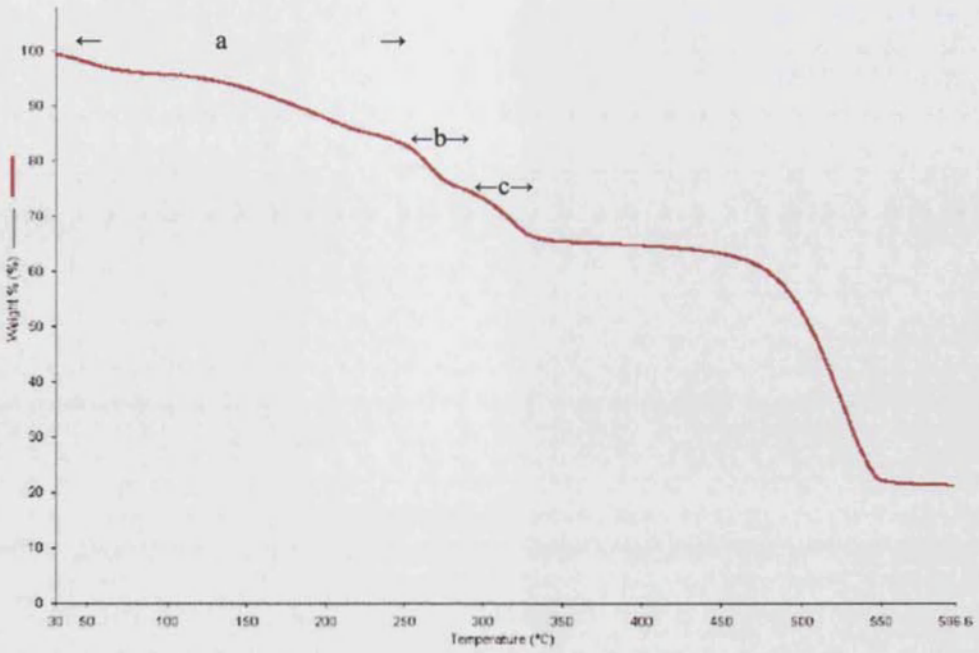

Figure 2.31. TGA data for **4**.

When X-ray powder data were collected on a sample of **4** that was heated to 375°C (**4a**), it could be observed that the positions and the intensities of the peaks changed from that of the starting material (Figure 2.32). The position of the new peaks indicates that **4** undergoes a transformation on heating to the previously reported $\{[Zn(tph)(H_2O)]\}_\infty$[5] (**4a**) (Figure 2.32). This solid state transformation can be rationalised by the loss of the dimethylammonium cations, one tph^{2-} ligand and the guest DMF molecules.

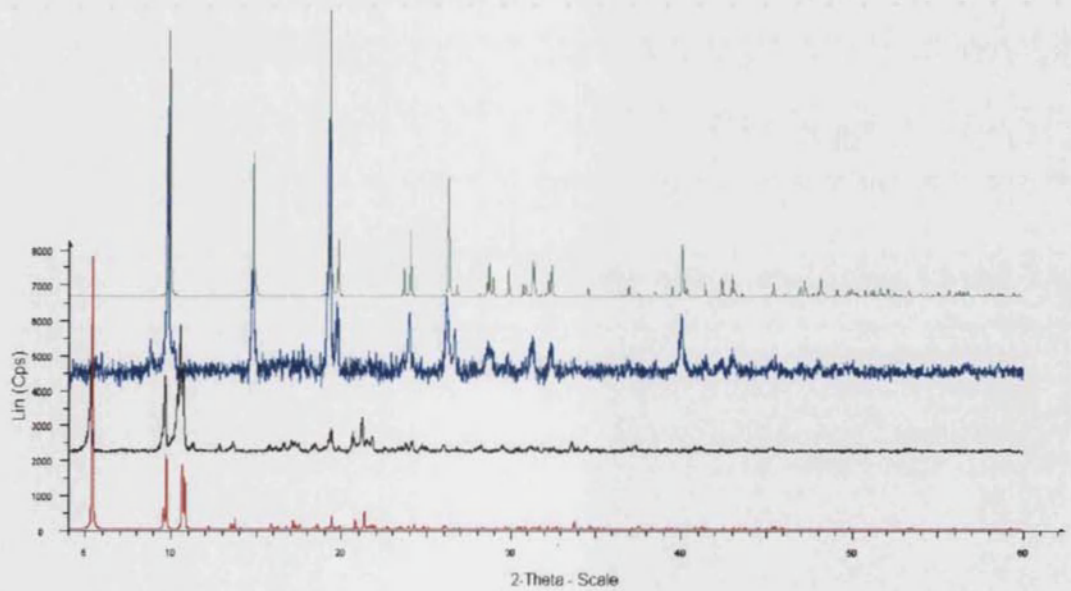

Figure 2.32. Powder data for **4** and **4a**. The red trace is the simulated powder pattern obtained from the single crystal data of **4**. The black trace is the experimental powder data for **4**, the blue trace is the experimental powder pattern for **4a** while the green trace is the simulated powder pattern for $\{[Zn(tph)(H_2O)]\}_\infty$

2.4.2 Guest removal experiments for $\{(Et_2NH_2)_2[Zn_3(tph)_4]\cdot 2.5DEF\}_\infty$ (6)

$\{(Et_2NH_2)_2[Zn_3(tph)_4]\cdot 2.5DEF\}_\infty$ (**6**) also contains guest solvent molecules within the pores. Thus **6** was another candidate for guest removal experiments but while this was being investigated, Biemmi and co-workers[24] reported that **6** lost the guest DEF molecules together with the $Et_2NH_2^+$ counter ions and one tph^{2-} in separate steps to give a new crystalline phase with the empirical formula of $[Zn_3(tph)_3]$.

2.5 Guest exchange experiments

Results in section 2.4.1 show that the DMF molecules could not be removed from within the pores without altering the structure of **4**, thus a different approach to obtain the guest free network was undertaken. A sample of **4** was put in low boiling solvents to facilitate guest solvent replacement. The aim was to exchange the DMF molecule with lower boiling solvents, thus accessing the free spaces within the pores at lower temperatures by removal of the more volatile guest molecules. Other authors have reported guest exchange reactions for dichloromethane,[19] acetone[25] and methanol.[18] Following these examples, samples of **4** were immersed in dichloromethane, methanol and acetone. The exchange processes were monitored by X-ray powder diffraction and TGA with data being collected after 10 minutes, 18 hours and 1 week.

In the cases of acetone and dichloromethane, there was no guest exchange as TGA experiments for the immersed samples showed the same % mass losses as the starting material. X-ray powder diffraction patterns were also unchanged thus further supporting this conclusion.

In the case of methanol a different scenario was observed. The powder pattern for the sample left over methanol for 10 minutes did not show any change in the peak positions but when the sample was left in the solvent for longer periods, the pattern changed completely until it matched that of $\{[Zn(tph)(H_2O)]\}_\infty$[5] (Figure 2.33). This suggests that methanol is not 'innocent', and following arguments presented by Allendorf and Greathouse,[26] the methanol might be attacking the zinc-oxygen bonds of the network to break it down with $\{[Zn(tph)(H_2O)]\}_\infty$ precipitating over time.

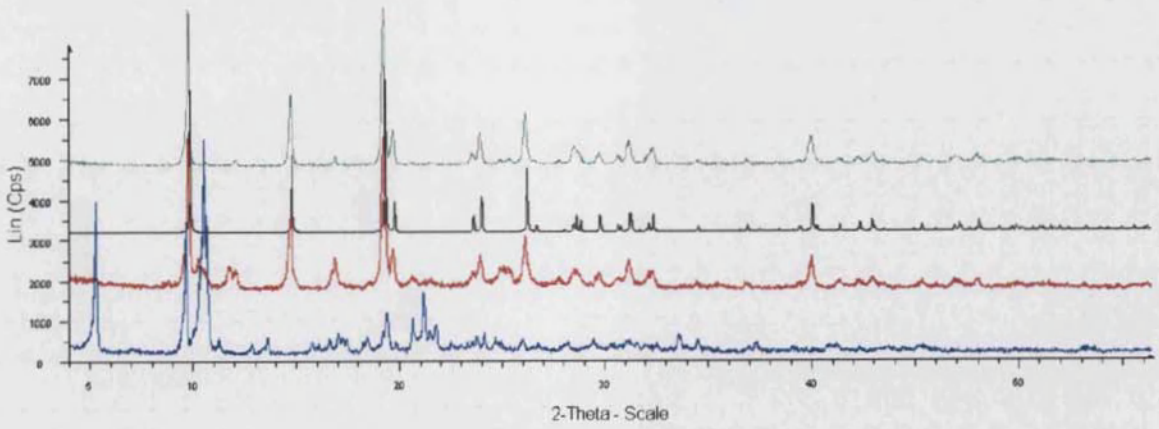

Figure 2.33. The powder data for the methanol exchange experiments of **4**. The blue trace is the powder plot for the starting material, the red trace is the powder trace for **4** immersed in methanol for 18 hours. The black trace is the simulated powder data for $\{[Zn(tph)(H_2O)]\}_\infty$ obtained from the CSD while the green trace is for **4** after immersion in methanol for 1 week.

2.6 Summary and conclusions

The results in this chapter have shown that the reaction of $Zn(NO_3)_2 \cdot 6H_2O$ with H_2tph is sensitive towards small changes in the reaction conditions such as pressure, temperature and solvent purity.

It was also demonstrated that secondary ammonium cations such as $Me_2NH_2^+$ and $Et_2NH_2^+$, exhibit a templating effect with the product of the reaction in the presence of cations being different that where cation formation was prevented.

The reaction between $Zn(NO_3)_2 \cdot 6H_2O$ and H_2tph was also found to be sensitive to the nature of the solvent. As described in Section 2.2.6, a change from DMF to DEF brought about a significant difference in the architecture of the network with the structure obtained from DEF being MOF-5.

The temperature at which the reaction is carried out plays a significant role in the nature of the product. The reaction of $Zn(NO_3)_2 \cdot 6H_2O$ and H_2tph at 95°C gave $\{[Zn(tph)(H_2O)] \cdot DMF\}_\infty$ (**1**) while a mixture of two products $\{[Zn_3(tph)_3(H_2O)_3] \cdot 4DMF\}_\infty$ (**2**) and $\{[Zn(tph)(DMF)]\}_\infty$ (**3**) was obtained when the temperature was increased to 115°C.

The reaction between $Zn(NO_3)_2 \cdot 6H_2O$ and H_2tph at 115°C was also found to be sensitive towards pressure. The only product of the reaction being $\{[Zn(tph)(DMF)]\}_\infty$ (**3**).

The reaction of $Zn(NO_3)_2 \cdot 6H_2O$ with 4,4'-biphenyldicarboxylate at 95°C was also studied in DMF. While tph^{2-} formed one compound at this temperature, a mixture of two compounds $\{[Zn(bpdc)(DMF)] \cdot 2DMF\}_\infty$ (**7**) and $\{[Zn_3(bpdc)_3(DMF)_2] \cdot 3DMF \cdot H_2O\}_\infty$ (**8**) was obtained from $bpdc^{2-}$.

The structure of $\{(Me_2NH_2)_2[Zn_3(tph)_4] \cdot DMF \cdot H_2O\}_\infty$ (**4**) was observed to be unstable towards the thermal removal of guest molecules and exposure to MeOH. In both the thermal and guest exchange experiments, **4** was converted into $\{[Zn(tph)(H_2O)]\}_\infty$

2.7 Further work

Since the $Zn(NO_3)_2 \cdot 6H_2O/H_2tph$ system was shown to be sensitive to temperature differences, the reaction could be carried out using temperatures outside the range discussed here. This study will indicate if the reaction products for this system are affected by temperatures other than 95°C and 115°C.

When the solution containing $Zn(NO_3)_2 \cdot 6H_2O$ and H_2tph was heated for 3 hours at 115°C, a mixture of $\{[Zn_3(tph)_3(H_2O)_3] \cdot 4DMF\}_\infty$ (**2**) and $\{[Zn(tph)(DMF)]\}_\infty$ (**3**) was formed. The latter product could be obtained in a pure form by applying pressure to the system. Pressure could also be applied to the reaction yielding $\{[Zn(bpdc)(DMF)] \cdot 2DMF\}_\infty$ (**7**) and $\{[Zn_3(bpdc)_3(DMF)_2] \cdot 3DMF \cdot H_2O\}_\infty$ (**8**) to try an isolate one of the products. If successful the robustness of the final network towards guest removal could be carried out using the experimental procedure highlighted here.

References:

1. L.S.Long; Y.P.Ren; L.H.Ma; Y.B.Jiang; R.B.Huang; L.S.Zheng, *Inorg. Chem. Commun.* **2003,** 6, 690.
2. H.Shepherd. *Synthesis and behaviour of selected metal-organic frameworks.* M.Chem.thesis, University of Bath, Bath, 2006.
3. H.Li; M.Eddaoudi; T.L.Groy; O.M.Yaghi, *J.Am.Chem.Soc.* **1998,** 120, 8571.
4. C.Oldham, *Comprehensive Coordination Chemistry.*; Pergamon Press.: Oxford., 1987; 2, p 439-441.
5. M.Edgar; R.Mitchell; A.Slawin; P.Lightfoot; P.Wright, *Chem.Eur.J.* **2001,** 7, 5168.
6. H.F.Clausen; R.D.Poulsen; A.D.Bond; M.S.Chevallier; B.B.Iversen, *J.Solid.State.Chem.* **2005,** 178, 3342.
7. A.J.Blake; P.Hubberstey; M.Schroder; C.C.Williams, *Chem.Commun.* **2005,** 5435.
8. H.Li; C.E.Davis; T.L.Groy; D.G.Kelley; O.M.Yaghi, *J.Am.Chem.Soc.* **1998,** 120, 2186.
9. A.Bondi, *J.Phys.Chem.* **1964,** 68, 441.
10. J.D.Lee, *Concise Inorganic chemistry.* 5th ed.; London, 1996; p 147.
11. A.W.Addison; T.N.Rao; J.Reedijk; J.van.Rijn; G.C.Verschoor, *J.Chem.Soc.Dalton.Trans.* **1984,** 1349.
12. J.Juillard, *Recommended methods for purification of solvents and tests for impurities.* J.F.Coetzee. ed.; Pergamon: Oxford, 1982; p 32.
13. T.Loiseau; H.Muguerra; G.Ferey; M.Haouas; F.Taulelle, *J.Solid.State.Chem.* **2005,** 178, 621.
14. S.M.Hawxwell; L.Brammer, *CrystEngComm* **2006,** 8, 474.
15. R.C.Friend. *Three dimensional co-ordination networks.* M.Chem.thesis, University of Bath., Bath., 2006.
16. N.L.Rosi; J.Eckert; M.Eddaoudi; D.T.Vodak; J.Kim; M.O'Keeffe; O.M.Yaghi, *Science* **2003,** 300, 1127.
17. M.Eddaoudi; H.Li; M.O'Keeffe; O.M.Yaghi, *Nature* **1999,** 402, 276.
18. J.H.Liao; T.J.Lee; C.T.Su, *Inorg. Chem. Commun.* **2006,** 9, 201.
19. N.L.Rosi; M.Eddaoudi; J.Kim; M.O'Keeffe; O.M.Yaghi, *Angew.Chem.Int.Ed.* **2002,** 41, 284.
20. Y.C.Liang; M.C.Hong; R.Cao; J.B.Weng; W.P.Su, *Inorg. Chem. Commun.* **2001,** 4, 599.
21. J.Tao; X.Yin; R.Huang; L.Zheng; S.W.Ng, *Inorg.Chem.Commun.* **2002,** 5, 975.
22. S.M.Hawxwell; H.Adams; L.Brammer, *Acta.Cryst.* **2006,** B62, 808.
23. F.Q.Zou; X.H.Bu; R.H.Zhang, *Inorg.Chem.* **2004,** 43, 5382.
24. E.Biemmi; T.Bein; N.Stock, *J.Solid State Sciences* **2006,** 8, 363.
25. B.Chen; N.W.Ockwig; A.R.Millward; D.S.Contreras; O.M.Yaghi, *Angew.Chem.Int.Ed.* **2005,** 44, 4745.
26. J.A.Greathouse; M.D.Allendorf, *J.Am.Chem.Soc.* **2006,** 128, 10678.

Chapter 3 Cadmium dicarboxylate networks

3.1 Introduction

As has been illustrated in Chapters 1 and 2, metal organic frameworks consisting of transition metals and dicarboxylates are very commonly studied with zinc being the metal of preference. Despite cadmium(II) also being a d^{10} metal fewer networks have been reported using this, in comparison to zinc(II). In the majority of the cases, the cadmium-dicarboxylate networks also include another ligand, which in many cases is an *N*-heterocyclic ligand.[1,2]

The structure of $\{[Cd(bpy)(tph)(H_2O)]\}_\infty$[1] (bpy = 2,2'-bipyridine, tph^{2-} = 1,4-benzenedicarboxylate) consists of 1-D zigzag chains. The chains are linked together into a 2-D 'herringbone' structure via $\pi\cdots\pi$ stacking between the pyridyl rings, and hydrogen bonding between the water and carboxylate groups.

In contrast, $\{[Cd(tph)(py)]\}_\infty$[2] (py = pyridine) forms a 3-D networks. This network was synthesised from $Cd(ClO_4)_2\cdot 6H_2O$ and 1,4-dicyanobenzene, with the latter being hydrolysed *in situ* to tph^{2-}. A similar hydrolysis was observed in the reaction of $Fe(ClO_4)_3$ and 4-pyridinecarbaldehyde, with the ligand precursor being hydrolysed to 4-pyridinecarboxylate.[3] When H_2tph and $Cd(ClO_4)_2\cdot 6H_2O$ were used as the starting materials in the synthesis of $\{[Cd(tph)(py)]\}_\infty$, the reaction failed to yield the same compound thus demonstrating the importance of the starting precursors in the formation of the network.

Apart from the networks reported by Thirumurugan and Rao[4] (Chapter 1), one other network containing cadmium and dicarboxylates as the only building blocks is $\{(Me_2NH_2)_2\cdot[Cd_3(1,3\text{-bdc})_4]\}_\infty$[5] (1,3-$bdc^{2-}$ = 1,3-benzenedicarboxylate). This structure consists of infinite 1-D chains composed of alternating hexacoordinate cadmium centres and carboxylate groups (Figure 3.1). The infinite chains are linked together by the benzene rings of the 1,3-bdc^{2-} ligands to form a 3-D network. The infinite chains constitute the Secondary Building Units (SBUs) of this network (Figure 3.1). Overall $\{(Me_2NH_2)_2\cdot[Cd_3(1,3\text{-bdc})_4]\}_\infty$ is an anionic network with the charges being balanced by the dimethylammonium cations present in the pores.

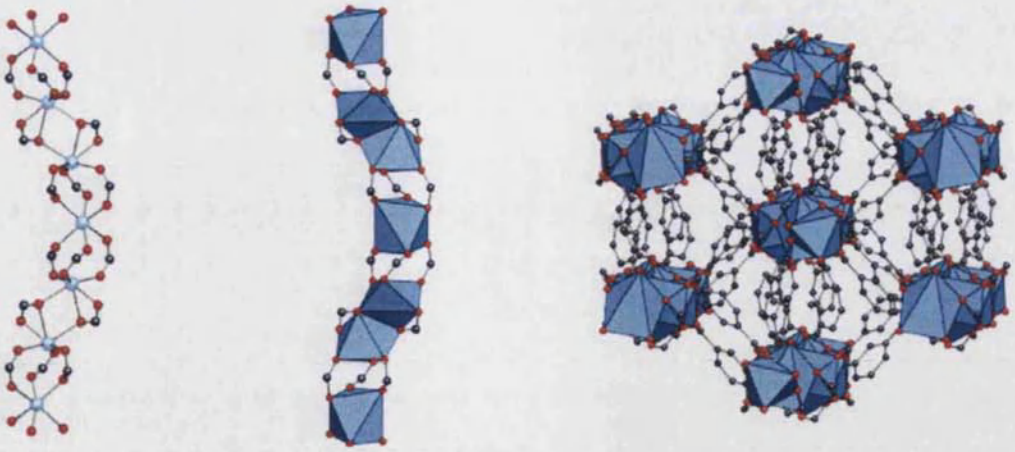

Figure 3.1. From left to right, the infinite 1-D chains of $\{(Me_2NH_2)_2{\cdot}[Cd_3(1,3\text{-bdc})_4]\}_\infty$ shown as balls and sticks, polyhedra and the 3-D network of $\{(Me_2NH_2)_2{\cdot}[Cd_3(1,3\text{-bdc})_4]\}_\infty$[5]

3.2 Aims

This chapter reports findings in relation to the sensitivity of the reaction between $Cd(NO_3)_2{\cdot}4H_2O$ and 1,4-benzenedicarboxylic acid towards changes in temperature, pH, pressure, the presence of ammonium cations and solvent. The network formed from the reaction of 4,4'-biphenyldicarboxylic acid and $Cd(NO_3)_2{\cdot}4H_2O$ is analysed and compared to the compounds obtained using tph^{2-} as the ligand.

Another aim in synthesising new networks was to assess their gas adsorption and catalytic properties. The networks were characterised using X-ray crystallography and thermogravimetric analysis. The catalytic properties of two networks are discussed at the end of this chapter while gas adsorption properties are explored in Chapter 4.

Results and discussion

3.2.1 Reaction of $Cd(NO_3)_2{\cdot}4H_2O$ and H_2tph in DMF at 115°C

$Cd(NO_3)_2{\cdot}4H_2O$ and two equivalents of H_2tph were dissolved separately in DMF and mixed at 115°C. Colourless crystals were obtained after standing at this temperature for five hours. Analysis of these crystals by X-ray crystallography revealed the compound to be $\{[Cd(tph)(DMF)]\}_\infty$ (**9**).

The asymmetric unit of **9** consists of one cadmium centre, two half tph^{2-} ligands and one coordinated DMF molecule (Figure 3.2). Crystallographic data for **9** are given in Table 3.1.

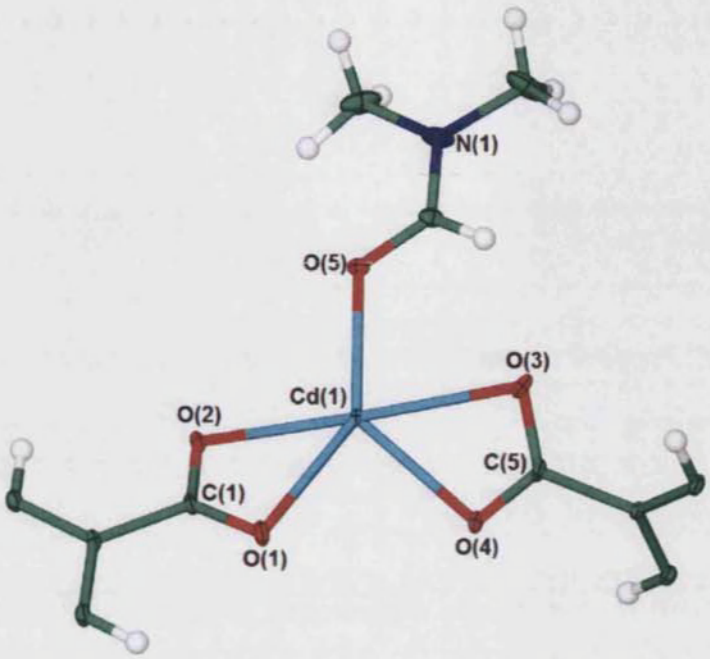

Figure 3.2. The asymmetric unit of **9** showing thermal ellipsoids at 30% probability.

Table 3.1. Crystallographic data for **9**.

Empirical formula	$C_{11}H_{11}CdNO_5$
M	349.61
T/ K	150(2)
Crystal system	Triclinic
Space group, *Z*	*P*-1, 2
a/ Å	7.4523(9)
b/ Å	9.7764(12)
c/ Å	9.8469(12)
α/ °	118.225(2)
β/ °	102.118(2)
γ/ °	91.358(2)
U/ Å^3	611.51(13)
Crystal size/ mm	0.06 x 0.04 x 0.01
Wavelength/ Å	0.68970
Theta range for data collected/ °	2.32 to 32.01

Reflections collected/ observed (>2σ)	8031/3856
Data completeness	0.903
Goodness of fit F^2	1.009
Final R indices (I>2σ(I))	$R1$ = 0.0372, $wR2$ = 0.0965
R indices (all data)	$R1$ = 0.0391, $wR2$ = 0.0972
Largest diff. peak and hole eÅ^{-3}	0.893 and -0.757

The cadmium centre in **9** is coordinated to seven oxygen atoms which belong to four tph^{2-} ligands and a DMF molecule (Figure 3.3). The carboxylate groups coordinate to the metal centre in the chelating bridging bidentate mode.

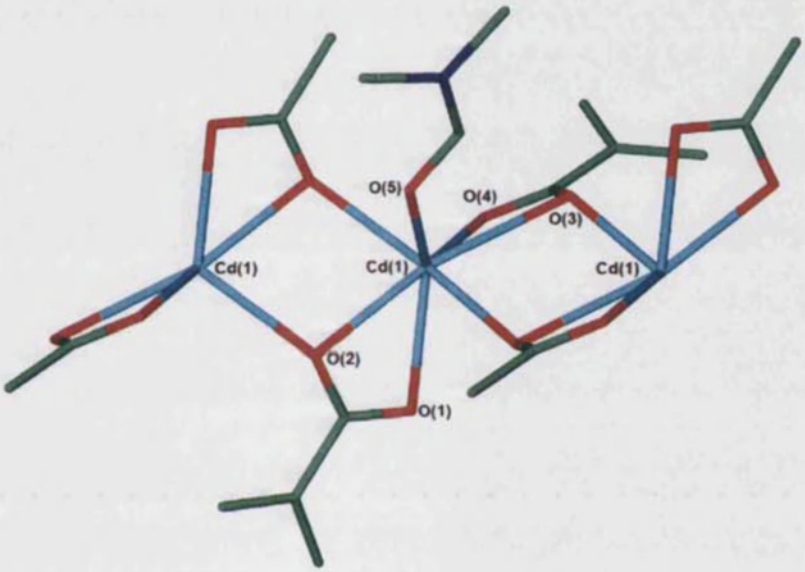

Figure 3.3. The coordination sphere of cadmium in **9**.

The carboxylate groups bridge the cadmium centres together into infinite 1-D chains (Figure 3.4). Following ideas developed by Rosi et *al*,[5] the chains of **9** can be considered as the SBU for this structure. The SBU of **9** is significantly different from that found in $\{(Me_2NH_2)_2{\cdot}[Cd_3(1,3\text{-bdc})_4]\}_\infty$ which was reported by Rosi et *al*.[5] The building unit of **9** consists of heptacoordinate metal centres which are connected together by chelating bridging bidentate carboxylate (Figure 3.4), while the latter SBU consists of hexacoordinate metal centres connected by chelating bridging bidentate and bridging bidentate carboxylates (Figure 3.1).

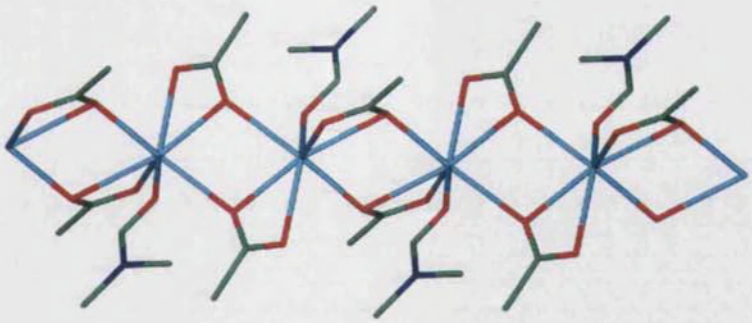

Figure 3.4. The 1-D infinite chain of **9**.

Although the DMF acts as a terminal point in the SBU of **9**, the chains are linked together by the benzene rings of the tph^{2-} ligands to form a 3-D network with rhombic shaped pores that are filled by the coordinated DMF molecules (Figures 3.5a and 3.5b).

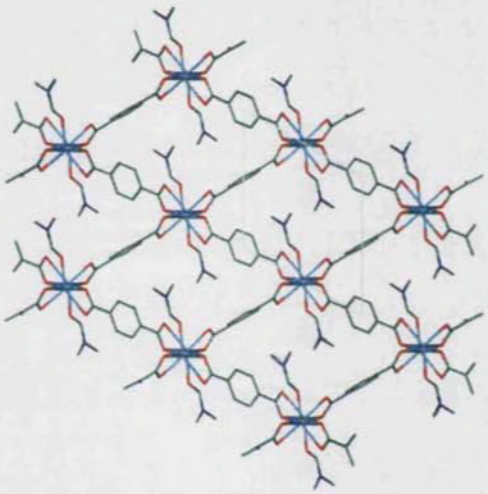

Figure 3.5a. The 3-D network of **9** viewed perpendicular to the (1 0 0) plane.

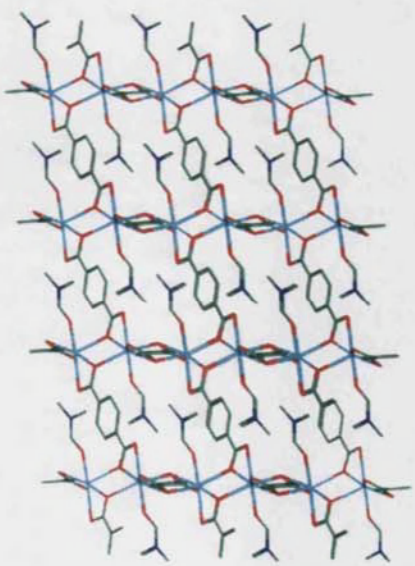

Figure 3.5b. The network of **9** viewed down the *c* axis.

Lists of selected bond lengths and angles for **9** are given in Tables 3.2 and 3.3 respectively. The oxygen atoms O(2) and O(3) that bridge between two cadmium centres bind in an asymmetric way (Figure 3.3 and Table 3.2). The angle of α (Table 3.1) is close to 120° and this is not commonly encountered in *P*-1 space groups. This angle forms a rhombic unit cell (Figure 3.5a).

Table 3.2. Selected bond lengths for **9**.[I]

Bond atoms	Distance/ Å	Bond atoms	Distance/ Å
Cd(1)-O(1)	2.494(2)	Cd(1)-O(3)#1	2.349(2)
Cd(1)-O(2)	2.2788(19)		
Cd(1)-O(3)	2.517(2)	O(1)-C(1)	1.243(3)
Cd(1)-O(4)	2.256(2)	O(2)-C(1)	1.283(3)
Cd(1)-O(5)	2.274(2)	O(3)-C(5)	1.269(4)
Cd(1)-O(2)#2	2.3947(19)	O(4)-C(5)	1.255(3)

Table 3.3. Selected bond angles for **9**.[I]

Atoms	Angle/ °
O(2)-Cd(1)-O(1)	54.87(7)
O(4)-Cd(1)-O(3)	54.70(7)
Cd(1)-O(2)-Cd(1)#2	102.68(7)
Cd(1)#1-O(3)-Cd(1)	104.80(8)
O(1)-C(1)-O(2)	121.8(2)
O(3)-C(5)-O(4)	121.7(2)

The network of **9** has the same stoichiometry as the 'paddle-wheel' structure of $\{[Zn(tph)(DMF)]\}_\infty$ (**3**) reported in Chapter 2. Nevertheless, the two networks differ significantly in their architectures. The zinc centres of **3** are pentacoordinated, while the cadmium centres of **9** are heptacoordinate. One explanation for this observation is the fact that cadmium is bigger than zinc and can therefore accommodate higher coordination numbers. The carboxylate groups adopt different coordination modes in the two

[I] Symmetry transformations used to generate equivalent atoms:
#1 -x+1 -y -z+1 #2 -x -y -z+1

compounds. While **3** consists of 2-D sheets, the network of **9** is 3-D. The pores of the two networks also differ with **3** having square voids and **9** possesing rhombic shaped pores.

3.2.2 Network dependency on temperature

As documented in Chapter 2, temperature plays a major role in determining the outcome of the reaction between $Zn(NO_3)_2 \cdot 6H_2O$ and H_2tph. Thus the dependency of the $Cd(NO_3)_2 \cdot 4H_2O$ and H_2tph reaction on the temperature was also investigated. A similar reaction to the one described in Section 3.2.1 was carried out at 95°C rather than 115°C. At 95°C, the reaction gave a mixture of two products, $\{[Cd_3(tph)_3(DMF)_4]\}_\infty$ (**10**) and $\{[Cd(tph)(DMF)]\}_\infty$ (**9**) with the latter being observed as the sole product from the reaction carried out at 115°C.

The asymmetric unit of **10** consists of one and a half cadmium centres, one and a half tph^{2-} ligands and two coordinated DMF molecules (Figure 3.6). Crystallographic data are summarised in Table 3.4.

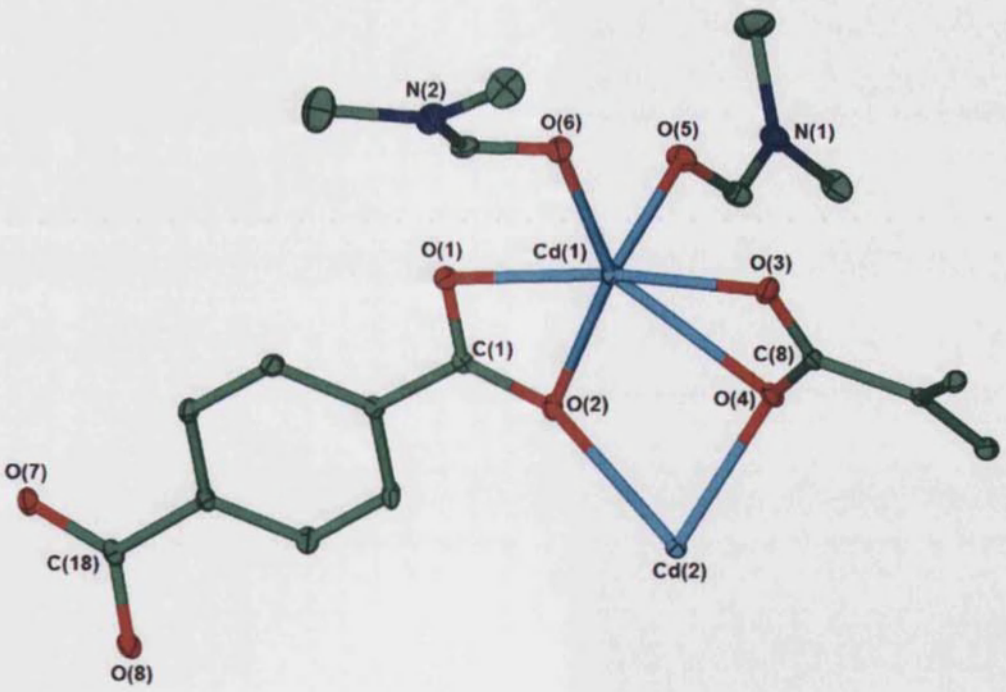

Figure 3.6. The asymmetric unit of **10** showing thermal ellipsoids at 30% probability. Hydrogen atoms are removed for clarity.

Table 3.4. Crystallographic data for **10**.

Empirical formula	$C_{36}H_{40}Cd_3N_4O_{16}$
M	1121.92
T/ K	150(2)
Crystal system	Monoclinic
Space group, *Z*	*C2/c*, 4
a/ Å	28.1090(4)
b/ Å	9.1930(1)
c/ Å	17.8780(2)
α/ °	90
β/ °	115.112(1)
γ/ °	90
U/ Å^3	4183.12(9)
Crystal size/ mm	0.25 x 0.1 x 0.05
Wavelength/ Å	0.71073
Theta range for data collected/ °	3.85 to 27.46
Reflections collected/ observed (>2σ)	29236/ 4411
Data completeness	0.995
Max. and min. transmission	0.93 and 0.85
Goodness of fit F^2	1.090
Final *R* indices (I>2σ(I))	$R1$ = 0.0220, $wR2$ = 0.0498
R indices (all data)	$R1$ = 0.0256, $wR2$ = 0.0512
Largest diff. peak and hole eÅ^{-3}	0.931 and -0.503

There are two different cadmium centres in the asymmetric unit. Cd(2) is coordinated to six oxygen atoms from six tph^{2-} ligands while the coordination sphere of Cd(1) is populated by seven oxygen atoms, five of which belong to three tph^{2-} ligands while the remaining two oxygen atoms, O(5) and O(6), belong to the coordinated DMF molecules.

The carboxylate groups of the tph^{2-} ligands adopt two different binding modes in the network of **10**. The group labelled as O(7)-C(18)-O(8) coordinates in a bridging bidentate mode, while the carboxylates labelled as O(3)-C(8)-O(4) and O(1)-C(1)-O(2) adopt the chelating bridging bidentate mode (Figure 3.7).

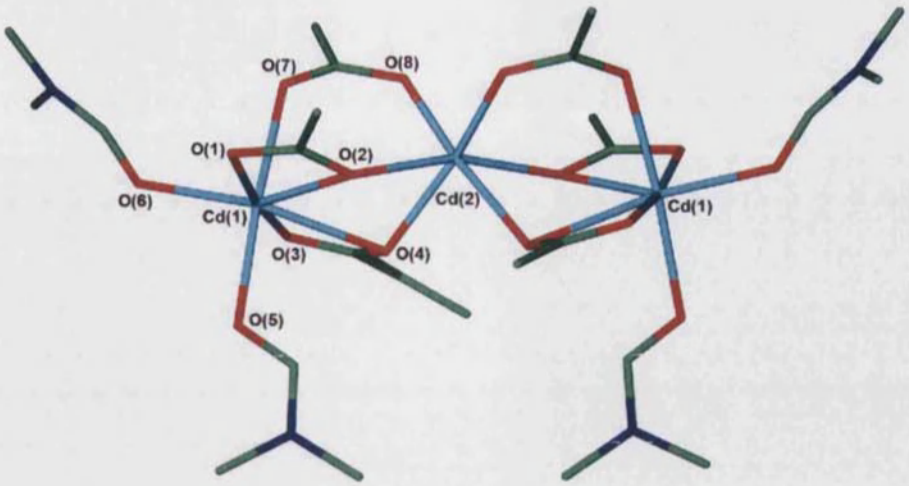

Figure 3.7. The three metal centre SBU of **10** and the coordinated DMF molecules.

The carboxylates adopting the chelating bridging bidentate mode link three cadmium centres together into $M_3(O_2CR)_6$ SBUs (Figure 3.7). The SBU consists of one octahedral cadmium centre, Cd(2), sandwiched between two heptacoordinate Cd(1) centres. Overall, six tph^{2-} ligands radiate from the SBU thus extending the network in the respective directions. The four coordinated DMF molecules act as terminal ligands thus preventing the network from growing in the third dimension. The network of **10** consists of 2-D sheets (Figure 3.8) that stack parallel to one another as observed in Figure 3.9. There are no significant interactions between the sheets.

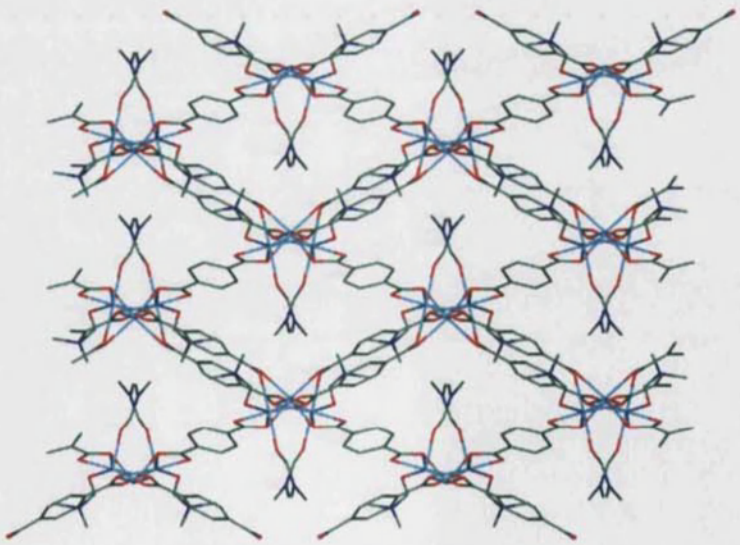

Figure 3.8. The 2-D sheet of **10** viewed perpendicular to the (101) plane.

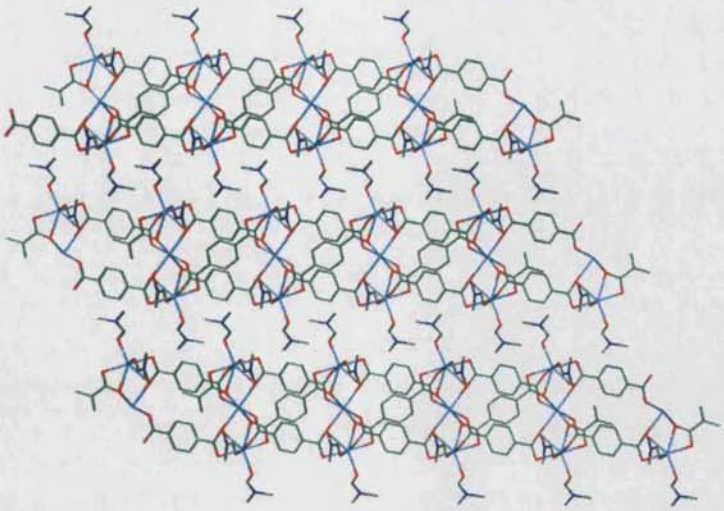

Figure 3.9. The packing of the 2-D sheets of **10** viewed down the *b* axis.

Selected bond lengths and angles for **10** are given in Tables 3.5 and 3.6 respectively. Apart from Cd(2)-O(4), the oxygen atoms O(2) and O(4) of the chelating bridging bidentate carboxylate form longer bonds to the cadmium centres than Cd(1)-O(1) and Cd(1)-O(3). O(2) and O(4) bridge between Cd(1) and Cd(2) while O(1) and O(3) coordinate to one metal centre each. Measurement of the distance between O(8)···Cd(1) and O(7)···Cd(2) (Figure 3.7 and Table 3.5) indicates that the respective atoms are too far apart for bonding to take place and thus the carboxylate group O(7)-C(18)-O(8) truly adopts the bridging bidentate mode.

Table 3.5. Selected bond lengths for **10**.[II]

Bond atoms	Distance/ °	Bond atoms	Distance/ °
Cd(1)-O(1)	2.3032(14)	Cd(2)-O(4)	2.2852(14)
Cd(1)-O(2)	2.4660(14)	Cd(2)-O(8)	2.2179(14)
Cd(1)-O(3)	2.2815(15)	O(1)-C(1)	1.264(2)
Cd(1)-O(4)	2.6029(15)	O(2)-C(1)	1.270(2)
Cd(1)-O(5)	2.2883(15)	O(3)-C(8)	1.253(3)
Cd(1)-O(6)	2.2605(15)	O(4)-C(8)	1.278(3)
Cd(1)-O(7)	2.2969(15)	O(7)-C(18)	1.256(3)
Cd(2)-O(2)	2.4610(14)	O(8)-C(18)	1.267(3)
Cd(1)#1···O(8)#2	3.701(4)	Cd(2)···O(7)#2	3.446(14)

[II] Symmetry transformations used to generate equivalent atoms:
#1 -x,y,-z+1/2 #2 –x,-y,-z+1

Table 3.6. Selected bond angles for **10**.[III]

Atoms	Angle/ °
O(1)-Cd(1)-O(2)	55.19(5)
O(2)-Cd(1)-O(4)	70.96(5)
O(3)-Cd(1)-O(4)	53.51(5)
O(4)-Cd(2)-O(2)	76.58(5)
O(8)-Cd(2)-O(2)	100.97(5)
O(8)#1-Cd(2)-O(4)	164.79(5)

Atoms	Angle/ °
Cd(2)-O(2)-Cd(1)	95.71(5)
Cd(2)-O(4)-Cd(1)	96.51(5)
O(7)-C(18)-O(8)	125.90(18)
C(18)-O(7)-Cd(1)	126.04(13)
C(18)-O(8)-Cd(2)	127.19(13)

3.2.3 Network dependency on pressure

As also described in Chapter 2, the product from the reaction between $Zn(NO_3)_2 \cdot 6H_2O$ and H_2tph was affected by changes in pressure, hence the sensitivity of the $Cd(NO_3)_2 \cdot 4H_2O/H_2tph$ reaction with respect to pressure was also investigated.

H_2tph was dissolved in DMF and placed in a pressure cell which was heated in an oil bath at 115°C. A solution of $Cd(NO_3)_2 \cdot 4H_2O$ in DMF was added, the reaction cell closed and pressurized with three atmospheres of nitrogen. The mixture was heated under pressure for five hours and colourless crystals were obtained. Analysis of the crystals by X-ray crystallography revealed the compound to be $\{[Cd_3(tph)_3(DMF)_4]\}_\infty$ (**11**). Crystallographic data for **11** are given in Table 3.7.

Table 3.7. Crystallographic data for **11**.

Empirical formula	$C_{36}H_{40}Cd_3N_4O_{16}$
M	1121.92
T/ K	150(2)
Crystal system	Triclinic
Space group, *Z*	*P*-1, 2
a/ Å	10.1270(1)
b/ Å	12.6120(1)

[III] Symmetry transformations used to generate equivalent atoms:
#1 -x,y,-z+1/2

c/ Å	16.6790(2)
α/ °	75.459(1)
β/ °	88.924(1)
γ/ °	87.271(1)
U/ Å^3	2059.65(4)
Wavelength/ Å	0.71073
Theta range for data collected/ °	3.65 to 31.00
Reflections collected/ observed (>2σ)	46686/11342
Data completeness	0.988
Goodness of fit F^2	1.057
Final R indices (I>2σ(I))	$R1$ = 0.0265, $wR2$ = 0.0605
R indices (all data)	$R1$ = 0.0332, $wR2$ = 0.0635
Largest diff. peak and hole eÅ^{-3}	1.424 and -1.301

The asymmetric unit of **11** consists of two full and two half cadmium centres, two full and two half tph^{2-} ligands and four coordinated DMF molecules (Figure 3.10). The cadmium centres of **11** are all hexacoordinated but the coordination spheres vary (Figures 3.11a and 3.11b). Cd(1) and Cd(3) are coordinated to three tph^{2-} ligands and two DMF molecules while the coordination spheres of Cd(2) and Cd(4) are populated by six oxygen atoms from six tph^{2-} ligands (Figures 3.11a and 3.11b). Cd(1) and Cd(3) are duplicated through the inversion centres located on Cd(2) and Cd(4). These symmetry operations give rise to three metal centre SBUs (Figures 3.11a and 3.11b).

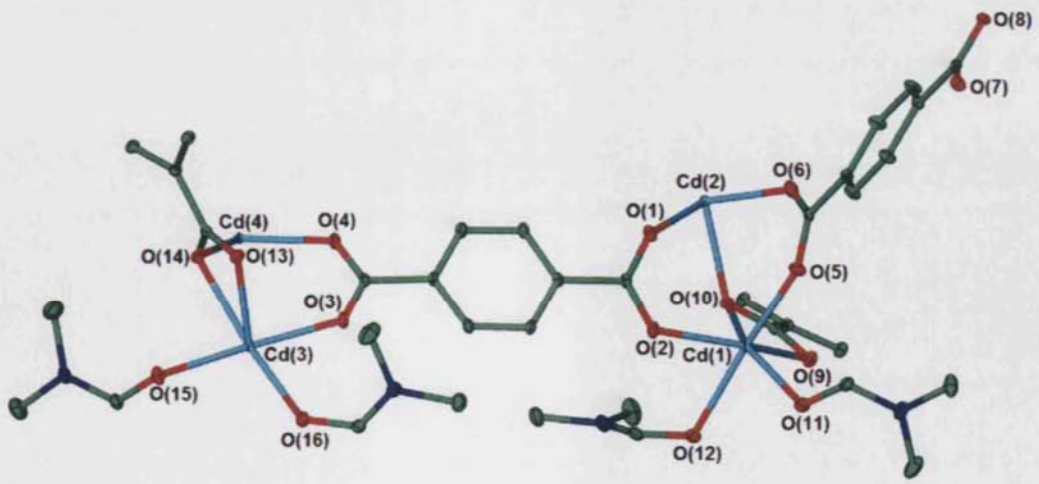

Figure 3.10. The asymmetric unit of **11** showing thermal ellipsoids at 30% probability. Hydrogen atoms are omitted for clarity.

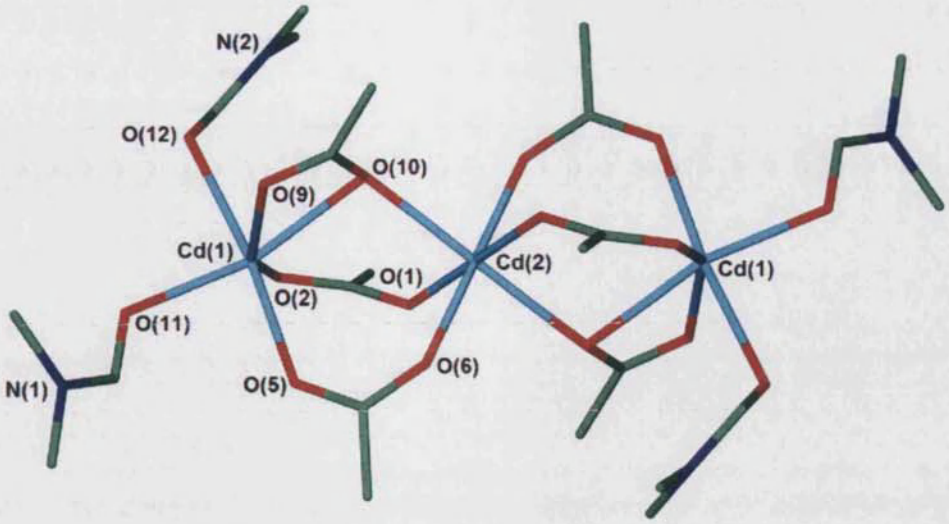

Figure 3.11a. One of the two three metal centre SBUs of **11**.

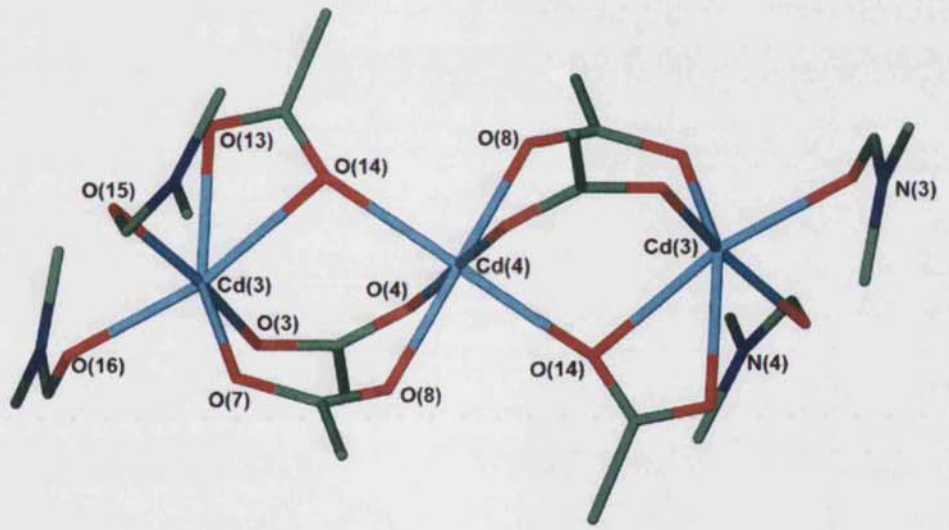

Figure 3.11b. The second three metal centre SBU of **11**.

The tph^{2-} ligands in **11** adopt the bridging bidentate and chelating bridging bidentate modes. The carboxylate groups link the metal centres to form distinct 3 metal centre $M_3(O_2CR)_6$ SBUs (Figures 3.11a and 3.11b). Both these nodes are present in the structure of **11**. Each SBU consist of three metals and six carboxylate groups. Although both building units consist of the same number of components and in both cases the carboxylate groups adopt four bidentate and two chelating bridging bidentate modes, the functional groups point at different angles (Figures 3.11a and 3.11b). This implies that the two different SBUs extend the network in different directions.

The two SBUs of **11** are connected together to form 2-D (3,6) sheets (Figure 3.12).[6] In the gross structure of **11**, the sheets pack parallel to one another with the coordinated DMF molecules pointing in the inter layer spaces (Figure 3.13).

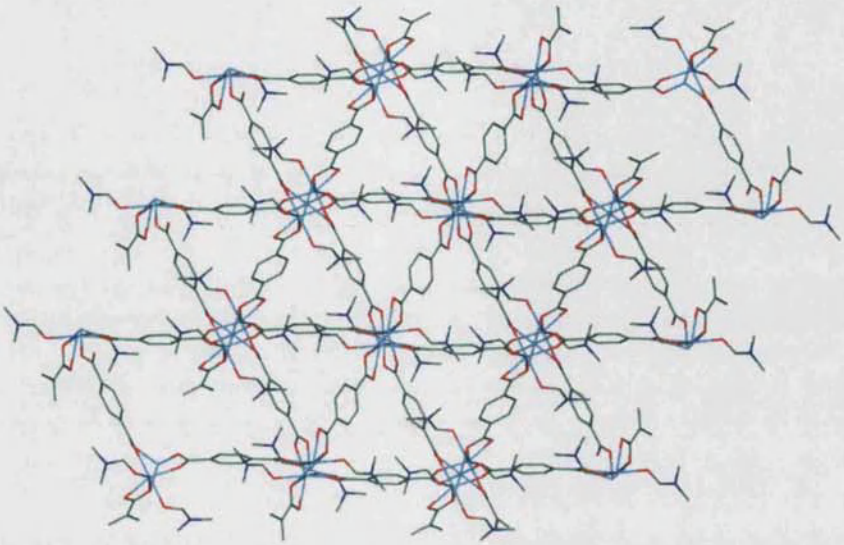

Figure 3.12. The 2-D sheet of **11** viewed down the *b* axis.

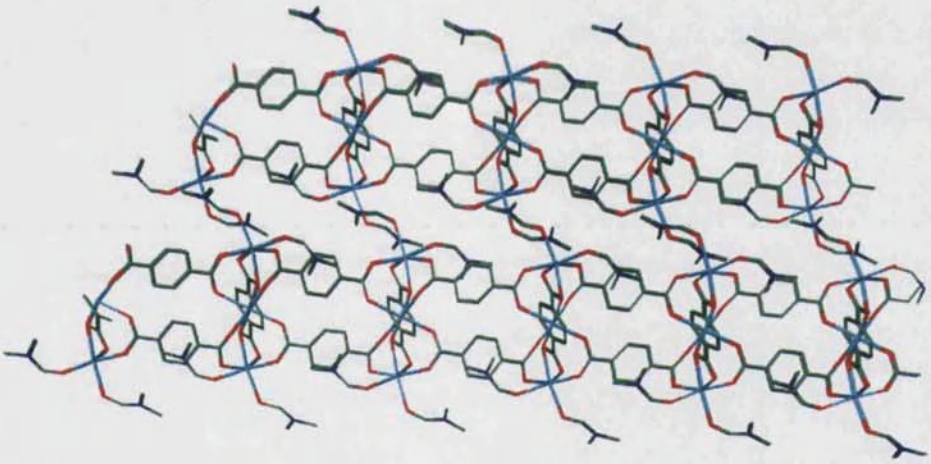

Figure 3.13. The parallel packing of the sheets in **11** viewed perpendicular to the (1 0 0) plane.

Lists of selected bond lengths and angles for **11** are summarised in Tables 3.8 and 3.9 respectively. The cadmium-oxygen bond lengths vary according to the binding mode of the carboxylate group with the longest distances associated with the oxygen atoms of the chelating bridging bidentate mode (Table 3.8). Measurement of the distance between cadmium centres and nearest non-bonded oxygen atoms (Figure 3.11a and 3.11b, Table 3.8) indicates that these atoms are too far apart for any bonding to occur. This justifies the bridging bidentate modes of the carboxylate groups.

Table 3.8. Selected bond lengths for **11**.[IV]

Bond atoms	Distance/ Å	Bond atoms	Distance/ Å
Cd(1)-O(2)	2.2021(13)	Cd(4)-O(4)	2.2161(14)
Cd(1)-O(5)	2.2296(13)	Cd(4)-O(8)#1	2.2651(12)
Cd(1)-O(9)	2.3641(13)	Cd(4)-O(14)	2.3244(12)
Cd(1)-O(10)	2.3707(13)	O(1)-C(1)	1.249(2)
Cd(1)-O(11)	2.2490(14)	O(2)-C(1)	1.267(2)
Cd(1)-O(12)	2.3977(14)	O(3)-C(8)	1.255(2)
Cd(2)-O(1)	2.2336(13)	O(4)-C(8)	1.249(2)
Cd(2)-O(6)	2.2449(13)	O(5)-C(9)	1.259(2)
Cd(2)-O(10)	2.3145(12)	O(6)-C(9)	1.253(2)
Cd(3)-O(3)	2.2158(13)	O(7)-C(16)	1.271(2)
Cd(3)-O(7)#1	2.2078(13)	O(8)-C(16)	1.251(2)
Cd(3)-O(13)	2.3827(13)	O(9)-C(17)	1.251(2)
Cd(3)-O(14)	2.3565(13)	O(10)-C(17)	1.279(2)
Cd(3)-O(15)	2.3564(13)	O(13)-C(27)	1.248(2)
Cd(3)-O(16)	2.2733(14)	O(14)-C(27)	1.280(2)
Cd(1)#3···O(1)	3.204(11)	Cd(1)#3···O(6)#3	3.566(13)
Cd(2)···O(2)	3.931(12)	Cd(2)···O(5)#3	3.622(13)
Cd(4)···O(3)	3.587(13)	Cd(4)···O(7)#4	3.898(12)
Cd(3)···O(4)#4	3.644(11)	Cd(3)···O(8)#4	3.224(13)

Table 3.9. Selected bond angles for **11**.[IV]

Atoms	Angle/ °	Atoms	Angle/ °
O(9)-Cd(1)-O(10)	55.50(4)	C(16)-O(7)-Cd(3)#2	119.60(12)
O(14)-Cd(3)-O(13)	55.60(4)	C(8)-O(4)-Cd(4)	133.36(12)
Cd(2)-O(10)-Cd(1)	103.16(5)	C(16)-O(8)-Cd(4)#2	138.19(12)
Cd(4)-O(14)-Cd(3)	102.93(5)	O(1)-C(1)-O(2)	125.54(17)
C(1)-O(2)-Cd(1)	118.47(11)	O(4)-C(8)-O(3)	126.75(17)
C(9)-O(5)-Cd(1)	132.45(12)	O(6)-C(9)-O(5)	126.50(17)

[IV] Symmetry transformations used to generate equivalent atoms:
#1 x y-1 z+1 #2 x y+1 z-1
#3 –x –y –z #4 –x+1 –y -z

C(1)-O(1)-Cd(2)	141.55(12)
C(8)-O(3)-Cd(3)	133.80(12)

O(8)-C(16)-O(7)	125.28(16)
O(9)-C(17)-O(10)	121.31(16)
O(13)-C(27)-O(14)	121.87(16)

The networks of **10** and **11** are supramolecular isomers as both have the formula $\{[Cd_3(tph)_3(DMF)_4]\}_\infty$ nevertheless, there are differences between the two compounds. The cadmium centres of **10** are hexa and hepta coordinated, with the cadmium-oxygen bond lengths varying from 2.2179(14)-2.6029(15) Å (Table 3.5). In contrast, the metal centres of **11** are all hexacoordinated with the cadmium-oxygen bond lengths falling in the range of 2.2021(13)-2.3827(13) Å (Table 3.8). The ligand carboxylate groups adopt two different binding modes which are the bridging bidentate and chelating bridging bidentate modes in both compounds.

The $M_3(O_2CR)_6$ SBU of **10** contains two hexacoordinate and one heptacoordinate metal centres (Figure 3.7) while there are two distinct $M_3(O_2CR)_6$ SBUs in **11** (Figure 3.11a and 3.11b). The cadmium centres in the SBU of **10** are connected together by four carboxylate groups coordinating in the chelating bridging bidentate mode and two bridging bidentate carboxylates (Figure 3.7). The SBUs of **11** consist of four bridging bidentate and two chelating bridging bidentate modes (Figures 3.11a and 3.11b). The overall structure of **10** consists of 2-D sheets with rhombic pores (Figure 3.8) while **11** has a 2-D (3,6) type topology that has triangular pores (Figure 3.12).

The calculated density for **11** is 1.81 g cm^{-1} while that for **10** it is 1.78 g cm^{-1}. As can be observed from Figures 3.9 and 3.13 the network of **11** is more compact than that of **10**. These differences might be attributed to the application of pressure to the system.

3.2.4 The templating effect of ammonium cations

Ammonium cations were found to exhibit a templating effect on the reaction of $Zn(NO_3)_2 \cdot 6H_2O$ and H_2tph in DMF leading to the formation of an anionic network. Thus, investigation of this templating effect was extended to the reaction of $Cd(NO_3)_2 \cdot 4H_2O$ and H_2tph.

$Cd(NO_3)_2 \cdot 4H_2O$ and two equivalents of H_2tph were dissolved in separate portions of DMF. The ligand solution was stirred and heated at 115°C. The $Cd(NO_3)_2 \cdot 4H_2O$ solution and Me_2NH_2Cl molecules were subsequently added. The reaction was left standing at 115°C for five hours during which time colourless crystals were obtained. Analysis of these crystals by single crystal X-ray crystallography showed this material to be $\{(Me_2NH_2)_2[Cd(tph)_2] \cdot 2DMF\}_\infty$ (**12**). Crystallographic data for **12** are given in Table 3.10.

Table 3.10. Crystallographic data for **12**.

Empirical formula	$C_{26}H_{38}CdN_4O_{10}$
M	679.00
T/ K	150(2)
Crystal system	Orthorhombic
Space group, *Z*	*Fdd*2, 8
a/ Å	9.7830(2)
b/ Å	21.2010(4)
c/ Å	27.8110(5)
α/ °	90
β/ °	90
γ/ °	90
U/ Å^3	5768.26(19)
Crystal size/ mm	0.13 x 0.13 x 0.13
Wavelength/ Å	0.71073
Theta range for data collected/ °	3.84 to 30.03
Reflections collected/ observed (>2σ)	15349/ 3873
Data completeness	0.996
Max. and min. transmission	0.76 and 0.70
Goodness of fit F^2	1.086
Final *R* indices (I>2σ(I))	$R1$ = 0.0225, $wR2$ = 0.0494
R indices (all data)	$R1$ = 0.0268, $wR2$ = 0.0509
Largest diff. peak and hole eÅ^{-3}	0.222 and -0.762

The asymmetric unit of **12** consists of half a cadmium centre, one tph^{2-} ligand, one dimethylammonium cation and two half occupancy DMF fragments (Figure 3.14). One of

the carbon atoms of the cation labelled as C(16)/C(16a) is disordered over two positions with site occupation factors of 0.5 at each position.

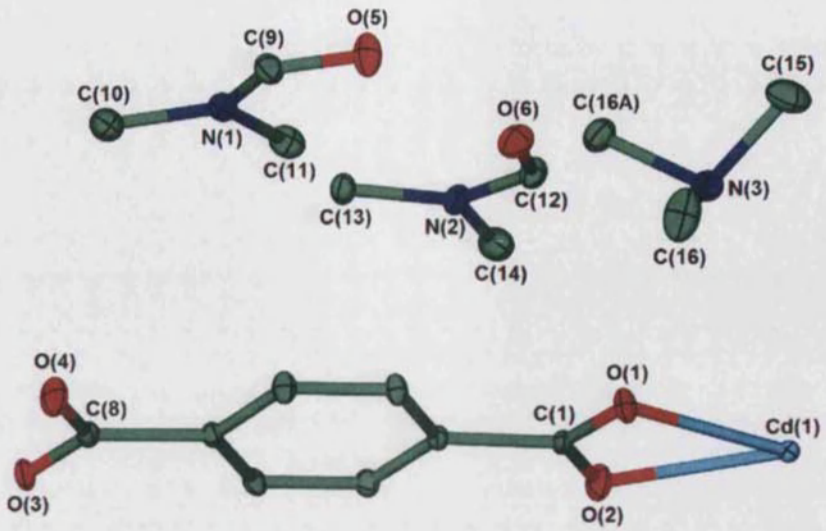

Figure 3.14. The asymmetric unit of **12** showing thermal ellipsoids at 30% probability. Hydrogen atoms are omitted for clarity.

The cadmium centre in **12** adopts octacoordinate geometry and the coordination sphere is occupied by eight oxygen atoms from four tph^{2-} ligands (Figure 3.15). The carboxylate groups coordinate in a chelating bidentate fashion only.

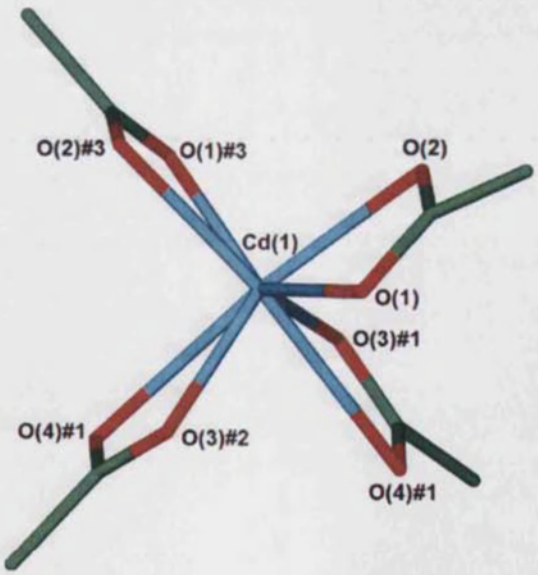

Figure 3.15. The coordination sphere of cadmium in **12**. The labelled symmetry operations are #1 –x+1/4,y-1/4,z-1/4, #2 x+3/4,-y+1/4,z-1/4 and #3 –x+1,y,z.

Selected lists of bond lengths and bond angles are given in Tables 3.11 and 3.12 respectively. The Cd(1)-O(4) (2.704(7) Å) bond length is significantly longer than the other

cadmium-oxygen bond lengths reported so far in this chapter (2.2021(13)-2.6029(15)Å) but nevertheless is still comparable to other cadmium-oxygen bond lengths found in the Cambridge Structural Database. The carboxylate group labelled as O(1)-C(1)-O(2) binds to the cadmium centre in a symmetrical fashion, while O(3)-C(8)-O(4) binds asymmetrically to Cd(1). This is illustrated through a comparison of the respective cadmium-oxygen bond lengths from Table 3.11.

Table 3.11. Selected bond lengths for **12**.

Bond atoms	Distance/ Å
Cd(1)-O(1)	2.4530(18)
Cd(1)-O(2)	2.391(2)
Cd(1)-O(3)	2.3143(15)
Cd(1)-O(4)	2.704(7)
O(1)-C(1)	1.247(3)
O(2)-C(1)	1.251(3)
O(3)-C(8)	1.257(3)
O(4)-C(8)	1.245(3)

Table 3.12. Selected bond angles for **12**.[v]

Atoms	Angle/ °
O(1)-Cd(1)-O(1)#3	141.56(8)
O(2)-Cd(1)-O(1)	53.66(6)
O(2)-Cd(1)-O(1)#3	98.39(7)
O(2)-Cd(1)-O(2)#3	94.57(12)
O(2)#3-Cd(1)-O(1)	98.39(7)
O(2)#3-Cd(1)-O(1)#3	53.66(6)
O(3)#1-Cd(1)-O(1)	125.55(5)
O(3)#1-Cd(1)-O(1)#3	76.05(6)
O(3)#1-Cd(1)-O(2)	93.58(6)

Atoms	Angle/ °
O(3)#1-Cd(1)-O(2)#3	129.70(5)
O(3)#1-Cd(1)-O(3)#2	117.74(8)
O(3)#2-Cd(1)-O(1)	76.05(6)
O(3)#2-Cd(1)-O(1)#3	125.55(5)
O(3)#2-Cd(1)-O(2)	129.70(5)
O(3)#2-Cd(1)-O(2)#3	93.58(6)
O(1)-C(1)-O(2)	122.2(2)
O(4)-C(8)-O(3)	123.1(2)

[v] Symmetry transformations used to generate equivalent atoms:
#1 -x+1/4,y-1/4,z-1/4 #2 x+3/4,-y+1/4,z-1/4
#3 -x+1,-y,z

12 forms a triply interpenetrated 3-D network (Figure 3.16). According to the nomenclature developed by A.F.Wells,[6] this compound belongs to the family of the diamandoind nets, with each node being four connected (Figure 3.17a) and the shortest pathway between the nodes consisting of six sides (Figure 3.17b).

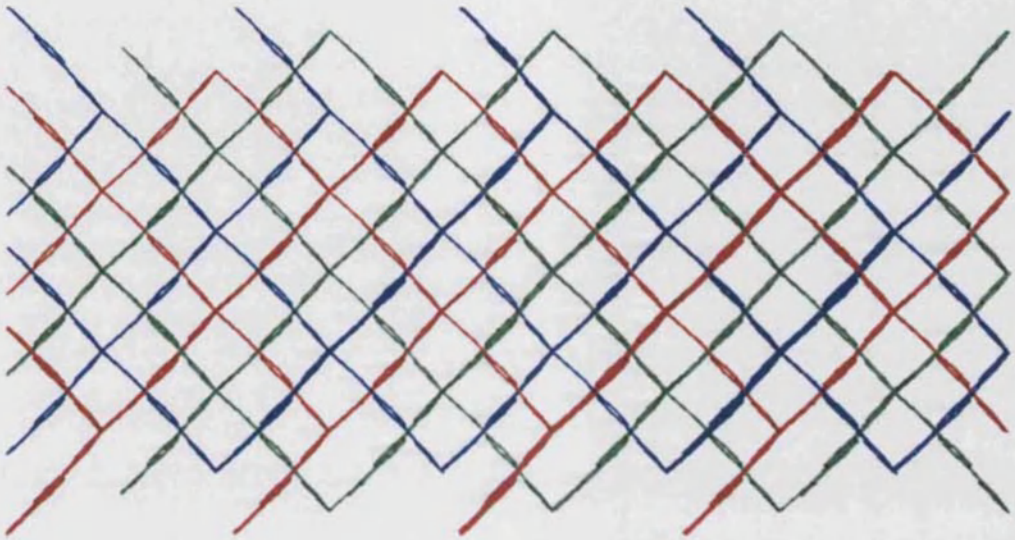

Figure 3.16. The triply interpenetrated network of **12** viewed down the *b* axis. Each network is coloured differently and the guest molecules and cations are omitted for clarity.

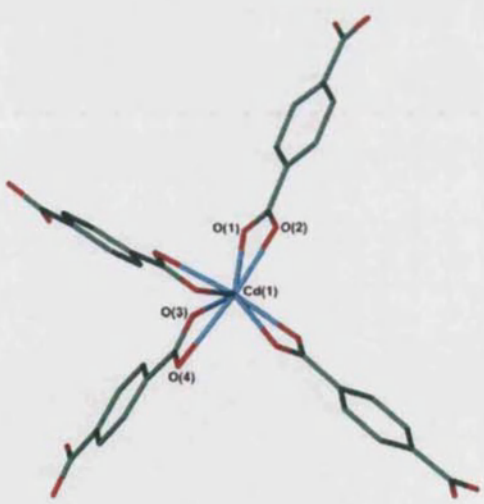

Figure 3.17a. The four connected node of **12**.

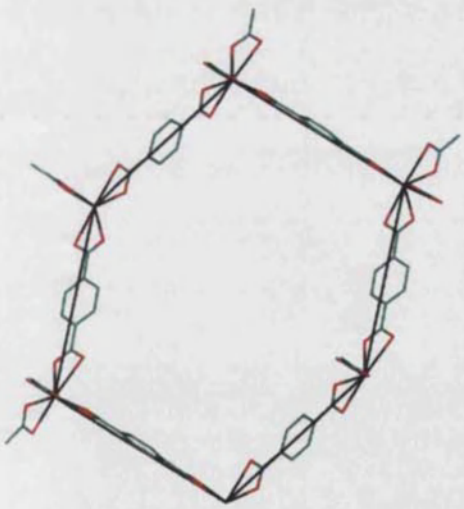

Figure 3.17b. The shortest pathway between the nodes of **12** being highlighted in black.

The network of **12** is anionic with two negative charges per cadmium centre. The dimethylammonium cations serve to balance the charges on the network.

The dimethylammonium cations are involved in hydrogen bond formation with the hydrogen atom H(3A) of the dimethylammonium cations interacting with O(3) and O(4) of the tph^{2-} ligand. There is an additional interaction between H(3B) and O(5) of the guest DMF molecule (Table 3.13).

Table 3.13. Hydrogen bonds with H··A < r(A) + 2.000Å and <DHA > 110° for **12**.[VI]

D-H	D(D-H)	d(H··A)	<DHA	d(D··A)	A
N3-H3A	0.89	2.21	139	2.941	O4 (–x+1, y-1/4, z-1/4)
N3-H3A	0.89	2.30	125	2.909	O3 (x+3/4, -y+1/4, z-1/4)
N3-H3B	0.89	1.80	158	2.646	O5 (-x+1/2, -y+1/2, z)

Table 3.14 shows a list of bite angles and oxygen-carbon-oxygen angles for **9**, **10**, **11** and **12**. Although one of the bite angles of **10** (53.51(5)°) and those of **12** are smaller than the others, this variation cannot be explained in terms of the different binding modes. A more striking observation is the difference in the oxygen-carbon-oxygen angle of the carboxylate groups. Although all atoms of the carboxylate groups are sp^2 hybridised, there are still slight variations in the oxygen-carbon-oxygen angles. The functional groups adopting the bridging bidenate modes having a wider oxygen-carbon-oxygen angle than the carboxylates coordinating in the other binding modes.

Table 3.14. Comparison of O-Cd-O, and O-C-O angles for **9**, **10**, **11** and **12**.

Compound	O-Cd-O angle/ °	O-C-O angle/ °
9	54.70(7) - 54.87(7)	121.7(2) - 121.8(2)
10	53.51(5) - 55.19(5)	121.83(17) - 125.90(18)
11	55.50(4) - 55.60(4)	125.54(17) - 126.75(17)
12	51.25(3) - 53.66(6)	122.2(2) - 123.1(2)

3.2.5 Network dependency on pH

The pH of the reaction solution that yielded **9** was found to be 5.5. When the pH of the reaction was adjusted to 4, by the addition of a few drops of concentrated HCl, **12** was obtained instead. This was confirmed by X-ray powder diffraction. This seems to

[VI] Symmetry transformations used to generate equivalent atoms:
[x+3/4, -y+1/4, z-1/4]

imply that the presence of acid and heat aids the hydrolysis of DMF. A similar observation was reported for the reaction between $Zn(NO_3)_2 \cdot 6H_2O$ and H_2tph (Chapter 2).

3.3 Impact of solvent change on the products

In Chapter 2 it was noted that the product of the reaction between $Zn(NO_3)_2 \cdot 6H_2O$ and H_2tph depends on the length of the alkyl chain in the solvent. When this reaction was carried out in *N,N*-diethylformamide (DEF) a different product was obtained than when DMF was employed. Consequently, the dependency of the reaction between $Cd(NO_3)_2 \cdot 4H_2O$ and H_2tph system on the length of the alkyl chain in the solvent was also investigated.

3.3.1 Reaction of $Cd(NO_3)_2 \cdot 4H_2O$ and H_2tph in DEF at 115°C

$Cd(NO_3)_2 \cdot 4H_2O$ and H_2tph were dissolved in separate portions of DEF. The H_2tph solution was stirred and heated up to 115°C and then the solution containing the $Cd(NO_3)_2 \cdot 4H_2O$ was added. Stirring was ceased and the reaction mixture was heated for five hours during which time yellow-orange crystals were obtained. The resulting compound was identified by single crystal X-ray crystallography to be $\{[Cd_3(tph)_3(DEF)_2]\}_\infty$ (**13**). Crystallographic data for **13** are given in Table 3.15.

Table 3.15. Crystallographic data for **13**.

Empirical formula	$C_{17}H_{17}Cd_{1.5}NO_7$
M	510.91
T/ K	150(2)
Crystal system	Monoclinic
Space group, *Z*	*C*2/*c*, 8
a/ Å	25.0960(11)
b/ Å	10.7885(5)
c/ Å	17.5107(8)
α/ °	90
β/ °	128.996(3)
γ/ °	90

U/ Å^3	3684.6(3)
Wavelength/ Å	0.6868
Crystal size	0.50 x 0.40 x 0.20
Theta range for data collected/ °	2.02 to 29.42
Reflections collected/ observed (>2σ)	18981/4936
Data completeness	0.953
Goodness of fit F^2	1.036
Final R indices (I>2σ(I))	$R1$ = 0.0255, $wR2$ = 0.0673
R indices (all data)	$R1$ = 0.0282, $wR2$ = 0.0691
Largest diff. peak and hole eÅ^{-3}	0.659 and -0.576

The asymmetric unit of **13** (Figure 3.18) consists of one and a half cadmium centres, one and a half tph^{2-} ligands and one coordinated DEF molecule which is disordered over two sites in a 7:3 ratio.

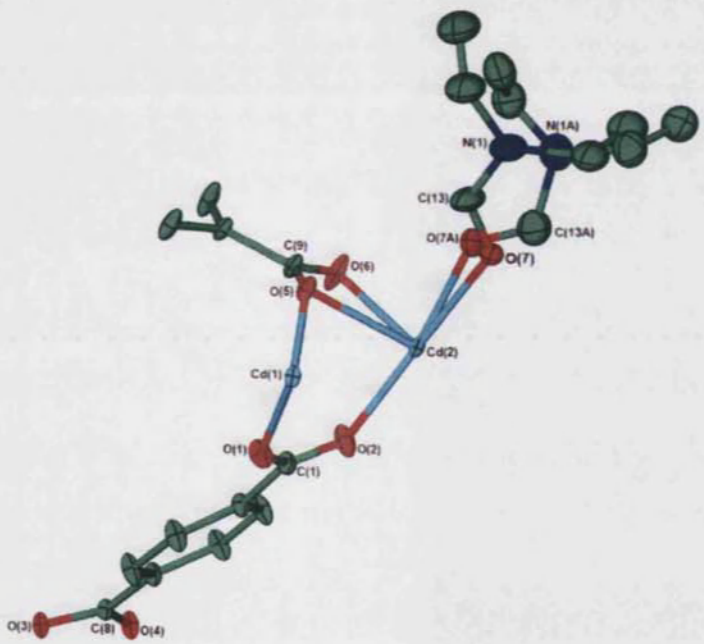

Figure 3.18. The asymmetric unit of **13** showing thermal ellipsoids at 30% probability. Hydrogen atoms are removed for clarity.

The two cadmium centres have different coordination geometries. Cd(1) adopts a distorted octahedral geometry with the coordination sphere being occupied by six oxygen atoms from six different tph^{2-} ligands. In contrast, Cd(2) is heptacoordinated to four tph^{2-} ligands and a DEF molecule (Figure 3.19).

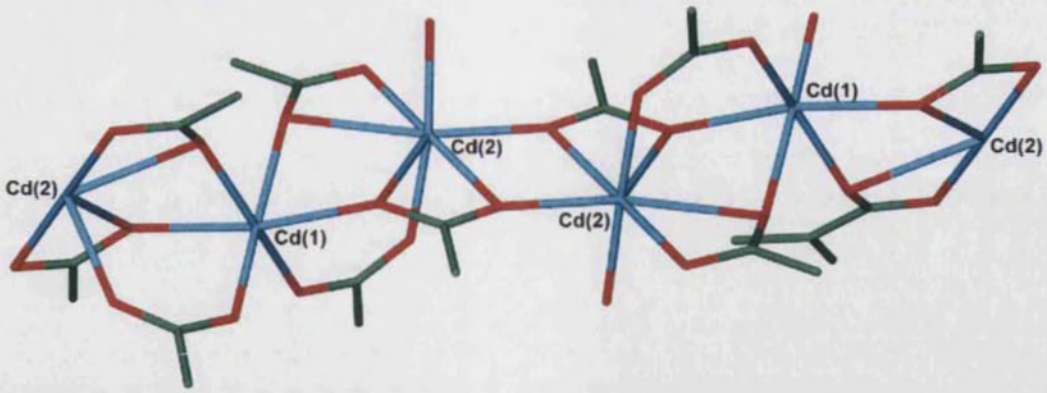

Figure 3.19. The 1-D infinite SBU chain of **13**.

The tph^{2-} ligands adopt three different binding modes in **13**. Two of the binding modes were observed in the compounds previously described in this chapter, namely the bridging bidentate and chelating bridging bidentate modes. The carboxylate group labelled as O(3)-C(8)-O(4) adopts a bi-chelating bridging bidentate mode with each oxygen atom being coordinated to two cadmium centres (Figure 3.20).

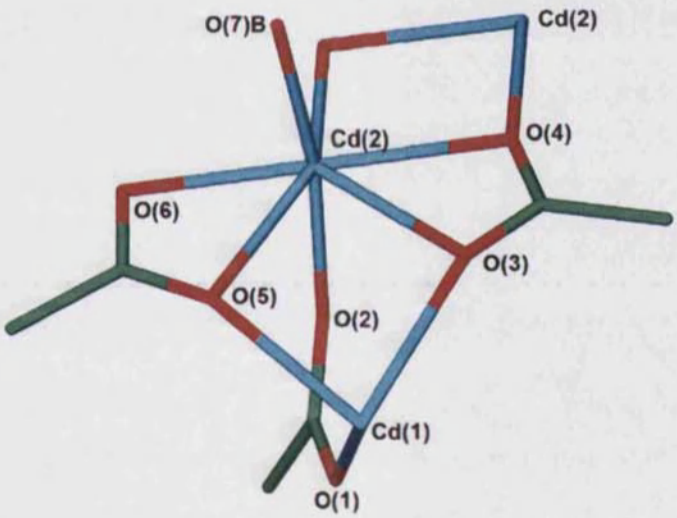

Figure 3.20. The bi-chelating bridging bidentate mode of **13**.

The carboxylate groups link the cadmium centres into a linear chain of hexa- and heptacoordinate metal centres (Figures 3.19). The chains have twice the number of heptacoordinate relative to octahedral metal centres. As in the network of **9** (Figure 3.4), the 1-D chains of **13** can be considered as the SBU of the network. Despite the terminal DEF ligands, the chains are bridged together via the benzene rings of the tph^{2-} ligands to form a 3-D network with rhombic pores (Figure 3.21).

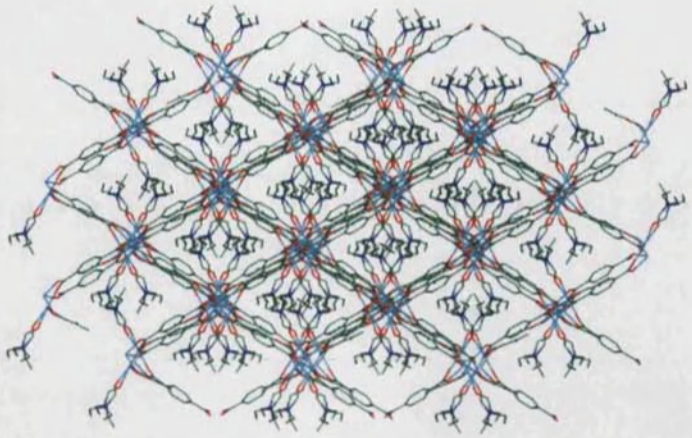

Figure 3.21. The 3-D network of **13** viewed down the *a* axis.

Lists of selected bond lengths and angles for **13** are given in Tables 3.16 and 3.17 respectively. The oxygen atoms O(3), O(4) and O(5), that bridge between two cadmium centres have unequal cadmium-oxygen bond lengths. Measurement of Cd(1)···O(2) and Cd(2)···O(1) indicates that the respective atoms are too far apart for any interaction to take place, thus the carboxylate group having oxygen atoms O(1) and O(2) truly adopts the bridging bidentate mode.

Table 3.16. Selected bond lengths for **13**.[VII]

Bond atoms	Length/ Å	Bond atoms	Length/ Å
Cd(1)-O(1)	2.1971(15)	O(4)-Cd(2)#5	2.3043(13)
Cd(1)-O(3)#1	2.3876(13)	Cd(2)-O(5)	2.5560(15)
O(3)-Cd(1)#2	2.3876(13)	Cd(2)-O(6)	2.2741(16)
Cd(1)-O(5)	2.3005(15)	Cd(2)-O(7)	2.279(5)
Cd(2)-O(2)	2.2209(18)	O(1)-C(1)	1.254(2)
Cd(2)-O(3)#1	2.4453(13)	O(2)-C(1)	1.239(3)
O(3)-Cd(2)#4	2.4453(13)	O(3)-C(8)	1.257(2)
Cd(2)-O(4)#1	2.3649(14)	O(4)-C(8)	1.259(2)
O(4)-Cd(2)#4	2.3649(13)	O(5)-C(9)	1.253(2)
Cd(2)-O(4)#3	2.3043(13)	O(6)-C(9)	1.248(3)
Cd(1)···O(2)	3.491(13)	Cd(2)···O(1)	3.676(15)

[VII] Symmetry transformations used to generate equivalent atoms:
#1 x,-y+1,z+1/2 #2 -x,-y+1,-z
#3 -x+1/2,y+1/2,-z+1/2 #4 x,-y+1,z-1/2
#5 -x+1/2,y-1/2,-z+1/2

Table 3.17. Selected bond angles for **13**.[VIII]

Atoms	Angle/ °	Atoms	Angle/ °
O(4)#2-Cd(2)-O(3)#1	53.92(4)	C(1)-O(1)-Cd(1)	129.91(14)
O(6)-Cd(2)-O(5)	53.44(5)	C(1)-O(2)-Cd(2)	135.91(15)
Cd(1)-O(5)-Cd(2)	95.31(5)	O(2)-C(1)-O(1)	126.62(18)
Cd(1)#3-O(3)-Cd(2)#4	96.06(4)	O(3)-C(8)-O(4)	120.27(16)
Cd(2)#5-O(4)-Cd(2)#4	103.64(5)	O(6)-C(9)-O(5)	121.92(18)

There are several similarities and differences between the networks obtained from the reaction of $Cd(NO_3)_2 \cdot 4H_2O$ and H_2tph at 115°C in DMF and DEF, $\{[Cd(tph)(DMF)]\}_\infty$ (**9**) and $\{[Cd_3(tph)_3(DEF)_2]\}_\infty$ (**13**) respectively.

The SBUs of **9** and **13** consist of 1-D infinite chains (Figures 3.3 and 3.19) that are bridged into 3-D networks by the tph^{2-} benzene rings. Both building units have terminal DMF or DEF molecules directed towards the inside of the rhombic pores (Figures 3.5b and 3.21).

The metal centres in the 1-D building units of **9** are all heptacoordinate while the nodes of **13** have metal centres adopting hexa- and heptacoordination (Figures 3.4 and 3.19). The carboxylate groups in **9** adopt the chelating bridging bidentate mode while **13** has a mixture of bridging bidentate and chelating bridging bidentate functional groups.

3.3.2 Templating effect of diethylammonium cations

In Section 3.2.4 it was demonstrated that dimethylammonium cations can template the products from the reaction of $Cd(NO_3)_2 \cdot 4H_2O$ and H_2tph. In Chapter 2, it was reported that the reaction of $Zn(NO_3)_2 \cdot 6H_2O$ and H_2tph is also templated by higher homologues such as diethylammonium cation. Thus, the effect of the latter cations on the reaction between $Cd(NO_3)_2 \cdot 4H_2O$ and H_2tph using DEF as the solvent was investigated.

[VIII] Symmetry transformations used to generate equivalent atoms:
#1 x,-y+1,z+1/2 #2 -x,-y+1,-z
#3 -x+1/2,y+1/2,-z+1/2 #4 x,-y+1,z-1/2
#5 -x+1/2,y-1/2,-z+1/2

A similar reaction to that which yielded **13** was carried out with diethylammonium chloride being added to the reaction mixture. This produced yellow-orange crystals which when analysed by X-ray powder diffraction were found to be **13**. Therefore in this case, the diethylammonium cations did not alter the gross network of the reaction product.

While both dimethyl and diethylammonium cations affected the product obtained from the reaction of $Zn(NO_3)_2 \cdot 6H_2O$ and H_2tph in DMF and DEF respectively, in the $Cd(NO_3)_2 \cdot 4H_2O/H_2tph$ scenario only the dimethylammonium cations in DMF acted as templates. The reason for the difference between the $Zn(NO_3)_2 \cdot 6H_2O$ and $Cd(NO_3)_2 \cdot 4H_2O$ reactions is not entirely understood yet and is being investigated further.

3.4 Increasing the length of the spacer in the dicarboxylate ligand

One way of increasing the pore size in the networks is by increasing the length of the linking group. In a similar manner to tph^{2-}, 4,4'-biphenyldicarboxylate ($bpdc^{2-}$) can also act as a rigid linear linker. In this section the reaction of $Cd(NO_3)_2 \cdot 4H_2O$ with H_2bpdc is investigated and the resulting network compared to that obtained with tph^{2-}.

$Cd(NO_3)_2 \cdot 4H_2O$ and one equivalent of H_2bpdc were dissolved in separate portions of DMF. The ligand solution was heated to 115°C and the $Cd(NO_3)_2 \cdot 4H_2O$ solution was then added. The reaction was left standing at this temperature for five hours during which time colourless crystals were obtained. The compound was analysed by X-ray crystallography and was found to be $\{[Cd_3(bpdc)_3(DMF)_2]\}_\infty$ (**14**).[7] Crystallographic data for **14** are given in Table 3.18.

Table 3.18. Crystallographic data for **14**.

Empirical formula	$C_{48}H_{38}Cd_3N_2O_{14}$
M	1203.47
T/ K	150(2)
Crystal system	Trigonal
Space group, *Z*	*R*-3, 3
a/ Å	14.0850(7)
b/ Å	14.0850(7)

c/ Å	19.7760(8)
α/ °	90
β/ °	90
γ/ °	120
U/ Å^3	3397.7(3)
Crystal size/ mm	0.15 x 0.05 x 0.05
Wavelength/ Å	0.71073
Theta range for data collected/ °	3.93 to 27.47
Reflections collected/ observed (>2σ)	21904/1248
Data completeness	0.990
Goodness of fit F^2	1.050
Final *R* indices (I>2σ(I))	*R*1 = 0.0457, *wR*2 = 0.1107
R indices (all data)	*R*1 = 0.0711, *wR*2 = 0.1266
Largest diff. peak and hole eÅ^{-3}	2.550 and -1.191

The asymmetric unit of **14** consists of two partial cadmium centres, one partial coordinated DMF molecule and half a bpdc^{2-} ligand (Figure 3.22). The site occupation factors for Cd(1) and Cd(2) are 0.33 and 0.167 respectively. Cd(1) is situated on a 3-fold rotation axis. Cd(2) is acted upon by two symmetry operations which are an inversion centre and a 3-fold rotation axis hence the site occupancy factor of 0.167. O(8) of the DMF molecule is also positioned on the 3-fold rotation axis with the consequence that the DMF ligand is disordered over 3 sites. Only one position for the DMF molecule is shown in Figure 3.22 for clarity.

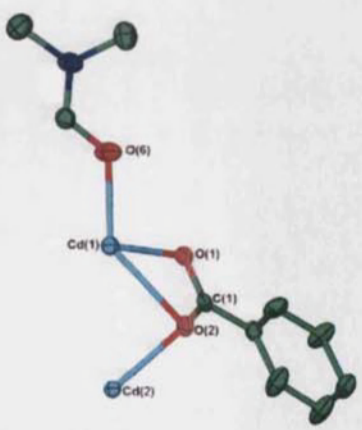

Figure 3.22. The asymmetric unit of **14** showing thermal ellipsoids at 30% probability. Hydrogen atoms are removed and only one position of the DMF molecule is shown for clarity.

Cd(1) has a heptacoordinate geometry while Cd(2) has hexacoordinate geometry. The coordination sphere of Cd(1) is filled by seven oxygen atoms, with six of these atoms belonging to three different $bpdc^{2-}$ ligands and the remaining site being occupied by a DMF molecule. The coordination sphere of Cd(2) is occupied by six oxygen atoms from six different $bpdc^{2-}$ ligands (Figure 3.23). Cd(1) is duplicated by the inversion centre located on Cd(2). This symmetry operation gives rise to a three metal centre unit.

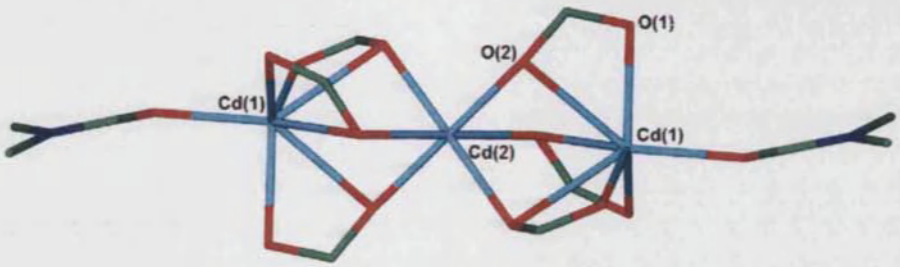

Figure 3.23. The three metal centre SBU of **14**.

The carboxylate groups of the $bpdc^{2-}$ ligands bind to the metal centres in a chelating bridging bidentate fashion only. The three metal centre units are bridged together by the carboxylate groups to form $M_3(O_2CR)_6$ SBU units (Figure 3.23).

The SBU has six ligands radiating from it while the shortest distance between two SBUs involves three ligands. Thus according to Wells,[6] this network can be represented as (3,6) (Figure 3.24). The gross structure of **14** consists of 2-D sheets, (Figure 3.25a) which pack in a staggered way with respect to one another (Figure 3.25b).

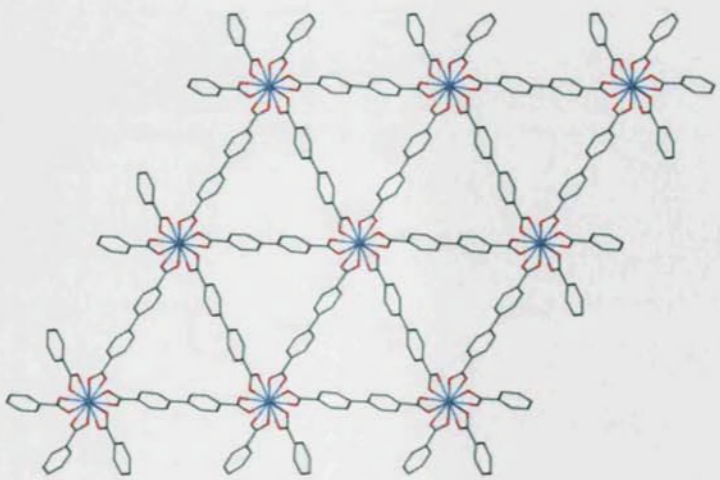

Figure 3.24. The (3,6), 2-D network of **14** viewed down the *c* axis.

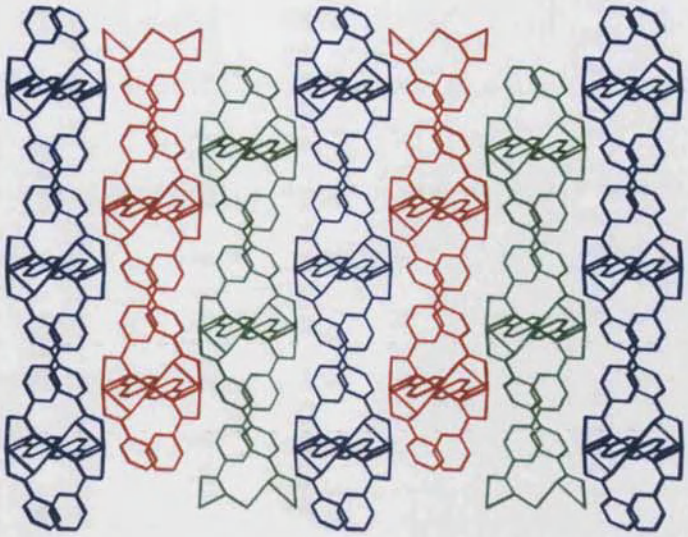

Figure 3.25a. The parallel packing of the sheets in **14** viewed down the *b* axis. The sheets are coloured differently for clarity.

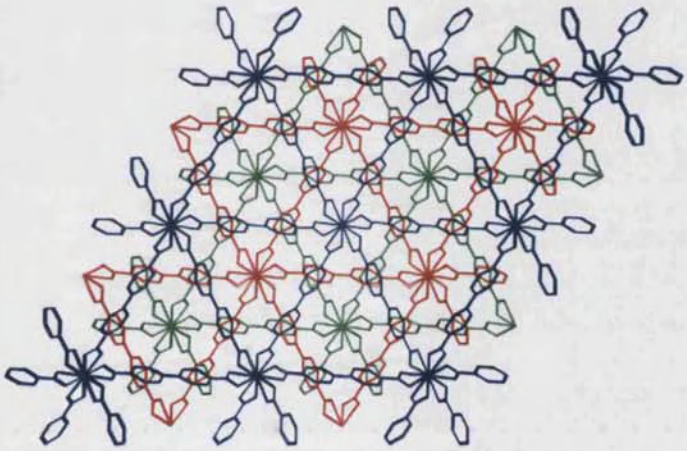

Figure 3.25b. The packing of the sheets of **14** as viewed down the *c* axis. The sheets are coloured differently for clarity.

Selected bond lengths and angles for **14** are shown in Tables 3.19 and 3.20. The cadmium-oxygen bond Cd(1)-O(2) (2.567(4)Å) is significantly longer than the other similar bond lengths (2.196(7)Å-2.263(3)Å) nevertheless, these bond lengths fall within the cadmium-oxygen bond length range for the other compounds reported in this chapter (2.1971(15)-2.704(7)Å). The bite angle of O(1)-Cd(1)-O(2) (53.89(12)°) (Table 3.19) is of comparable size to similar angles in $\{[Cd_3(tph)_3(DMF)_4]\}_\infty$ (**11**) (54.87(7)°, 54.70(7)°), and $\{[Cd_3(tph)_3(DEF)_2]\}_\infty$ (**13**) (53.92(4)° and 53.44(5)°). This implies that the $bpdc^{2-}$ can form similar binding modes to tph^{2-} as expected.

Table 3.19. Selected bond lengths for **14**.

Bond atoms	Distance/ Å
Cd(1)-O(1)	2.263(3)
Cd(1)-O(2)	2.567(4)
Cd(1)-O(6)	2.196(7)
Cd(2)-O(2)	2.259(3)
O(1)-C(1)	1.255(6)
O(2)-C(1)	1.267(6)

Table 3.20. Selected bond angles for **14**.[IX]

Atoms	Angle/ °
Cd(2)-O(2)-Cd(1)	86.96(11)
O(1)-C(1)-O(2)	122.0(5)
O(1)#1-Cd(1)-O(2)#1	53.89(12)

The architecture of **14** shares similarities to $\{[Cd_3(tph)_3(DMF)_4]\}_\infty$ (**10**) and $\{[Cd_3(tph)_3(DMF)_4]\}_\infty$ (**11**). The SBUs of **10** and **14** consists of two heptacoordinate and one hexacoordinate metal centres. The networks of **11** and **14** are of the same type, namely 2-D (3,6) (Figures 3.12 and 3.24 respectively). Nevertheless there are differences between the compounds **10**, **11** and **14**.

While the SBUs of both **10** and **14** are connected to other parts of the network via six tph^{2-} ligands, the former is coordinated to four terminal DMF molecules (Figure 3.7) while **14** has two terminal DMF molecules per SBU (Figure 3.23). The gross architectures of the two networks also vary significantly as can be observed from Figures 3.8 and 3.24.

There are several differences between **11** and **14**. The carboxylate groups of **14** adopt the chelating bridging bidentate mode only (Figure 3.23) while two different carboxylate binding modes are found in **11** (Figures 3.11a and 3.11b). Another difference between the SBUs of **11** and **14** is the amount of coordinated DMF ligands. There are two terminal DMF ligands in every SBU of **14** and four DMF molecules in each of the two SBUs of **11**.

3.5 Thermal properties of the networks

The thermal stability of the cadmium-based networks was also analysed. Potential network candidates chosen for this study were **9**, **12**, **13** and **14**, on the following basis:

[IX] Symmetry transformations used to generate equivalent atoms:
#1 -x+y+2 -x+1 z

12 has uncoordinated DMF molecules inside the pores. If these guest molecules can be removed without the collapse of the network, then the free space resulting form such evacuation could be possibly used for gas storage.

While **9, 13** and **14** do not have free guest molecules but instead the DMF or DEF molecules are found coordinated to the metal centres. If the respective ligands can be removed without the decomposition of the networks, then once again free space will be available for gas adsorption. After the removal of the coordinated molecules from **9, 13** and **14**, the resulting compounds will also afford metal centres with vacant coordination sites. The resulting networks may then have the potential to exhibit Lewis acid type catalytic activity.

In order to investigate the stability of the networks with respect to solvent removal processes, a method similar to that used in the previous chapter was employed. Information about the thermal stability of the networks and the temperatures at which the solvent/guest molecules are lost from within the pores was obtained from thermogravimetric analysis measurements (TGA). The X-ray powder data for the pre- and post-heated samples were compared and this comparison gave an indication of the stability of the networks with respect to temperature. The results obtained are detailed in the following section.

3.5.1 Guest solvent removal experiments for $\{(Me_2NH_2)_2[Cd(tph)_2]\cdot 2DMF\}_\infty$ (12)

Thermogravimetric data were collected for **12** (Figure 3.26) within the temperature range of 30-600°C at a heating rate of 10°C per minute. The TGA data show a stable plateau for the temperature range of 30-110°C. This indicates that no solvent molecules are lost within this temperature range (region a). Two mass losses of approximately 10% each occur from 110-200°C and these correspond to the loss of the guest DMF molecules (region b). There is a small plateau from 200-240°C (region c) and after this region the network shows signs of decomposition.

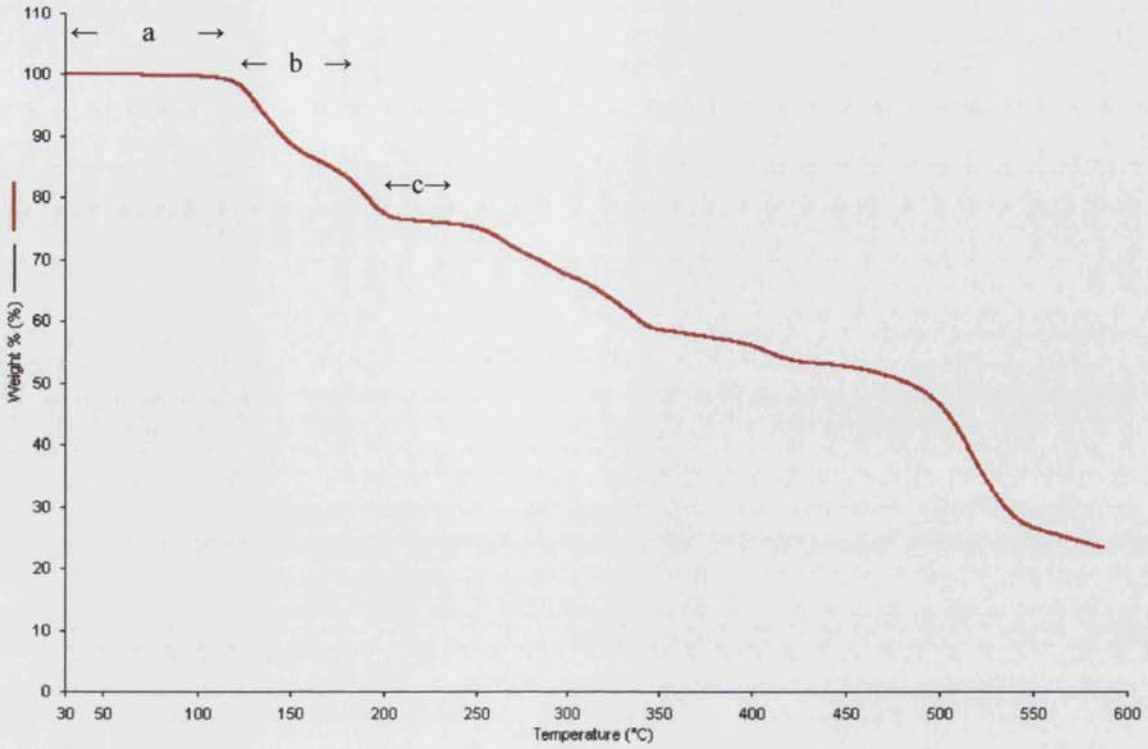

Figure 3.26. Plot of %mass loss against temperature in °C for **12**.

A fresh sample of **12** was heated to 210°C for 1 minute and the resulting compound was analysed by X-ray powder diffraction. Both microanalysis and comparison of the powder diffraction pattern with that of **12** (Figure 3.27) suggest that the network undergoes a change on heating.

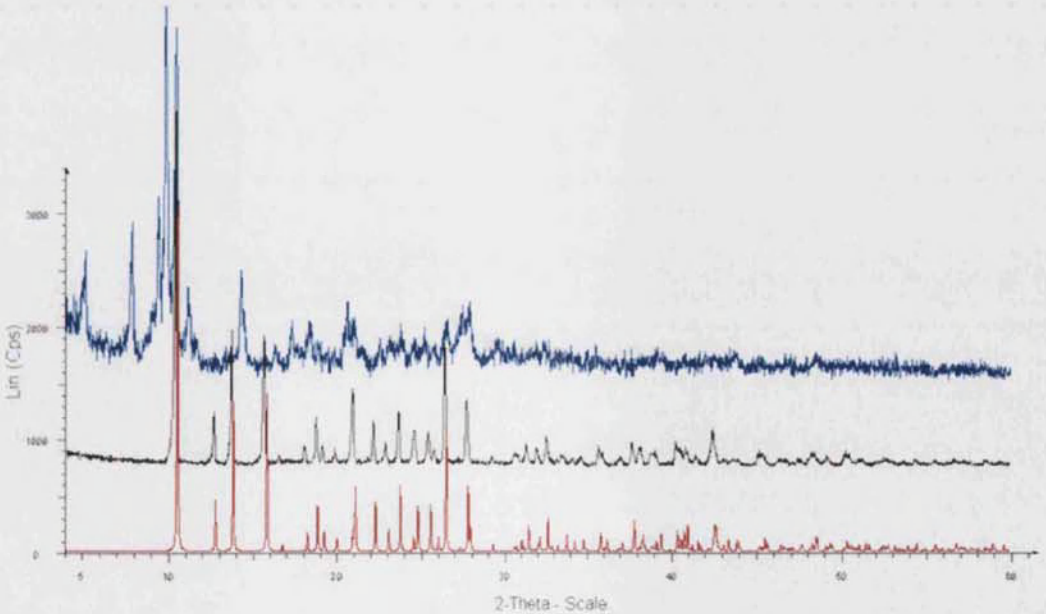

Figure 3.27. Powder data for **12** and heated **12**. The red trace is the simulated powder pattern from the single crystal data, the black trace is the experimental powder pattern for **12** while the blue trace is the experimental powder pattern for **12** heated at 210°C for 1 minute.

3.5.2 DMF removal experiments for $\{[Cd(tph)(DMF)]\}_\infty$ (9)

The TGA of **9** was recorded using the same experimental procedure as that for **12**. The data for **9** (Figure 3.28) show a plateau in the region of 30-180°C. This indicates that there is no solvent loss in this temperature range. This plateau is followed by a rapid mass loss of 10% between 180-210°C (region a), and a second 10% mass loss in the region between 210-350°C (region b). There is very little mass loss in the range of 350-420°C (region c). Beyond 420°C the network starts to decompose to ultimately form CdO (calculated mass 37%, found 36%). It can be noted that while the first 10% mass loss occurs over a narrow temperature range, the second mass loss occurs over a wider temperature range.

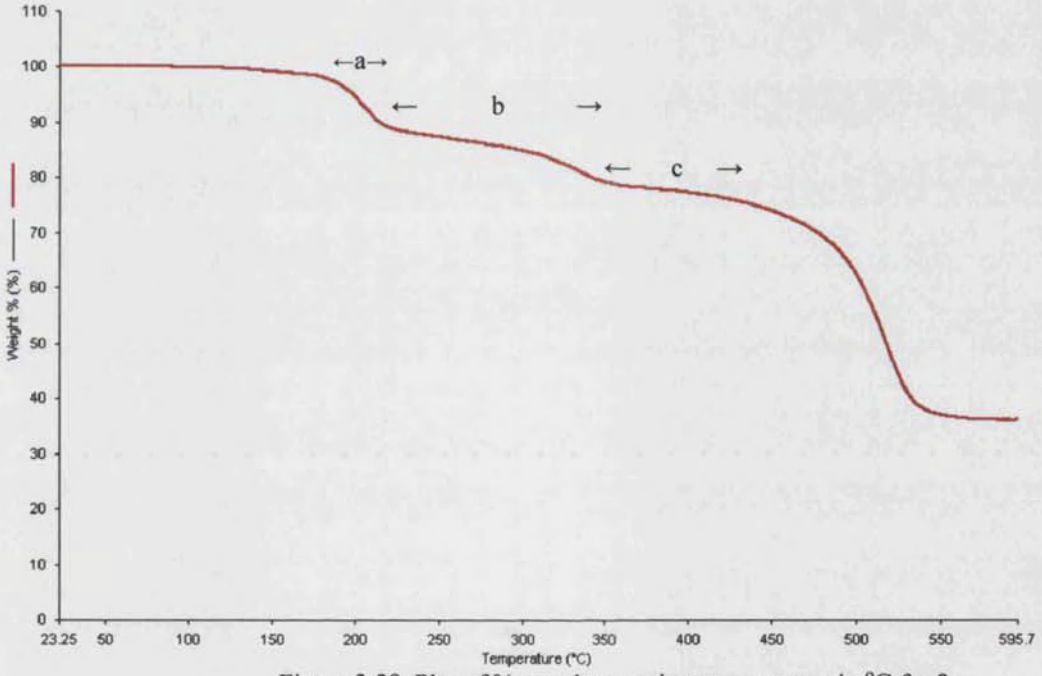

Figure 3.28. Plot of %mass loss against temperature in °C for **9**.

The two 10% losses account for the total amount of DMF in **9**, which is calculated at 20.9%. All the DMF ligands are in a similar environment in this compound and the fact that the coordinated molecules were lost at different rates and in two distinct steps instigated further investigation.

Microanalytical results for **9a** (**9** heated at 250°) and **9b** (**9** heated at 400°C) correlated with empirical formulae of $\{[Cd(tph)(DMF)_{0.5}]\}_\infty$ for **9a** (C, H and N required for $\{[Cd(tph)(DMF)_{0.5}]\}_\infty$ C 36.4, H 2.42, N 2.24%, found C 36.2, H 2.66, N 2.65%), and

{[Cd(tph)]}$_\infty$ for **9b** (C, H and N required for {[Cd(tph)]}$_\infty$ C 34.7, H 1.46, found C 34.4, H 1.94) respectively. X-ray powder data for **9a** (Figure 3.29) and **9b** (Figure 3.30) were collected and compared to the single crystal X-ray data of **9**. The X-ray powder plot of **9a** contains all the peaks for **9** plus additional ones. Essential differences in the position and relative intensities of the peaks are observed on comparing the data for **9** with that for **9b**. This suggests that the network of **9** is undergoing a more complex reaction than just loss of DMF.

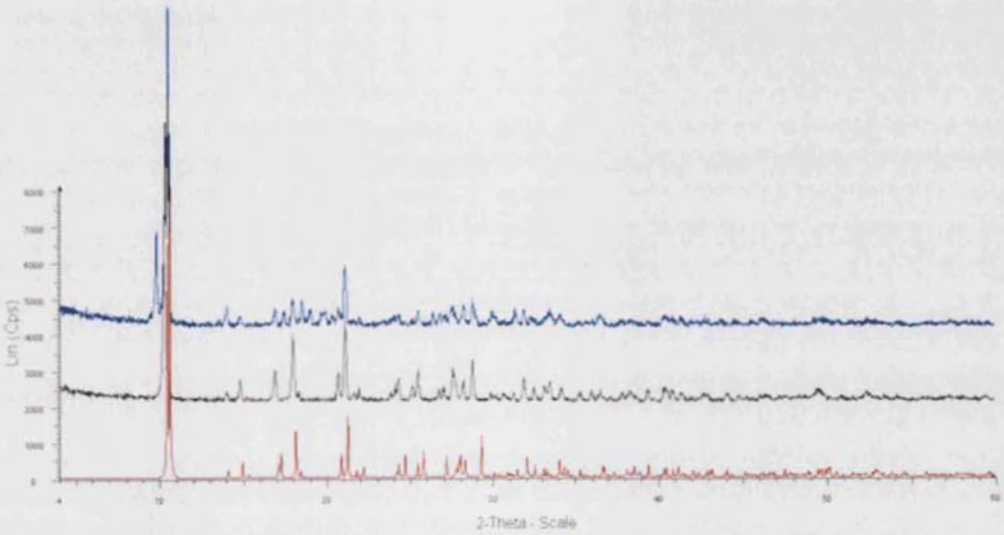

Figure 3.29. Comparison of the powder patterns for **9** and **9a**. The red trace is the simulated powder pattern from the single crystal data. The black trace is the experimental powder pattern for **9** while the blue trace is the experimental powder data for **9a**.

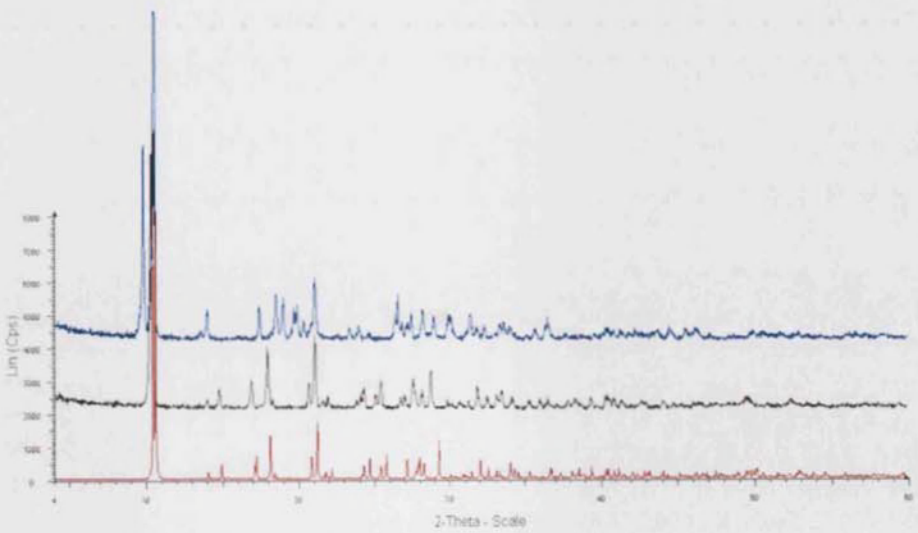

Figure 3.30. Comparison of the powder plots for **9** and **9b**. The red trace is the simulated powder pattern from the single crystal. The black trace is the experimental powder data for **9** while the blue trace is the experimental powder plot for **9b**.

3.5.3 DEF removal experiments for $\{[Cd_3(tph)_3(DEF)_2]\}_\infty$ (13)

$\{[Cd_3(tph)_3(DEF)_2]\}_\infty$ (**13**) contains coordinated DEF molecules that can be potentially removed from their coordinated sites to yield a Lewis acidic network. TGA data were collected for **13** using the same experimental conditions as previously used for **9** and **12**. The TGA data for **13** (Figure 3.31) show a plateau in the temperature range of 30-210°C. This is then followed by a 10% mass loss over the temperature range of 210-310°C to form **13a** (region a). A plateau is then observed between the region of 310-370°C (region b) indicating that **13a** is stable within this temperature range. A rapid loss of 10% by mass occurs within the range of 370-400°C to give **13b**. There is a small final plateau (region c) in the temperature range of 400-440°C and eventually the network decomposes to CdO (calculated 37%, found 35%)

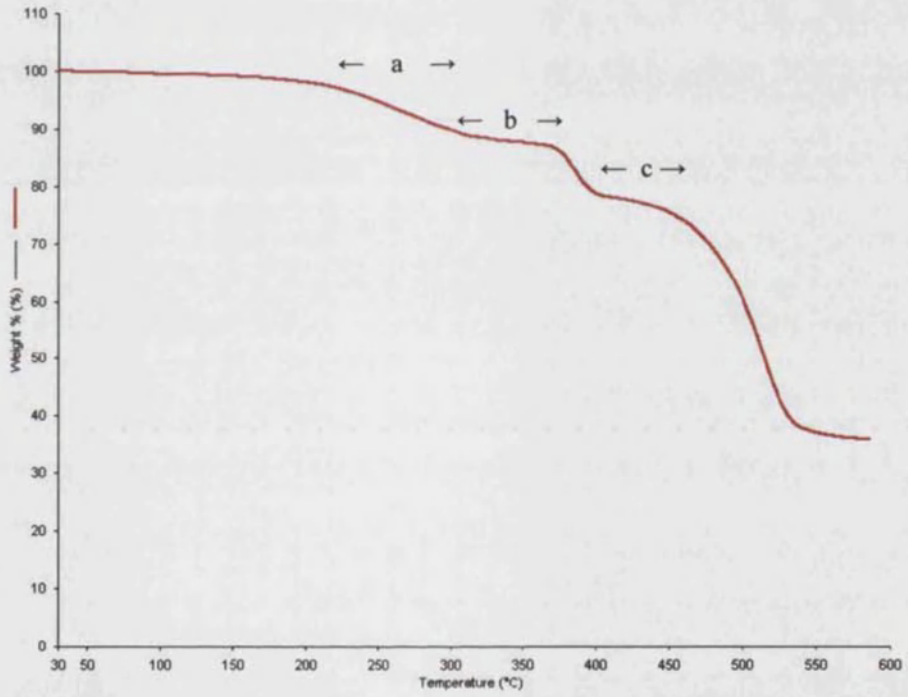

Figure 3.31. Plot of % mass loss against temperature in °C for **13**.

The first mass loss (region a) is equivalent to 1 DEF molecule calculated to be 9.7%. Thus **13a** has the empirical formula of $\{[Cd_3(tph)_3(DEF)]\}_\infty$ which was also confirmed by microanalysis (C, H, N required for $\{[Cd_3(tph)_3(DEF)]\}_\infty$ C 37.4, H 2.49, N 1.51%, found C 36.9, H 2.97, N 1.73%). The second mass loss is equivalent to another DEF molecule and thus **13b** has the empirical formula of $\{[Cd(tph)]\}_\infty$ This was also verified by microanalysis (C, H, N required for $\{[Cd(tph)]\}_\infty$ C 34.7, H 1.46, found C 34.5,

H 1.97). When the X-ray powder patterns for **13a** (Figure 3.32) and **13b** (Figure 3.33) were compared to that of **13** it was noted that there was no change in the peak position but broadening had occurred. This suggests that the network remains intact even though there might be signs for some loss of crystallinity.

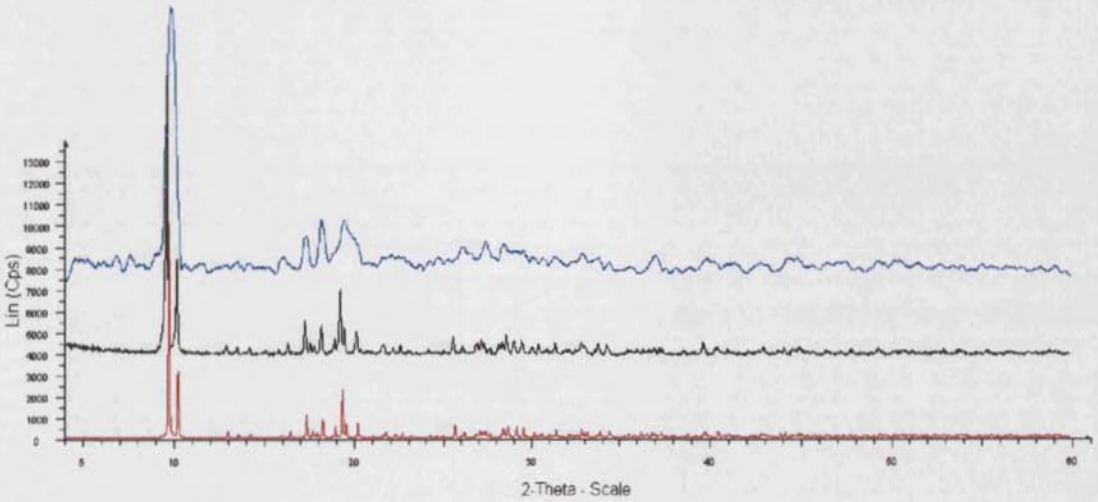

Figure 3.32. Comparison of powder data for **13** and **13a**. The red trace is the simulated powder pattern from the single crystal experiment. The black trace is the experimental powder data for **13**,and the blue trace is the experimental powder data for **13a**.

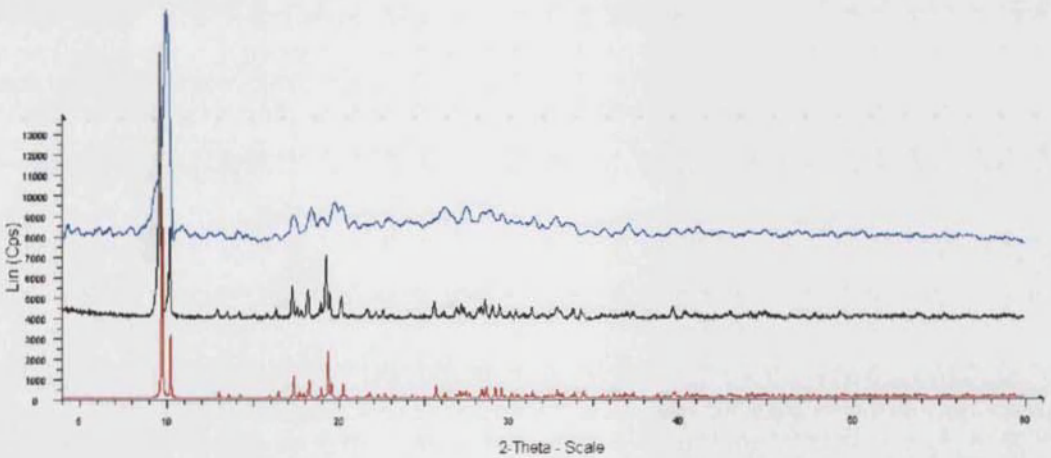

Figure 3.33. Comparison of powder data for **13** and **13b**. The red trace shows the simulated powder pattern obtained from single crystal experiments. The black trace is the experimental powder data for **13** while the blue trace is the experimental powder data for **13b**.

A comparison of the temperatures at which **9** loses the coordinated DMF (180-210°C and 210-350°C) and the temperatures at which **13** loses the coordinated DEF (240-310°C and 370-400°C) shows that the latter molecules are lost at higher temperatures than

the former. This may reflect the fact that DEF has a higher boiling point than DMF and thus once uncoordinated it needs higher temperatures to be evacuated from within the pores.

3.5.4 DMF removal experiments for $\{[Cd_3(bpdc)_3(DMF)_2]\}_\infty$ (14)

The TGA data for **14** (Figure 3.34) show that the coordinated DMF molecules are bound much tighter to the cadmium centres than in **9**. **14** was found to be stable up to 380°C. Within the temperature range 380-430°C the network loses 16% by mass (region a) which is equivalent to the calculated mass of two DMF molecules (17%). Beyond 430°C the compound decomposes fairly rapidly to CdO (calculated mass 32%, found 31%). A fresh sample of **14** was heated to 430°C in the TGA for 1 minute to give **14a**, and then submitted for microanalysis. The results obtained suggested that **14a** has the empirical formula of $\{[Cd(bpdc)]\}_\infty$ (C, H, N required $\{[Cd(bpdc)]\}_\infty$ C 47.7, H 2.29 %, found C 47.7, H 2.50 %).

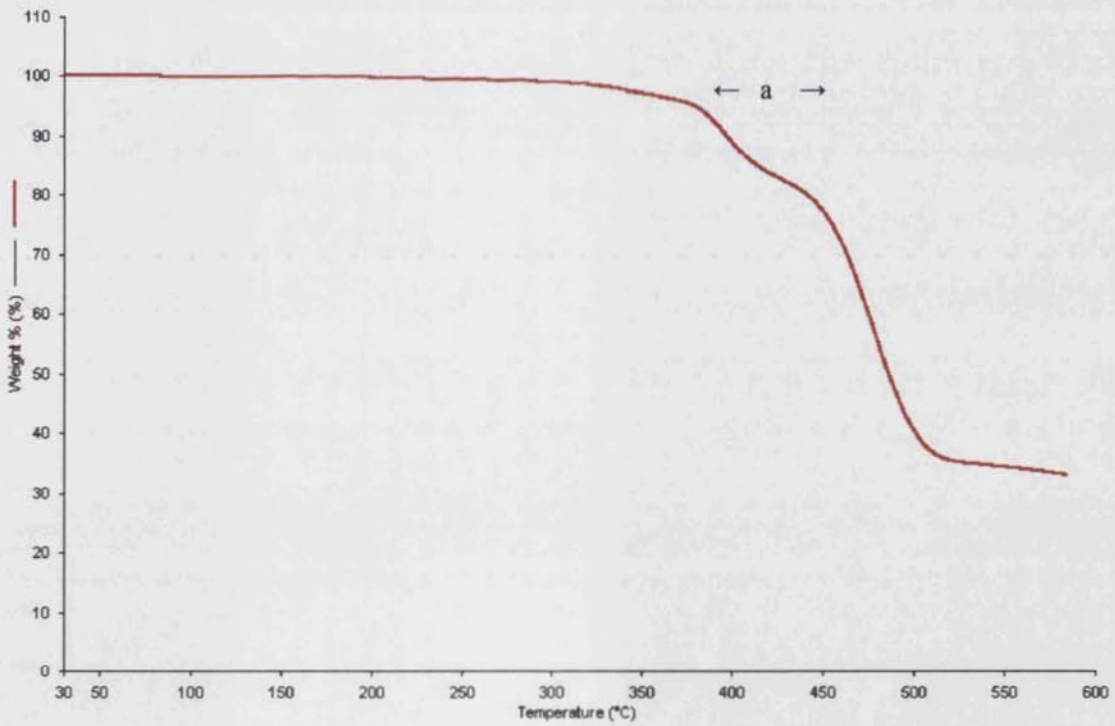

Figure 3.34. Plot of % mass loss against temperature in °C for **14**.

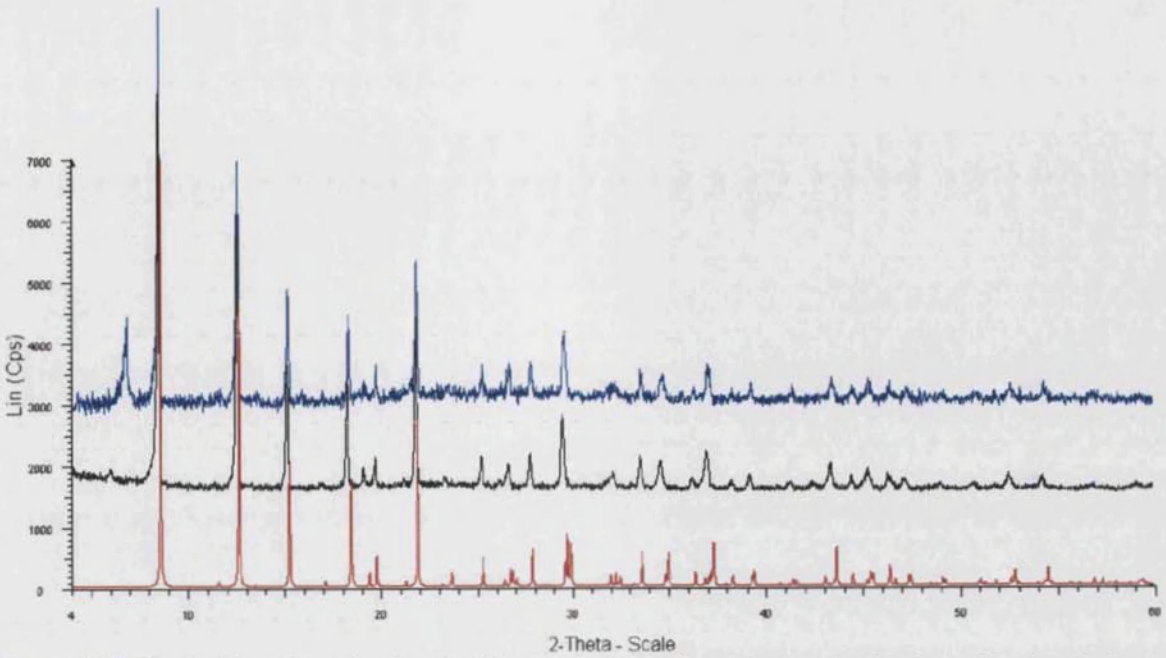

Figure 3.35. Comparison of powder data for **14** and **14a**. The red trace is the simulated powder plot obtained from the single crystal experiments. The black trace is the experimental powder data for **14** while the blue trace is the experimental powder data for **14a**.

As can be observed from the comparison of the powder plots for the heated sample of **14** and prior to heating samples, apart from the additional peak at $2\theta = 7$, the two plots are similar. Thus the TGA, microanalysis and powder data suggest that the coordinated DMF molecules can be removed with the final network still retaining its integrity.

3.6 Guest exchange reactions

Since the network of $\{(Me_2NH_2)_2[Cd(tph)_2]\cdot 2DMF\}_\infty$ **(12)** did not survive the removal of the guest DMF molecules from within the pores, an alternative approach to obtain the guest free network was investigated. **12** was immersed in low boiling solvents such as acetone, chloroform and methanol. The aim of this experiment was to exchange the high boiling DMF guest molecules with a more volatile solvent, so that the new guests could be removed at lower temperatures thus increasing the chances of keeping the network intact on heating.

The length of time that the sample was exposed to solvents ranged from ten minutes to three days. TGA and X-ray powder data were collected for the samples left over chloroform and acetone for ten minutes, one hour, one day and three days. The samples

showed similar mass losses at equivalent temperature ranges to those used for **12**. The X-ray powder patterns of **12** before or after exposure to either chloroform or acetone were identical. This suggests that the guest DMF molecules were not exchanged for acetone or chloroform.

In the case where **12** was immersed in methanol, the results differed from those obtained from the other two solvents. When **12** was washed with methanol for 10 minutes a significant change was observed in the powder pattern with these changes being augmented on further standing over methanol (Figure 3.36).

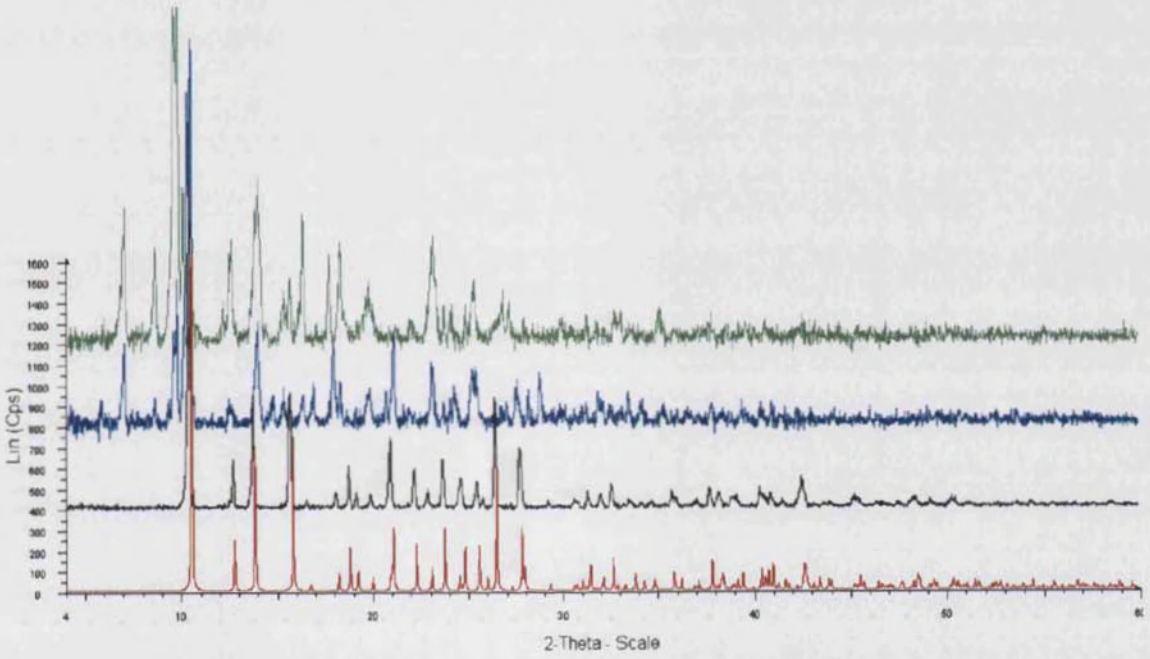

Figure 3.36. The red trace is the simulated powder plot for **12**, the black trace is the experimental powder data for **12**. The blue trace is the powder pattern for **12** washed with MeOH for 10 minutes, while the green trace is the powder pattern for **12** left over MeOH for 3 days.

In Chapter 2 it was noted that on immersing in methanol, the X-ray powder plot of $\{(Me_2NH_2)_2[Zn_3(tph)_4]\cdot DMF\cdot H_2O\}_\infty$ also undergoes a transformation. Following arguments developed by Allendorf and Greathouse,[9] it can be postulated that the changes in the powder patter can be attributed to the reactivity of methanol. In particular, methanol may be breaking the cadmium-oxygen bonds, dissolving the network and eventually forming a more stable alternative network.

$\{[Cd_3(tph)_3(DEF)_2]\}_\infty$ **(13)** was also immersed in methanol and once again the powder pattern of the samples that came in contact with the solvent changed significantly from that of the starting material. This indicates that the network of **13** might also be undergoing a transformation to form a new phase.

3.7 Catalytic properties of $\{[Cd_3(tph)_3]\}_\infty$ (13b) and $\{[Cd_3(bpdc)_3]\}_\infty$ (14a)

Acylation of alcohols is a frequently used process in organic chemistry.[10] Lewis acids such as $Sc(OTf)_3$,[11] $La(OTf)_3$,[12] $Cu(OTf)_2$,[13] $Hf(OTf)_4$ and $Zr(OTf)_4$[14] are frequently used to promote this reaction. Zeolites and metal organic frameworks containing Lewis-acid sites have also been used as catalysts in acylation reactions. [15,16,17]

As has been demonstrated in Section 3.5, the coordinated solvent molecules of $\{[Cd_3(tph)_3(DEF)_2]\}_\infty$ **(13)** and $\{[Cd_3(bpdc)_3(DMF)_2]\}_\infty$ **(14)** could be removed whilst the networks remained intact. This process gave networks that have both empty pores as well as vacant coordination sites on the metal centres. Thus **13b** and **14a** were tested for their catalytic abilities using phenol and acetic anhydride as reagents (Figure 3.37).

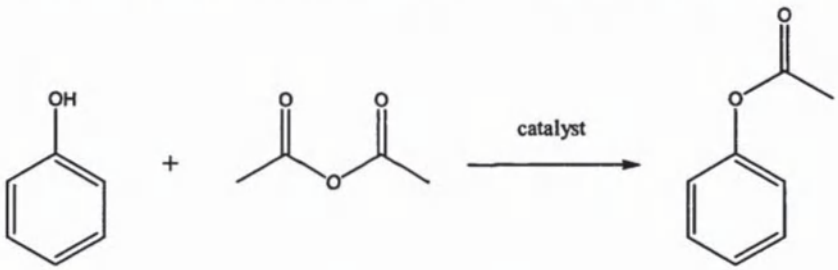

Figure 3.37. Schematic representation of the acylation reaction of phenol.

3.7.1 Acylation reactions of Phenol

Catalytic amounts, (0.01 mmol) of $\{[Cd_3(tph)_3(DEF)_2]\}_\infty$ **(13)** and $\{[Cd_3(bpdc)_3(DMF)_2]\}_\infty$ **(14)** were heated at 410° and 400°C respectively for one minute under a flow of N_2. The heated networks were then transferred to a Schlenk tube and heated at 100°C under vacuum for one hour. Phenol (6 mmol) and excess acetic anhydride (9 mmol) were dissolved in dry dichloromethane and added to the catalyst. The reaction was stirred at room temperature for three days. The solvent volume was removed under reduced pressure, and the product was purified by column chromatography using 4:1 hexane/ ethyl acetate as the mobile phase.

The presence of phenylacetate in both reactions was confirmed by ^{1}H and ^{13}C NMR spectroscopy. A control experiment was set up which included phenol and acetic anhydride in the absence of the catalysts. The starting materials were retrieved unchanged after 2 weeks. These observations confirm that the reaction was catalysed by the presence of the networks.

The acylation reactions did not proceed to completion as was confirmed by the presence of unreacted starting material after three days. The conversion ratios are 16% and 18% for **13b** and **14a** respectively. Speculations for the incompletion of the reaction might be due to the permanent lodging of the product inside the cavities. Favourable $\pi\cdots\pi$ interactions between the network aromatic ligands and phenol might also contribute to the retention of the product inside the pores hence, once formed phenylacetate renders the catalyst inactive.

The gas adsorption behaviour of these two networks is explored in detail in Chapter 4.

3.8 Conclusions

The sensitivity of the reaction of $Cd(NO_3)_2{\cdot}6H_2O$ and H_2tph to variations in the reaction conditions such as temperature, pressure and solvent purity were discussed in this chapter.

The first variable in the reaction to be assessed was the temperature. When the reaction was performed at 115°C, $\{[Cd(tph)(DMF)]\}_\infty$ (**9**) was formed, whereas at 95°C a mixture of two compounds, $\{[Cd(tph)(DMF)]\}_\infty$ (**9**) and $\{[Cd_3(tph)_3(DMF)_4]\}_\infty$ (**10**) was obtained. A similar temperature dependency was described for the reaction between $Zn(NO_3)_2{\cdot}6H_2O$ and H_2tph system in Chapter 2. Natajaran observed similar temperature effects in other dicarboxylate systems.[18]

As in the case of the $Zn(NO_3)_2{\cdot}6H_2O/H_2tph$ system, the reaction between $Cd(NO_3)_2{\cdot}4H_2O$ and H_2tph was also affected by pressure. When the reaction was carried out under three atmospheres of nitrogen, $\{[Cd_3(tph)_3(DMF)_4]\}_\infty$ (**11**) was obtained. On

comparing the two supramolecular isomers of **10** and **11** it was noted that the sheets of the latter pack tighter than the former with the consequence that **11** has a higher density than **10**. Thus one can speculate that the increased pressure favours the formation of the denser packed phase.

The dependency of the reaction between $Cd(NO_3)_2 \cdot 4H_2O$ and H_2tph on the presence of secondary ammonium cations as templates was also reported. While dimethylammonium cations in DMF templated the formation of **12**, bigger analogues such as diethylammonium cations in DEF proved ineffective. This demonstrates that in this specific case the secondary cations behave differently towards the $Cd(NO_3)_2 \cdot 4H_2O$ and $Zn(NO_3)_2 \cdot 6H_2O$ systems.

When 4,4'-biphenyldicarboxylate was used as the ligand, $\{[Cd_3(bpdc)_3(DMF)_2]\}_\infty$ (**14**) was formed. The gross structure of **14** consists of 2-D (3,6) sheets. As was mentioned in Section 3.4, when tph^{2-} was reacted in an analogous way to $bpdc^{2-}$, the two networks differed significantly. $\{[Cd_3(tph)_3(DMF)_4]\}_\infty$ (**11**) also consists of 2-D (3,6) sheets but as highlighted in previous parts of the chapter, there are significant differences between the networks of **11** and **14**.

Also noteworthy is the reactivity of $\{(Me_2NH_2)_2[Cd(tph)_2]\cdot 2DMF\}_\infty$ (**12**) and, $\{[Cd_3(tph)_3(DEF)_2]\}_\infty$ (**13**) towards methanol. The X-ray powder patterns of **12** and **13** undergo significant changes when the compounds are submerged in MeOH for ten mins. One possible explanation for this observation is that methanol dissolves the networks and a more stable compound is eventually precipitated. Other authors[19] have reported similar crystal dissolution and reprecipitation but in their cases, the process occurs over a longer period of time.

The coordinated solvent molecules in **13** and **14** were removed thermally with the solvent free networks still being intact, as suggested by X-ray powder crystallography. The empty pore networks were shown to exhibit Lewis acidic catalytic properties as demonstrated through the acylation of phenol.

3.9 Further work

The reaction of $Cd(NO_3)_2 \cdot 4H_2O$ with tph^{2-} was shown to form different products at different temperatures. The reaction can be carried out using a wider temperature range, thus this will aid in understanding the product distribution as a function of temperature. The temperature effect on this particular reaction can also be investigated in DEF.

The reactions of $Cd(NO_3)_2 \cdot 4H_2O$ with tph^{2-} and $bpdc^{2-}$ were found to differ significantly. The sensitivity of the reaction between $Cd(NO_3)_2 \cdot 4H_2O$ and H_2bpdc towards changes in temperature and pressure can be investigated.

The catalytic reactions of **13b** and **14a** can be investigated further. The reaction conditions such as temperature and solvent can be varied in order to optimise the yield of the reaction. The catalytic reactions of the network can also be extended to include condensation reactions of amines and thiols starting from thiophenols and aminophenols.

References:

1. H.B.Xu; Z.M.Su; K.Z.Shao; Y.H.Zhao; Y.Xing; Y.C.Liang; H.J.Zhang; D.X.Zhu, *Inorg.Chem.Commun.* **2004,** 7, 260.
2. H.K.Fun; S.S.S.Raj; R.G.Xiong; J.L.Zuo; Z.Yu; X.Z.You, *J.Chem.Soc.,Dalton Trans.* **1999**, 1915.
3. R.G.Xiong; S.R.Wilson; W.Lin, *J.Chem.Soc.,Dalton Trans.* **1998**, 4089.
4. A.Thirumurugan; C.N.R.Rao, *J.Mater.Chem.* **2005,** 15, 3852.
5. N.L.Rosi; K.Kim; M.Eddaoudi; B.Chen; M.O'Keeffe; O.M.Yaghi, *J.Am.Chem.Soc.* **2005,** 127, 1504.
6. A.F.Wells, *Three-dimensional nets and polyhedra.* ed.; John Wiley and Sons, Inc.: United States of America, 1977; p 3-21.
7. T.L.Savarese. *Crystal engineering of cadmium network structures.* M.Chem.thesis, University of Bath., Bath., 2004.
8. F.Q.Zou; X.H.Bu; R.H.Zhang, *Inorg.Chem.* **2004,** 43, 5382.
9. J.A.Greathouse; M.D.Allendorf, *J.Am.Chem.Soc.* **2006,** 128, 10678.
10. K.L.Chandra; P.Saravanan; R.K.Singh; V.K.Singh, *Tetrahedron* **2002,** 58, 1369.
11. K.Ishihara; M.Kubota; H.Yamamoto, *Synlett.* **1996**, 265.
12. E.W.P.Damen; L.Braamer; H.W.Sheeren, *Tetrahedron Lett.* **1998,** 39, 6081.
13. P.Saravanan; V.K.Singh, *Tetrahedron Lett.* **1999,** 40, 2611.
14. S.Kobayashi; M.Moriwaki; I.Hachiya, *Tetrahedron Lett.* **1996,** 37, 4183.
15. B.Chiche; A.Finiels; C.Gauthier; P.Geneste, *Org.Chem.* **1986,** 51, 2128.
16. Q.L.Wang; Y.Ma; X.Ji; H.Yan; Q.Qiu, *J.Chem.Soc.Chem.Commun.* **1995**, 2307.
17. K.Suzuki; H.Kitagawa; T.Mukaiyama, *Bull.Chem.Soc.Jpn.* **1993,** 66, 3729.
18. S.Natajaran. In *Transformation of a Low-Dimensional MOF Solid:Is there an Intermediate?*, Chemistry of Coordination Space, London, 11-13th July, 2006; London, 2006.
19. C.Thompson; N.R.Champness; A.N.Khlobystov; C.J.Roberts; M.Schroder; S.J.B.Tendler; M.J.Wilkinson, *J. Micro.* **2004,** 214, 261.

Chapter 4 Gas adsorption properties of $\{[Cd_3(tph)_3]\}_\infty$ and $\{[Cd_3(bpdc)_3]\}_\infty$

This chapter focuses on the gas adsorption properties of $\{[Cd_3(tph)_3]\}_\infty$ **(13b)** and $\{[Cd_3(bpdc)_3]\}_\infty$ **(14a)**; the synthesis of which were discussed in Chapter 3. A brief introduction to the theory behind gas-solid adsorption will be followed by the discussion of the results.

4.1 Introduction to the theory of gas-solid adsorption

As discussed in Chapter 1, metal organic frameworks can adsorb gas molecules.[I] J.W.Gibbs expressed the concept of adsorption by solid media as, 'the amount of fluid in excess of that which would be present if the adsorbent had no influence on the behaviour of the fluid'.[2]

To measure the adsorption properties, a solid porous material (adsorbent) is exposed to a gaseous species (adsorbate). When the gas molecules interact with the adsorbent there is a decrease in the pressure of the system. A plot of the pressure at equilibrium/saturated vapour pressure, p/p^o, (x-axis) against the amount of gas adsorbed, n (y-axis) is called an isotherm.

The amount of gas molecules that bind to the framework depends on several factors such as the surface area available for adsorption, the chemical properties of this surface and the shape and size of the pores.[3] Each of these points will be discussed separately in the coming paragraphs.

In general, the quantity of gas molecules adsorbed by a metal organic framework is proportional to its surface area, thus the bigger the area, the higher the amount of adsorbate species. Langmuir surface areas reported to date for metal organic frameworks range from 500 to 4500 m^2/g. [4-11] The surface area shown by these compounds is far larger than the maximum theoretical surface area for porous carbons (2630 m^2/g) and zeolites.[3]

[I] The term adsorption denotes condensation of gases on a free surface as opposed to the bulk.[1]

The pores, or empty spaces of a network are classified according to the IUPAC scheme.[12,13] This nomenclature divides the pores into three classes according to their diameters. The largest pores have a diameter bigger than 50 nm and are called Macropores. Voids with a diameter of 2-50 nm are termed Mesopores, while the term Micropores refers to compounds with empty space of less than 2 nm in diameter.

The shape of the experimental isotherm is dependent on the volume of the pores. Brunauer, Deming, Deming and Teller recognized six types of isotherms (Figure 4.1).[14]

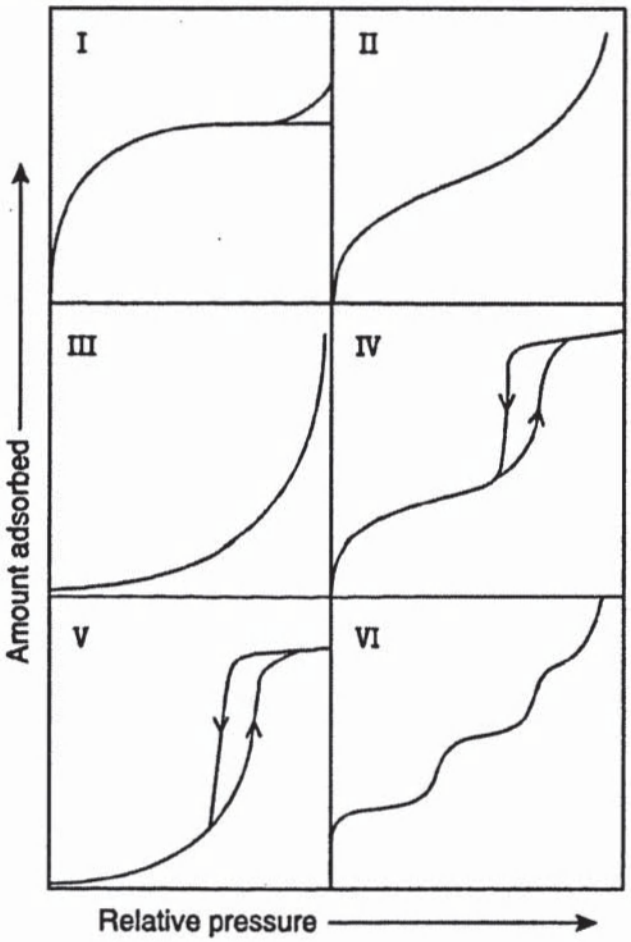

Figure 4.1. The six different types of isotherms.

Microporous materials show Type I isotherms (Figure 4.1), as the pores fill up rapidly with the adsorbate molecules at relatively low pressure before reaching a plateau. At this point, all the empty spaces are occupied by the guest molecules and thus no further uptake is observed.

Isotherm Types II, III and VI are indicative of non-porous or macroporous materials. The distinction between Type II and III isotherms reflects the strength of

interaction between the fluid and the network. In the former case the guest species experience a stronger interaction with the adsorbent than in Type III. Type VI isotherms result from adsorption measurements on macroporous materials and are characterised by stepwise multilayer adsorption.

Mesoporous materials exhibit Types IV or V isotherms. The difference between the two results depends on the strength of interaction between the gas molecules and the network. When the interaction between the two species is strong, the resulting isotherm is Type IV while with a weak interaction the plot obtained is Type V. When gases are desorbed from mesoporous compounds, capillary condensation comes into play and this is the reason for the hysteretic loop in the mid-pressure region.[3]

The strength of interaction between the pores and the fluids is dependent on the chemical properties of both the adsorbent and adsorbate. Different types of gases, such as hydrogen, carbon dioxide, nitrogen, krypton and ethene can be adsorbed onto networks. The mentioned guest molecules have different chemistry and thus will interact differently with networks. For example, Lewis acidic sites inside the pores can form stronger bonds to ethene and hydrogen than krypton or nitrogen. The presence of lone pairs, aromatic rings and polar molecules can also affect adsorption.

4.2 Measurement of surface area

The surface area is an important factor in determining the amount of gas adsorbed by a compound. Irving Langmuir developed a mathematical method of calculating the surface area of a porous material by using data from the isotherm.[15-17] He stated that there is a dynamic equilibrium between the gas molecules adsorbed onto a surface, the free adsorbate species and the solid. This results in an adsorption of a monolayer of gas molecules. Assuming that the surface of the adsorbent is uniform and that the gas molecules form a monolayer only, then measurement of the area is proportional to the product of the number of adsorbed gas molecules and the cross-section area of each molecule.

Thus according to the kinetic theory of gases, the number of molecules hitting the surface per cm^2 per second (N) can be calculated by:

$$N = NP/(2\pi MRT)^{1/2} \quad (1)$$

N = Avogadro's number

P = pressure of the gas

M = molecular weight of the gas

R = gas constant

T = absolute temperature

If θ_o represents the fraction of the surface unoccupied by the gas molecules, the number of collisions with the uncovered surface can be calculated from:

$$N^1 = k P\theta_o \qquad (k = N/(2\pi MRT)^{1/2}) \quad (2)$$

While the number of gas molecules adhering to the surface is calculated by:

$$N_{ads} = k P\theta_o A_1 \quad (3)$$

A_1 = condensation coefficient and represents the probability of a gas molecule being adsorbed to the surface upon collision.

The rate of desorption can be calculated from:

$$N_{des} = N_m \theta_1 \nu e^{-E/RT} \quad (4)$$

N_m = number of gas molecules in a complete monolayer

θ_1 = fraction of surface occupied by gas molecules

E = energy of adsorption

ν = is the vibrational frequency of the adsorbed gas molecules

Applying the steady state equilibrium concept, the rate of adsorption is equal to the rate of desorption, thus equation 3 is equal to equation 4:

$$k\, P\theta_o A_1 = N_m \theta_1 v e^{-E/RT} \quad (5)$$

substituting θ_o for $1-\theta_1$ in equation 5 then gives

$$\theta_1 = k\, PA_1 / N_m\, v e^{-E/RT} + k\, PA_1 \quad (6)$$

Assuming that the energy of adsorption E is constant, then the terms $kA_1/ N_m\, v e^{-E/RT}$ of equation 6, can be combined into one constant, K, and up to the inclusion of one monolayer of coverage of gases equation 6 can be expressed as:

$$\theta_1 = N_1/N_m = W_1/ W_2 \quad (7)$$

N_1 and N_m are the number of gas molecules in the incomplete and complete monolayer and W_1 W_2 are the weights adsorbed relative to the weight adsorbed in a completed monolayer. Thus substituting W_1/ W_2 in equation 6 gives:

$$W_1/ W_2 = KP/ 1 + KP \quad (8)$$

Equation 8 can be linearised to:

$$P/ W_1 = 1/KW_2 + P/ W_2 \quad (9)$$

Thus having established W_2, the sample surface area S_t can then be calculated from equation 7:

$$S_t = N_m A = W_2 N_1 A/ M \quad (10)$$

A = cross sectional area of the gas molecules.

The Langmuir surface area assumes monolayer coverage and hence it can only be used to calculate the surface area from Type I isotherms. Hence the equation fails to give an accurate result for surface areas from isotherm Types II to V. However, other algorithms such as those developed by Temkin and Freundlich, do cater for the variables not included in the Langmuir equation. These variables are, multilayer adsorption and variations in heat

of adsorption.[18] Another formula that is commonly used is the BET. Like in the Temkin and Freundlich equations, the BET equation also assumes multiple layer coverage. The latter can be expressed as:

$$V/V_m = cz/(1-z)(1-(1-c)z) \quad (11)$$

$z = p/p^*$

p^* = pressure above a layer of adsorbate thicker than one molecule

V_m = volume corresponding to monolayer coverage

c = constant ($c = e^{(\Delta desH - \Delta vapH)/RT}$)

4.3 Results and discussion

As discussed in Chapter 3, the coordinated DMF or DEF molecules of $\{[Cd_3(tph)_3(DEF)_2]\}_\infty$ **(13)** and $\{[Cd_3(bpdc)_3(DMF)_2]\}_\infty$, **(14)** can be removed from within the pores, with the resulting networks maintaining their integrity. The coordinated DMF and DEF molecules of **13** and **14** were thus removed as described in Chapter 3, to form $\{[Cd_3(tph)_3]\}_\infty$ **(13b)** and $\{[Cd_3(bpdc)_3]\}_\infty$ **(14a)** and gas adsorption measurements on the latter two compounds was performed.

4.3.1 Isotherms for 14a

A sample of $\{[Cd_3(bpdc)_3(DMF)_2]\}_\infty$, **(14)** was heated at 400°C for 1 minute, under a flow of nitrogen, to form $\{[Cd_3(bpdc)_3]\}_\infty$, **(14a)**. The sample was loaded onto the Micromeritics ASAP 2400 apparatus and heated at 100°C for 4 hours under vacuum. The dry mass was recorded at 0.0891g and the nitrogen adsorption and desorption isotherms for this sample measured. Repetitive adsorption measurements on different samples of **14a** were conducted.

The isotherm obtained for this compound is of Type IV (Figure 4.2) and as such is indicative of a mesoporous material that shows strong interaction between the guest and host species. The adsorption isotherm shows an initial small uptake of gas which is followed by a plateau. After this plateau there is a second uptake of gas molecules that is characteristic of capillary condensation. Mesoporous materials have multilayer adsorption

and thus the BET equation is more appropriate to calculate the surface area of **14a**. The BET surface area is calculated to be 21.75m^2/g with the BET constant c (equation 11) being 268.54. The value of c is relatively high, and since it is bigger than 200, it indicates the presence of micropores. On analysing the data from a relative pressure range of 0-0.7 (Figure 4.3), it can be noted that until a relative pressure of 0.3 the isotherm is of the Langmuir type (monolayer coverage) (Type I in Figure 4.1) while the remainder follows the BET predicted plot.

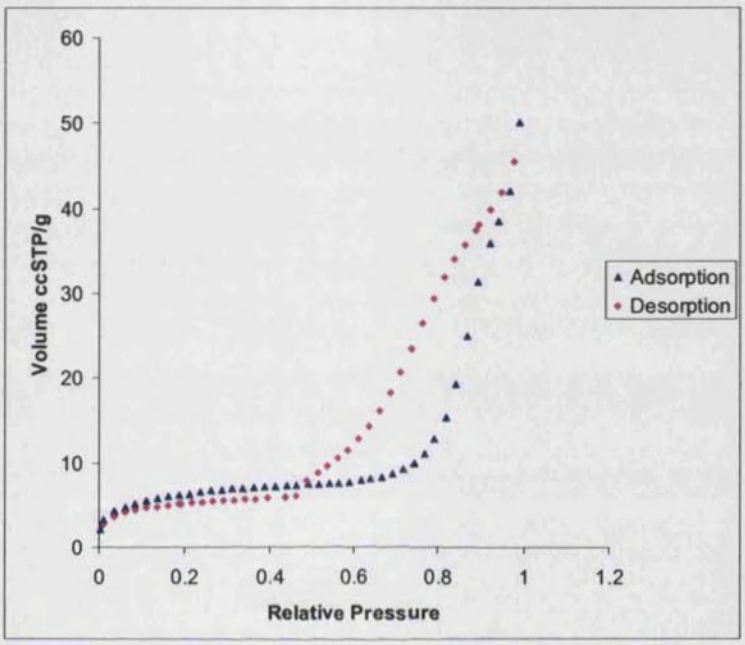

Figure 4.2. N_2 adsorption and desorption isotherms for **14**.

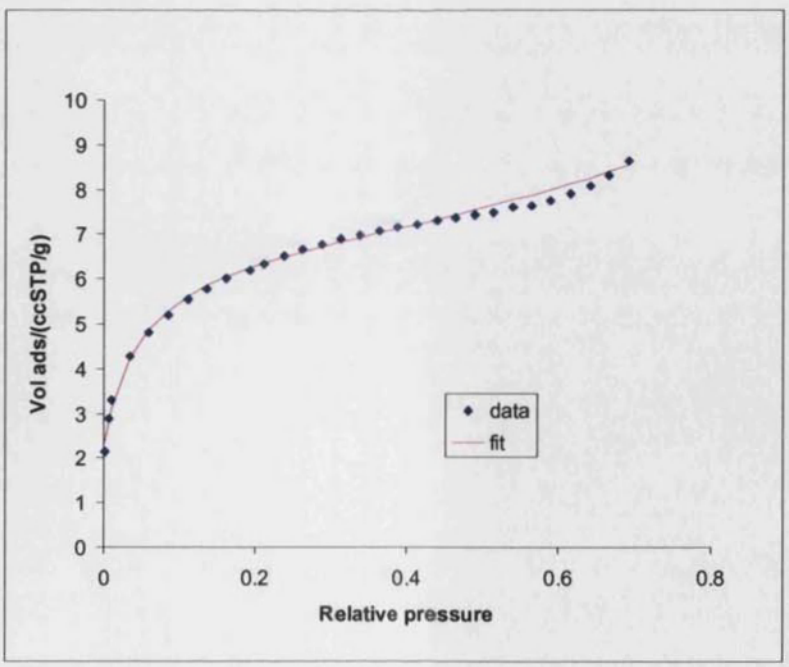

Figure 4.3. Langmuir fit for relative pressure range of 0-0.3 and BET fit for 0.3-0.7 relative pressure range.

As can be noted from Figure 4.2, the amount of gas desorbed in the relative pressure range of 0-0.45 is lower than the volume of gas adsorbed. This discrepancy is due to a machine error in reading volumes of low values.

The shape of the isotherm (Figure 4.2) obtained for **14a** is peculiar to this type of material. An approximate estimate of the size of the pore dimensions can be obtained using single crystal X-ray data collected on **14**. Thus using the above mentioned data, an approximation of the size of the edges of the triangular pores of **14a** are 14Å (closest distance between two cadmium apices of the triangle) (Figure 4.4). As was demonstrated in the introduction, metal organic frameworks have voids of this dimension should form Type I isotherm rather than Type IV.

14a is a fine powder and thus the structure of this material could not be determined by single crystal X-ray crystallography. Results obtained from X-ray powder diffraction illustrated that the structures of **14** and **14a** are comparable, thus the architecture of the parent material (**14**) will be used as a representative of **14a**. As explained in the previous chapter, the crystal structure of **14** consists of 2-D (3,6) type sheets therefore one possible explanation for the shape of the isotherm can be the following. Rather than filling the voids of the triangular pores, the nitrogen atoms pack in the spaces in between the 2-D sheets of **14a** (Figure 4.5).

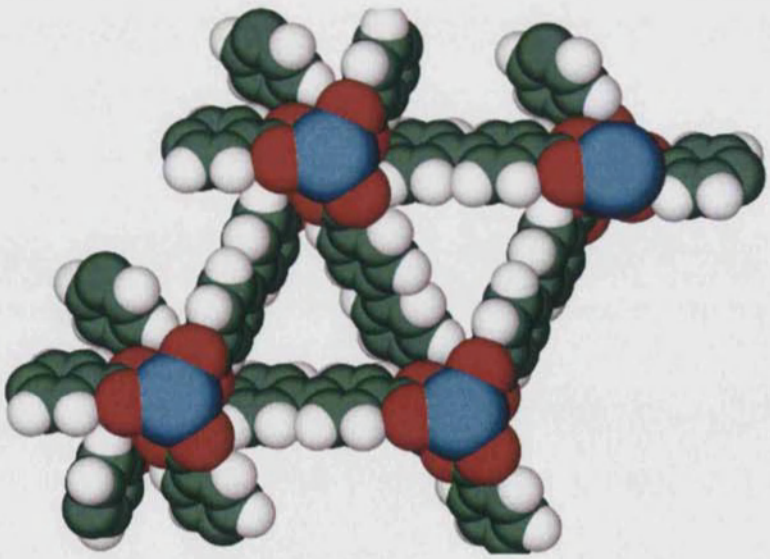

Figure 4.4.The triangular shaped pores of **14** with the coordinated DMF molecules removed. The blue, red, green and white spheres represent Cd, O, C and H respectively.

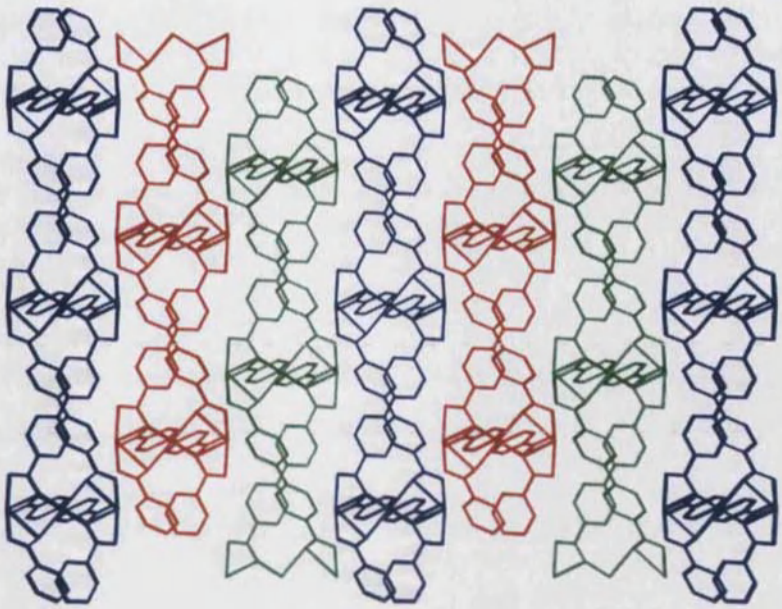

Figure 4.5. The parallel packing of the sheets in **14** viewed down the *b* axis. The sheets are coloured differently for clarity.

The desorption pathway of the isotherm obtained for **14a** (Figure 4.2) is different from the standard Type IV isotherms described by the IUPAC system (Figure 4.1). de Boer[19] stated that one reason for deviations from ideality is due to the shape of the pores. He predicted an isotherm similar to the one observed in Figure 4.2, and he labelled it as Type IV-D. de Boer postulated that this is characteristic of assembly for plate like capillaries. This is consistent with the packing motif of **14a** (Figure 4.5).

The hysteretic loop in the mid-pressure desorption region of **14a** can also arise due to 'kinetic trapping effect',[20] structural changes of the framework on adsorption[3] or due to changes in the packing of the gas molecules inside the pores.[19] 'Kinetic trapping effect' occurs when equilibrium between the gas molecules adsorbed inside the pores and the free gas molecules occurs relatively slowly. The 'trapping' of the gas molecules can be due to interactions between the host and guest species or due to the shape of the pores.

As mentioned in earlier, **14a** is a fine crystalline powder and thus the change in shape of the pores on adsorption and desorption could not be investigated using single crystal X-ray crystallography. In order to confirm that the hysteresis is not due to 'kinetic trapping effect', kinetic measurements were carried out.

The kinetic study was carried out using hydrogen as the gaseous species. Plots of mass and pressure changes over time were obtained to give an indication of how fast the gas moves in and out of the network.

A fresh sample of **14a** was prepared in a similar way as described for the N_2 adsorption experiments. Multiple hydrogen adsorption/desorption experiments, (up to 8 experiments) were carried out with all the individual runs being identical. The repeatability suggests that multiple adsorption/desorption cycles can be performed with the structure keeping its integrity.

A plot of mass or pressure against time (Figures 4.6a and 4.6b) shows stepwise decrease in the two measured parameters. The sharp steps indicate that the guest species move out of the pores very rapidly. This implies that equilibrium between the remaining sorbed molecules and the unbound guest species outside the network is reached quickly. Therefore this rules out any 'kinetic trapping effects' in the hysterisis of the desorption path.

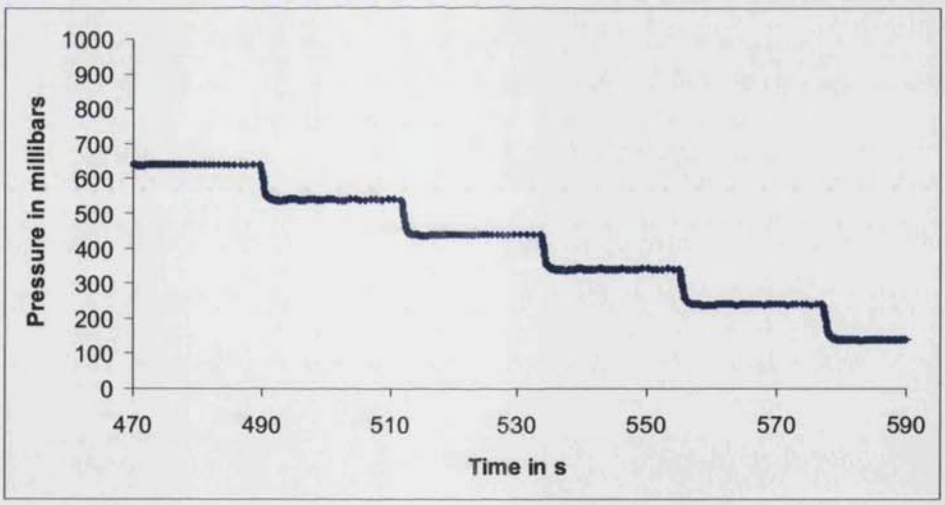

Figure 4.6a. Plot of pressure against time for the H_2 desorption steps of **14a**.

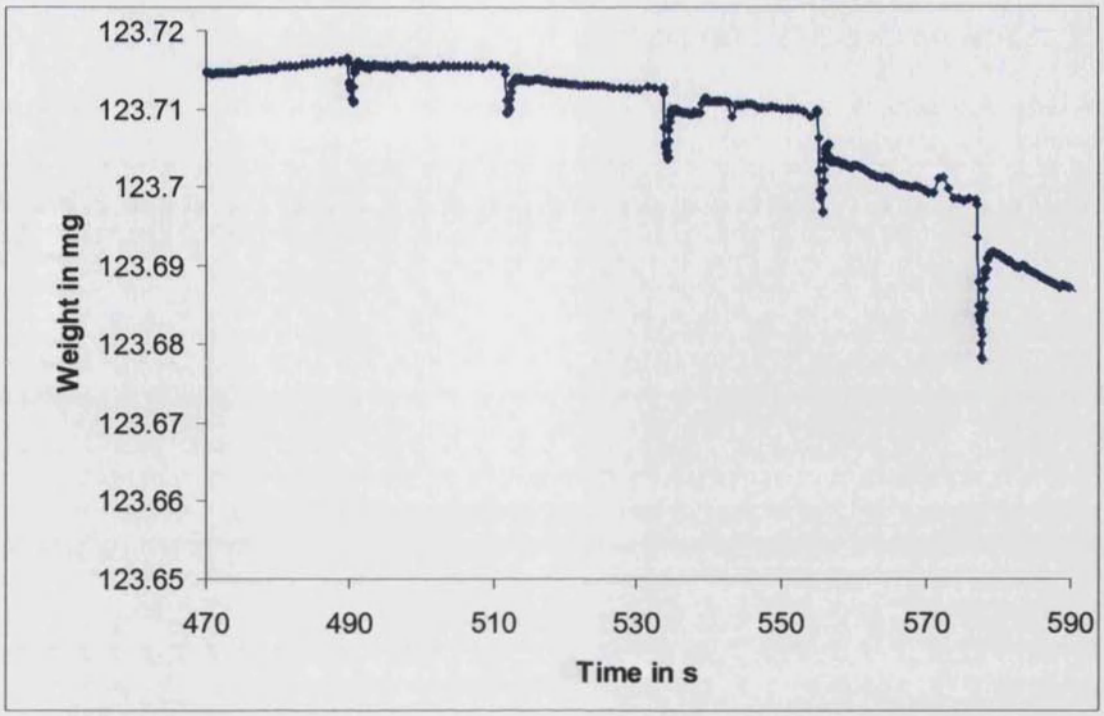

Figure 4.6b. Plot of Mass against time for the H_2 desorption steps of **14a**.

4.3.2 Isotherms for 13b

As stated earlier, the coordinated DEF molecules of $\{[Cd_3(tph)_3(DEF)_2]\}_\infty$ (**13**), can be removed without the destruction of the structure. Thus a sample of **13** was heated at 410°C for 1 minute under a flow of nitrogen to give **13b**. The latter compound was then loaded onto the Micromeritics ASAP 2400 apparatus and heated at 100°C for 4 hours under vacuum. The dry mass was recorded at 0.1215 g and the nitrogen adsorption and desorption isotherms were recorded.

The nitrogen isotherm for **13b** was observed as a straight line. This is due to the low BET surface area of the sample (3.99 m^2/g). For effective gas adsorption measurement a minimum surface area of 20 m^2 is required. This implies that approximately 5.0 g of **13b** is needed. Due to the sample preparation method and equipment limitations, this is not possible and thus alternative routes, such as using small gas molecules, such as hydrogen or more sensitive systems like krypton must be used to obtain isotherms for **13b**. Measurements using both gases were carried out.

At 77K, hydrogen forms a supercritical fluid. Supercritical fluids always form monolayers on surfaces, irrespective of their porosities.[13] Therefore a Type I isotherm was observed for **13b** (Figure 4.7). A hysteresis on desorption is noticeable and as in the case of **14a**, kinetic studies (Figure 4.8) eliminated the possibility that this results from a 'kinetic trapping effect'.

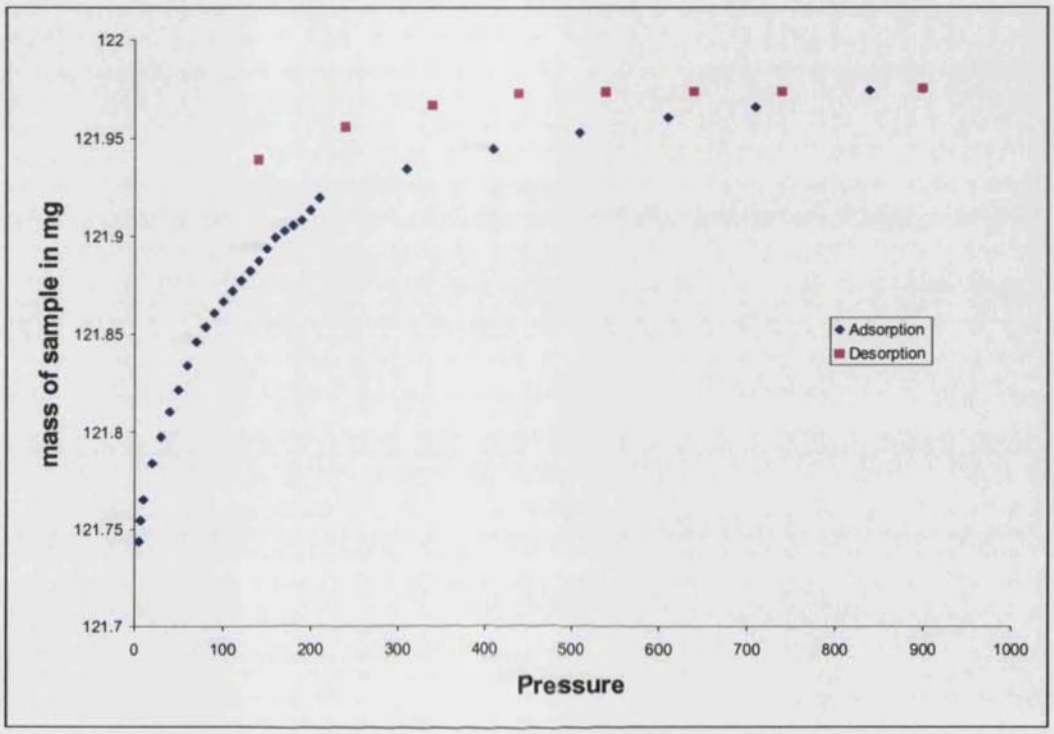

Graph 4.7. H_2 isotherms for **13b**.

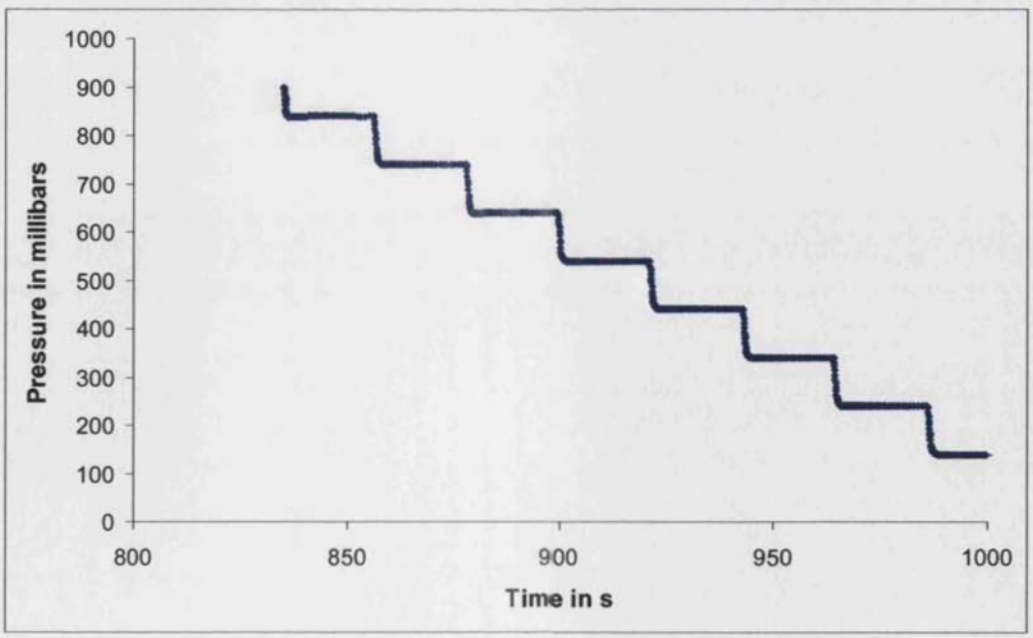

Figure 4.8. Plot of pressure against time for the H_2 desorption steps of **13b**.

13b is a fine powder and thus the structure of this compound could not be characterised by single crystal X-ray crystallography. Thus a direct comparison of the structure of the pores before and after adsorption is not possible.

13b was also analysed using krypton. For this particular system, the ASAP machine can only analyse adsorption within the pressure range of 0.1-0.5 millibars. The points of the isotherm of **13b** in this particular relative pressure region form a straight line and thus no further results could be extrapolated from this measurement.

4.4 Conclusions

The stability of $\{[Cd_3(tph)_3(DEF)_2]\}_\infty$ **(13)** and $\{[Cd_3(bpdc)_3(DMF)_2]\}_\infty$ **(14)** towards guest removal was analysed in Chapter 3 while the gas adsorption properties of $\{[Cd_3(tph)_3]\}_\infty$ **(13b)** and $\{[Cd_3(bpdc)_3]\}_\infty$ **(14a)** were discussed in this chapter.

13b and **14a** were found to have BET surface areas of 3.99 m^2/g and 21.75m^2/g respectively. The adsorption and desorption pathways for both compounds could be repeated several times without altering the framework.

The surface areas of **13b** and **14a** are very small when compared to other metal organic frameworks (Chapter 1). The amount of gases adsorbed by the two mentioned compounds is relatively small and thus **13b** and **14a** are not good candidates for gas storage materials.

The nitrogen molecules fill the inter-sheet spaces rather than the triangular pores of **14a**. The reason why this happens needs to be investigated further.

4.5 Further work

Nitrogen sorption experiments should also be carried out on a fresh sample of **14**. This compound should also exhibit interlayer adsorption properties. If the crystals are still intact after the adsorption process, then analysis by X-ray crystallography must reveal the way the adsorbent molecules pack in between the layers of the framework

The adsorption of ethene by **14a** can also be investigated. If **14a** is proved to store ethene reversibly, the hydrogenation catalytic abilities of the network can then be carried out. The catalytic abilities can be tested by exposing the network to a mixture of ethene and hydrogen and analysing the product gas mixture by GC/MS.

References:

1. T.J.Barton; L.M.Bull; W.G.Klemperer; D.A.Loy; B.McEnaney; M.Misono; P.A.Monson; G.Pez; G.W.Scherer; J.C.Vartuli; O.M.Yaghi, *Chem.Mater.* **1999,** 11, 2633.
2. D.Nicholson; N.G.Parsonage, *Computer Simulation and the Statistical Mechanics of Adsorption.* ed.; Academic press.: London., 1982; 1.
3. A.J.Fletcher; K.M.Thomas; M.J.Rosseinsky, *J.Sol.State.Chem.* **2005,** 178, 2491.
4. D.Li; K.Kaneko, *J.Phys.Chem.B.* **2000,** 104, 8940.
5. S.S.Y.Chui; S.M.F.Lo; J.P.H.Charmant; A.G.Orpen; I.D.Williams, *Science* **1999,** 283, 1148.
6. S.I.Noro; S.Kitagawa; M.Kondo; K.Seki, *Angew.Chem.Int.Ed.* **2000,** 39, 2081.
7. M.Kondo; T.Okubo; A.Asami; S.I.Noro; T.Yoshitomi; S.Kitagawa; T.Ishii; H.Matsuzaka; K.Seki, *Angew.Chem.Int.Ed.* **1999,** 38, 140.
8. M.Kondo; T.Yoshitomi; K.Seki; H.Matsuzaka; S.Kitagawa, *Angew.Chem.Int.Ed.* **1997,** 36, 1725.
9. M.Eddaoudi; J.Kim; N.L.Rosi; D.Vodak; J.Wachter; M.O.Keeffe; O.M.Yaghi, *J.Am.Chem.Soc.* **2002,** 295, 469.
10. K.Seki, *Langmuir* **2002,** 18, 2441.
11. K.Seki, *Chem.Commun.* **2001,** 16, 1496.
12. IUPAC., *Manual of symbols and terminology. Pure.Appl.Chem.* **1972,** 31, 578.
13. K.S.W.Sing; D.H.Everett; R.A.W.Haul; L.Moscou; R.A.Rierotti; J.Rouquerol; T.Siemieniewska, *Pure Appl. Chemistry* **1985,** 57, 603.
14. S.Brunauer; L.S.Deming; W.E.Deming; E.Teller, *J.Am.Chem.Soc.* **1940,** 62, 1723.
15. I.Langmuir, *J.Am.Chem.Soc.* **1915,** 37, 1139.
16. I.Langmuir, *J.Am.Chem.Soc.* **1918,** 40, 1361.
17. I.Langmuir, *J.Am.Chem.Soc.* **1913,** 35, 931.
18. P.W.Atkins; J.dePaula, *Physical chemistry.* 7th. ed.; Oxford Uni.Press.: Oxford., 2002; p 992.
19. J.H.deBoer. In *The Structure and Properties of Porous Materials.*, Proceedings of the Tenth Symposium of the Colston Research Society., University of Bristol., 24th-27th March., 1958; D.H.Everett; F.S.Stone, Butterworths scientific publications.: University of Bristol., 1958; p 68-94.
20. X.Zhao; B.Xiao; A.J.Fletcher; K.M.Thomas; D.Bradshaw; M.J.Rosseinsky, *Science* **2004,** 306, 1012.

Chapter 5 Networks from bis-β-diketonate ligands

5.1 Introduction

In the field of metal organic frameworks, the most frequently used ligands are dicarboxylates. As has been illustrated in Chapters 1, 2 and 3, the success of dicarboxylates is due to a number of facts. The dicarboxylate ligands bind to a wide range of metal cations to form neutral networks. As previously discussed, dicarboxylates have a variety of binding modes and also have the ability to form Secondary Building Units (SBUs), which provide networks with additional stability towards the loss of solvent molecules, as well as preventing interpenetration.

The major objective of the research in this chapter was to find a family of ligands that share similar properties to dicarboxylates and hence use them to form networks in an analogous manner. One homologous family of compounds that are good candidates to fulfil this function are β-diketonate ligands. This will be illustrated through examples from the literature using 2,4-pentanedione (Hacac), which is the simplest member of the family.

5.1.1 2,4-pentanedionate (acac⁻) complexes with different metals

On deprotonation, 2,4-pentanedione (Hacac) forms complexes with most metal cations. Some examples include complexes with *p*-block metals such as $Al(acac)_3$,[1] $Ga(acac)_3$,[2] $Sn(acac)_2$,[3] transition metals such as $Fe(acac)_3$,[4] $Zr(acac)_4 \cdot 10H_2O$,[5] $[Co(acac)_2]_4$,[6] $[Ni(acac)_2]_3$[7] and lanthanides such as $La(acac)_3 \cdot 3H_2O$.[8]

Different approaches have been employed for the synthesis of metal β-diketonate complexes but usually the preferred method includes direct metal-ligand complexation, using metal nitrates or sulphates as starting materials. The metal salts are usually dissolved together with the ligand while a suitable base is left to diffuse into the solution to deprotonate the ligand and initiate the formation of the complexes.

Two other starting materials that have been used are halide and carbonyl metal complexes, but more drastic conditions are required to replace halides and carbonyls by the

β-diketonate ligands. A general experimental procedure for the preparation of metal-acac complexes from the latter two starting metal compounds involves the reflux of the metal salts with Hacac in a suitable solvent. The different synthetic routes for the preparation of metal-diketonate complexes have been summarised by Mehrotra.[2]

5.1.2 Charges on the resulting metal-acac complexes

In order to form complexes, Hacac ligands must be deprotonated first. This results in an anionic species with the negative charge being stabilised across both the oxygen atoms and the three adjoining carbons, via resonance (Figure 5.1). When the β-diketonate ligands are coordinated to cationic metals, the overall charges on the metal and ligand are balanced, leading to the formation of neutral complexes. As discussed previously, this is a desirable feature of networks because it avoids the inclusion of counter ions.

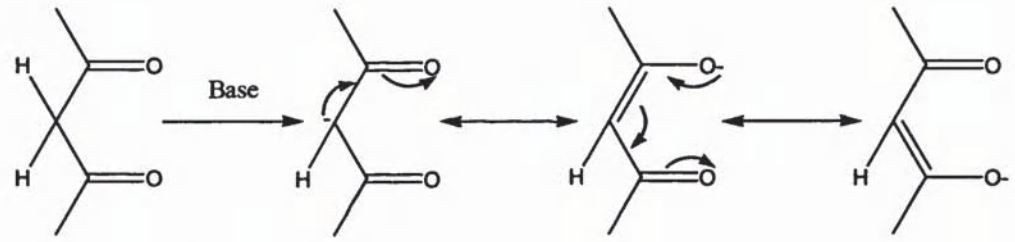

Figure 5.1. Resonance structures of 2,4-pentanedionate.

5.1.3 Stability of the metal-ligand complexes

It is important that the complexes formed between the β-diketonates and the metals will be of reasonable stability so that the overall networks will be robust. The ligand 2,4-pentanedionate has been reported to form quite robust and stable complexes with a wide range of metals. The stability of some of these complexes has been compared to the aromatic stability found in aromatic six-membered rings such as benzene.[9]

5.1.4 Ability of β-diketonate ligands to form Secondary Building Units (SBUs)

An important milestone in the field of metal organic frameworks was the discovery of SBUs. Carboxylates are renowned for forming SBUs and this feature is potentially shared by β-diketonates. For example, in the complex $[Co(acac)_2]_4$[6] the oxygen

atoms of the β-diketonato ligands adopt three different binding modes. In one mode both the oxygen atoms of the β-diketonato group coordinate to one metal such as in the case of O(1) and O(2) (Figure 5.2). The second binding mode is observed by O(3) and O(4) and consists of one oxygen atom O(3), that bridges to two metal centres while the remaining oxygen atom, O(4) binds to one metal. The last binding mode observed in $[Co(acac)_2]_4$ is represented by O(5) and O(6) where both the oxygen atoms bridge between two metal centres (Figure 5.2). Similar binding modes were observed in $[Ni(acac)_2]_3$.[7] If the latter two binding modes are extended into networks, the [M(μ-L)] motif will act as an SBU.

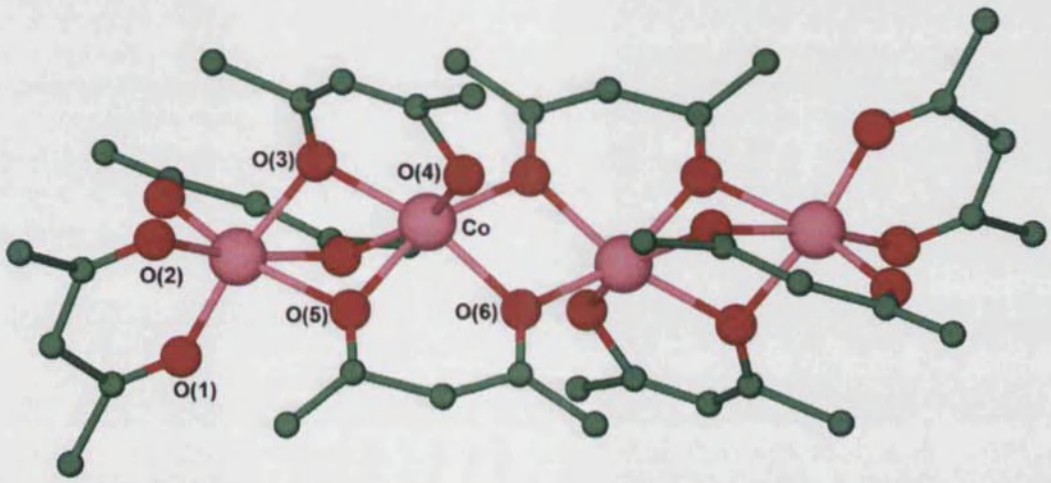

Figure 5.2. The structure of $[Co(acac)_2]_4$.[6] RES file obtained from the CSD.

5.1.5 Complexes from bis-β-diketonate ligands

Various bis-β-diketones have been synthesised[10-12] but only rarely have they been used in the formation of metal organic frameworks.

One example where a bis-β-diketonate ligand was used to form discrete complexes is $Co_4(tae)_4(dpa)_4$[13] (H_2tae = 3,4-diacetyl-2,5-dioxohexane, dpa = di-2-pyridylamine). The authors used a 1:1 mixture of di-2-pyridylamine (dpa) and 3,4-diacetyl-2,5-dioxohexane (Figure 5.3a). The amine acted as both a base and a ligand. The cobalt adopted an octahedral geometry with the coordinated base acting as a terminating group. Overall the complex forms square units with the formula $Co_4(tae)_4(dpa)_4$.

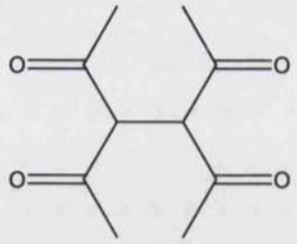

Figure 5.3a. 3,4-diacetyl-2,5-dioxohexane (H_2tae).

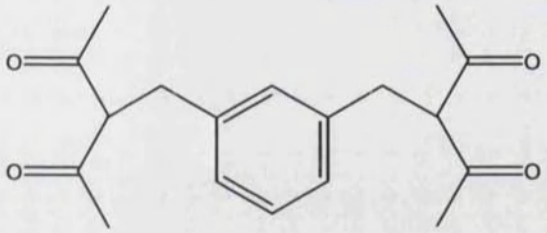

Figure 5.3b. 3,3'-(1,3-phenylenedimethylene)di-2,4-pentanedione.

Two further examples of molecular squares obtained from copper(II) and a bis-β-diketonate ligand are those reported by Maverick et *al*[14] and Bradbury et *al.*[15] The ligands used in the formation of these complexes are 3,3'-(1,3-phenylenedimethylene)di-2,4-pentanedione (Figure 5.3b) and 3,3'-(2,7-naphthalenediyldimethylene)di-2,4-pentanedione. The discrete molecules obtained from 3,3'-(1,3-phenylenedimethylene)di-2,4-pentanedionate consist of two copper centres bridged by two ligands (Figure 5.4). The metal centres adopt a square planar geometry but when nitrogen-containing bases were added, the bases coordinated to the copper centres to give square pyramidal geometry about the metal centre.[14, 15]

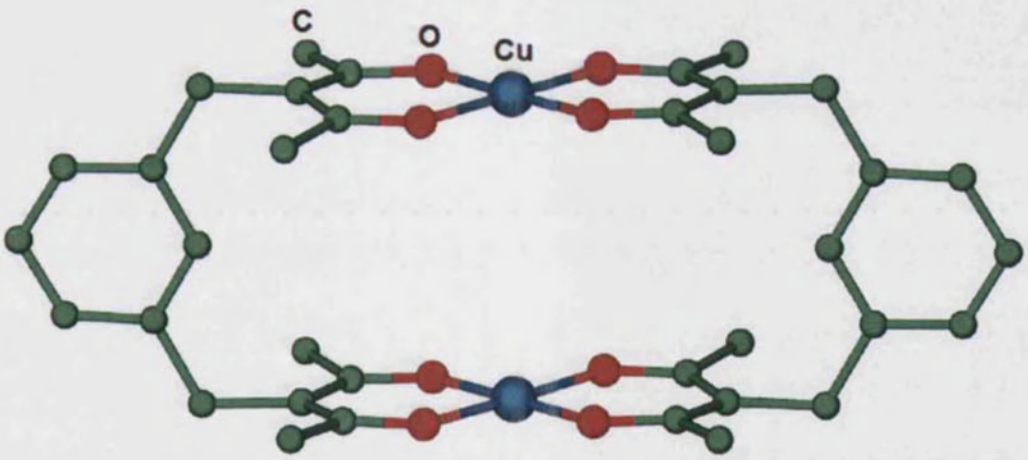

Figure 5.4. Dimeric complex of (3,3'-[1,3-phenylenedimethylene]di-2,4-pentanedionato)copper(II).

Bailar and Oh[16] studied the reactions of several bis-β-diketones such as, 3,4-diacetyl-2,5-dioxohexane (H_2tae), 3,3'-(1,4-phenylenedimethylene)di-2,4-pentanedione and 3,6-diacetyl-2,7-dioxooctane (Figures 5.5a and 5.5b), with different metal salts. They used three different ways to form networks, namely:

a) Direct network formation by mixing metal salt solutions to solutions containing bis-β-diketonate ligands in the presence of a base.

b) Solid phase ligand replacement by heating $M(acac)_x$ with bis-β-diketones under an atmosphere of nitrogen.

c) Refluxing solutions of $M(acac)_x$ with bis-β-diketones in xylene or decalin.

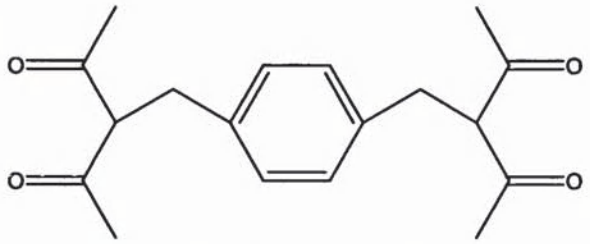

Figure 5.5a. 3,3'-(1,4-phenylenedimethylene)di-2,4-pentanedione.

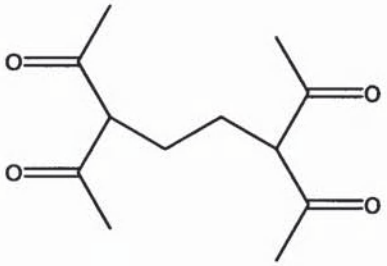

Figure 5.5b. 3,6-diacetyl-2,7-dioxooctane.

No crystal structures for any of the compounds formed were reported. Instead the compounds were characterised by microanalysis and thermogravimetric experiments. Based on these results, the authors proposed three different structures (Figures 5.6a- 5.6c).

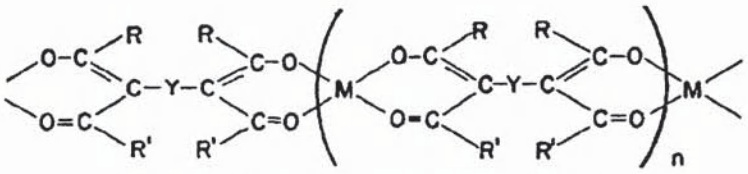

Figure 5.6a.[16] Infinite 1-D chain network (n > 1).

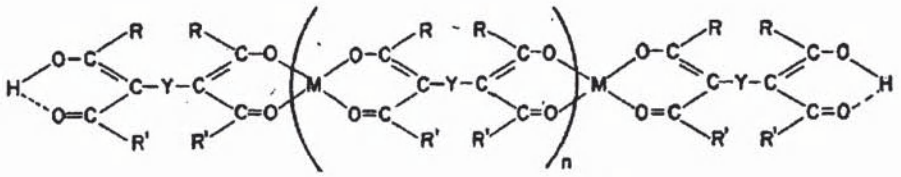

Figure 5.6b.[16] Finite L-M-L chains (n > 1).

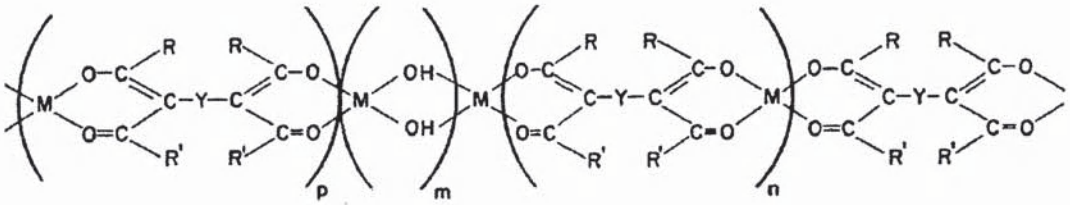

Figure 5.6c.[16] The third type of 1-D network (p, n and m > 1).

The first type of network consists of one dimensional infinite L-M-L chains (Figure 5.6a). The second type of compound consists of finite L-M-L chains with two

ligands at the end remaining uncoordinated and hence acting as terminal points to the polymer growth (Figure 5.6b). The third type of compound reported consists of three parts, namely two -L-M-L- moieties connected by bridging -M-$(OH)_2$-M- fragments as shown in Figure 5.6c.

Lindoy et *al*[17] reported complexes from a bis-β-diketonate ligand containing sulphur atoms. The ligand 3,3'-ethane-1,2-diylbissulfanyl-bis-pentane-2,4-dione (Figure 5.7) contains two 2,4-pentanedione moieties linked together at the 3-positions by an -S-CH_2-CH_2-S- bridge. On coordination to cobalt(II) and nickel(II), 3,3'-ethane-1,2-diylbissulfanyl-bis-pentane-2,4-dionate acted as a tetradentate ligand to give complexes of the formula $[ML(H_2O)_2]\cdot H_2O$[17] (M = Co(II) or Ni(II), L= 3,3'-ethane-1,2-diylbissulfanyl-bis-pentane-2,4-dionato). The keto groups coordinate to the metal centres via one oxygen atom, while the sulphur atoms also coordinate. Two water molecules which are coordinated to the metal centre act as terminal ligands (Figure 5.8). As stated in Section 5.1, the 2,4-pentanedionate ligand usually binds to metal centres via its two oxygen atoms. In this case however, steric factors prevent one of the oxygen atoms from each group from binding to the metal centres.

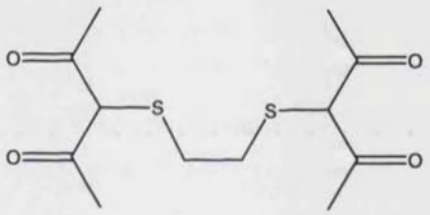

Figure 5.7. 3,3'-ethane-1,2-diylbissulfanyl-bis-pentane-2,4-dione.

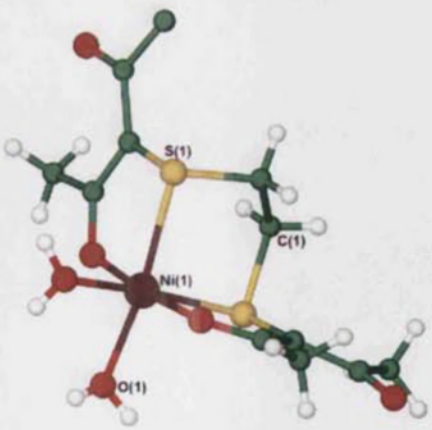

Figure 5.8. The structure of $[NiL(H_2O)_2]\cdot H_2O$ (L=3,3'-ethane-1,2-diylbissulfanyl-bis-pentane-2,4-dionate). Some hydrogen atoms are omitted for clarity.

Other networks incorporating an S-S linker between the β-diketone functional groups were obtained from 3,3'-monothio-di-2,4-pentanedionate and 3,3'-dithio-di-2,4-pentanedionate. Endo et *al*[18] reported ruthenium complexes including these two ligands. The authors took a different approach to the synthesis of the complexes. Instead of synthesising the bis-β-diketonate ligands and then reacting them with metal nitrates, they reacted $Ru(acac)_3$ with SCl_2 and S_2Cl_2 respectively. The proton at the 3-position of 2,4-pentanedionate was then substituted for the sulphur atoms which linked two $Ru(acac)_3$ complexes, affording $[Ru_2(acac)_4(L)]$ (L= 3,3'-mono/dithio-di-2,4-pentanedionate).

As demonstrated above, no network structures containing bis-β-diketonate ligands have previously been fully characterised. Consequently, the aim of the work of this chapter is to obtain and characterise networks from various bis-β-diketone ligands such as 3,4-diacetyl-2,5-dioxohexane (H_2tae), 3,3'-(1,4-phenylenedimethylene)di-2,4-pentanedione and 3,3'-dithio-di-2,4-pentanedione together with metal nitrates using an appropriate base such as Et_3N.

5.2 Results and Discussion

5.2.1 Synthesis of 3,4-diacetyl-2,5-dioxohexane (H_2tae)

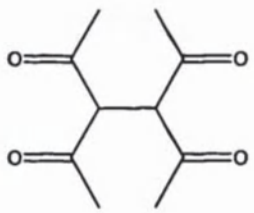

Figure 5.9. 3,4-diacetyl-2,5-dioxohexane (H_2tae).

The ligand 3,4-diacetyl-2,5-dioxohexane (H_2tae) (Figure 5.9) was synthesised following a literature procedure.[10] Sodium acetylacetonate (Na[acac]) was added to diethyl ether and the mixture was stirred vigorously with nitrogen bubbling through. A solution of iodine in diethyl ether was added dropwise to the stirred Na[acac] suspension and after the complete addition of iodine, the diethyl ether was left to evaporate overnight. The yellow solid obtained was washed with water and recrystallised from methanol to give H_2tae. The ligand was characterised by microanalysis, ^1H and ^{13}C NMR, mass spectrometry and X-ray crystallography.

5.2.2 Networks from $Zn(NO_3)_2 \cdot 6H_2O$ and 3,4-diacetyl-2,5-dioxohexane

In Chapter 2, networks formed from dicarboxylates and $Zn(NO_3)_2 \cdot 6H_2O$ were investigated. The same metal salt was used here in reactions with tae^{2-}. The networks formed were found to be dependent on the solvent mixture used.

$Zn(NO_3)_2 \cdot 6H_2O$ was dissolved in DMF and H_2tae was dissolved in $CHCl_3$. The two solutions were mixed together and Et_3N was allowed to diffuse into the solution. The white powder that precipitated out of solution was removed by filtration and the remaining solution was allowed to stand for several weeks after which colourless crystals were obtained. This compound was subsequently analysed by single crystal X-ray crystallography using synchrotron radiation. The crystalline compound was identified as $\{[Zn(tae)(DMF)] \cdot 0.6CHCl_3 \cdot 0.4DMF\}_\infty$ (**15**). Powder X-ray diffraction and C, H, N microanalysis revealed that the white powder that formed initially does not have the same chemical composition as the crystals. The initial powder did not dissolve in any solvent and thus could not be recrystallised or analysed by mass spectrosmetry, hence no further judgements could be made about the nature of this material.

The asymmetric unit of **15** (Figure 5.10) consists of one zinc atom, one tae^{2-} ligand, one coordinated DMF ligand and partial occupancy $CHCl_3$ and DMF guest molecules (Figure 5.10). The $CHCl_3$ and uncoordinated DMF molecules share the same site with site occupation factors of 0.6 and 0.4 respectively. Crystallographic data for **15** are given in Table 5.1.

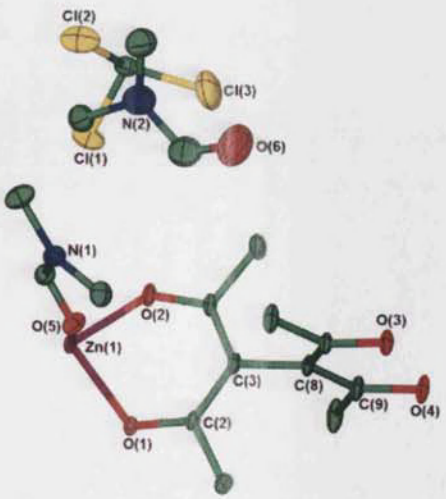

Figure 5.10. The asymmetric unit of **15** showing thermal ellipsoids at 30% probability. Hydrogen atoms are omitted for clarity.

Table 5.1. Crystallographic data for **15**.

Formula	$C_{14.80}H_{22.40}Cl_{1.8}N_{1.40}O_{5.40}Zn$
M	435.38
T/ K	150(2)
Crystal system	Orthorhombic
Space group, *Z*	*Pbca*, 8
a/ Å	13.2930(4)
b/ Å	16.1758(5)
c/ Å	18.5027(6)
α/ °	90
β/ °	90
γ/ °	90
U/ Å^3	3978.5(2)
Crystal size/ mm	0.06 x 0.05 x 0.03
Wavelength/ Å	0.69340
Theta range for data collected/ °	2.21 to 29.67
Reflections collected/ observed (>2σ)	21702, 4444
Data completeness	0.991
Max. and min. transmission	1.00 and 0.25
Goodness of fit F^2	1.042
Final *R* indices (I>2σ(I))	$R1$ = 0.0471 $wR2$ = 0.1240
R indices (all data)	$R1$ = 0.0656 $wR2$ = 0.1321
Largest diff. peaks and hole eÅ^{-3}	0.890 and -0.599

The zinc centres have distorted trigonal bipyramidal geometry with τ[19] being 0.76. The axial positions on the zinc centre are occupied by oxygen atoms, O(1) and O(3), from tae^{2-} ligands, while the equatorial positions are occupied by three oxygen atoms, O(2) and O(4) from two different tae^{2-} and O(5) from the coordinated DMF ligand (Figure 5.11). The bite angles for the tae^{2-} ligand are 88.54(7)° and 88.46(7)° (Table 5.3).

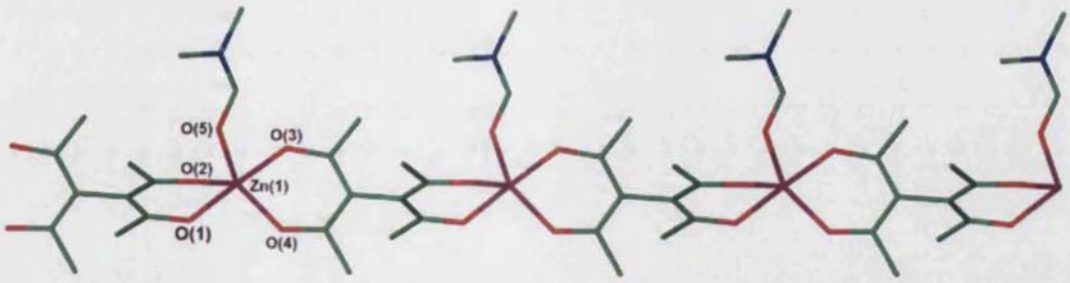

Figure 5.11. The 1-D chain of **15** as viewed down the *a* axis.

The zinc-oxygen bonds vary in length with two of these bonds, Zn(1)-O(2) and Zn(1)-O(4) being slightly shorter than the others (Table 5.2). The zinc-oxygen bond Zn(1)-O(5) from the coordinated DMF is longer than the zinc-oxygen bond lengths from the coordinated tae^{2-}.

Table 5.2. Selected bond lengths for **15**.[1]

Bond atoms	Distance/ Å
Zn(1)-O(1)	2.0172(16)
Zn(1)-O(2)	1.9705(19)
Zn(1)-O(3)#1	2.0160(17)
Zn(1)-O(4)#1	1.9721(17)
Zn(1)-O(5)	2.052(2)
O(1)-C(2)	1.274(2)
O(2)-C(4)	1.285(2)
O(3)-C(7)	1.276(2)
O(4)-C(9)	1.279(3)
O(5)-C(11)	1.238(3)
O(6)-C(15)	1.244(19)

Table 5.3. Selected bond angles for **15**.[1]

Atoms	Angle/ °
O(1)-Zn(1)-O(5)	88.28(8)
O(2)-Zn(1)-O(1)	88.54(7)
O(2)-Zn(1)-O(3)#1	94.98(7)
O(2)-Zn(1)-O(4)#1	130.72(9)
O(2)-Zn(1)-O(5)	105.15(8)
O(3)#1-Zn(1)-O(1)	176.39(7)
O(3)#1-Zn(1)-O(5)	91.54(8)
O(4)#1-Zn(1)-O(1)	88.65(7)
O(4)#1-Zn(1)-O(3)#1	88.46(7)
O(4)#1-Zn(1)-O(5)	123.92(9)
C(11)-O(5)-Zn(1)	124.63(19)
O(5)-C(11)-N(1)	124.7(3)
O(6)-C(15)-N(2)	123.6(14)

[1] Symmetry transformations used to generate equivalent atoms:
#1 -x+3/2,y-1/2,z

15 forms 1-D infinite chains (Figure 5.11) with the coordinated DMF molecules having an alternating arrangement along the 1-D chain (Figure 5.12). This is a result of the ligand conformation. Steric hindrance between the tae^{2-} methyl groups force the two diketonate groups in each ligand to be approximately perpendicular to one another.

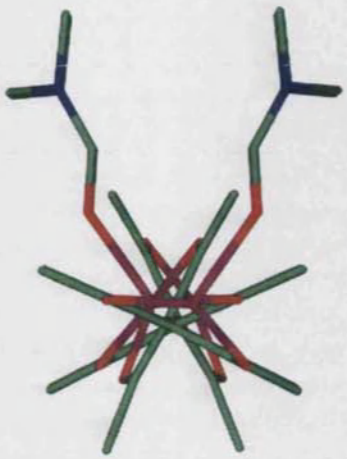

Figure 5.12. The 1-D chain of **15** as viewed down the b axis.

A similar reaction was undertaken with the $Zn(NO_3)_2 \cdot 6H_2O$ being dissolved in DMSO and the ligand H_2tae dissolved in MeOH. Et_3N vapour was left to diffuse into the solution. The white powder that precipitated out of solution was removed by filtration, and the filtrate was left to stand for several weeks, during which time colourless crystals were formed. Single crystal X-ray data were collected using synchrotron radiation and the compound was identified as $\{[Zn_3(tae)_3(MeOH)(DMSO)_{4.2}]0.8DMSO\}_\infty$ (**16**). The powder material that formed initially does not have the same formula as the crystals as indicated by microanalysis and powder diffraction experiments. As in the case of **15**, the powder was found to be insoluble in any solvent and thus could not be either recrystallised or successfully characterised by mass spectrometry.

The asymmetric unit of **16** (Figure 5.13) consists of three independent zinc centres, three tae^{2-} ligands, one coordinated methanol and five dimethylsulfoxide molecules. Crystallographic data for **16** are given in Table 5.4.

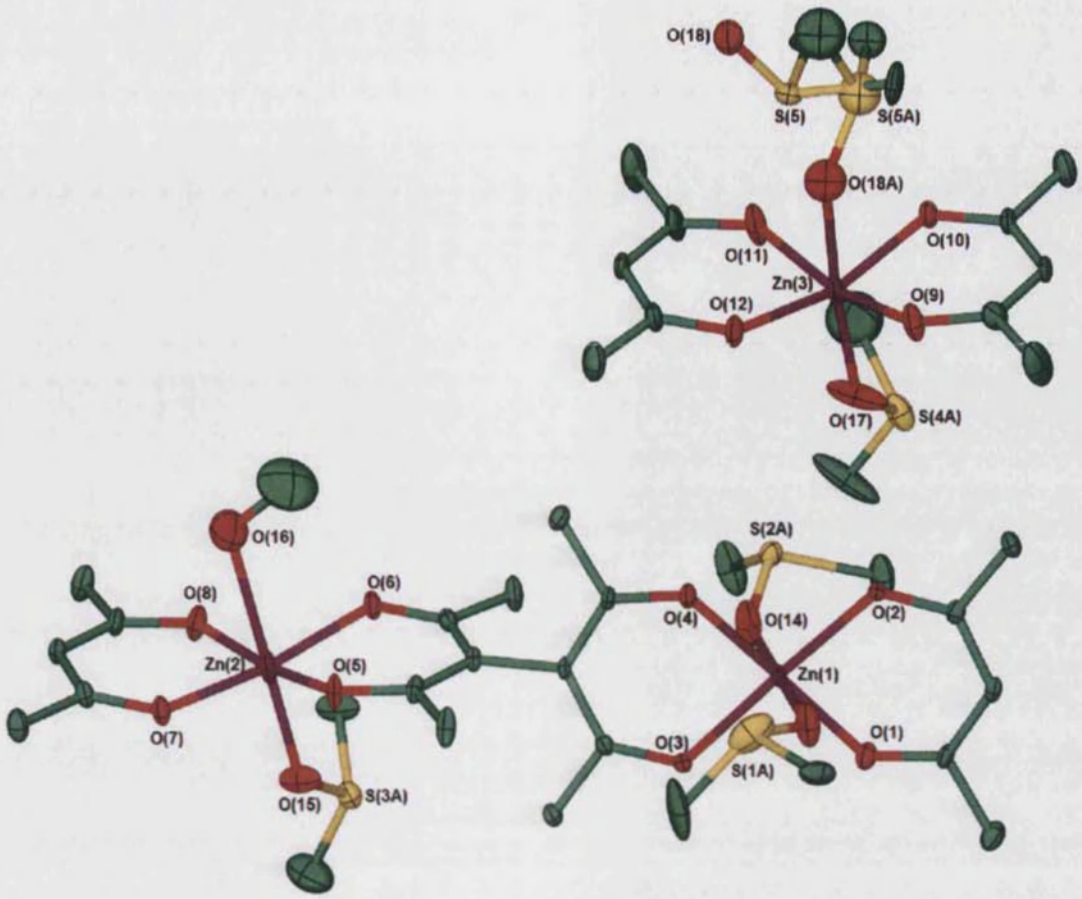

Figure 5.13. The asymmetric unit of **16** showing thermal ellipsoids at 30% probability. Hydrogen atoms are omitted for clarity. The partial DMSO ligands containing the sulphur atoms labelled S(1) to S(4) have been removed for clarity while both parts of the DMSO molecule labelled S(5) and S(5a) are shown.

Table 5.4. Crystallographic data for **16**.

Formula	$C_{41}H_{70}O_{18}S_5Zn_3$
M	1207.38
T/ K	150(2)
Crystal system	Orthorhombic
Space group, *Z*	*Pbca*, 8
a/ Å	16.3499(13)
b/ Å	15.4909(13)
c/ Å	42.062(3)
α/ °	90
β/ °	90
γ/ °	90
U/ Å^3	10653.3(15)

Crystal size/ mm	0.05 x 0.05 x 0.02
Wavelength/ Å	0.84590
Theta range for data collected/ °	4.26 to 31.95
Reflections collected/ observed (>2σ)	52160, 6391
Data completeness	0.988
Max. and min. transmission	0.96 and 0.94
Goodness of fit F^2	1.037
Final R indices (I>2σ(I))	$R1$ = 0.0707 $wR2$ = 0.1879
R indices (all data)	$R1$ = 0.1216 $wR2$ = 0.2197
Largest diff. peaks and hole eÅ^{-3}	1.135 and -1.129

Zn(1) and Zn(2) have both distorted octahedral geometry, but the coordination spheres of these metal centres differ. Both are coordinated to four oxygen atoms from two tae^{2-} ligands, but while the two remaining sites on Zn(1) are occupied by two oxygen atoms, O(13) and O(14), from two coordinated DMSO molecules, Zn(2) is coordinated to one DMSO oxygen atom O(15), and an oxygen, O(16), from a coordinated MeOH molecule. The coordination sphere of Zn(3) is populated by four oxygen atoms from two tae^{2-} ligands while an oxygen atom, O(17), from a coordinated DMSO molecule fills a fifth coordination site. The remaining sixth site is either left vacant or else occupied by an oxygen atom, O(18a), from a DMSO ligand. Thus, Zn(3) adopts two different geometries, distorted octahedral and distorted square pyramidal (τ^{19} = 0.003). The major geometry for this zinc atom is distorted square pyramidal as indicated by the site occupation factor of the coordinated DMSO fragment based on O(18A).

All the DMSO molecules are disordered over two sites. Four of the coordinated DMSO molecules, with the sulphur atoms labelled S(1)/ S(1A), S(2)/ S(2A), S(3)/ S(3A) and S(4)/ S(4A), have a site occupancy factor of 0.50 over each site. The fifth DMSO molecule with the sulphur atom labelled S(5)/ S(5A), is also disordered over two sites but in this case one fragment of the molecule, labelled S(5a), O(18a) is coordinated to the zinc centre, Zn(3), while the second position, labelled as S(5), O(18) remains uncoordinated (Figure 5.13). The site occupation factors are 0.20 for the coordinated fragment and 0.80 for the uncoordinated DMSO moiety.

All of the zinc-oxygen bonds involving the β-diketonate ligands are equivalent within experimental error (Table 5.5). Apart from Zn(3)-O(17) and Zn(2)-O(15), the zinc-oxygen bond lengths involving the coordinated DMSO ligands are significantly longer than the metal-β-diketonato bonds (Table 5.5). Zn(3)-O(18A) (2.43(13)Å) is significantly longer than the other Zn-O bonds but the 20% site occupancy of O(18A) makes this distance the least reliable. The bite angles of **16** are of comparable size to those of $\{[Zn(tae)(DMF)]\cdot 0.6CHCl_3\cdot 0.4DMF\}_\infty$ (**15**) (Tables 5.3 and 5.6 respectively).

Table 5.5. Selected bond lengths for **16**.

Bond atoms	Distance/ Å	Bond atoms	Distance/ Å
Zn(1)-O(1)	2.03(2)	Zn(3)-O(11)	2.01(2)
Zn(1)-O(2)	2.039(18)	Zn(3)-O(12)	1.99(2)
Zn(1)-O(3)	2.039(18)		
Zn(1)-O(4)	2.025(19)	Zn(1)-O(14)	2.18(2)
Zn(2)-O(5)	1.999(19)	Zn(1)-O(13)	2.20(2)
Zn(2)-O(6)	2.03(2)	Zn(2)-O(15)	2.12(3)
Zn(2)-O(7)	2.020(19)	Zn(3)-O(17)	2.05(3)
Zn(2)-O(8)	1.99(2)	Zn(3)-O(18A)	2.43(13)
Zn(3)-O(9)	1.98(2)		
Zn(3)-O(10)	2.00(2)	Zn(2)-O(16)	2.36(4)

Table 5.6. Selected bond angles for **16**.

Atoms	Angle/ °	Atoms	Angle/ °
O(1)-Zn(1)-O(2)	87.0(8)	S(1)-O(13)-Zn(1)	131.0(18)
O(4)-Zn(1)-O(3)	87.6(8)	S(1A)-O(13)-Zn(1)	126.0(17)
O(5)-Zn(2)-O(6)	87.6(8)	S(2)-O(14)-Zn(1)	128.0(18)
O(8)-Zn(2)-O(7)	88.9(8)	S(2A)-O(14)-Zn(1)	135(2)
O(9)-Zn(3)-O(10)	87.7(9)	S(3)-O(15)-Zn(2)	113.9(16)
O(12)-Zn(3)-O(11)	88.7(9)	S(3A)-O(15)-Zn(2)	133.0(16)
		S(4)-O(17)-Zn(3)	117(2)
O(14)-Zn(1)-O(13)	178.9(12)	S(4A)-O(17)-Zn(3)	135.9(19)
O(15)-Zn(2)-O(16)	170.4(12)	S(5A)-O(18A)-Zn(3)	133(8)
O(17)-Zn(3)-O(18A)	169(3)		

16 forms 1-D infinite chains along the *b* axis. Two types of chains are formed with one type consisting of alternating -Zn(1)-Zn(2)-Zn(1)- centres while the second type consists of -Zn(3)- centres only. The chains pack parallel to one another (Figure 5.14) with the chains consisting of -Zn(3)- units being sandwiched between two -Zn(1)-Zn(2)-Zn(1)- moieties.

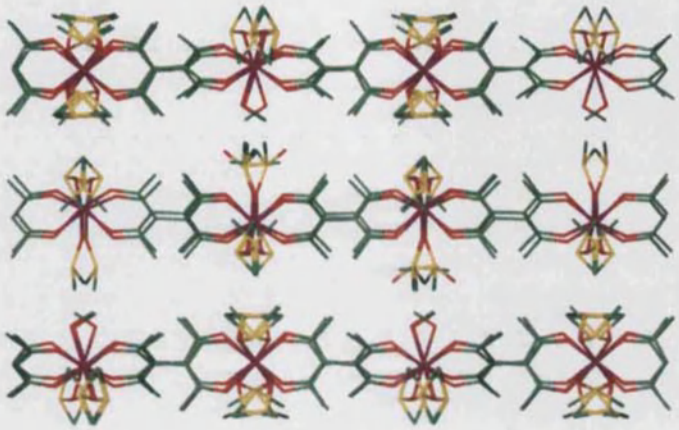

Figure 5.14. Packing of the 1-D chains in the structure of **16** as viewed down the *b* axis.

5.2.3 2-D networks and the formation of SBU from bis-β-diketonate ligands

A reaction between H_2tae and $Zn(NO_3)_2 \cdot 6H_2O$ was also carried out using methanol only instead of DMF/$CHCl_3$ as the solvent. In this case no powder was formed prior to the formation of the crystals. Two 2-D networks were obtained from this reaction. The compounds, **17** and **18**, formed simultaneously with the latter forming in minor quantities.

Although the crystals of **17** were not of good quality, the data collected using synchrotron radiation were good enough to establish the core structure of the network.

The core unit of **17** was found to be $\{[Zn_2(\mu\text{-tae})_2]\}_\infty$ (Figure 5.15). Two different zinc centres and four half tae^{2-} ligands make up the asymmetric unit. Residual electron density suggest that there might be two additional atoms with the distances from the zinc centres close enough for bonding to take place. Results from microanalysis suggest that these atoms can be assigned to be oxygen atoms from coordinated water molecules to give an overall formula of $\{[Zn_2(\mu\text{-tae})_2(OH_2)_2]\}_\infty$

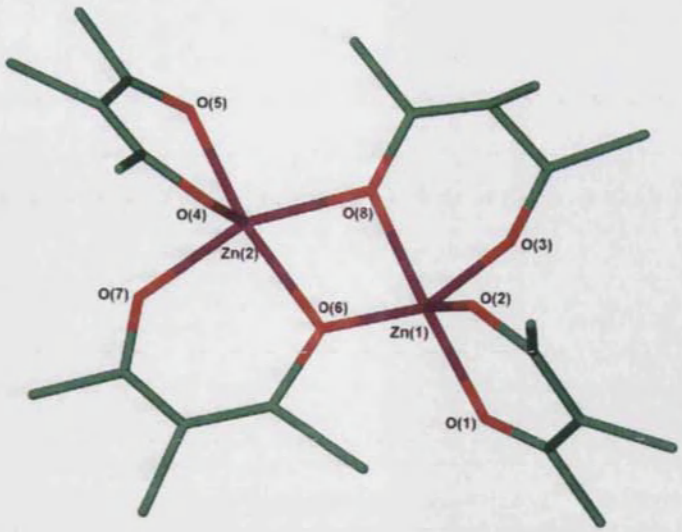

Figure 5.15. Core unit of **17**.[II]

The oxygen atoms of the diketonate groups adopt two different binding modes. In the first case one of the oxygen atoms bridges between two different metal centres as can be observed from O(8) and O(6) in Figure 5.15, while the second oxygen atom of the same diketonate group coordinates to one metal centre only. This binding mode is similar to the chelating bridging bidentate mode of the dicarboxylates described in Chapters 2 and 3. The second binding mode adopted by the diketonate groups in **17** is a bidentate mode where both oxygen atoms bind to one metal centre as in the case of O(1) and O(2) (Figure 5.15). The tae^{2-} ligands of **17** link the two zinc centres together to form a dimer, which because of the bridging nature of the tae^{2-} ligands can be considered to be an SBU. This bridging motif has been observed in complexes of 2,4-pentanedionate such as $[Co(acac)_2]_4$[6] and $[Ni(acac)_2]_3$,[7] as described in Section 5.1.

The overall network of **17** consists of 2-D sheets which are composed of distorted rectangular motifs based on four linked SBUs. The rectangular motifs alternate at approximately 90° with respect to one another to form a 'Basket-Weave network' structure (Figure 5.16).[20]

[II] Due to the low quality data, only the heavy atoms could be modelled anisotropically. The positions of the oxygen atoms from the coordinated water molecules could not be determined accurately.

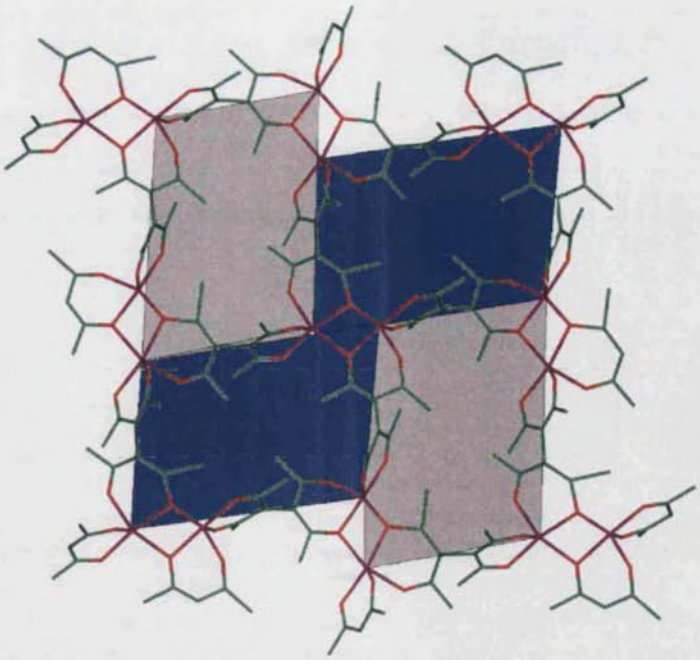

Figure 5.16. The 'Basket-Weave' (4,4) network of **17**.

The crystals of **18** were plates as opposed to the round crystals of **17**. **18** was also characterised by single crystal X-ray crystallography using synchrotron radiation. The asymmetric unit of $\{[Zn_2(\mu\text{-tae})_2(MeOH)_2]\cdot 2MeOH\}_\infty$ (**18**) (Figure 5.17) consists of two zinc atoms, two tae^{2-} ligands, two coordinated and two uncoordinated methanol molecules. The oxygen atoms of the uncoordinated methanol molecules are disordered over two positions with site occupation factors of 0.50 each. Crystallographic data for compound **18** are given in Table 5.7.

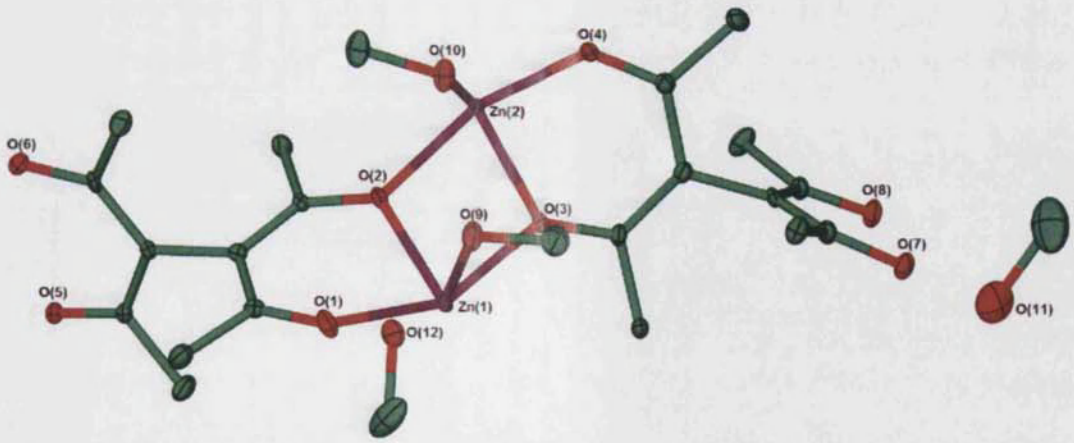

Figure.5.17. The asymmetric unit of **18** showing thermal ellipsoids at 30% probability. Only one position of the oxygen atoms of the uncoordinated MeOH molecules is shown and the hydrogen atoms are omitted for clarity.

Table 5.7. Crystallographic data for **18**.

Formula	$C_{24}H_{38}O_{12}Zn_2$
M	649.28
T/ K	150(2)
Crystal system	Monoclinic
Space group, *Z*	$P2_1/c$, 2
a/ Å	10.470(3)
b/ Å	13.926(3)
c/ Å	10.476(3)
α/ °	90
β/ °	109.048(4)
γ/ °	90
U/ Å^3	1443.9(6)
Crystal size/ mm	0.03 x 0.03 x 0.02
Wavelength/ Å	0.69040
Theta range for data collected/ °	3.47 to 26.67
Reflections collected/ observed (>2σ)	9539, 4556
Data completeness	0.993
Max. and min. transmission	0.96 and 0.94
Goodness of fit F^2	0.954
Final *R* indices ($I>2\sigma(I)$)	$R1 = 0.0718$ $wR2 = 0.1659$
R indices (all data)	$R1 = 0.0896$ $wR2 = 0.1741$
Largest diff. peaks and hole eÅ^{-3}	2.204 and -0.928

There are two crystallographically different zinc centres in **18** and both have a distorted octahedral geometry. The coordination spheres of both metal centres are occupied by six oxygen atoms, five from tae^{2-} ligands and one from a coordinated methanol molecule.

The binding modes of the tae^{2-} in **18** are similar to those found in **17**. The core of **18** consists of dimeric {[Zn_2(μ-tae)$_2$(MeOH)$_2$]} units. The network formed by **18** is similar to that of **17** and consists of 2-D 'Basket-Weave' sheet (Figure 5.18).

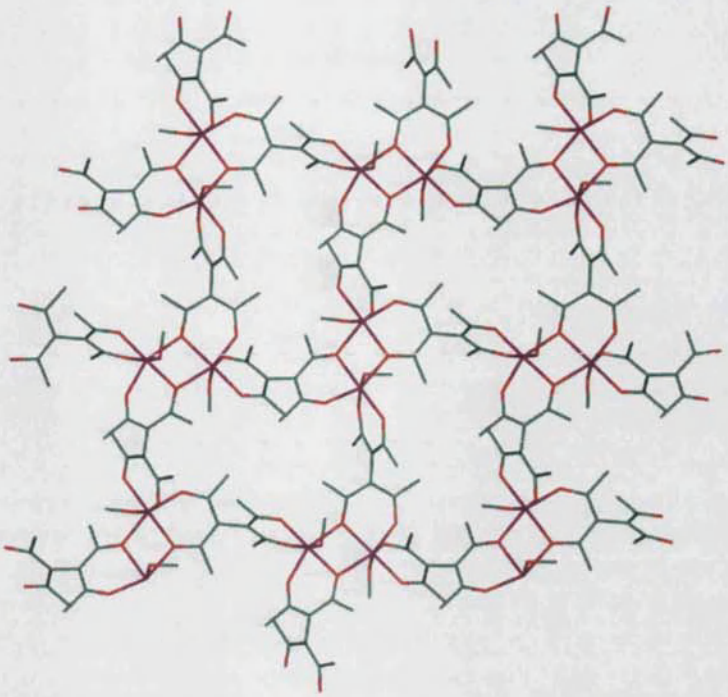

Figure 5.18. The 'Basket-Weaved' network of **18** as viewed perpendicular to the (0 0 1) plane.

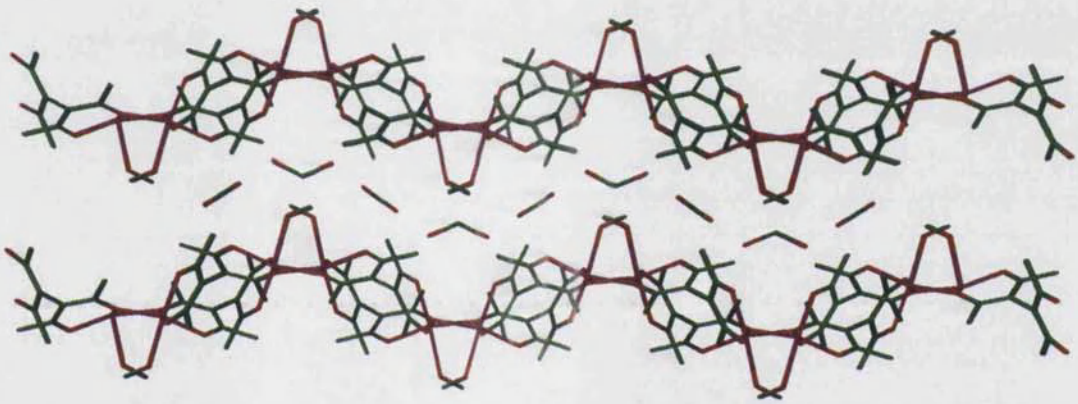

Figure 5.19. Two 2-D sheets of **18** packed parallel to one another with the guest methanol molecules packing in between the sheets.

The sheets pack parallel to one another with four disordered methanol guest molecules, two from each formula unit per sheet, packing in between the sheets (Figure 5.19). The methanol guest molecules play an important role in the overall packing of the sheets. Measurement of the distance between the methanolic hydrogen and the ligand oxygen atoms indicate the presence of strong hydrogen bonding (Table 5.8).

The hydrogen atoms of the coordinated methanol molecules could not be found in the X-ray analysis. Measurement of the distances between the oxygen atoms O(9) and

O(10) (2.680(9)Å), however indicates the possibility of strong hydrogen bonding between the two. The guest methanol with the oxygen atom O(12) is hydrogen bonded to O(9) of the coordinated methanol molecule. The distance between the latter two oxygen atoms being 2.784(10) Å. H(12) and H(12A) are hydrogen bonded to the ketonate atoms O(4) and O(1) respectively from two different sheets, thus holding the two sheets together (Figure 5.20). The hydrogen atoms, H(11) and H(11D) from the guest methanol molecules are bound to the ketonate oxygen atoms O(7) and O(6) from one sheet only (Figure 5.20).

Table 5.8. Hydrogen bonds with H··A < r(A) +2.000Å and <DHA> 110° for **18**.[III]

D-H	d(D-H)	d(H··A)	<DHA	d(D··A)	A
O(11)-H(11)	0.840	1.99	164	2.809	O(7)
O(11A)-H(11D)	0.840	2.01	169	2.839	O(6)#1
O(12)-H(12)	0.840	2.03	158	2.822	O(4)
O(12A)-H(12A)	0.840	1.94	164	2.755	O(1)

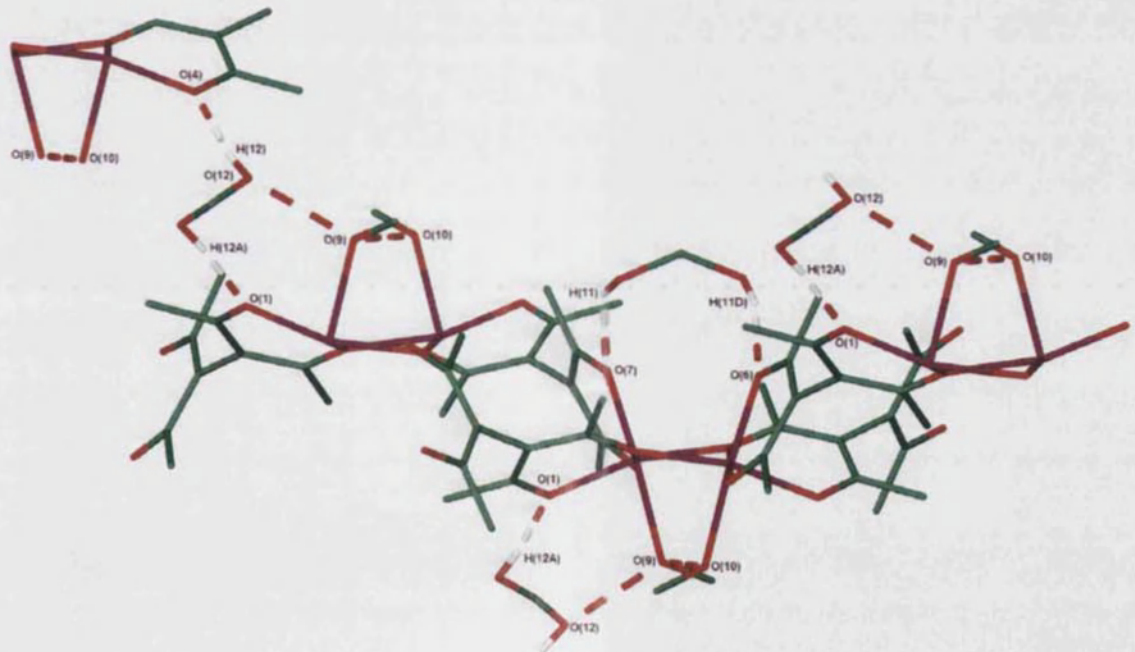

Figure 5.20. The hydrogen bonding present in **18**.

The zinc-oxygen bond lengths of **18** range from 2.025(6) Å to 2.277(6) Å (Table 5.9). The oxygen atoms that bridge between two metal centres such as O(2) and O(3)

[III] Symmetry transformations used to generate equivalent atoms:
#1 x+1,y-1,z+1

(Figure 5.17) form longer bonds to the zinc centres than the oxygen atoms that bind to one metal centre only such as O(1) and O(4). The latter bond lengths are comparable to the bridging bidentate zinc-oxygen bond lengths of **15** and **16**. Also noteworthy is the difference between the zinc-methanol and the zinc-tae^{2-} bond lengths. The zinc-oxygen bonds from the methanol are slightly longer than the zinc-tae^{2-} bonds. The bite angles of the tae^{2-} ligand found in **18** (Figure 5.17) range from 82.9(2)° to 88.3(2)° (Table 5.10). The bite angles of the chelating bridging bidentate O(1)-Zn(1)-O(2) and O(3)-Zn(2)-O(4) (Figure 5.17) are smaller than the bite angles of the bridging bidentate O(5)#2-Zn(2)-O(6)#2 and O(8)#1-Zn(1)-O(7)#1 while the bridging bidentate angles for **18** are comparable to similar bite angles of compounds **15** and **16** (Tables 5.3 and 5.6 respectively).

Table 5.9. Selected bond lengths for **18**.[IV]

Bond atoms	Distance/ Å	Bond atoms	Distance/ Å
Zn(1)-O(1)	2.051(6)	Zn(2)-O(2)	2.082(6)
Zn(1)-O(2)	2.100(5)	Zn(2)-O(3)	2.099(5)
Zn(1)-O(3)	2.081(6)	Zn(2)-O(4)	2.045(6)
Zn(1)-O(7)#1	2.025(6)	Zn(2)-O(5)#2	1.994(5)
Zn(1)-O(8)#1	1.989(5)	Zn(2)-O(6)#2	2.032(6)
Zn(1)-O(9)	2.277(6)	Zn(2)-O(10)	2.268(6)
O(9)--O(10)	2.680(9)	O(9)--O(12)	2.784(10) Å

Table 5.10. Selected bond angles for **18**.[IV]

Atoms	Angle/ °	Atoms	Angle/ °
O(1)-Zn(1)-O(2)	82.9(2)	O(8)#1-Zn(1)-O(7)#1	88.3(2)
O(4)-Zn(2)-O(3)	83.0(2)	Zn(2)-O(2)-Zn(1)	102.4(2)
O(5)#2-Zn(2)-O(6)#2	88.2(2)	Zn(1)-O(3)-Zn(2)	102.4(2)

The SBU observed in **18** is similar to that of **17** as is the 2-D 'Basket-Weave' network of these compounds.

[IV] Symmetry transformations used to generate equivalent atoms:
#1 -x+2,y+1/2,-z+1 #2 -x+1,y-1/2,-z

5.3 Comparison between the reactions of 1,3-diacetyl-3,5-dioxohexane with $Cd(NO_3)_2 \cdot 4H_2O$ and $Zn(NO_3)_2 \cdot 6H_2O$.

As illustrated in Chapter 2, $Cd(NO_3)_2 \cdot 4H_2O$, like $Zn(NO_3)_2 \cdot 6H_2O$, also forms networks with dicarboxylates. Consequently, the reactions of $Cd(NO_3)_2 \cdot 4H_2O$ with H_2tae in the presence of a base were studied.

5.3.1 Reactions of H_2tae with $Cd(NO_3)_2 \cdot 4H_2O$

The dependency of the reaction of H_2tae and $Cd(NO_3)_2 \cdot 4H_2O$ on the solvent mixture in the presence of Et_3N was studied. The only crystals of sufficient quality for characterisation by single crystal X-ray diffraction were obtained when methanol was used as the only solvent. The formula of the compound obtained from this reaction was found to be $\{[Cd_2(\mu\text{-tae})_2(OH_2)_2] \cdot 2.5H_2O\}_\infty$ (**19**).

The asymmetric unit of **19** (Figure 5.21) consists of two cadmium centres, two tae^{2-} ligands, two coordinated water molecules, one full and two partial water solvent molecules. The partial guest water molecules, O(12) and O(13) have site occupancy factors of 0.75 each. Crystallographic data for **19** are given in Table 5.11.

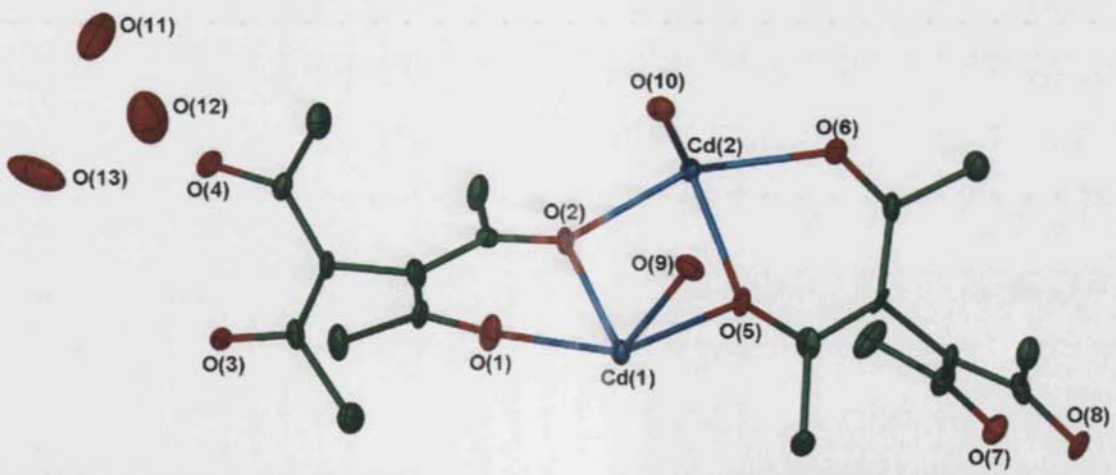

Figure 5.21. The asymmetric unit of **19** showing thermal ellipsoids at 30% probability. Hydrogen atoms are omitted for clarity.

Table 5.11. Crystallographic data for **19**.

Formula	$C_{20}H_{33}Cd_2O_{12.50}$
M	698.26
T/ K	150(2)
Crystal system	Orthorhombic
Space group, *Z*	$P2_12_12_1$, 4
a/ Å	11.9762(10)
b/ Å	14.2223(12)
c/ Å	15.5903(14)
α/ °	90
β/ °	90
γ/ °	90
U/ Å^3	2655.5(4)
Crystal size/ mm	0.02 x 0.02 x 0.01
Wavelength/ Å	0.69340
Theta range for data collected/ °	2.09 to 24.07
Reflections collected/ observed (>2σ)	10941, 4505
Data completeness	0.993
Goodness of fit F^2	1.003
Final *R* indices ($I>2\sigma(I)$)	$R1 = 0.0495$ $wR2 = 0.0973$
R indices (all data)	$R1 = 0.0876$ $wR2 = 0.1120$
Largest diff. peaks and hole eÅ^{-3}	1.175 and -0.815

There are two crystallographically different cadmium centres, Cd(1) and Cd(2). Both metal centres adopting a distorted octahedral geometry. The coordination sphere of Cd(1) is populated by five oxygen atoms from tae^{2-} ligands and one oxygen atom, O(9), from a water molecule. The coordination sphere of Cd(2) is also coordinated to vie oxygen atoms from tae^{2-} ligands and a water oxygen atom, O(10).

The tae^{2-} ligands adopts two different binding modes, namely, chelating bridging bidentate and bidentate. The two bite angles of the mentioned binding modes are of different magnitudes (Table 5.13). The chelating bridging bidentate angles, O(5)-Cd(2)-O(6) and O(1)-Cd(1)-O(2), are smaller than the bridging bidentate angles, O(3)-Cd(2)-O(4)

and O(7)-Cd(1)-O(8) (Figure 5.22). This difference was also observed in $\{[Zn_2(\mu\text{-tae})_2(MeOH)_2]\cdot 2MeOH\}_\infty$ (**18**).

Table 5.12. Selected bond lengths and hydrogen bond distances for **19**.[v]

Bonding atoms	Distance/ Å
Cd(1)-O(1)	2.215(6)
Cd(1)-O(2)	2.277(7)
Cd(1)-O(5)	2.306(6)
Cd(1)-O(7)#1	2.220(6)
Cd(1)-O(8)#1	2.209(8)
Cd(1)-O(9)	2.309(7)
Cd(2)-O(2)	2.299(6)
Cd(2)-O(3)#2	2.228(7)
Cd(2)-O(4)#2	2.222(7)

Bonding atoms	Distance/ Å
Cd(2)-O(5)	2.270(7)
Cd(2)-O(6)	2.231(7)
Cd(2)-O(10)	2.323(6)
O(3)···O(9)	2.653(10)
O(7)···O(10)	2.599(9)
O(8)···O(11)	2.79(1)
O(9)···O(10)	2.84(1)
O(11)···O(12)	2.85(2)
O(12)···O(13)	2.74(2)

Table 5.13. Selected bond angles for **19**.[v]

Atoms	Angle/ °
O(1)-Cd(1)-O(2)	76.5(3)
O(4)#2-Cd(2)-O(3)#2	79.6(3)
O(6)-Cd(2)-O(5)	75.9(2)
O(8)#1-Cd(1)-O(7)#1	79.2(3)
Cd(1)-O(2)-Cd(2)	100.4(3)
Cd(2)-O(5)-Cd(1)	100.3(2)
O(1)-Cd(1)-O(9)	94.6(3)

Atoms	Angle/ °
O(2)-Cd(1)-O(9)	98.9(3)
O(5)-Cd(1)-O(9)	78.6(3)
O(7)#1-Cd(1)-O(9)	90.2(3)
O(2)-Cd(2)-O(10)	77.1(2)
O(3)#2-Cd(2)-O(10)	91.9(3)
O(5)-Cd(2)-O(10)	97.1(3)
O(6)-Cd(2)-O(10)	96.1(3)

Due to the bridging nature of the tae^{2-} oxygen atoms, the two cadmium centres are linked together into dimeric units which can be considered as an SBU (Figure 5.22). Overall the water molecules act as terminal points in the network of **19**, thus preventing the network growth in the third dimension. The gross structure consists of 2-D 'Basket-Weaved' sheets (Figure 5.23).

[v] Symmetry transformations used to generate equivalent atoms:
#1 -x+1 y-1/2 -z+1/2 #2 -x+2 y+1/2 -z+1/2

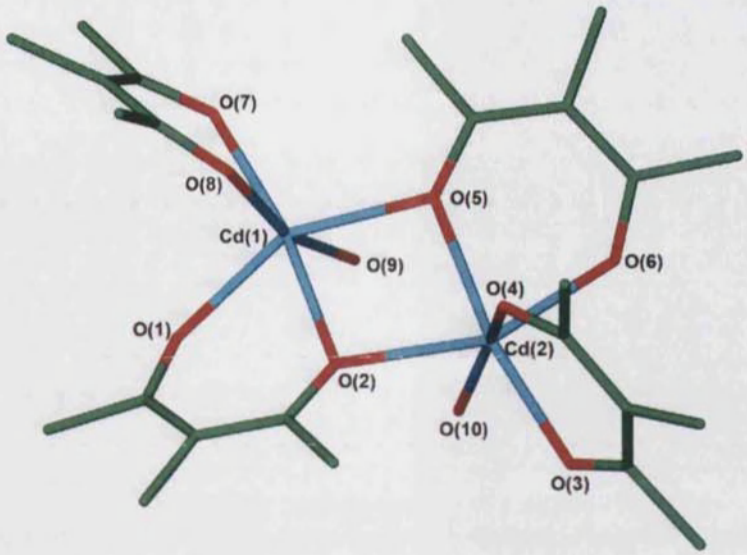

Figure 5.22. The dimers present in **19**.

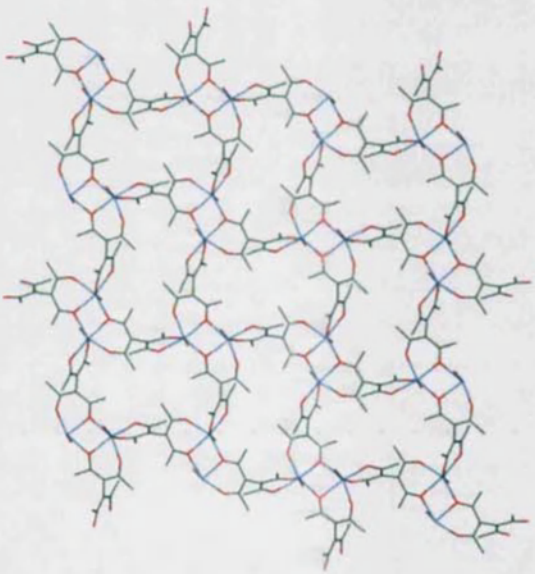

Figure 5.23. The 2-D 'Basket-Weave' sheet of **19** as viewed down the *c* axis.

The 2-D sheets pack parallel to each other with two full and four 3/4 uncoordinated water molecules per two formula units, lying between the adjacent sheets (Figure 5.24). The hydrogen atoms of the water molecules could not be located accurately and thus were omitted from the final refinement. The O···O distances (Table 5.12) involving the oxygen atoms from the waters and the tae^{2-} keto groups range from 2.599(9) Å to 2.85(2) Å. These distances being consistent with the presence of strong hydrogen bonding. The two coordinated water molecules labelled O(9) and O(10) are hydrogen bonded to each other (Figure 5.25).

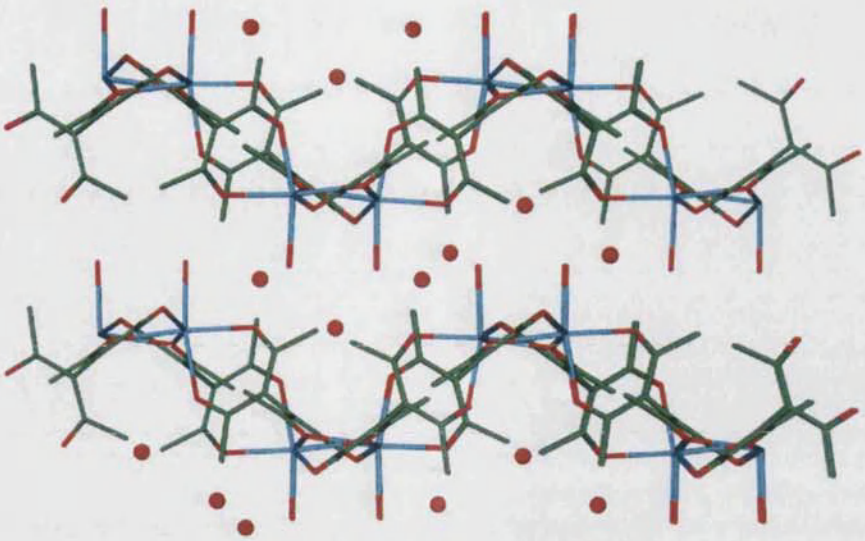

Figure 5.24. Packing of the sheets as viewed down the *b* axis. The sheets are shown as sticks while the uncoordinated water molecules are represented as balls.

The coordinated water molecules play a key role in the packing of the overall network. Hydrogen bonding between the oxygen atoms O(9) and O(10), from one sheet and O(7) and O(3) from an adjacent sheet hold the two sheets together (Figure 5.25). There is extensive hydrogen bonding between the uncoordinated water fragments based on O(11), O(12) and O(13).

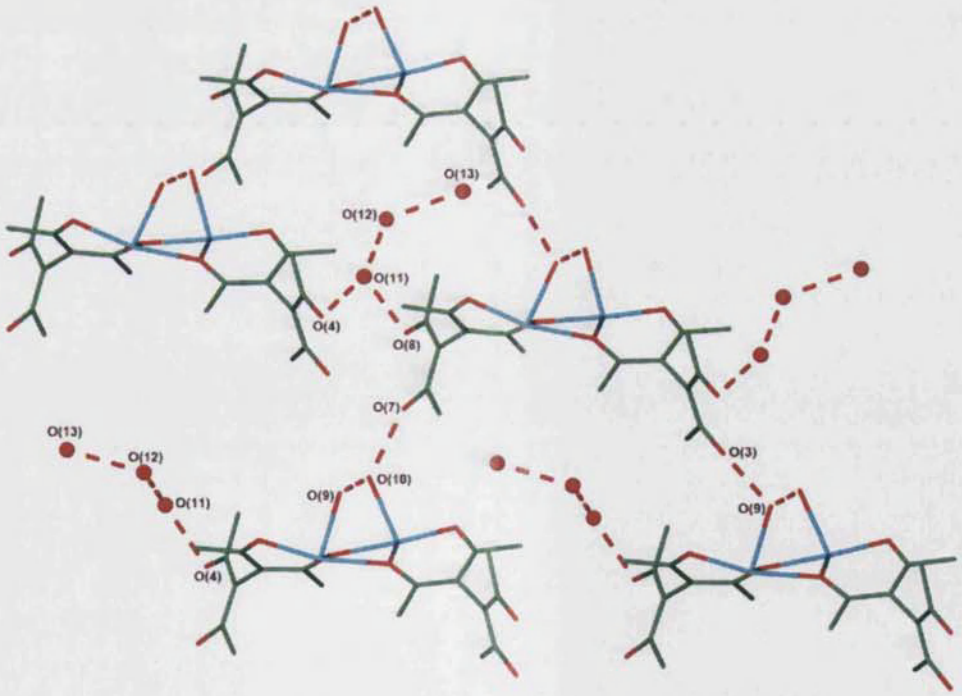

Figure 5.25. The hydrogen bonding present in **19**. The gross network is represented as sticks while the oxygen atoms of the uncoordinated water molecules are represented as balls.

On comparing the structures of **17**, **18** and **19** it can be noted that the tae^{2-} ligand adopts the same two binding modes in the three complexes. Due to the bridging nature of the ligand, the metal centres are linked together into dimeric units which can be regarded as SBUs. In all three compounds, the SBUs are extended to form 2-D 'Basket-Weaved' network with the core unit of the structure consisting of $[M_2(\mu\text{-tae})_2]$ (M = Cd or Zn). The sheets of **17**, **18** and **19** are isostructural.

One other similarity between **18** and **19** is the presence of hydrogen bonding between the coordinated and uncoordinated solvent molecules as well as the keto atoms of the ligand. The hydrogen bonding is important in the determination of the overall packing of the sheets.

5.4 Engineering the networks

As mentioned in Section 5.2, due to steric hindrance the keto groups of the H_2tae ligand are oriented at approximately 90° to one another. In order to remove this constraint, a bigger and more flexible spacer was introduced between the β-diketone functional groups. Thus 3,3'-(1,4-phenylenedimethylene)di-2,4-pentanedione (H_2pdp) (Figure 5.26) was synthesised following an experimental procedure suggested by Fernelius *et al.*[19]

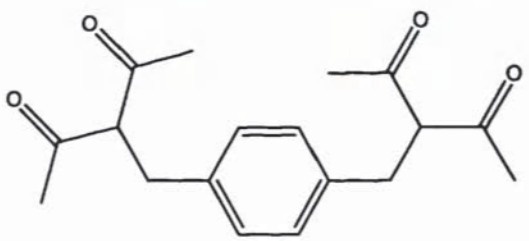

Figure 5.26. 3,3'-(1,4-phenylenedimethylene)di-2,4-pentanedione (H_2pdp).

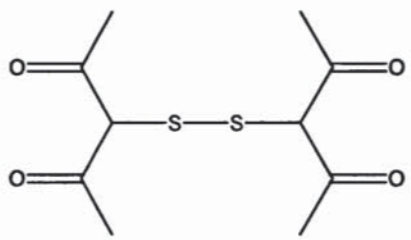

Figure 5.27. 3,3'-dithio-di-2,4-pentanedione (H_2dtp).

As detailed in Section 5.1, discrete molecules from bis-β-diketonates incorporating a sulphur moiety in between the keto groups have also attracted attention. In

order to study any resulting networks from such ligands, 3,3'-dithio-di-2,4-pentanedione (H_2dtp) (Figure 5.27) was synthesised following an experimental procedure suggested by Angeli and Mangani.[11] The above two mentioned ligands were reacted with suitable metal nitrate salts in the presence of a base.

5.4.1 Synthesis of 3,3'-(1,4-phenylenedimethylene)di-2,4-pentanedione (H_2pdp)

2,4-pentanedione was added to a stirred refluxed solution containing excess K-*tert*-butoxide in 2-methylpropan-2-ol (*tert*-butanol). After one and a half hours, 1,4-dibromomethylbenzene was added in small increments. After the complete addition of 1,4-dibromomethylbenzene, the reaction was left at reflux for an additional hour, then potassium iodide was added. Five hours later, the reaction mixture was cooled to room temperature and the solvent was removed under reduced pressure. The resulting solid was washed with water and recrystallised from hot *tert*-butanol.[12] H_2pdp was characterised by ^{1}H and ^{13}C{^{1}H} NMR, microanalysis and X-ray crystallography.

5.4.2 Reactions of 3,3'-(1,4-phenylenedimethylene)di-2,4-pentanedione with metal nitrates

In Section 5.1.6, the discrete complexes obtained form 3,3'-(1,3-phenylenedimethylene)di-2,4-pentanedione (Figure 5.2) and 3,3'-(2,7-naphthalenediyldimethylene)di-2,4-pentanedione were discussed. These two ligands are positional isomers of 3,3'-(1,4-phenylenedimethylene)di-2,4-pentanedione, (H_2pdp). While positioning the β-diketone functional groups on carbons 1 and 3 of the benzene ring gave discrete complexes, the 1,4 functionalised benzene ligand (H_2pdp) is expected to give one, two or three dimensional networks depending on the reaction conditions used. Thus H_2pdp was reacted with $Zn(NO_3)_2{\cdot}6H_2O$ and $Cd(NO_3)_2{\cdot}4H_2O$ and a base in an attempt to obtain networks that could be characterised and studied further.

Following the same experimental procedure as for the synthesis of **15** to **19**, $Zn(NO_3)_2{\cdot}6H_2O$ and $Cd(NO_3)_2{\cdot}4H_2O$ were dissolved in a range of solvents and mixed with solutions of H_2pdp. Et_3N vapour was left to diffuse into the solutions.

As in the reactions with tae^{2-}, a powder precipitated immediately but, after separating the powder from the solution by filtration, no crystals were obtained from the filtrate. Different crystal growth methods were used to increase the chances of obtaining single crystals suitable for X-ray crystallography analysis but all attempts were unsuccessful.

5.4.3 Synthesis of 3,3'-dithio-di-2,4-pentanedione (H_2dtp)

3,3'-dithio-di-2,4-pentanedione was synthesised from 2,4-pentanedione and sulphur monochloride (S_2Cl_2).[11] 2,4-pentanedione was cooled to 0°C under an atmosphere of nitrogen, S_2Cl_2 was then added dropwise to the cooled stirred solution. When a yellow solid precipitated, ice cold water was added and the solid was filtered, washed with excess water, dried and recrystallised from hot petroleum ether. H_2dtp was characterised by ^1H and ^{13}C NMR, microanalysis and powder X-ray crystallography. Data obtained from the latter technique were compared to the simulated spectrum obtained from the reported structure.[21]

5.4.4 Reactions of 3,3'-dithio-di-2,4-pentanedione with metal salts

In Section 5.1.6, ruthenium discrete molecules from 3,3'-dithio-di-2,4-pentanedionato (H_2dtp) were reported, in a reaction where the ligand was assembled during the reaction.[16] In order to investigate whether networks containing dtp^{2-} could be formed in a similar manner as the ones described previously in this chapter, the reactions of H_2dtp with other metal salts were investigated.

The same experimental procedure as for the synthesis of compounds **15** to **19** was used. In addition, reactions were carried out by first deprotonating the H_2dtp ligand with a suitable base followed by the slow diffusion of a metal nitrate solution into the dtp^{2-} solution. The range of metal cations used included Al(III),Cu(II), Co(II), Cd(II) and Zn(II).

In all cases the solutions darkened and eventually turned black. The black colour of the reactions suggested that decomposition was occurring. An alternative base to Et_3N, namely K-*tert*-butoxide was used and the same observations were noted.

Reactions between copper or zinc nitrates and dtp^{2-} were carried out using different solvents namely DMF, DMSO and MeOH. In both cases, the rate of decomposition differed according to the solvent used, with the complexes decomposing faster in DMF than DMSO and most slowly in MeOH.

In order to investigate whether it is the deprotonated ligand or the metal-dtp^{2-} mixture that breaks down, two control experiments were performed. The first control experiment was conducted to test the stability of dtp^{2-}. Triethylamine was added to a solution of H_2dtp without the addition of the metal cations. The solution remained colourless and no signs of decomposition were observed thus implying that the deprotonated ligand species dtp^{2-} is stable. This was further confirmed by NMR measurements. In order to confirm that it is the metal-dtp^{2-} mixture that is unstable, a second control test was carried out. HNO_3 was added to a solution of H_2dtp and $Zn(NO_3)_2 \cdot 6H_2O$. In this case, there was no white precipitate and the solution remained colourless. The HNO_3 prevented the deprotonation of the ligand hence hindered the formation of dtp^{2-}. Thus it can be concluded that the deprotonated ligand is stable in the absence of metal cations and the mixture of H_2dtp and metal salts solution is also stable in the presence of an acid. However the mixture of dtp^{2-} and metal salt solution decomposes rapidly.

5.5 Reaction of $Fe_2(SO_4)_3$ and 3,3'-dithio-di-2,4-pentanedione

The only reaction using H_2dtp that did not lead to decomposition was that with $Fe_2(SO_4)_3$. A solution of $Fe_2(SO_4)_3$ in water was added dropwise to a solution of the deprotonated ligand (dtp^{2-}) in MeOH. The red-brown powder (**20**) that was obtained was filtered and dried in air. The compound was found to be soluble in halogenated solvents such as chloroform and dichloromethane. However, various attempts to recrystallise the compound failed and in all cases microcrystalline material was obtained.

IR spectroscopy of **20** shows broad peaks at 3450 cm^{-1} [ν (OH) hydrogen bonded] and 1610 cm^{-1} [ν CO]. The sample was submitted to electrospray mass spectroscopy and the highest *m/z* peak was observed at 1133.4. This suggests the compound contains three iron centres, three dtp^{2-} ligands, three methoxide ligands and three methanol molecules. Table 5.14 summarises the mass spectrometry data.

Table 5.14. Mass spectrometry data for **20**.

m/z	Fragment formula	Fragments lost
948.5	$[Fe_3(dtp)_3]^+$	3 MeO^-, 3 MeOH
894.3	$[Fe_2(dtp)_3]^+$	Fe^{3+}
632.0	$[Fe_2(dtp)_2]^+$	dtp^{2-}
371.8	$[Fe_2(dtp)]^+$	dtp^{2-}
316.9	$[Fe(dtp)]^+$	Fe^{3+}

All the results obtained from the different experiments suggest that this compound is a stable discrete molecule made up of iron(III), dtp^{2-}, methoxides and methanol components.

5.6 Summary and conclusion

In Section 5.1 it was stated that bis-β-diketonates have the potential to form networks in an analogous way to dicarboxylates and this hypothesis has been proven by results reported in this chapter.

The first examples of metal organic frameworks containing bis-β-diketonates were characterised fully are reported herein. Bis-β-diketonates were able to form 1-D networks such as in the cases of $\{[Zn(tae)(DMF)]\cdot 0.6CHCl_3\cdot 0.4DMF\}_\infty$ **(15)** and $\{[Zn_3(tae)_3(MeOH)(DMSO)_{4.2}]0.8DMSO\}_\infty$ **(16)** or 2-D networks such as $\{[Zn_2(\mu\text{-}tae)_2(OH_2)_2]\}_\infty$ **(17)** and $\{[Zn_2(\mu\text{-}tae)_2(MeOH)_2]\cdot 2MeOH\}_\infty$ **(18)**.

Results outlined here also highlight the dependency of the networks on the solvent mixture. In the case of $Zn(NO_3)_2\cdot 6H_2O$ and tae^{2-}, solvent mixtures of DMF/$CHCl_3$ and DMSO/MeOH gave 1-D chains while MeOH gave 2-D sheets.

Bis-β-diketonates were found to have different binding modes such as the chelating bridging bidentate and bidentate modes. Due to the ability of binding in more than one mode, when coordinated to metal centres the bis-β-diketonates gave rise to SBUs in different structures (**17**, **18** and **19**) containing different metals such as zinc and cadmium. The 2-D 'Basket-Weaved' networks of **17**, **18** and $\{[Cd_2(\mu\text{-}$

tae)$_2$(OH$_2$)$_2$]·2.5H$_2$O}$_\infty$ (**19**) contain a repetitive [M$_2$(μ-tae)$_2$] motif (M = Zn, Cd) with the overall networks being isostructural.

5.7 Further work

A common problem encountered throughout this work involving bis-β-diketonates was the rapid formation of insoluble products that resulted in the precipitation of a powdery material. One way of avoiding this problem and increasing the chances of obtaining single crystals suitable for X-ray crystal analysis, is to grow networks in controlled steps thus relying less on the kinetics of crystal growth.

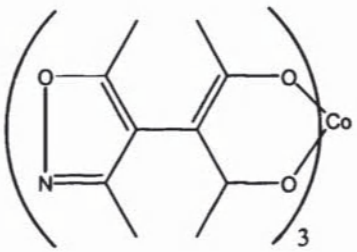

Figure 5.28. The protected version of the ligand. The β-diketonate group is shown coordinated to Co(III) with the isoxazole ring still intact.

One strategy involves the protection of one side of the ligand in the form of isoxazole ring, and then coordinating the free β-diketonate side to a metal to form discrete metal complexes (Figure 5.28). The isoxazole ring can then be reduced[22] and hydrolysed[23] following literature procedures to give β-diketonate moiety, which could then be coordinated to a second metal centre.

Although this method of obtaining the discrete metal-β-diketonato-β-diketone complexes involves several synthetic steps, it is worth investigating. If successful, it will give control over the formation of networks, and allow the possibility of forming mixed metal networks.

References:

1. R.C.Young, *Inorg.Synth.* **1946,** 2, 25.
2. R.K.Mehrotra; R.C.Mehrotra, *Can.J.Chem.* **1961,** 39, 795.
3. P.F.R.Ewigs; P.G.Harrison; D.E.Fenton, *J.Chem.Soc.Dalton Trans.* **1974,** 821.
4. H.Reihlem; A.Gruhl; G.V.Hessling, *Annalen.* **1929,** 472, 268.
5. G.T.Morgan; A.R.Bowen, *J.Chem.Soc.* **1924,** 125, 1259.
6. F.A.Cotton; R.C.Elder, *Inorg.Chem.* **1965,** 4, 1145.
7. M.B.Hursthouse; M.A.Laffey; P.T.Moore; D.B.New; P.R.Raithby; P.Thornton, *J.Chem.Soc.Dalton Trans.* **1982,** 307.
8. G.Urbain, *Bull.Soc.Chim.* **1896,** 15, 338.
9. M.Calvin; K.W.Wilson, *J.Am.Chem.Soc.* **1945,** 2003.
10. R.G.Charles, *Organic Syntheses.* **1959,** 39, 61.
11. A.Angeli; A.Mangnani, *Gazz.Chim.Ital.* **1894,** 24, 342.
12. W.C.Fernelius; D.F.Martin; M.Shamma, *J.Am.Chem.Soc.* **1959,** 81, 1509.
13. S.R.Breeze; G.D.Enright; S.Wang; Y.Zhang, *J.Am.Chem.Soc.* **1998,** 120, 9398.
14. A.W.Maverick; F.E.Klavetter, *Inorg.Chem.* **1984,** 23, 4129.
15. J.R.Bradbury; S.C.Buckingham; A.W.Maverick; G.G.Stanley; Q.Yao, *J.Am.Chem.*Soc. **1986,** 108, 7403.
16. C.Bailar.Jr; J.S.Oh, *J.Inorg.Nucl.Chem.* **1962,** 24, 1225.
17. L.F.Lindoy; S.X.Luo; J.C.McMurtrie; P.Turner; G.Wei; X.Y.Zhang; B.S.Zheng; H.W.Zhu, *Dalton Trans.* **2005,** 1349.
18. A.Endo; H.Nagao; K.Shimizu; M.Sibasaki, *Inorg.Chim.Acta.* **2004,** 357, 3443.
19. A.W.Addison; T.N.Rao; J.Reedijk; J.V.Rijn; G.C.Verschoor, *J.Chem.Soc.Dalton.Trans.* **1984,** 1349.
20. K.W.Henderson; A.R.Kennedy; L.Macdonald; D.J.MacDougal, *Inorg.Chem.* **2003,** 42, 2839.
21. R.D.G.Jones; L.F.Power, *Acta.Crystallogr..* **1976,** B32, 1801.
22. R.F.Jones; S.J.Hollis; J.M.Iley, *Tetrahedron: Assym.* **2000,** 11, 3273.
23. M.Nitta; T.Kobayashi, *J.Chem.Soc.Chem.Comm.* **1982,** 877.

Chapter 6 Functionalised β-diketonate ligands

6.1 Introduction

2,4-pentanedione can be functionalised at three distinct positions without affecting the ability of its monoanion to act as a ligand. Functional groups can be added onto 2,4-pentanedione at carbons 1, 3 and 5 (Figure 6.1). Such substitutions will influence the stability of the metal complexes formed.[1] For example nitro, cyano and halide groups at the 3-position will exhibit an electron withdrawing effect [2] and hence tend to weaken the bonds between the oxygen atoms and metal centres.[3] Various functionalised 2,4-pentanedione ligands have been synthesised and used in the formation of networks.

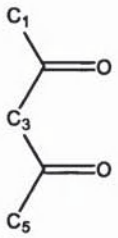

Figure 6.1. 2,4-pentanedione with carbons 1,3 and 5-labelled as such.

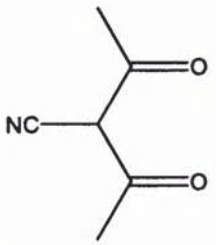

Figure 6.2. 3-cyano-2,4-pentanedione (Hcpd)

A brief overview of different complexes containing a variety of functionalised β-diketonate ligands follows, along with a description of 3-cyano-2,4-pentanedionato based networks synthesised during the course of this project.

6.1.1 Networks from 3-cyano-2,4-pentanedione (Hcpd)

One functionalised β-diketone that has been reported in the literature is 3-cyano-2,4-pentanedione (Hcpd) (Figure 6.2).[4,7,8] The β-diketonate (cpd^-) derived from this dione has been used to form complexes with cobalt(II) and copper(II).[4,7]

Bis(3-cyano-2,4-pentanedionato)copper(II)[7] was synthesised from an aqueous solution of $Cu(NO_3)_2 \cdot 2.5H_2O$, to which Hcpd together with propylamine in ethanol were added. In the crystal structure each copper centre has square pyramidal geometry. The four equatorial positions are occupied by four oxygen atoms from two ligands while a nitrogen

atom from the cyano group of another ligand fills the axial position. This forms a 1-D chain as is illustrated in Figure 6.3a.

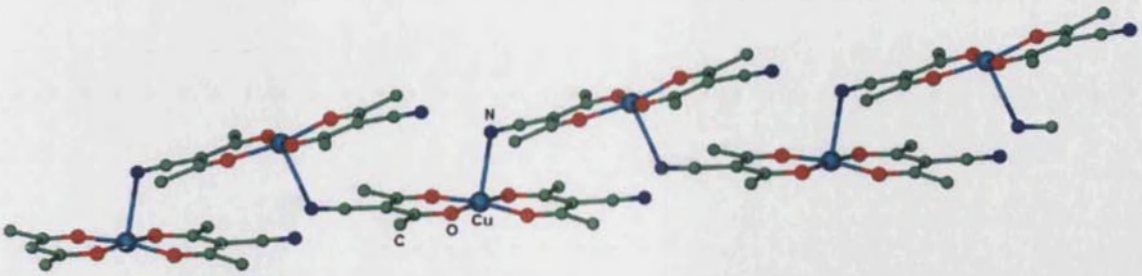

Figure 6.3a. 1-D chain of bis(3-cyano-2,4-pentanedionato)copper(II).[7]

When $CoCl_2$ was reacted with a solution of Na cpd in ethanol, pink-red crystals were obtained.[4] In this case the cobalt centre adopts an octahedral geometry. In a similar way to the copper complex, the equatorial positions on the metal are occupied by four oxygen atoms from two different ligands. However, in this case two nitrogen atoms from two adjacent molecules occupy the remaining two axial positions to give a 3-D structure (Figure 6.3b)

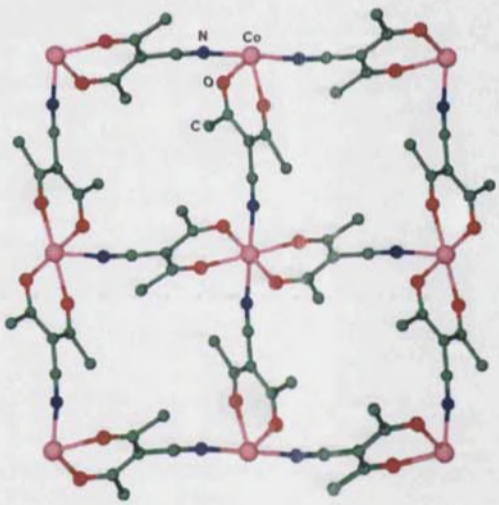

Figure 6.3b. Part of the 3-D network of bis(3-cyano-2,4-pentanedionato)cobalt(II).[4]

6.1.2 Pyridyl functionalised β-diketonates

When the proton on carbon number 3 is substituted by a pyridyl group, 3-(4-pyridyl)-2,4-pentanedione (Hppd) is obtained (Figure 6.4). Hppd has been used by several authors to form metal complexes. Some of the metal cations used to form complexes with this ligand are aluminium(III), iron(III), cadmium(II), zinc(II), beryllium(II) and copper(II).[9-11]

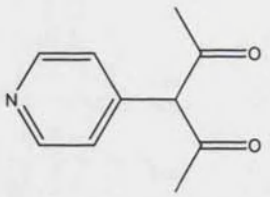

Figure 6.4. 3-(4-pyridyl)-2,4-pentanedione (Hppd).

Hppd was reacted with salts of aluminium(III) and iron(III) together with $NaHCO_3$ as a base. The resulting products were tris(3-[4-pyridyl]-2,4-pentanedionato)aluminium(III) and tris(3-[4-pyridyl]-2,4-pentanedionato)iron(III).[10] Both metals adopt an octahedral geometry with six oxygen atoms from three different ligands filling the coordination sphere. One interesting feature of these complexes is the fact that two of the three chelate metallocycles are non-planar.[10] This distortion in the metal-ligand rings causes deviation of the angles between the lone pairs on the nitrogen atoms away from the ideal 120°. The authors claim that this deviation is an inherent feature of metal diketonate complexes with aromatic groups substituted at the 3-position. Furthermore they state that this deviation minimises the molecular volume and hence allows for tighter packing of the molecules.

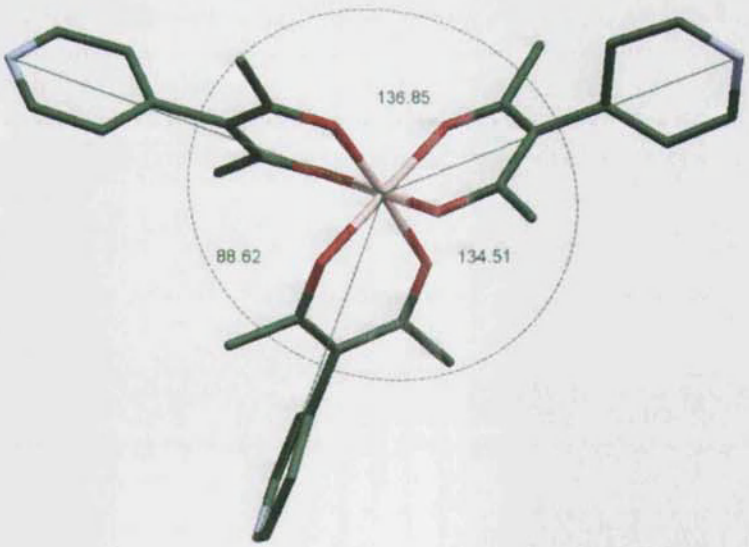

Figure 6.5. The deviation from the ideal 120° angles between the pyridyl rings in $[Al(ppd)_3]$.[10]

The orientation of the lone pairs on the nitrogen atoms has a significant implication for the networks formed from the $[M(ppd)_3]$ complexes (M = Al or Fe) and a second metal such as cadmium(II) or cobalt(II).[10] Since two of the pyridyl groups are

oriented at approximately 90° to each other, mixed-metal squares were obtained instead of a honeycomb network. $\{Cd[Fe(ppd)_3]_2(NO_3)_2{\cdot}2H_2O\}_\infty$ forms a sheet structure based on a heterobimetallic square motif and the same gross structure was observed for $\{Co[Al(ppd)_3]_2Cl_2{\cdot}4CHCl_3{\cdot}2CH_3OH\}_\infty$ (Figure 6.6). In this case the cobalt centre adopts a distorted octahedral geometry with the two axial positions being occupied by terminal chloro ligands.

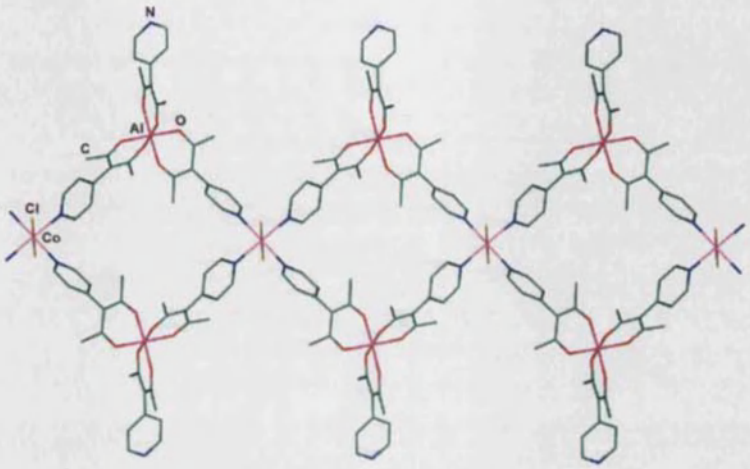

Figure 6.6. The 1-D network of $\{Co[Al(ppd)_3]_2Cl_2{\cdot}4CHCl_3{\cdot}2CH_3OH\}_\infty$ viewed perpendicular to the (0,0,1) plane.[10]

When the connecting metal adopts a T-shaped geometry, the network observed differs from the ones described above. In $\{Cd[Al(ppd)_3](CH_3OH)Br_2{\cdot}2CHCl_3{\cdot}2CH_2OH\}_\infty$[10] the cadmium centres adopt a T-shaped configuration and there are two types of pores in the network as shown in Figure 6.7.

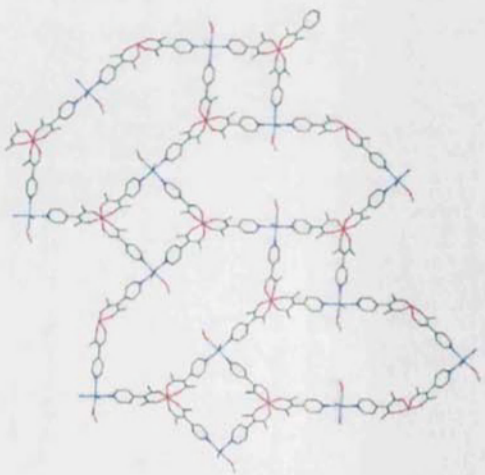

Figure 6.7. The mixed pore types present in $\{Cd[Al(ppd)_3](CH_3OH)Br_2{\cdot}2CHCl_3{\cdot}2CH_2OH\}_\infty$[10]

Beryllium(II) also coordinates to the 3-(4-pyridyl)-2,4-pentanedionate ligand, adopting a tetrahedral geometry where two 3-(4-pyridyl)-2,4-pentanedionate ligands fill the coordination sphere of the metal to yield bis(3-[4-pyridyl]-2,4-pentanedionato) beryllium(II).[11] Since the lone pairs of the cyano groups in $[Be(ppd)_2]$ are pointing at an angle of 180° with respect to each other, this molecule can be viewed as a rigid linear linker. $[Be(ppd)_2]$ was reacted with a range of cadmium salts and the structures of the networks formed were dependent on the counter ion.[11] For example, the nitrate complex $\{Cd[Be(ppd)_2](MeOH)(NO_3)_2 \cdot CHCl_3 \cdot 0.5MeOH\}_\infty$[8] has an infinite 1-D chain geometry with the cadmium centres coordinating to two pyridyl moieties. The coordination sphere of cadmium is further occupied by two bidentate nitrates and a methanol ligand to give the cadmium heptacoordinate geometry. In contrast, cadmium thiocyanate gave a 2-D network with the formula $\{Cd[Be(ppd)_2](NCS)_2 \cdot 0.5MeOH\}_\infty$[11] This consists of chains of $CdBe(ppd)_2$ which are intertwined via pairs of bridging thiocyanate ligands.

The lone pair of the nitrogen atom of the ligands cpd^- and ppd^- is at an angle of 180° with respect to the diketone functional group, hence these ligands can be described as rigid linear linkers. A degree of flexibility has been introduced to Hppd by the insertion of an additional methylene group between the pyridyl ring and the diketone group. The effect that this flexibility has on the overall networks was investigated when 3-(4-pyridylethylene)-2,4-pentanedione (Hpep) (Figure 6.8) was used to form mixed metal networks.

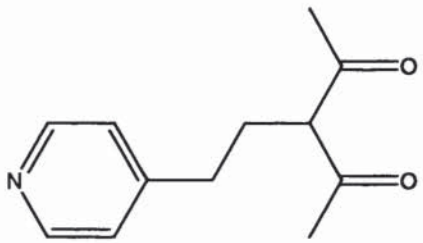

Figure 6.8. 3-(4-pyridylethylene)-2,4-pentanedione (Hpep).

When coordinated to beryllium, the metal geometry was once again tetrahedral. The pyridyl moieties in the complex $[Be(pep)_2]$ adopt an *anti* conformation relative to each other when viewed along the C-C bond of the aliphatic spacer.[11]

When $[Be(pep)_2]$ was reacted with $Cd(NO_3)_2 \cdot 4H_2O$, a 2-D bilayer framework with the formula $\{[Cd_2(Be(pep)_2]_3(MeOH)(NO_3)_3(NO_3) \cdot 4.5MeOH\}_\infty$ was formed.[11] The nitrate ions form bridges in the network as shown in Figure 6.9.

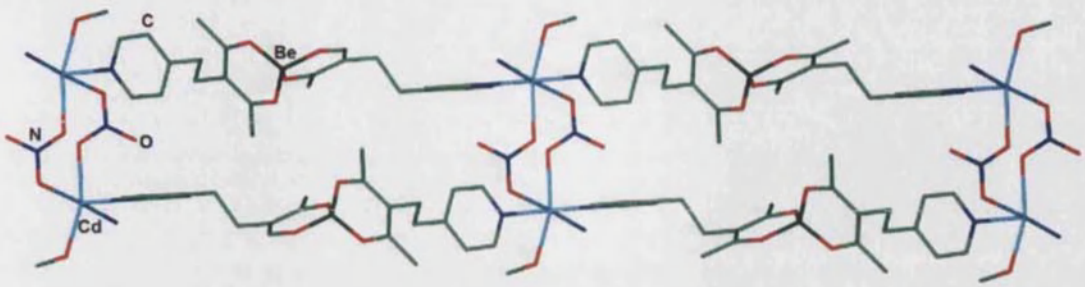

Figure 6.9. The bridging nitrates in $\{[Cd_2(Bepep)_2]_3(MeOH)(NO_3)_3(NO_3) \cdot 4.5MeOH\}_\infty$[11]

6.1.3 1-substituted and 1,5- substituted β-diketones

Instead of substituting at the 3-position, β-diketones can be substituted at the 1- or 1,5- positions. When the substituent bears a ligating group, the orientation of the donor lone pair with respect to the diketonate group is different from that with 3-substituent. The effect that this variation has on the overall network was analysed by Chernega et *al.*[11]

An example of a 1-substituted ligand is 1-(4-pyridyl)-1,3-butanedione (Hpdd) (Figure 6.10),[11] which on coordination to beryllium(II) gives bis(1-[4-pyridyl]-1,3-butanedionato)beryllium(II) ($[Be(pdd)_2]$). Unlike in the 3-substituted isomers, the pyridyl groups of $[Be(pdd)_2]$ are arranged mutually at angles other than 180° and hence this building unit cannot be considered as a linear linker.

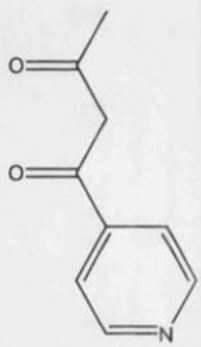

Figure 6.10. 1-(4-pyridyl)-1,3-butanedione (Hpdd).

When [Be(pdd)$_2$] was coordinated to cadmium(II), a network with square voids having the formula {Cd[Be(pdd)$_2$]$_2$I$_2$·2CHCl$_3$}$_\infty$[11] was formed. The cadmium centres have octahedral geometry with the coordination sphere being populated by four pyridyl groups in the equatorial plane and two terminal iodides in the axial positions. The voids inside the squares are filled by chloroform molecules (Figure 6.11).

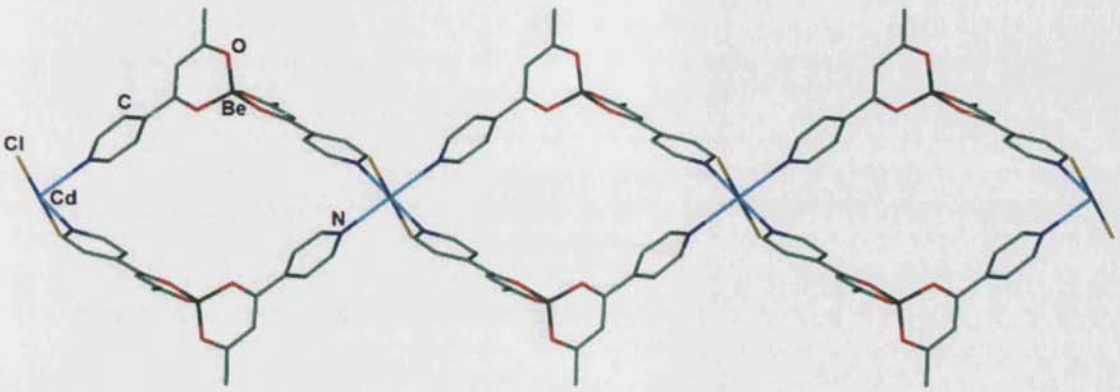

Figure 6.11. The network of {Cd[Be(pdd)$_2$]$_2$I$_2$}·2CHCl$_3$ viewed perpendicular to the *a* axis.[11]

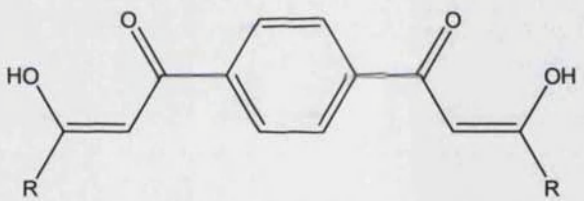

Figure 6.12. 1,1'-(1,4-phenyl)bisbutane-1,3-dione (H$_2$pbd) (R=H)

Interesting complexes from 1,1'-(1,4-phenyl)bisbutane-1,3-dione (H$_2$pbd) (Figure 6.12) were obtained on coordination of the pbd^{2-} ligand to copper(II), iron(III), and gallium(III).[12] For example, in the copper structure the motif has the formula of [Cu$_3$(pbd)$_3$(DMF)]·DMF,[12] and it consists of discrete trimers. The copper centres are situated at the apices of a triangle with the ligands constituting the sides of the triangular complex (Figure 6.13). Two of the copper centres have a square planar geometry while the third copper centre has a square-pyramidal geometry.

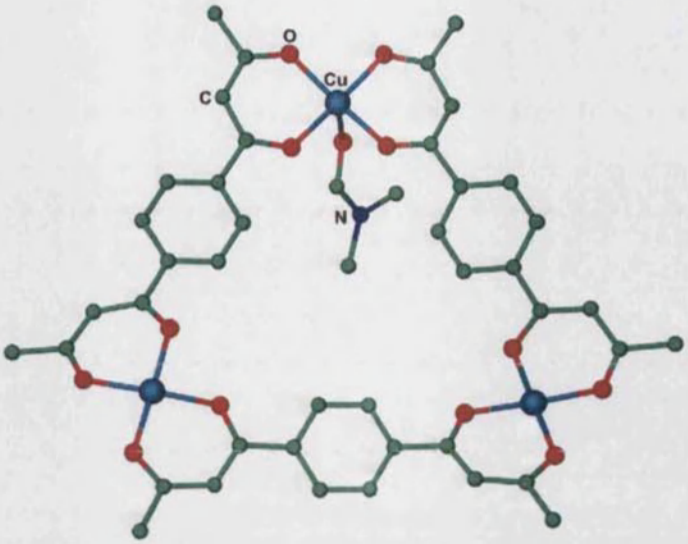

Figure 6.13. The triangular discrete units of $[Cu_3(pbd)_3(DMF)]\cdot DMF$.[12]

Very recently, Clegg and co-workers[13] reported 1-D and 2-D networks from similar copper complexes incorporating ligands such as 1,1'-(1,3-phenylene)-bis(4,4-dimethylpentane-1,3-dione) (H_2pdmp) (Figure 6.12 R = *t*Bu). The resulting molecules were found to consist of dimeric units made from two copper centres and two ligands. *N*-heterocyclic ligands such as 4,4'-dipyridyl sulphide were added to the dimeric units and the nitrogen atoms of 4,4'-dipyridyl sulphate coordinated to the free site on the copper centres in a similar way as DMF coordinated to $[Cu_3(pbd)_3(DMF)]$. The addition of 4,4'-bipyridyl sulphide (dps) afforded a 1-D network of the formula $\{[Cu_2(pdmp)_2dps]\cdot 2THF\}_\infty$

6.2 Results and discussion

No mixed metal networks incorporating 3-cyano-2,4-pentanedione have been reported so far. Thus Hcpd was synthesised and coordinated to metal centres to form discrete $M(cpd)_x$ complexes. The discrete complexes were characterised and then further reacted with a second metal to give mixed metal networks.

6.2.1 Ligand synthesis

3-cyano-2,4-pentanedione (Hcpd) was synthesised following a literature procedure.[8] To a stirred solution of 2,4-pentanedione in dichloromethane, $ClSO_2NCO$ was added dropwise followed by DMF. The resulting orange solution was washed with water and the organic fraction dried over Na_2SO_4. The product was purified by column

chromatography on silica gel using 4:1 hexane-diethyl ether mixture as the mobile phase. The ligand was characterised by ^{1}H, ^{13}C NMR and IR spectroscopy as well as microanalysis. As in the case of 2,4-pentanedione, Hcpd was found to exist exclusively in the enol form.[14,15]

6.2.2 Copper complexes from 3-cyano-2,4-pentanedionato (cpd⁻)

$CuCl_2 \cdot 2H_2O$ and two equivalents of Hcpd were dissolved in methanol and placed in a flask. A small sample tube was filled with Et_3N and this was inserted in the flask with the reagents. Vapour diffusion methods[16] afforded blue crystals which were characterised by microanalysis, IR spectroscopy and X-ray powder diffraction. All analyses indicated that the product was $[Cu(cpd)_2]$ (**21**), which has been previously reported by Angelova *et al,*[7] and discussed in Section 6.1.1.

When $Cu(NO_3)_2 \cdot 2.5H_2O$ was used instead of $CuCl_2 \cdot 2H_2O$ a different product was obtained. The crystals formed were paler in colour than **21** and single crystal X-ray crystallography revealed that the product was $[Cu_6(\mu_3\text{-}OMe)_4(\mu\text{-}OMe)_2(cpd)_6]$ (**22**). Crystallographic data for **22** are summarised in Table 61. Three crystallographically distinct copper centres, three cpd⁻ ligands and three methoxy ligands are present in the asymmetric unit (Figure 6.14). Two of the copper atoms, Cu(1) and Cu(2) have a square pyramidal geometry, τ [17] = 0.15 and 0.06 respectively, while Cu(3) has a square planar geometry.

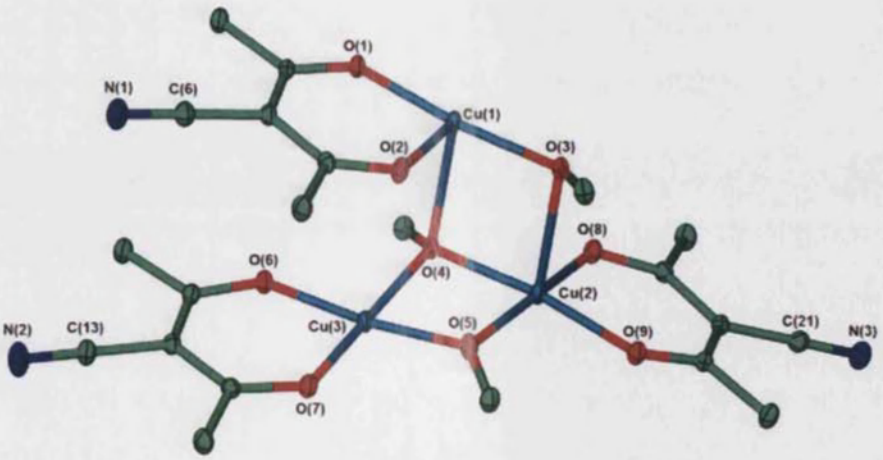

Figure 6.14. The asymmetric unit of **22** showing thermal ellipsoids at 30% probability. Hydrogen atoms are omitted for clarity.

Table 6.1. Crystallographic data for **22**.

Empirical formula	$C_7H_9CuNO_3$
M	656.08
T/ K	150(2)
Crystal system	Triclinic
Space group, *Z*	*P*-1, 2
a/ Å	8.6030(1)
b/ Å	10.6410(2)
c/ Å	14.7610(3)
α/ °	102.936(1)
β/ °	100.006(1)
γ/ °	104.594(1)
U/ Å^3	1235.97(4)
Crystal size/ mm	0.1 x 0.1 x 0.1
Wavelength/ Å	0.71073
Theta range for data collected/ °	3.39 to 30.88
Reflections collected/ observed (>2σ)	32325/ 5097
Data completeness	0.989
Max. and min. transmission	0.84 and 0.77
Goodness of fit F^2	1.043
Final *R* indices (I>2σ(I))	$R1$ = 0.0387, $wR2$ = 0.0907
R indices (all data)	$R1$ = 0.0657, $wR2$ = 0.0997
Largest diff. peak and hole eÅ^{-3}	0.913 and -0.650

A centre of inversion in the molecule duplicates the components in the asymmetric unit to form hexamer units (Figure 6.15).

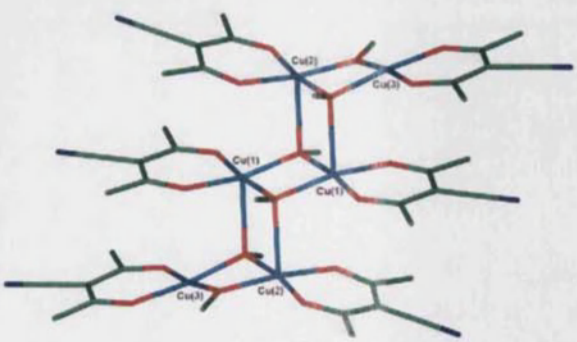

Figure 6.15. The hexamer unit of **22** viewed perpendicular to the (1,0,0) plane.

Although both Cu(1) and Cu(2) adopt a square pyramidal geometry their environments differ significantly. Cu(1) is coordinated to two oxygen atoms from one cpd⁻ ligand and three methoxy ligands each bridging between three copper centres. In the case of Cu(2), the coordination sphere similarly includes two oxygen atoms from a cpd⁻ ligand and three methoxy oxygen atoms, but one of the methoxy groups, O(5), bridges between two copper centres (Figure 6.14). Finally, Cu(3) is coordinated to two oxygen atoms from one cpd⁻, one methoxy oxygen, O(5), that bridges to two metal centres and one methoxy oxygen, O(3), that bridges to three metal centres (Figure 6.15).

In the gross structure, the hexamers pack alongside each other as shown in Figure 6.16. The planes of the cpd⁻ ligands coordinated to Cu(2) and Cu(3) are not parallel to each other as can be observed from Figure 6.16. As a result of this kink, the nitrogen atom, N(2) is 2.666(2) Å away from the nearest Cu(3) centre in the adjacent hexamer. Thus, as in the case of [Cu(cpd)$_2$], intermolecular forces link these hexamer to form a 2-D ladder.

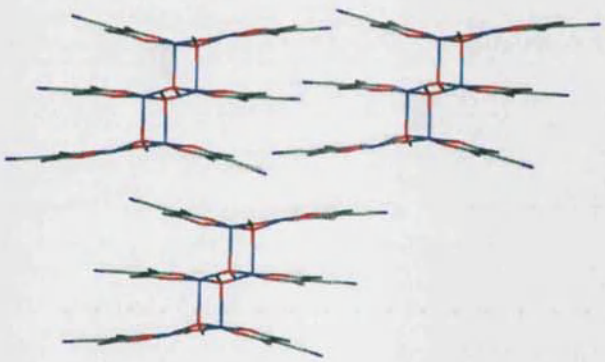

Figure 6.16. The packing of the molecules in the extended structure of **22**.

The bond distances between the oxygen atoms and the copper centres for μ_3-methoxy-copper differ in lengths as can be observed from Table 6.2. The axial copper-methoxy oxygen bond lengths are longer than the equatorial bonds. This can be observed from the comparison of the bond distances of Cu(1)-O(4) (2.4178(17)Å) and Cu(2)-O(3) (2.3916(17)Å) to Cu(1)-O(3) (1.9394(15)Å) , Cu(2)-O(4) (1.9567(15)Å) and Cu(2)-O(5) (1.9042(16)Å).

The axial copper-methoxy oxygen bond lengths of **22,** Cu(1)-O(4) (2.4178(17) Å) and Cu(2)-O(3) (2.3916(17) Å), are close to the axial copper-nitrogen bonds of **21** Cu(1)-

N(2) (2.468(3)Å), while the C-N bond lengths of the two compounds are of comparable length.

Table 6.2. Selected bond lengths for **22**.

Bond atoms	Distances/ Å
Cu(1)-O(1)	1.9232(15)
Cu(1)-O(2)	1.9269(16)
Cu(1)-O(3)	1.9394(15)
Cu(1)-O(4)	2.4178(17)
Cu(2)-O(3)	2.3916(17)
Cu(2)-O(4)	1.9567(15)
Cu(2)-O(5)	1.9042(16)
Cu(2)-O(8)	1.9325(16)
Cu(2)-O(9)	1.9235(16)
Cu(3)-O(4)	1.9472(16)
Cu(3)-O(5)	1.8973(16)
Cu(3)-O(6)	1.9173(16)
Cu(3)-O(7)	1.9146(17)
N(1)-C(6)	1.151(3)
N(2)-C(13)	1.146(3)
N(3)-C(21)	1.145(3)

Table 6.3. Selected bond angles **22**.[I]

Atoms	Angle/ °
O(1)-Cu(1)-O(2)	92.53(7)
O(2)-Cu(1)-O(3)	94.32(7)
Cu(1)-O(3)-Cu(1)#1	100.12(7)
Cu(1)#1-O(3)-Cu(2)	103.88(7)
O(4)-Cu(2)-O(3)	86.81(6)
O(5)-Cu(2)-O(3)	95.67(7)
O(8)-Cu(2)-O(3)	94.54(6)
O(9)-Cu(2)-O(3)	98.08(6)
O(9)-Cu(2)-O(8)	91.66(7)
O(5)-Cu(3)-O(4)	78.95(7)
O(7)-Cu(3)-O(6)	92.42(7)

22 was found to be insoluble in most common solvents such as acetone, acetonitrile, dichloromethane, 1,2-dichlorobenzene, dimethylsulfoxide, ethanol, hexane and toluene, and only sparingly soluble in *N,N*-dimethylformamide. Due to the low solubility of **22** all attempts to form mixed metal networks by coordinating the free nitrogen of the cyano groups to silver centres failed. The starting materials were retrieved unreacted in all cases.

[I] Symmetry transformations used to generate equivalent atoms:
#1 -x+1,-y+1,-z+1

6.2.3 Tris(3-cyano-2,4-pentanedionato)iron(III)

Tris(3-cyano-2,4-pentanedionato)iron(III), [Fe(cpd)$_3$] (**23**), was synthesised using the same procedure as for **22** but using $Fe(NO_3)_3 \cdot 9H_2O$ and three equivalents of Hcpd. Crystallographic data for **23** are summarised in Table 6.4. Two molecules are present in the asymmetric unit as illustrated in Figure 6.17. Both iron centres adopt distorted octahedral geometry.

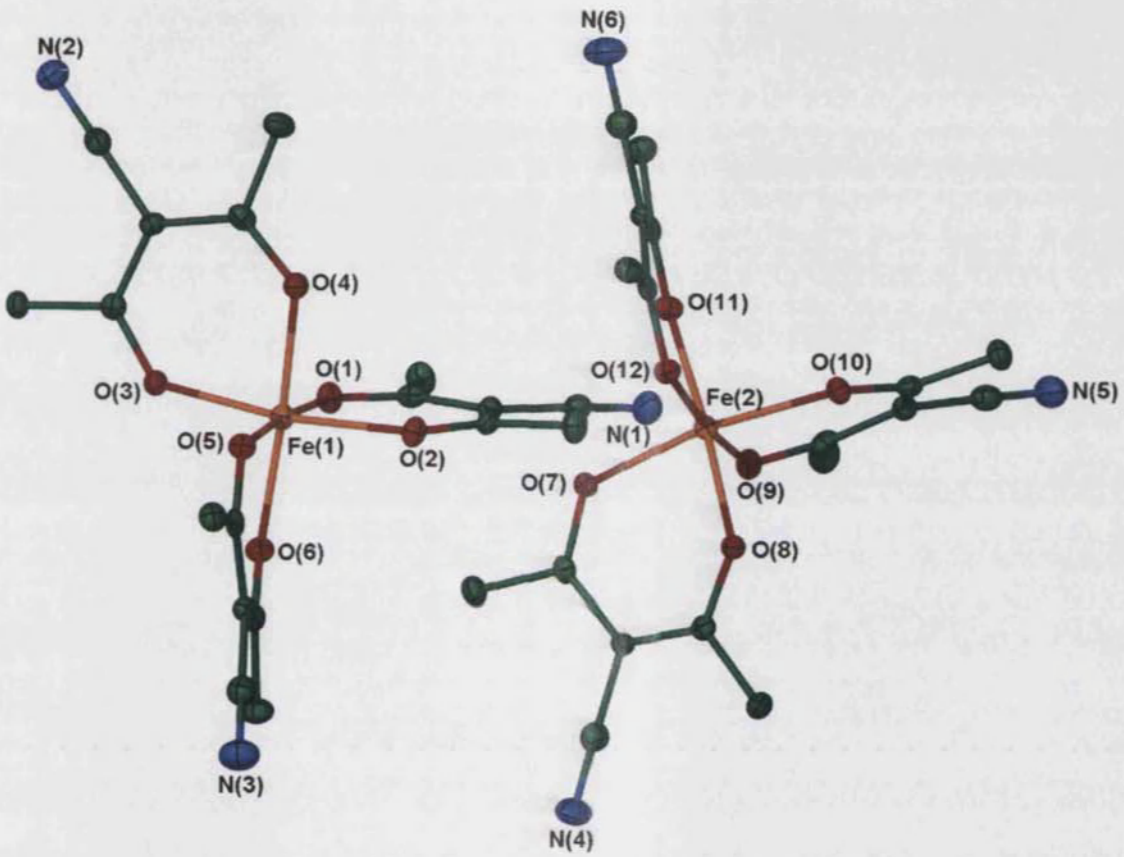

Figure 6.17. The asymmetric unit of **23** showing thermal ellipsoids at 30% probability. Hydrogen atoms are omitted for clarity.

Table 6.4. Crystallographic data for **23**.

Formula	$C_{18}H_{18}FeN_3O_6$
M	428.20
T/ K	150(2)
Crystal system	Monoclinic
Space group, *Z*	$P2_1/c$, 8
a/ Å	15.3320(2)

b/ Å	13.0220(2)
c/ Å	21.3520(4)
α/ °	90
β/ °	113.256(1)
γ/ °	90
U/ Å^3	3916.36(1)
Crystal size/ mm	0.25 x 0.125 x 0.025
Wavelength/ Å	0.71073
Theta range for data collected/ °	3.66 to 30.03
Reflections collected/ observed (>2σ)	71520, 5305
Data completeness	0.997
Max. and min. transmission	1.002 and 0.875
Goodness of fit F^2	0.958
Final *R* indices (I>2σ(I))	*R*1 = 0.0526, *wR*2 = 0.1112
R indices (all data)	*R*1 = 0.1643, *wR*2 = 0.1460
Largest diff. peaks and hole eÅ^{-3}	0.472 and -0.441

The coordination sphere around each metal centre contains six oxygen atoms from three different cpd$^-$ ligands. The values for the iron-oxygen bond lengths of **23** (Table 6.5) are comparable to one another. The carbon-nitrogen bond lengths of the cyano groups are also comparable to each other and to those of **22**. The oxygen-iron-oxygen bond angles in **22** (Table 6.6) deviate significantly from the expected 90° and 180° for an ideal octahedral complex. The iron atoms do not lie within any of the ligand planes. This can be observed by inspection of the angles between the cpd$^-$ planes and the Fe-O-O planes (Table 6.7). The net result is a buckling effect as illustrated in Figure 6.18, which effects the angles at the iron centres with respect to the nitrogen atoms of the cpd$^-$ ligands such that, the cyano groups are either contracted towards one another or else moved apart. In each molecule one of the angles between the cyano groups expands while the other two contracted from the ideal value of 120°. These deviations are more marked in the molecule based on Fe(2) (Figure 6.18).

Table 6.5. Selected bond lengths for **23**.

Bond atoms	Distance/ Å
Fe(1)-O(1)	1.986(2)
Fe(1)-O(2)	1.987(2)
Fe(1)-O(3)	1.981(2)
Fe(1)-O(4)	1.995(2)
Fe(1)-O(5)	1.995(2)
Fe(1)-O(6)	1.994(2)
Fe(2)-O(7)	1.994(2)
Fe(2)-O(8)	1.989(2)
Fe(2)-O(9)	1.995(2)

Bond atoms	Distance/ Å
Fe(2)-O(10)	1.990(2)
Fe(2)-O(11)	1.989(2)
Fe(2)-O(12)	1.980(2)
N(1)-C(6)	1.141(4)
N(2)-C(12)	1.153(4)
N(3)-C(18)	1.147(4)
N(4)-C(24)	1.150(4)
N(5)-C(30)	1.160(4)
N(6)-C(35)	1.142(4)

Table 6.6. Selected bond angles for **23**.

Atoms	Angle/ °
O(1)-Fe(1)-O(2)	86.75(9)
O(1)-Fe(1)-O(4)	95.48(9)
O(1)-Fe(1)-O(5)	174.60(9)
O(1)-Fe(1)-O(6)	91.12(9)
O(2)-Fe(1)-O(4)	86.24(9)
O(2)-Fe(1)-O(5)	89.47(9)
O(2)-Fe(1)-O(6)	95.42(9)
O(3)-Fe(1)-O(1)	88.94(9)
O(3)-Fe(1)-O(2)	171.29(9)
O(3)-Fe(1)-O(4)	86.64(9)
O(3)-Fe(1)-O(5)	95.31(9)
O(3)-Fe(1)-O(6)	92.22(9)
O(5)-Fe(1)-O(4)	88.11(9)
O(6)-Fe(1)-O(4)	173.29(9)
O(6)-Fe(1)-O(5)	85.41(9)

Atoms	Angle/ °
O(7)-Fe(2)-O(9)	87.08(9)
O(8)-Fe(2)-O(7)	84.98(8)
O(8)-Fe(2)-O(9)	97.21(9)
O(8)-Fe(2)-O(10)	88.10(9)
O(10)-Fe(2)-O(7)	170.05(9)
O(10)-Fe(2)-O(9)	86.71(9)
O(11)-Fe(2)-O(7)	91.97(9)
O(11)-Fe(2)-O(8)	175.38(9)
O(11)-Fe(2)-O(9)	86.08(9)
O(11)-Fe(2)-O(10)	95.34(9)
O(12)-Fe(2)-O(7)	97.33(9)
O(12)-Fe(2)-O(8)	90.88(9)
O(12)-Fe(2)-O(9)	171.11(9)
O(12)-Fe(2)-O(10)	89.90(9)
O(12)-Fe(2)-O(11)	86.06(9)

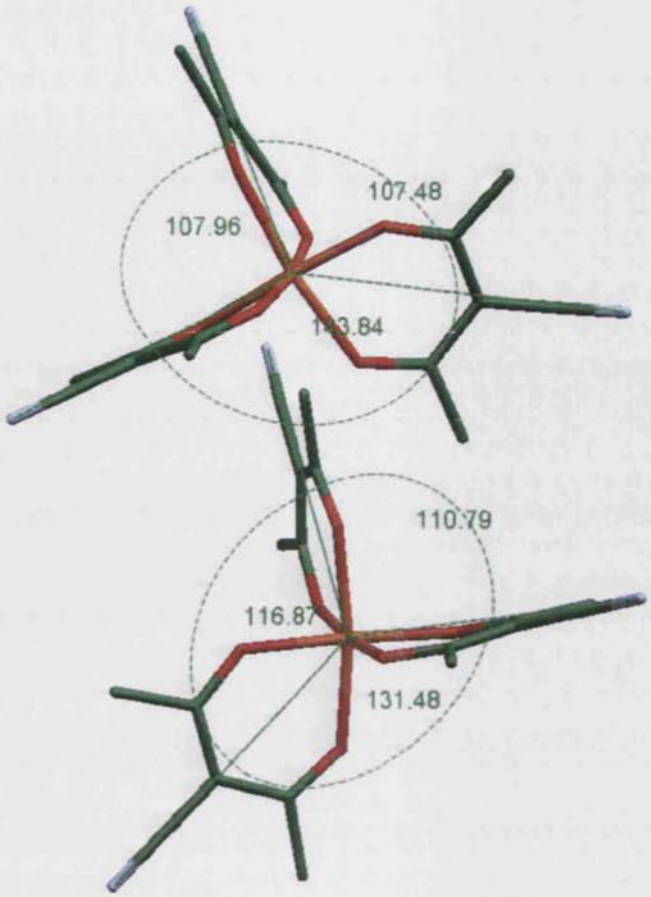

Figure 6.18. The angles between the cyano groups of $[Fe(cpd)_3]$.

Table 6.7. Angles between the cpd^- ligand planes and Fe-O-O planes for **23**.

cpd^- ligand plane atoms	Fe-O-O plane atoms	Angle between planes/ °
C(1) to C(5), N(1)	Fe(1)-O(1)-O(2)	2.65
C(7) to C(12), N(2)	Fe(1)-O(3)-O(4)	2.43
C(13) to C(18), N(3)	Fe(1)-O(5)-O(6)	17.09
C(19) to C(24), N(4)	Fe(2)-O(8)-O(7)	23.30
C(25) to C(30), N(5)	Fe(2)-O(9)-O(10)	8.79
C(32) to C(36), N(6)	Fe(2)-O(11)-O(12)	10.80

As noted in Section 6.1.2, Chernega and co-workers[10] have observed this phenomenon for tris(3-[4-pyridyl]-2,4-pentanedionato)aluminium(III) and tris(3-[4-pyridyl]-2,4-pentanedionato)iron(III). In those cases the authors claimed that this shift can

be attributed to the aromatic group attached at position 3 of the ligand. In the case of **23**, there are no aromatic groups so this argument does not hold here.

6.2.4 Tris(3-cyano-2,4-pentanedionato)aluminium(III)

When $Al(NO_3)_3 \cdot 9H_2O$ was reacted with Hcpd in an analogous way to that used to form **23**, the reaction did not give any product in high yield. Hence an alternative method was employed to form $[Al(cpd)_3]$. $Al(NO_3)_3 \cdot 9H_2O$ and Hcpd were dissolved in a mixture of methanol/water (50/50 v/v) to which $NaHCO_3$ in methanol/water was added slowly with continuous stirring. A white powder precipitated after the complete addition of the base. This was separated by filtration and washed with water to remove unreacted base. The product was dried in air, dissolved in $CDCl_3$ and analysed by ^1H and ^{13}C NMR spectroscopy. Comparison of the X-ray powder diffraction patterns of the product and the free ligands showed they were different compounds. Results from FAB mass-spectrometry further confirmed the formation of $[Al(cpd)_3]$ (**24**). The molecular mass ion was observed as the sodium salt at *m/z* 422 ($[M+Na]^+$), other fragments such as $[HAl(cpd)_2]^+$ at 275 and $[Al(cpd)]^+$ at *m/z* 159 where also observed.

Comparison of the X-ray powder patterns for **23** and **24** showed significant differences confirming they are not isostructural. This is consistent with the fact that in the case of the aluminium complex there are water molecules incorporated in the structure which influences the way the molecules pack hence giving rise to a different powder spectrum. The presence of the water molecules in **24** was further confirmed by NMR spectrometry and microanalysis.

6.3 Mixed metal networks

The discrete compounds **21**, **23** and **24** were reacted with silver(I) salts in an attempt to form mixed metal networks. Silver(I) was chosen as the metal source for two reasons. Firstly as a d^{10} metal, silver(I) can adopt different geometries such as linear, trigonal planar or tetrahedral and secondly, silver(I) is known to form robust bonds with the lone pair of the nitrile group.

6.3.1 Mixed metal networks from [Cu(cpd)$_2$] and silver(I)

In [Cu(cpd)$_2$] (**21**) the two cyano groups are pointing at approximately 180° from one another. Depending on the coordination geometry that the silver centre adopts, the final networks from **21** and silver(I) can be either 1-D, 2-D or 3-D. Networks incorporating silver are known to depend on the counter ions used.[18,19] **21** was thus reacted with a range of AgX salts (X = nitrate, phenoxide, camphorate and triflate) but only the reactions with $AgNO_3$ afforded a crystalline material that could be characterised by single crystal X-ray crystallography.

21 was dissolved in DMF and $AgNO_3$ was dissolved in MeOH. The latter solution was layered on top of the former and the sample tube covered with foil. Slow diffusion of the solutions allowed the formation of {Ag[Cu(cpd)$_2$]NO_3}$_\infty$(**25**). The crystallographic data for **25** are given in Table 6.8. The asymmetric unit consists of one copper centre, two cpd$^-$ ligands, one silver centre and one nitrate ion (Figure 6.19).

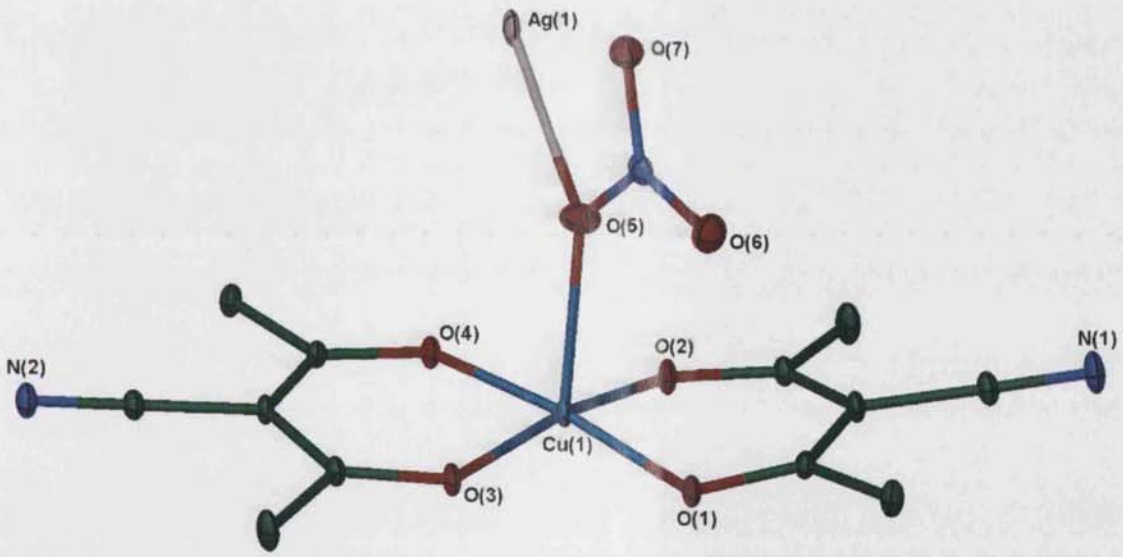

Figure 6.19. Asymmetric unit of **25** with thermal ellipsoids at 30% probability. Hydrogen atoms are omitted for clarity.

Table 6.8. Crystallographic data for **25**.

Formula	$C_{12}H_{12}AgCuN_3O_7$
M	481.66
T/ K	150(2)
Crystal system	Triclinic
Space group, *Z*	*P*-1, 2
a/ Å	7.7735(2)
b/ Å	8.4210(2)
c/ Å	13.4553(4)
α/ °	91.187(1)
β/ °	97.692(1)
γ/ °	117.238(1)
U/ Å^3	772.71(4)
Crystal size/ mm	0.3 x 0.05 x 0.05
Wavelength/ Å	0.6751
Theta range for data collected/ °	3.39 to 30.88
Reflections collected/ observed (>2σ)	9381/ 4564
Data completeness	0.882
Max. and min. transmission	0.8675 and 0.4985
Goodness of fit F^2	1.043
Final *R* indices (I >2σ(I))	*R*1 = 0.0216, *wR*2 = 0.0564
R indices (all data)	*R*1 = 0.0242, *wR*2 = 0.0581
Largest diff. peak and hole eÅ^{-3}	0.496 and -0.699

The copper adopts a distorted square pyramidal geometry with τ = 0.076.[17] A selected list of bond lengths and angles are given in Tables 6.9 and 6.10. The four equatorial positions on the copper are occupied by oxygen atoms, O(1)-O(4), from two different cpd$^-$ ligands while the axial position is occupied by an oxygen atom O(5) from a nitrate ion which also binds to the silver centre (Figure 6.19). The silver adopts a distorted T-shape geometry whereby the coordination sphere is occupied by O(5), N(1) and N(2) with the nitrogen atoms coming from the cyano groups of two cpd$^-$ ligands.

Table 6.9. Selected bond lengths for **25**.[II]

Bond atoms	Bond length/ Å
Cu(1)-O(1)	1.9264(10)
Cu(1)-O(2)	1.9301(9)
Cu(1)-O(3)	1.9396(9)
Cu(1)-O(4)	1.9415(9)
Cu(1)-O(5)	2.2229(12)
N(1)-C(6)	1.1576(17)
N(2)-C(12)	1.1508(17)
Ag(1)-N(1)#2	2.1366(12)
Ag(1)-N(2)#1	2.1185(12)
Ag(1)-O(5)	2.4802(13)

Table 6.10. Selected bond angles for **25**.[II]

Atoms	Angle/ °
O(1)-Cu(1)-O(2)	92.19(4)
O(1)-Cu(1)-O(5)	98.92(5)
O(2)-Cu(1)-O(5)	92.89(5)
O(3)-Cu(1)-O(4)	91.91(4)
O(3)-Cu(1)-O(5)	98.33(5)
O(4)-Cu(1)-O(5)	87.85(5)
N(1)#2-Ag(1)-O(5)	94.40(5)
N(2)#1-Ag(1)-O(5)	102.95(5)
N(2)#1-Ag(1)-N(1)#2	161.76(5)

The two cyano groups of the cpd$^-$ ligands bind to the silver in an approximately linear fashion to form a 1-D chain, while the bridging nitrates coordinates to the silver atoms from one chain and to copper atoms from another chain to generate ladders (Figure 6.20) which pack parallel to each other as shown in Figure 6.21. Weak hydrogen bond interactions between oxygen atoms O(7) form the nitrate groups of one ladder and the methyl hydrogen atoms H(1C) (O(7)···H(1C) 2.382Å) from the cpd$^-$ ligands of adjacent ladder are also present.

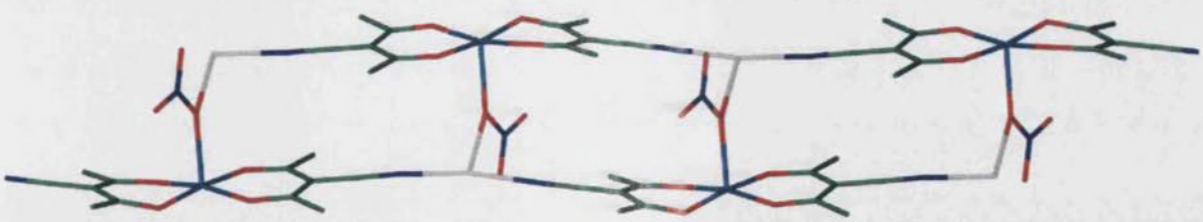

Figure 6.20. 1-D ladder in the structure of $\{Ag[Cu(cpd)_2]NO_3\}_\infty$ viewed perpendicular to the (1,0,0) plane.

[II] Symmetry transformations used to generate equivalent atoms:
#1 -x+1,-y+1,-z+1 #2 -x+1,-y,-z

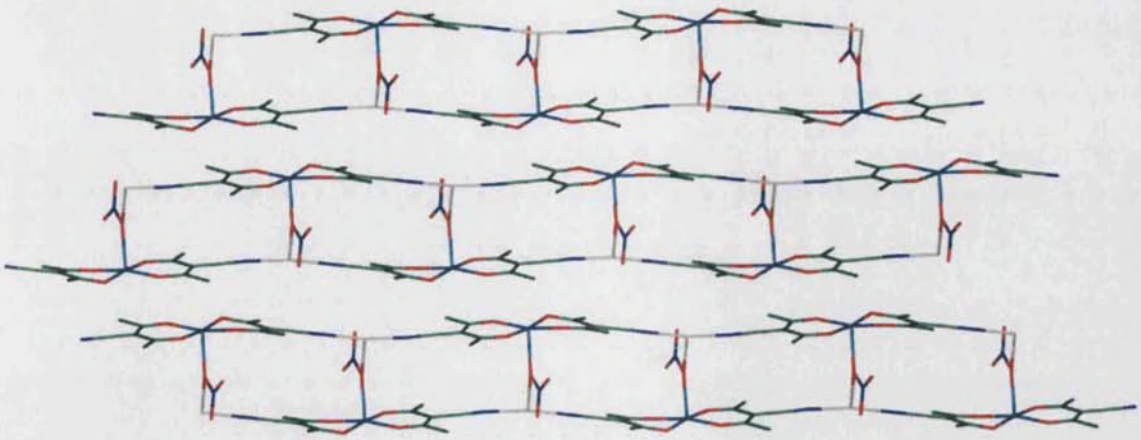

Figure 6.21. Stacking of the ladders in $\{Ag[Cu(cpd)_2]NO_3\}_\infty$ viewed down the *a* axis.

A comparison of the cyano bond lengths for **21** and **25** shows that there is no significant change in the C-N bond length between the coordinated and uncoordinated cyano groups.

6.3.2 Mixed metal complexes from [Fe(cpd)$_3$] and silver

[Fe(cpd)$_3$] (**23**) was dissolved in appropriate solvents and reacted with either silver(I) salts or Zn_2(acetate)$_4$, as the latter has vacant axial sites. Only crystals from the $AgNO_3$ reactions were obtained. The networks formed from **23** and $AgNO_3$ were found to be dependent on the solvent mixtures.

6.3.2.1 Reaction of [Fe(cpd)] with $AgNO_3$ in acetone/methanol

23 was dissolved in acetone and a solution of $AgNO_3$ in methanol was carefully layered on top. The vial was covered with foil and left in the dark to allow slow diffusion of the two solutions into each other. Three different compounds, **26**, **27** and **28** were isolated from this reaction and identified by X-ray crystallography as $\{Ag_2[Fe_2(\mu\text{-OMe})_2(cpd)_4](NO_3)_2{\cdot}C(CH_3)_2O\}_\infty$, $\{Ag[Fe_2(\mu\text{-OMe})_2(cpd)_4]NO_3\}_\infty$ and $\{Ag[Fe(cpd)_3]NO_3\}_\infty$ respectively.

26 and **27** were obtained after leaving the reaction standing for two weeks, and both compounds had light red colouration with the former consisted of small hexagonal plates while the latter were long blocks. **26** was the major compound while **27** was only

formed in minor quantities as no trace of this compound was found in the X-ray powder spectrum recorded for the mixture. Due to the low yield of **26**, a second reaction was undertaken and left for one month but the crystals that formed appeared to be darker in colour. X-ray powder diffraction data showed that **26** was absent from the reaction that was left for one month with a new compound, **28** being formed.

The asymmetric unit of **26** consists of two iron centres, two methoxy ligands, four cpd⁻ ligands, two silver centres, two nitrate counter ions and a guest acetone molecule (Figure 6.22). Crystallographic data for **26** are summarised in Table 6.11.

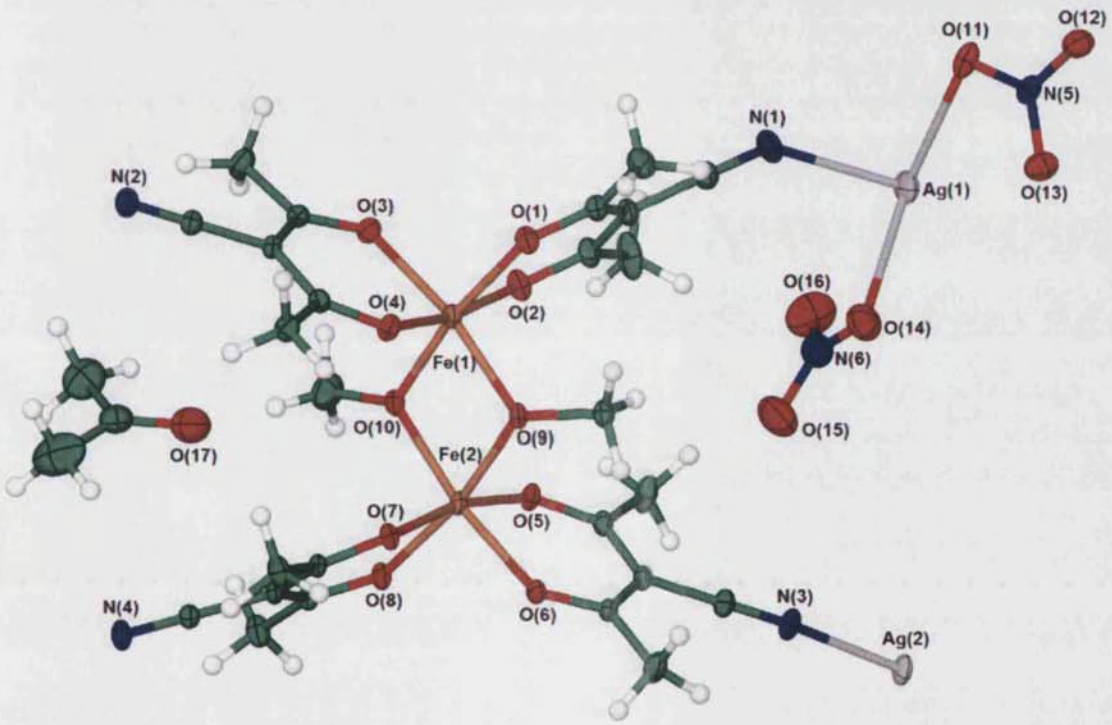

Figure 6.22. The asymmetric unit of **26** showing thermal ellipsoids at 30% probability.

Table 6.11. Crystallographic data for **26**.

Formula	$C_{29}H_{36}Ag_2Fe_2N_6O_{17}$
M	1068.08
T/ K	150(2)
Crystal system	Monoclinic
Space group, *Z*	$P2_1/n$, 4
a/ Å	17.2710(2)
b/ Å	12.5520(2)

c/ Å	18.9510(3)
α/ °	90
β/ °	111.2170(10)
γ/ °	90
U/ Å^3	3829.83(10)
Crystal size/ mm	0.17 x 0.13 x 0.08
Wavelength/ Å	0.71073
Theta range for data collected/ °	3.52 to 30.03
Reflections collected/ observed (>2σ)	74741/ 6904
Data completeness	0.996
Max. and min. transmission	0.809 and 0.744
Goodness of fit F^2	1.012
Final *R* indices (I >2σ(I))	*R*1 = 0.0585, *wR*2 = 0.1348
R indices (all data)	*R*1 = 0.1123, *wR*2 = 0.1586
Largest diff. peak and hole eÅ^{-3}	1.572 and -0.929

The two iron centres have distorted octahedral geometry. Four oxygen atoms from the cpd$^-$ ligands and two oxygen atoms from the methoxy ligands populate the coordination sphere of each metal centre. The methoxy ligands bridge the two iron centres together to form the core building unit of [$Fe_2(\mu\text{-}OMe)_2(cpd)_4$]. The closest distance between the two iron centres is 3.0783(9) Å.

The two silver centres adopt different geometries. Ag(1) has a distorted tetrahedral geometry which is occupied by two oxygen atoms O(11) and O(14) from two separate nitrate counter ions and two nitrogen atoms N(1) and N(2) from two cpd$^-$ ligands. Ag(2) adopts a distorted trigonal planar geometry with the coordination sphere being filled by one oxygen atom, O(12), from a nitrate counter ion and two nitrogen atoms N(3) and N(4) from two cyano groups. Thus, all the cyano nitrogen atoms are coordinated to silver centres. The closest distance between two silver centres is 3.3232(6) Å.

The network of **26** consists of sheets with the guest acetone molecules residing inside the spaces within the sheets (Figure 6.23). The two sheets pack parallel to one another as shown in Figure 6.24.

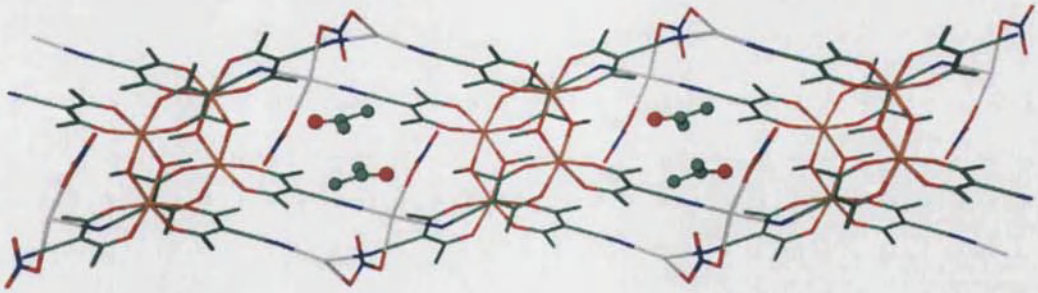

Figure 6.23. The sheet of **26**. The network is represented as sticks while the guest acetone molecules are represented as balls and sticks.

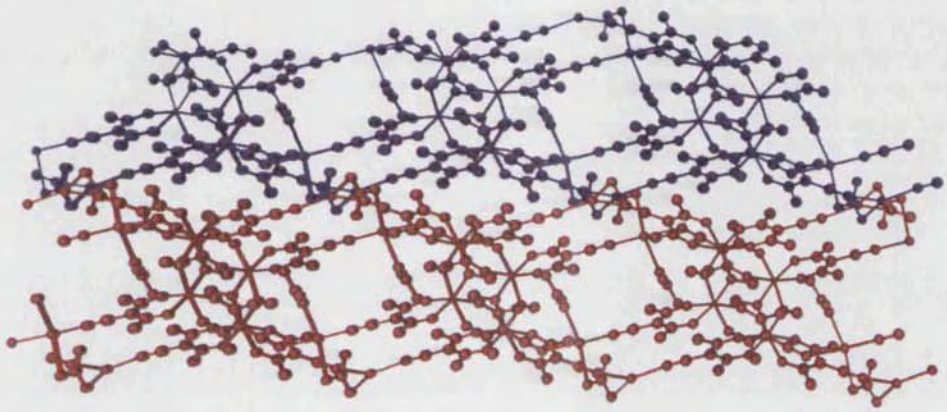

Figure 6.24. Two sheets packed parallel to one another.

On comparing the average carbon-nitrogen bond lengths of the cyano groups of **26** (1.140 Å) (individual bond lengths given in Table 6.12) to the average cyano bond length of $[Fe(cpd)_3]$, **23** (1.150 Å), it can be noticed that the two average values are of comparable magnitude. Moreover, there are no significant differences between the coordinated and uncoordinated nitrogen-oxygen bond lengths of the nitrate ions based as N(5) and N(6) (Table 6.12).

The average bite angle of the cpd^- ligands in **26** (individual bond angles given in Table 6.13) (85.2°) is smaller than the cpd^- average bite angle of $[Fe(cpd)_3]$ (87.8°) (individual bond angles given in Table 6.6). The angles between the Fe-O-O and the cpd^- ligand planes of **26** (Table 6.14) show that the angles between the planes vary from 11.47° to 14.46°. While these values are comparable to those for **23** (Table 6.7), the angles for **26** have a smaller range than those for **23** (2.43° to 23.30°).

Table 6.12. Selected bond lengths for **26**.[III]

Bond atoms	Bond lengths/ Å	Bond atoms	Bond lengths/ Å
Fe(1)-O(1)	2.008(3)	Fe(1)-O(9)	1.977(3)
Fe(1)-O(2)	1.999(3)	Fe(1)-O(10)	1.956(3)
Fe(1)-O(3)	1.993(3)	Fe(2)-O(9)	1.976(3)
Fe(1)-O(4)	2.017(3)	Fe(2)-O(10)	1.948(3)
Fe(2)-O(5)	2.017(3)	Ag(1)-N(1)	2.311(5)
Fe(2)-O(6)	2.008(3)	Ag(1)-N(2)#1	2.251(4)
Fe(2)-O(7)	2.020(3)	Ag(1)-O(11)	2.564(4)
Fe(2)-O(8)	2.016(3)	Ag(1)-O(14)	2.446(5)
N(1)-C(6)	1.140(7)	Ag(2)-N(3)	2.160(4)
N(2)-C(12)	1.146(6)	Ag(2)-N(4)#1	2.226(4)
N(3)-C(18)	1.139(6)	Ag(2)-O(12)#2	2.439(4)
N(4)-C(24)	1.136(6)		
O(11)-N(5)	1.239(5)	O(14)-N(6)	1.218(7)
O(12)-N(5)	1.241(5)	O(15)-N(6)	1.251(8)
O(13)-N(5)	1.250(5)	O(16)-N(6)	1.261(8)

Table 6.13. Selected bond angles for **26**.[III]

Atoms	Angle/ °	Atoms	Angle/ °
O(2)-Fe(1)-O(1)	85.08(14)	O(6)-Fe(2)-O(5)	85.02(13)
O(3)-Fe(1)-O(4)	85.77(13)	O(8)-Fe(2)-O(7)	85.07(13)
Fe(2)-O(9)-Fe(1)	102.29(13)	Fe(2)-O(10)-Fe(1)	104.13(14)
N(2)#1-Ag(1)-N(1)	136.7(2)	N(2)#1-Ag(1)-O(11)	101.71(14)
N(1)-Ag(1)-O(11)	94.87(17)	N(3)-Ag(2)-O(12)#2	122.79(15)
N(1)-Ag(1)-O(14)	87.24(19)	N(3)-Ag(2)-N(4)#1	141.57(16)
O(14)-Ag(1)-O(11)	130.44(15)	N(4)#1-Ag(2)-O(12)#2	92.84(15)
N(2)#1-Ag(1)-O(14)	110.16(18)		

[III] Symmetry transformations used to generate equivalent atoms:
#1 x+1/2,-y+1/2,z-1/2 #2 -x+1,-y+1,-z

Table 6.14. Angles between the cpd⁻ ligand plane and Fe-O-O plane for **26**.

cpd⁻ ligand plane atoms	Fe-O-O plane atoms	Angle between planes/ °
C(1) to C(6), N(1)	Fe(1)-O(1)-O(2)	11.47
C(7) to C(12), N(2)	Fe(1)-O(3)-O(4)	12.42
C(13) to C(18), N(3)	Fe(2)-O(5)-O(6)	14.12
C(19) to C(24), N(4)	Fe(2)-O(7)-O(8)	14.46

The second compound obtained from the reaction between $[Fe(cpd)_3]$ and $AgNO_3$ left standing for two weeks is $\{Ag[Fe_2(\mu\text{-}OMe)_2(cpd)_4]NO_3\}_\infty$ **27**. The asymmetric unit of **27** (Figure 6.25) consists of two iron centres, two methoxy ligands, four cpd⁻ ligands, one nitrate anion and one silver centre. Crystallographic data for **27** are given in Table 6.15. Two bridging methoxy ligands replaced two of the original cpd⁻ ligands in **23** to give core units of $[Fe_2(\mu\text{-}OMe)_2(cpd)_4]$. The geometry around each iron centre is distorted octahedral with the coordination spheres being populated by two oxygen atoms from two methoxy ligands and four oxygen atoms from two cpd⁻ ligands. The silver adopts a distorted tetrahedral geometry, and the coordination sphere of the silver is occupied by three nitrogen atoms N(1), N(2) and N(4) from three cpd⁻ cyano groups and one oxygen atom from a nitrate counter ion. One of the nitrogen atoms of the cpd⁻ ligands, N(3), remains uncoordinated. The overall network is dominated by 1-D ladder motif (Figure 6.26).

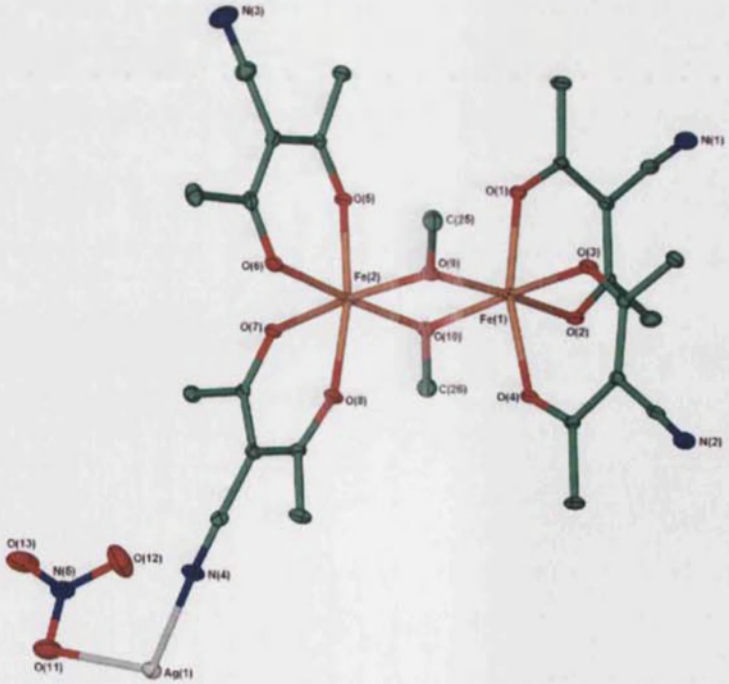

Figure 6.25. Asymmetric unit of **27** showing thermal ellipsoids at 30% probability. Hydrogen atoms are omitted for clarity.

Table 6.15. Crystallographic data for **27**.

Empirical formula	$C_{26}H_{30}AgFe_2N_5O_{13}$
M	840.12
T/ K	150(2)
Crystal system	Triclinic
Space group, *Z*	*P*-1, 2
a/ Å	11.1107(5)
b/ Å	11.3532(5)
c/ Å	13.0922(6)
α/ °	99.941(1)
β/ °	93.406(1)
γ/ °	96.678(1)
U/ Å^3	1610.30(13)
Crystal size/ mm	0.06 x 0.06 x 0.04
Wavelength/ Å	0.84600
Theta range for data collected/ °	4.21 to 33.07
Reflections collected/ observed (>2σ)	12013/ 5503
Data completeness	0.910
Max. and min. transmission	0.955, 0.910
Goodness of fit F^2	1.067
Final *R* indices ($I>2\sigma(I)$)	$R1 = 0.0427$, $wR2 = 0.1006$
R indices (all data)	$R1 = 0.0515$, $wR2 = 0.1063$
Largest diff. peak and hole eÅ^{-3}	1.042, -1.012

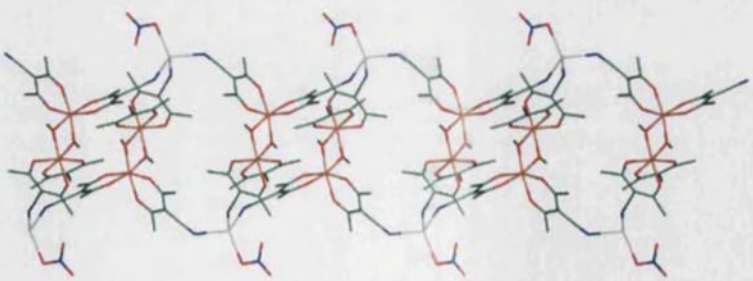

Figure 6.26. 1-D ladder of $\{Ag[Fe_2(\mu\text{-}OMe)_2(cpd)_4]NO_3\}_\infty$ (**27**) viewed perpendicular to the (0,1,0) plane.

The bond lengths of the cyano groups do not show significant alterations when coordinated to the silver centres. This can be deduced from the comparison of the range for the C-N bond lengths of **23** (Table 6.5) (1.142(4)-1.160(4)Å) and **27** (1.143(5)-1.152(5)Å)

(Table 6.16) and between the coordinated, C(6)-N(1) (1.148(5)Å), C(12)-N(2) (1.144(5)Å) and C(24)-N(4) (1.143(5)Å), and uncoordinated C(18)-N(3) (1.152(5)Å) bonds of **27**.

The average bite angle of the cpd$^-$ ligands in **27** (85.2°) (Table 6.17) is the same as the average ligand bite angle of **26** (85.2°) (Table 6.13).

Table 6.16. Selected bond lengths for **27**.[IV]

Bond atoms	Bond length/ Å	Bond atoms	Bond length/ Å
Fe(1)-O(1)	2.007(2)	Ag(1)-N(1)#2	2.344(4)
Fe(1)-O(2)	1.986(2)	Ag(1)-N(2)#1	2.312(3)
Fe(1)-O(3)	2.027(3)	Ag(1)-O(11)	2.381(3)
Fe(1)-O(4)	2.020(2)	Ag(1)-N(4)	2.364(3)
Fe(1)-O(9)	1.969(2)	N(1)-C(6)	1.148(5)
Fe(1)-O(10)	1.962(2)	N(2)-C(12)	1.144(5)
Fe(2)-O(5)	2.001(2)	N(3)-C(18)	1.152(5)
Fe(2)-O(6)	2.006(3)	N(4)-C(24)	1.143(5)
Fe(2)-O(7)	2.006(2)		
Fe(2)-O(8)	2.018(2)	N(5)-O(11)	1.266(4)
Fe(2)-O(9)	1.995(2)	N(5)-O(12)	1.235(5)
Fe(2)-O(10)	1.963(2)	N(5)-O(13)	1.220(4)

Table 6.17. Selected bond angles for **27**.[IV]

Atoms	Angles/ °	Atoms	Angles/ °
Fe(1)-O(9)-Fe(2)	101.46(10)	N(1)#2-Ag(1)-O(11)	116.55(12)
Fe(1)-O(10)-Fe(2)	102.87(11)	N(2)#1-Ag(1)-O(11)	108.00(11)
O(2)-Fe(1)-O(1)	85.57(10)	N(4)-Ag(1)-O(11)	116.86(11)
O(4)-Fe(1)-O(3)	84.41(10)	N(2)#1-Ag(1)-N(1)#2	112.31(12)
O(5)-Fe(2)-O(6)	85.51(10)	C(6)-N(1)-Ag(1)#2	134.1(3)
O(7)-Fe(2)-O(8)	85.44(10)	C(12)-N(2)-Ag(1)#1	137.4(3)
N(1)#2-Ag(1)-N(4)	102.92(12)	C(24)-N(4)-Ag(1)	158.4(3)
N(2)#1-Ag(1)-N(4)	98.90(11)		

[IV] Symmetry transformations used to generate equivalent atoms:
#1 -x+3,-y+2,-z+1 #2 -x+3,-y+2,-z

$\{Ag[Fe(cpd)_3]NO_3\}_\infty$, (**28**) was obtained when the reaction between $[Fe(cpd)_3]$ and $AgNO_3$ was left standing for one month. The asymmetric unit of **28** consists of one iron centre, three cpd$^-$ ligands, one silver atom and one nitrate anion (Figure 6.27). Crystallographic data for **28** are given in Table 6.18.

The iron centre adopts a distorted octahedral geometry. The coordination sphere of the iron is populated by six oxygen atoms from three cpd$^-$ ligands. Two nitrogen atoms from the cyano groups and one oxygen atom from the nitrate ion occupy the T-shaped coordination sphere of the silver centre. One of the nitrogen atoms, N(2), of the cpd$^-$ ligand remains uncoordinated.

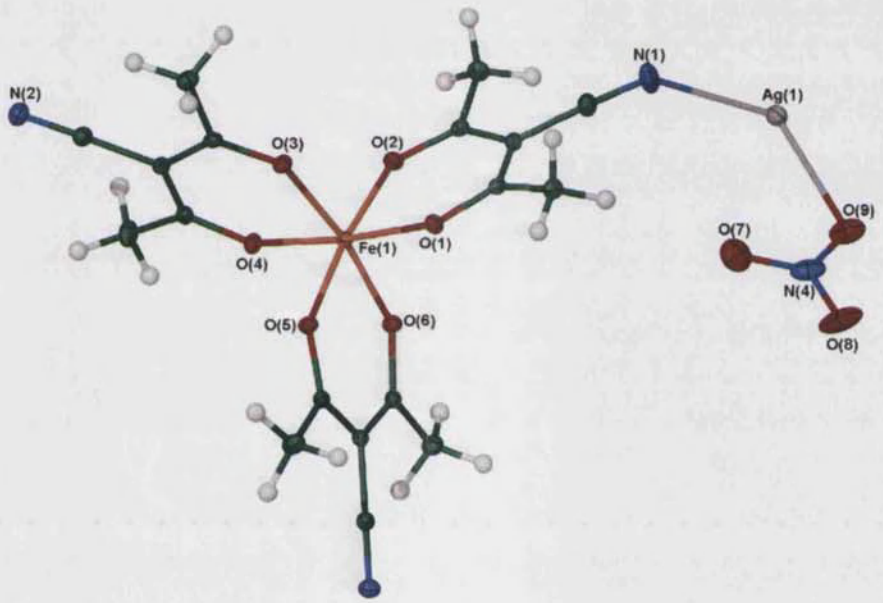

Figure 6.27. Asymmetric unit of **28** showing thermal ellipsoids at 30% probability.

Table 6.18. Crystallographic data for **28**.

Formula	$C_{18}H_{18}AgFeN_4O_9$
M	598.08
T/ K	150(2)
Crystal system	Monoclinic
Space group, *Z*	$P2_1/c$, 4
a/ Å	14.0460(1)
b/ Å	11.3220(1)
c/ Å	15.0110(1)

α/ °	90
β/ °	116.650(1)°
γ/ °	90
U/ Å^3	2133.57(3)
Crystal size/ mm	0.25 x 0.25 x 0.2
Wavelength/ Å	0.71073
Theta range for data collected/ °	5.61 to 30.03
Reflections collected/ observed (>2σ)	54883/ 5597
Data completeness	0.981
Max. and min. transmission	0.73, 0.61
Goodness of fit F^2	1.054
Final R indices (I>2σ(I))	$R1$ = 0.0266, $wR2$ = 0.0691
R indices (all data)	$R1$ = 0.0305, $wR2$ = 0.0712
Largest diff. peak and hole eÅ^{-3}	0.565, -0.752

28 forms 1-D chains (Figure 6.28) and there are no significant interactions between the chains.

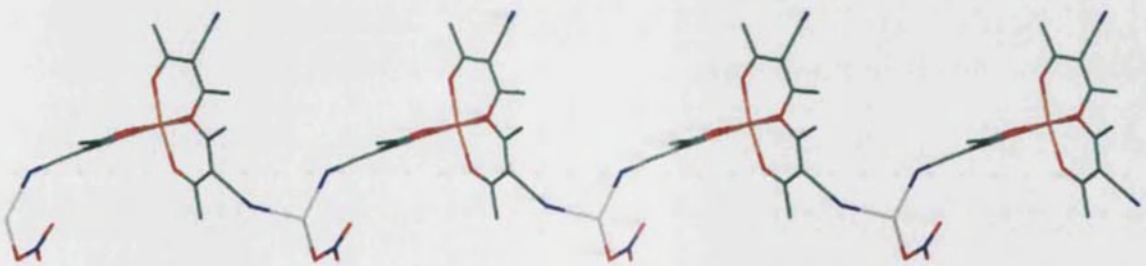

Figure 6.28. 1-D chain of **28** viewed perpendicular to the (1,0,0) plane.

The average bond length of the nitrile group in **28** (1.148 Å) (individual bond lengths are given in Table 6.19) does not differ significantly from the average bond length of the nitrile group in [Fe(cpd)$_3$] (**23**) (1.149 Å). One other comparison between the two compounds is the buckling of the cpd$^-$ ligands and the angle between the nitrogen atoms of the cpd$^-$ (Figures 6.18 and 6.29). In **28**, the angle between the nitrogen atoms of the cpd$^-$ ligand still deviates away from 120° (Figure 6.29) while the angles between the cpd$^-$ ligand planes and the Fe-O-O planes of **28** (Table 6.21) fall in the range of similar angles of **23** (2.43-23.30°) (Table 6.7).

Table 6.19. Selected bond lengths for **28**.[v]

Bond atoms	Lengths/ Å	Bond atoms	Lengths/ Å
Fe(1)-O(1)	1.9655(11)	Ag(1)-O(9)	2.3320(17)
Fe(1)-O(2)	1.9892(11)	Ag(1)-N(3)#1	2.3523(15)
Fe(1)-O(3)	1.9747(11)	Ag(1)-N(1)	2.2999(18)
Fe(1)-O(4)	1.9979(11)		
Fe(1)-O(5)	1.9964(11)	O(7)-N(4)	1.254(3)
Fe(1)-O(6)	1.9998(11)	O(8)-N(4)	1.237(3)
N(1)-C(6)	1.149(2)	O(9)-N(4)	1.264(3)
N(2)-C(12)	1.147(2)	N(3)-C(18)	1.149(2)

Table 6.20. Selected bond angles for **28**.[v]

Atoms	Angles/ °	Atoms	Angles/ °
O(1)-Fe(1)-O(2)	87.00(4)	O(4)-Fe(1)-O(6)	87.85(5)
O(1)-Fe(1)-O(3)	90.64(5)	O(4)-Fe(1)-O(3)	86.04(4)
O(1)-Fe(1)-O(5)	88.34(5)	O(5)-Fe(1)-O(4)	96.02(5)
O(1)-Fe(1)-O(6)	95.88(5)	O(5)-Fe(1)-O(6)	86.05(4)
O(2)-Fe(1)-O(6)	88.62(5)	O(9)-Ag(1)-N(3)#1	121.11(6)
O(3)-Fe(1)-O(2)	96.93(5)	N(1)-Ag(1)-N(3)#1	99.41(6)
O(3)-Fe(1)-O(5)	88.95(5)	N(1)-Ag(1)-O(9)	133.76(6)

Table 6.21. Angles between cpd$^-$ ligand plane and Fe-O-O plane for **28**.

cpd$^-$ ligand plane atoms	Fe-O-O plane atoms	Angle between planes/ °
C(1) to C(6), N(1)	Fe(1)-O(1)-O(2)	6.26
C(7) to C(12), N(2)	Fe(1)-O(3)-O(4)	3.71
C(13) to C(17), N(3)	Fe(1)-O(5)-O(6)	19.45

[v] Symmetry transformations used to generate equivalent atoms:
#1 x-1,-y+1/2,z-1/2 #2 x+1,-y+1/2,z+1/2

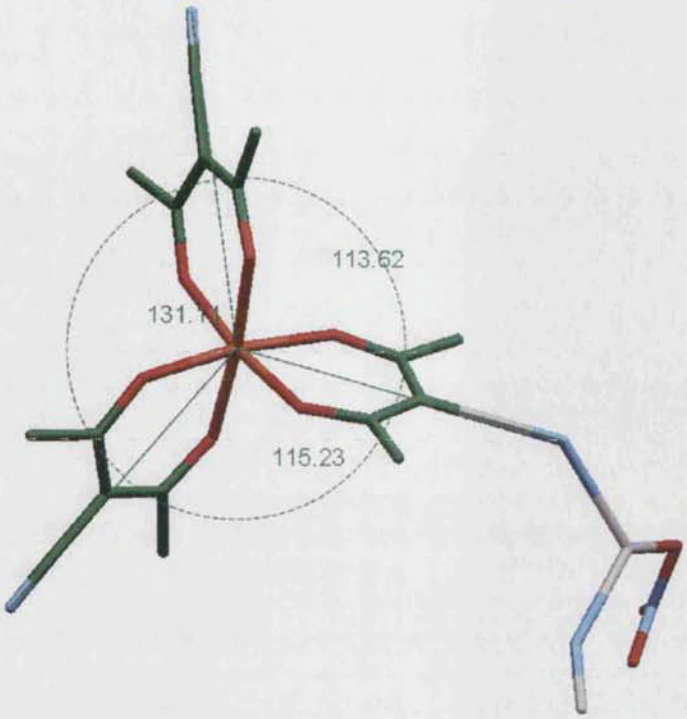

Figure 6.29. The angles between the nitrogen atoms of the cpd⁻ ligands of **28**.

6.3.2.2 Reaction between [Fe(cpd)$_3$] and AgNO$_3$ in methanol

When [Fe(cpd)$_3$] was reacted with AgNO$_3$ in methanol, three products were obtained. These were identified as being, {Ag[Fe$_2$(μ-OMe)$_2$(cpd)$_4$]NO$_3$}$_\infty$, (**27**) and {Ag[Fe(cpd)$_3$]NO$_3$}$_\infty$ (**28**), also obtained from the reaction using an acetone/methanol solvent mixture, and a new product identified as {Ag[Fe$_2$(μ-OMe)$_2$(cpd)$_4$](OH)·0.4H$_2$O}$_\infty$, (**29**). The product distribution also varied. In the acetone/methanol mixture **27** was obtained in minor quantities, while in the reaction using methanol only **27** was obtained as a major product while **29** was obtained in minor quantities.

The asymmetric unit of **29** (Figure 6.30) consists of half an iron centre, half a methoxy ligand, one cpd⁻ ligand, one quarter silver centre and three oxygen fragments with site occupancy factors of 0.1, 0.1 and 0.5 for O(s1), O(h2) and O(h1) respectively. The methoxy carbon is disordered over two sites in a 32:18 ratio and only the major position is shown in Figure 6.30. Crystallographic data for **29** are given in Table 6.22.

In order to balance the charge on the network, an additional 0.25 negative charge per asymmetric unit is required. Therefore it seems likely that the partial hydroxide counter

ion is located over 2 of the three partial oxygen sites and that one of these sites must be O(h1). As the hydrogen atoms attached to oxygen atoms O(h1), O(h2) and O(s1) could not be reliably located they were omitted from the final structure and consequently the assignment of hydroxide versus water fragments is ambiguous. The shortest distances between the oxygen atoms O(s1)···O(h2) is 2.778(3) Å which suggests the presence of strong OH···O hydrogen bonding.

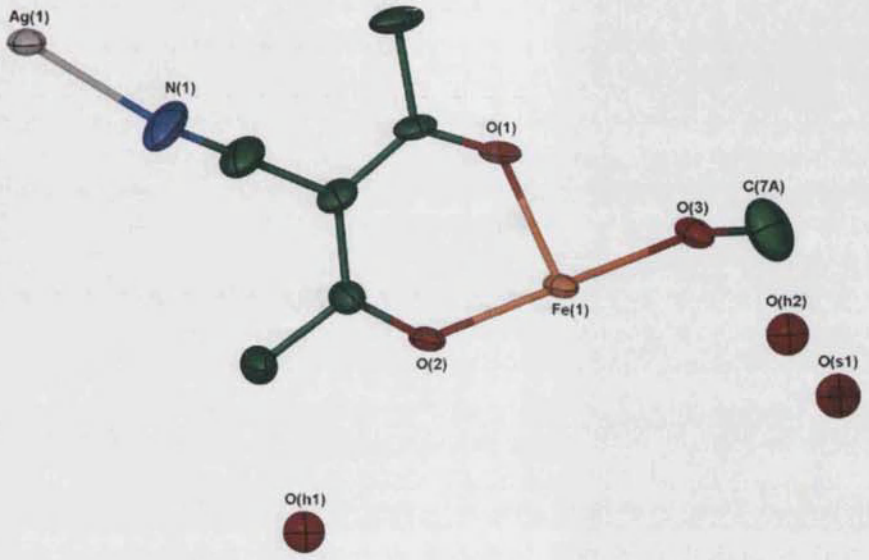

Figure 6.30. Asymmetric unit of **29** showing thermal ellipsoids at 30% probability. Hydrogen atoms are omitted for clarity.

Table 6.22. Crystallographic data for **29**.

Empirical formula	$C_{26}H_{31.8}AgFe_2N_4O_{11.4}$
M	797.49
T/ K	173(2)
Crystal system	Orthorhombic
Space group, *Z*	*Pccm*, 2
a/ Å	7.6634(5)
b/ Å	9.6825(7)
c/ Å	27.1105(19)
α/ °	90
β/ °	90
γ/ °	90
U/ Å^3	2011.6(2)

Crystal size/ mm	0.06 x 0.06 x 0.04
Wavelength/ Å	0.84600
Theta range for data collected/ °	4.37 to 33.11
Reflections collected/ observed (>2σ)	13713/ 1594
Data completeness	0.960
Max. and min. transmission	0.96, 0.93
Goodness of fit F^2	1.036
Final R indices (I>2σ(I))	$R1$ = 0.0646, $wR2$ = 0.2246
R indices (all data)	$R1$ = 0.0814, $wR2$ = 0.2420
Largest diff. peak and hole eÅ^{-3}	1.190, -0.518

The iron centre adopts a distorted octahedral geometry. A selected list of bond lengths and angles are given in Tables 6.23 and 6.24 respectively. The coordination sphere of the iron contains four oxygen atoms, O(1) and O(2) from two cpd$^-$ ligands, and two oxygen atoms, O(3), from methoxy ligands. The methoxy ligands bridge between two iron centres to give core units of [$Fe_2(\mu\text{-}OMe)_2(cpd)_4$] (Figure 6.31). The silver atoms adopt a tetrahedral geometry and are coordinated to four nitrogen atoms from four cpd$^-$ ligands (Figure 6.32).

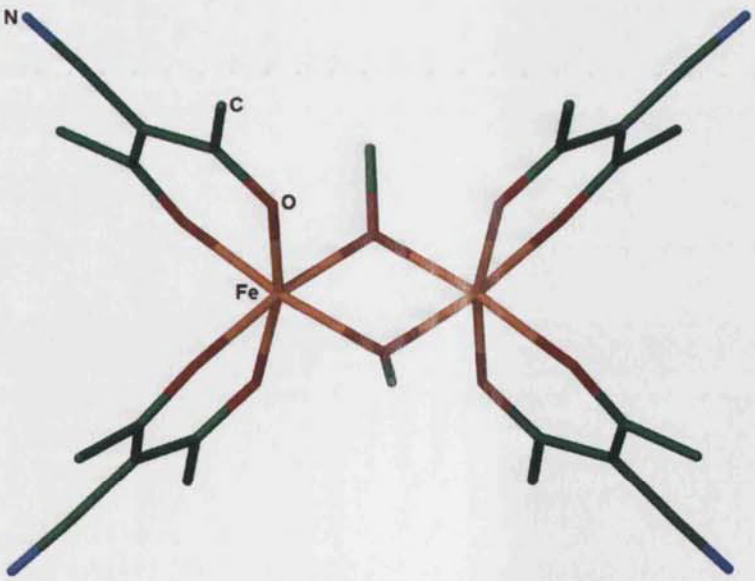

Figure 6.31. The $Fe_2(\mu\text{-}OMe)_2(cpd)_4$ core of **29**.

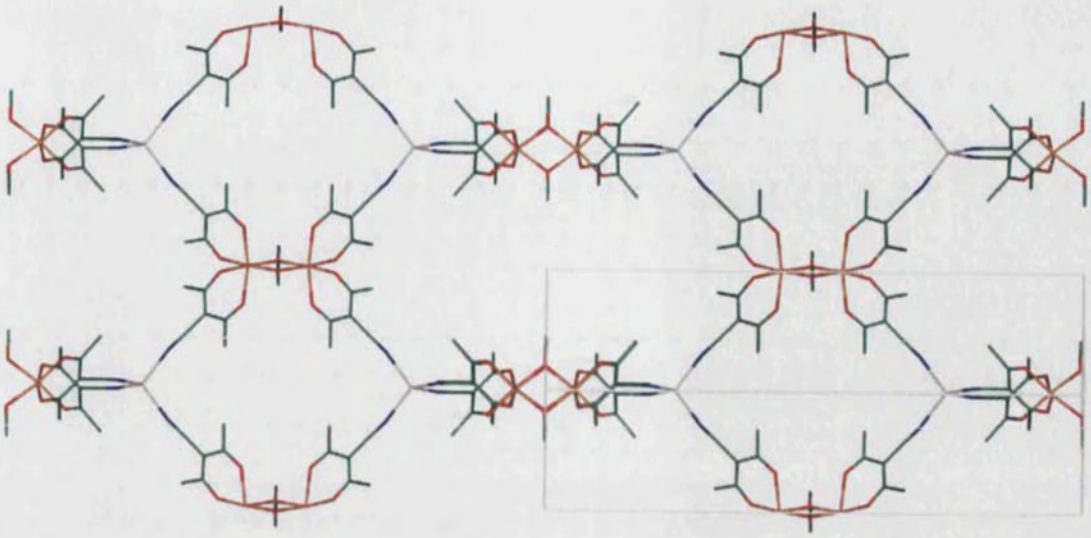

Figure 6.32. The hexagonal voids of **29**.

All the cyano nitrogen atoms in **29** are coordinated to silver centres to give a 3-D network which can be compared to the PtS net. The $[Fe_2(\mu\text{-}OMe)_2(cpd)_4]$ core units of **29** (Figure 6.33a) can be considered as a rectangular secondary building unit (SBU) which play the same structural role as the square planar platinum(II) atoms in the PtS structure (Figure 6.33b). Similarly, the silver centres in **29** (Figure 6.33c) and the sulphur in PtS adopt tetrahedral geometry (Figure 6.33d) and when comparing the network of **29** to the PtS structure, it can be observed the overall architectures are similar.

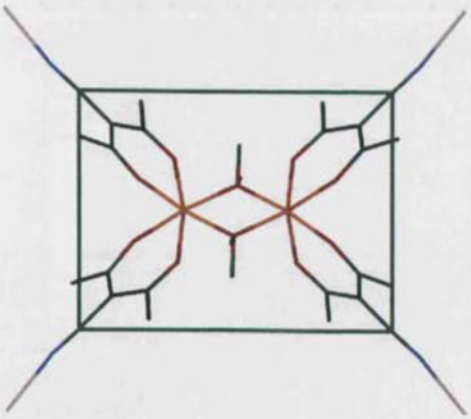

Figure 6.33a. Square SBU of **29**.

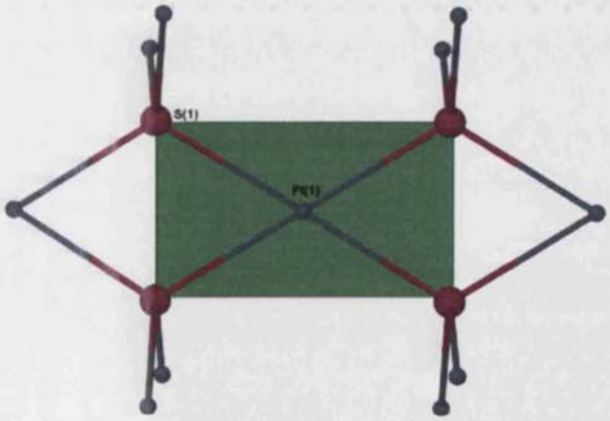

Figure 6.33b. Square motif of PtS.

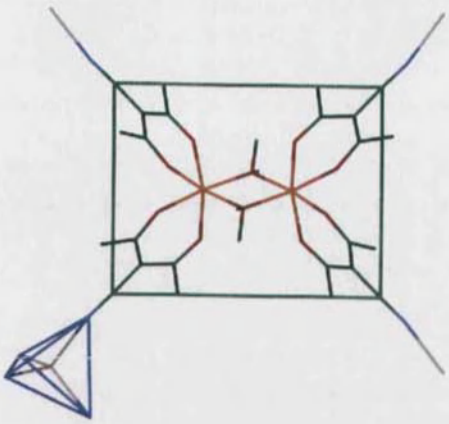

Figure 6.33c. Tetrahedral geometry around the silver in **29**.

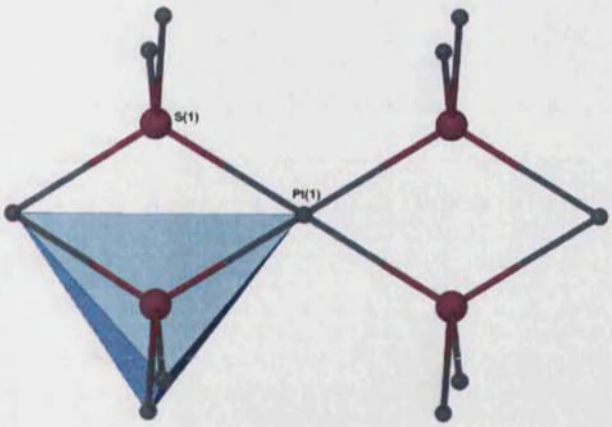

Figure 6.33d. Tetrahedral geometry around the sulphur in PtS.

The gross structure of **29** consists of two independent networks that interpenetrate (Figure 6.34).

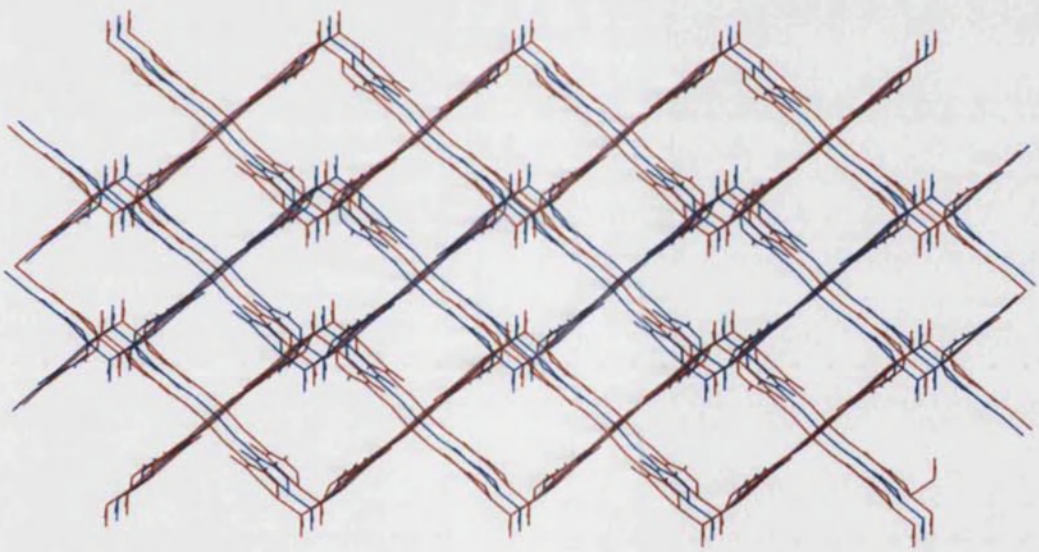

Figure 6.34. Two independent and interpenetrated nets (coloured red and blue) of **29**.

In $\{Ag_2[Fe_2[\mu\text{-}OMe)_2(cpd)_4](NO_3)_2 \cdot C(CH_3)O\}_\infty$ (**26**) as in **29**, all the nitrogen atoms of the cyano groups are coordinated to the silver centres. The carbon-nitrogen bond lengths of **26** (1.140(7), 1.146(6),1.139(6) and 1.136(6) Å) (Table 6.12) are comparable to the carbon-nitrogen bond lengths in **29** (1.157(9) Å) (Table 6.23) while the silver-nitrogen bond of **29** (2.210(6)Å) falls within the range of silver-nitrogen distances observed for **26** (2.160(4)-2.311(5)Å).

Table 6.23. Selected bond lengths for **29**.

Bond atoms	Length/ Å
Fe(1)-O(1)	2.004(3)
Fe(1)-O(2)	2.016(3)
Fe(1)-O(3)	1.967(3)
Ag(1)-N(1)	2.210(6)
N(1)-C(6)	1.157(9)

Table 6.24. Selected bond angles for **29**.[VI]

Atoms	Angle/ °
O(1)-Fe(1)-O(2)	85.69(14)
O(3)-Fe(1)-O(2)	172.05(16)
O(3)-Fe(1)-O(1)	93.53(16)
N(1)#2-Ag(1)-N(1)	110.0(4)
N(1)#1-Ag(1)-N(1)#2	107.1(5)
N(1)#2-Ag(1)-N(1)#3	111.4(4)
C(6)-N(1)-Ag(1)	169.6(8)

6.3.3 (3-cyano-2,4-pentanedionato)silver(I)

When a solution of $[Al(cpd)_3]$ (**24**) was dissolved in DMF and layered on a solution of $AgNO_3$ in methanol, colourless crystals were obtained. Single crystal X-ray analysis revealed the compound to be $\{[Ag(cpd)]\}_\infty$ (**30**). This indicates that the starting material $[Al(cpd)_3]$ has undergone a transmetallation reaction whereby the aluminium was replaced by silver. Given the relative hardness of aluminium and silver, it is surprising that the softer silver(I) centre has displaced aluminium(III) from the hard cpd^- oxygen donors.

The asymmetric unit in this structure consists of one silver centre and one ligand (Figure 6.35). The silver acts as a T-shaped connector and is bound to two oxygen atoms from two different ligands and one cyano nitrogen atom. The resulting network consists of 2-D sheets (Figure 6.36) which are held together by Ag···O contacts (2.65Å). Crystallographic data for **30** are given in Table 6.25.

[VI] Symmetry transformations used to generate equivalent atoms:
#1 -x-2,y,-z+1/2 #2 x,-y-2,-z+1/2
#3 -x-2,-y-2,z

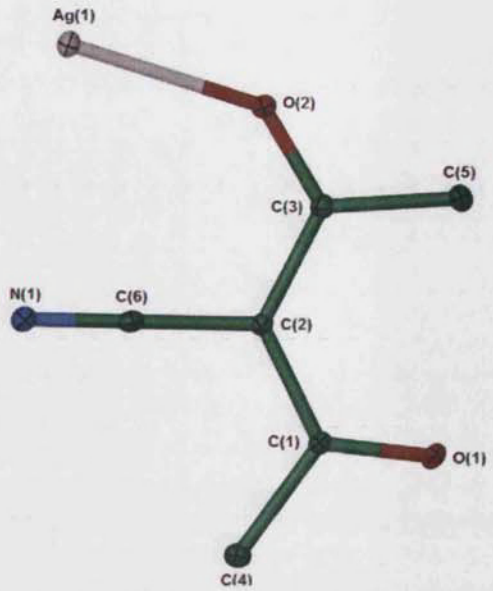

Figure 6.35. Asymmetric unit of **30** with thermal ellipsoids shown at 30% probability. Hydrogen atoms are removed for clarity.

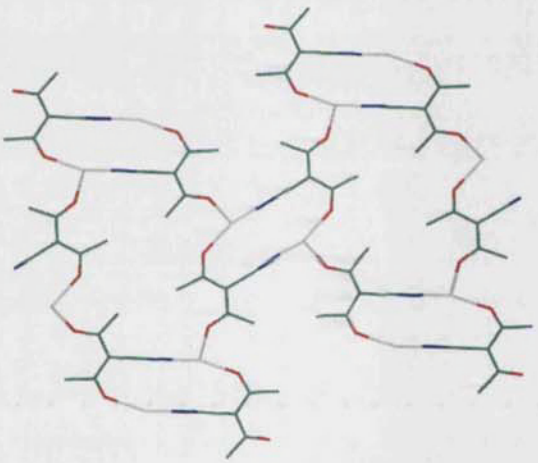

Figure 6.36. The 2-D sheets of **30** viewed down the *a* axis.

Table 6.25. Crystallographic data for **30**.

Empirical formula	$C_6H_6AgNO_2$
M	231.99
T/ K	150(2)
Crystal system	Monoclinic
Space group, *Z*	$P2_1/c$, 4
a/ Å	3.7884(2)
b/ Å	13.46346)
c/ Å	12.8252(6)

α/ °	90
β/ °	93.679(1)
γ/ °	90
U/ Å^3	652.50(5)
Crystal size/ mm	0.0.5 x 0.02 x 0.02
Wavelength/ Å	0.67510
Theta range for data collected °	2.87 to 30.93
Reflections collected/ observed (>2σ)	8153/ 1811
Data completeness	0.927
Goodness of fit F^2	1.004
Final R indices (I >2σ(I))	$R1$ = 0.0268, $wR2$ = 0.0618
R indices (all data)	$R1$ = 0.0354, $wR2$ = 0.0652
Largest diff. peak and hole eÅ^{-3}	1.111 and -0.727

It is noteworthy that in the structure of **30** the keto groups are trans to one another (Figure 6.37). In all other compounds reported in this chapter as well as all previously reported compounds containing cpd$^-$, both keto oxygen atoms face in the same direction relative to the ligand backbone, thus allowing it to act in a bidentate fashion.

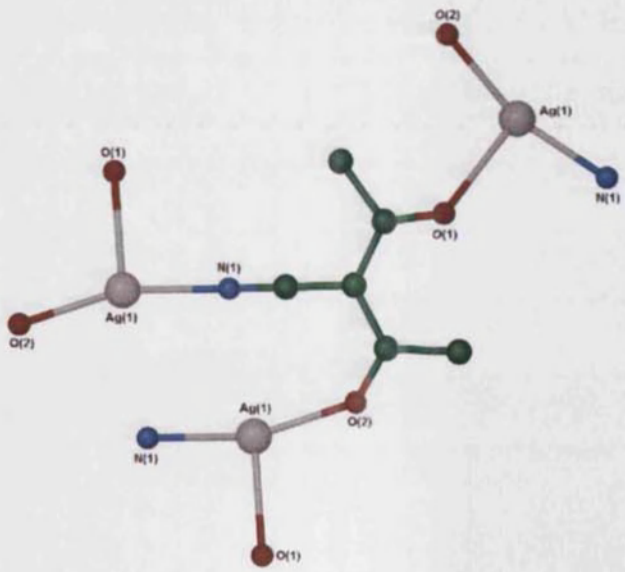

Figure 6.37. The coordination environment around one of the cpd$^-$ ligands in **30**.

Due to the ligand oxygen orientation in **30**, the keto groups bind to different metal centres causing loss of the six-membered ring conjugation. In **30**, the two oxygen-silver bond lengths (Table 6.26) vary significantly. The bond lengths of Ag(1)-O(2) and Ag(1)-

O(1) are 2.2187(16) Å and 2.5126(15) Å respectively. This difference implies that the two silver-oxygen bonds are not similar and thus supports the argument behind the loss of the six-membered ring conjugation where the two metal-oxygen atoms will be of comparable values.

Table 6.26. Selected bond lengths for **30**.

Bond atoms	Bond lengths/ Å
O(1)-C(1)	1.248(2)
O(2)-C(3)	1.255(3)
Ag(1)-N(1)	2.156(2)
Ag(1)-O(1)	2.5126(15)
Ag(1)-O(2)	2.2187(16)

Table 6.27. Selected bond angles for **30**.[VII]

Bond atoms	Bond angle/ °
O(2)-Ag(1)-O(1)#2	101.15(6)
N(1)#1-Ag(1)-O(2)	162.10(7)
N(1)#1-Ag(1)-O(1)#2	93.57(6)
C(1)-O(1)-Ag(1)#3	130.06(14)
C(3)-O(2)-Ag(1)	138.12(15)
C(6)-N(1)-Ag(1)#1	178.1(2)

The silver-oxygen bond lengths of **30** can be compared to those of $[\{Ag(hfacac)\}_2(H_2O)]$[20] (hfacac = 1,1,5,5-hexafluoroacetylacetone), where the β-diketonate ligand acts as a bidentate ligand thus retaining the conjugation.

The bond length of Ag(1)-O(2) of **30** is comparable to the silver-water oxygen bond length (2.263Å) of $[\{Ag(hfacac)\}_2(H_2O)]$ while, Ag(1)-O(1) of **30** is significantly longer than the silver-hfacac oxygen (average length of 2.40Å) of $[\{Ag(hfacac)\}_2(H_2O)]$.

6.4 Summary and conclusions

3-cyano-2,4-pentanedionate has previously been used to form complexes with cobalt and copper. Before this work, the iron and aluminium discrete molecules had not been reported nor had any mixed metal networks containing this ligand. In this chapter several mixed metal complexes from 3-cyano-2,4-pentanedionate are reported.

$[Cu(cpd)_2]$, $[Cu_6(\mu_3\text{-}OMe)_4(\mu\text{-}OMe)_2(cpd)_6]$, $[Fe(cpd)_3]$ and $[Al(cpd)_3]$ were synthesised from metal salts and Hcpd in the presence of a base. The copper complex

[VII] Symmetry transformations used to generate equivalent atoms:
#1 -x,-y+1,-z+2 #2 x+1,-y+3/2,z-1/2
#3 x-1,-y+3/2,z+1/2

obtained was dependent on the initial copper salt used. $Cu(NO_3)_2 \cdot 2.5H_2O$ gave $[Cu_6(\mu_3\text{-}OMe)_4(\mu\text{-}OMe)_2(cpd)_6]$ while $CuCl_2 \cdot 2H_2O$ formed the previously reported compound $[Cu(cpd)_2]$. The influence of the starting material on the final product has not been reported in the literature.

$[Cu(cpd)_2]$, $[Fe(cpd)_3]$ and $[Al(cpd)_3]$ were reacted with $AgNO_3$ solutions to obtain mixed metal complexes. Novel 1-D and 2-D networks were obtained.

Different mixed metal networks from $[Fe(cpd)_3]$ were formed from the same solution. $\{Ag[Fe_2(\mu\text{-}OMe)_2(cpd)_4]NO_3\}_\infty$ **(27)**, and $\{Ag[Fe(cpd)_3]NO_3\}_\infty$ **(28)** were obtained from different reactions using both a mixture of acetone and methanol or methanol on its own as the solvent. $\{Ag_2[Fe_2(\mu\text{-}OMe)_2(cpd)_4](NO_3)_2 \cdot C(CH_3)O\}_\infty$ **(26)** was obtained only from the former solvent mixture while $\{Ag[Fe_2(\mu\text{-}OMe)_2(cpd)_4](OH) \cdot 0.4H_2O\}_\infty$ **(29)** formed only from the latter.

Methanol was deprotonated and replaced two of the original cpd^- ligands to give $[Fe_2(\mu\text{-}OMe)_2(cpd)_4]$ secondary building units. One other feature that was observed in **27** and **28** is that not all nitrogen atoms of the cyano groups coordinate to the silver. This unexpected feature made it hard to predict the topology of the final network.

The $[Fe_2(\mu\text{-}OMe)_2(cpd)_4]$ core units of **26**, **27** and **29** can be considered as SBUs, however the orientation of the cyano groups in these dimers differ with **26** and **29** forming planar SBUs while **27** forms distorted tetrahedral SBUs (Figure 6.38a). The chirality around the iron centres in the dimers is also different with the metal centres adopting opposite chirality in the dimers of **26** and **29** whereas for **27** they both have the same chirality (Figure 6.28b).

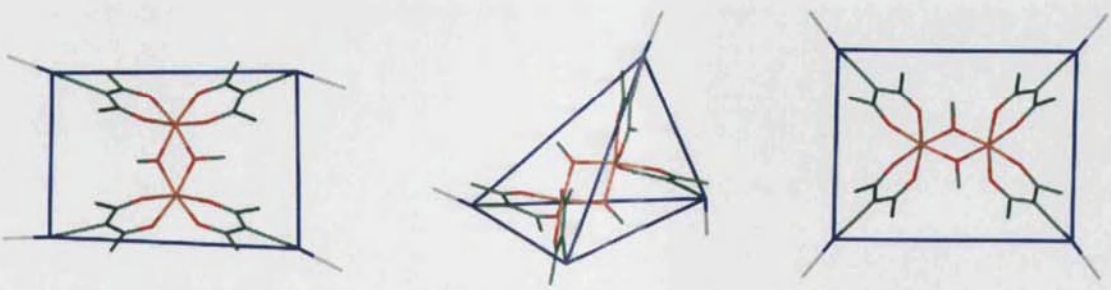

Figure 6.38a. The planar and tetrahedral $[Fe_2(\mu\text{-}OMe)_2(cpd)_4]$ dimers of **26**, **27** and **29** respectively.

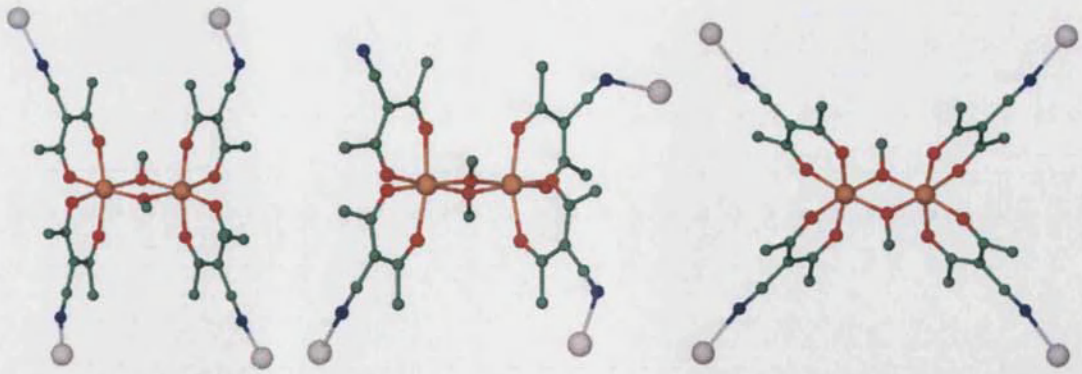

Figure 6.38b. The chirality around the iron centres in **26**, **27** and **29** respectively.

The aluminium complex $[Al(cpd)_3]$ undergoes transmetallation reaction with $AgNO_3$ replacing the aluminium. This demonstrates that silver nitrate is not a good silver source to react with $[Al(cpd)_3]$.

When the mixed metal networks were formed, they were found to be relatively stable towards light. $\{Ag[Cu(cpd)_2]NO_3\}_\infty$ (**25**), **26**, **27**, **28** and **29** did not show any signs of blackening even after being exposed to direct light for at least two months. This is an indication that photolytic decomposition to silver oxide does not readily occur. In contrast $\{[Ag(cpd)]\}_\infty$ (**30**) undergone decomposition after three weeks.

6.5 Further work

Copper(I) is also a d^{10} metal and like silver(I) it can adopt different geometries. Thus it would be of interest to see whether the topology of the networks obtained from 3-cyano-2,4-pentanedionate were retained if **21** ($Cu(cpd)_2$) and **23** ($Fe(cpd)_3$) were reacted with $[Cu(MeCN)_4]PF_6$.

It would also be interesting to see the final topologies resulting from ligands where the cyano groups were replaced by carboxylate or pyridyl functional groups. In order to investigate this, (2-acetyl-3-oxo)butanoic acid (Figure 6.39) [21] and 3-(4-pyridyl)-2,4-pentanedione (Hppd) (Figure 6.4) have to be synthesised and coordinated to metal centres.

One other investigation worth pursuing is potential network syntheses on placing the ligand cyano groups at positions 1 and 5 rather than at position 3 of the dione. When coordinated to different metal centres, the ligand 1,3-di(4-benzonitrile)-1,3-propanedione

(Figure 6.40) will allow this investigation. This ligand can be synthesised via a Claisen condensation reaction between 4-acetyl-benzonitrile and 4-cyano-methylbenzoate using BF_3 as a Lewis acid.

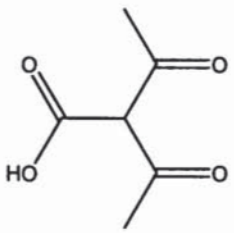

Figure 6.39. (2-acetyl-3-oxo)butanoic acid.

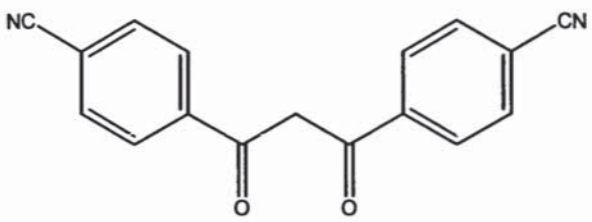

Figure 6.40. 1,3-di(4-benzonitrile)-1,3-propanedione.

References:

1. C.Tsiamis; S.Cambonis; C.Hadjikostas, *Inorg. Chem.* **1987,** 26, 26.
2. R.Sahai; R.Verma, *J.Indian.Chem.Soc.* **1981,** 58, 640.
3. M.Tanaka; T.Shono; K.Shinra, *Bull.Chem.Soc.Jpn.* **1969,** 42, 3190.
4. O.Angelova; J.Matsichek; M., Atanosova; G.Petrov, *Inorg. Chem.* **1991,** 30, 1943.
5. D.P.Graddon; T.T.Nyein, *Austral.J.Chem.* **1973,** 26, 1901.
6. G.P.Graddon; K.B.Heng, *Austral.J.Chem.* **1972,** 75, 2247.
7. O.Angelova; I.Matsichek, *Acta.Crystallogr.* **1989,** C45, 710.
8. J.A.Belot; V.W.Day; A.L.Rheingold; R.D.Sommer; C.M.Silvernail, *Polyhedron* **2001,** 20, 3113.
9. B.Chen; F.R.Fronczek; A.W.Maverick, *Inorg. Chem.* **2004,** 43, 8209.
10. A.N.Chernega; V.D.Vreshch; A.B.Lysenko; J.A.K.Howard; H.Krautscheid; J.Sieler; K.V.Domasevitch, *Dalton Trans.* **2004,** 18, 2899.
11. A.N.Chernega; K.V.Domasevitch; A.B.Lysenko; J.Sieler; V.D.Vreshch, *Polyhedron* **2005,** 24, 917.
12. J.K.Clegg; L.F.Lindoy; B.Moubaraki; K.S.Murray; J.C.McMurtrie, *Dalton Trans.* **2004,** 16, 2417.
13. J.K.Clegg; K.Gloe; M.J.Hayter; O.Kataeva; L.F.Lindoy; B.Moubaraki; J.C.McMurtrie; K.S.Murray; D.Shilter, *Dalton Trans.* **2006,** 3977.
14. W.Caminati; J.U.Grabow, *J.Am.Chem.Soc.* **2005,** 128, 854.
15. J.Emsley; Y.Y.Lewina; P.A.Bates; M.Motevalli; M.B.Hursthouse, *J.Chem.Soc.Perkin Trans.2* **1989,** 527.
16. G.H.Stout; L.H.Jensen, *X-Ray Structure Determination.* 2nd ed.; John Wiley & Sons, Inc.: United States of America, 1989; p 74-78.
17. A.W.Addison; T.N.Rao; J.Reedijk; J.V.Rijn; G.C.Verschoor, *J.Chem.Soc.Dalton.Trans.* **1984,** 1349.
18. A.J.Blake; N.R.Champness; P.Hubberstey; W.S.Li; M.A.Withersby; M.Schroder, *Coord.Chem.Rev.* **1999,** 183, 117.
19. T.L.Ho, *Chem.Rev.* **1975,** 75, 1.
20. C.Xu; T.S.Corbitt; M.J.Hampden-Smith; T.T.Kodas; E.N.Duesler, *J.Chem.Soc.Dalton Trans.* **1994,** 2841.
21. M.W.Rathke; P.J.Cowan, *J.Org.Chem.* **1985,** 50, 2622.

Chapter 7 Experimental section

7.1 Introduction

All chemicals were bought from Aldrich Chemical Co. and used without further purification.

Single crystal X-ray diffraction data for **1-4, 7, 8, 10-12, 14, 22, 23, 26, 28,** were carried out at the University of Bath on a Nonius Kappa CCD diffractometer at a temperature of 150K.

Single crystal X-ray data for **5, 6, 9, 13, 15, 16-18, 25, 27, 29, 30** were collected at Daresbury SRS Stations 9.8 or 16.2 SMX.

The solution of all structures was carried out using SHELX-97 while refinements were completed using SHELXL-97. More information can be found in the attached electronic media (CD)

X-ray powder diffraction data were recorded at the University of Bath on a Bruker D8 powder diffractometer fitted with Goebel mirrors and a 0.2mm beam slit. Samples were packed in 0.5 mm diameter capillary tubes. The scan speed was set to 1 sec per step with a 0.2 mm step size. Unless stated otherwise, the X-ray powder data matched the simulated powder pattern generated from the single crystal data. This is indicative that the single crystal used for data collection was a good representative of the bulk material.

Thermogravimetric analysis were carried out on a TGA 7 thermogravimetric analyser from a temperature range of 30° to 600°C at a rate of 10°C per minute under a flow of N_2.

IR measurements were carried out using a Nicolet Nexus FT-IR instrument.

Microanalysis were carried out by the service at the Department of Chemistry, University of Bath.

Mass spectra were acquired by the EPSRC National Mass Spectrometry Service Centre, University of Swansea and by the service at the Department of Chemistry, University of Bath.

NMR spectra were recorded at 298 K on Bruker Avance 300 MHz NMR spectrometer and referenced (for ^{1}H) to residual protio solvent signals (δ 7.24 for $CDCl_3$) and to resonances for ^{13}C $\{^{1}H\}$ (δ 77.2 for $CDCl_3$).

Nitrogen sorption measurements were carried out on a Micromeritics ASAP 2400 apparatus while hydrogen and krypton sorption measurements were conducted on a Hiden intelligent gravimetric analyser (IGA).

7.2 Compounds reported in Chapter 2

7.2.1 Synthesis of $\{[Zn(tph)(H_2O)]\cdot DMF\}_\infty$ (1).

0.500g (1.68 mmol) $Zn(NO_3)_2\cdot 6H_2O$ were dissolved in 10 mL *N,N*-dimethylformamide (DMF). 0.501g (3.02 mmol) 1,4-benzenedicarboxylic acid (H_2tph) were dissolved in 50 mL DMF and placed in a 250 mL round bottomed flask fitted with a condenser and a thermometer. The solution containing the ligand was stirred and heated to 95°C and the $Zn(NO_3)_2\cdot 6H_2O$ solution was then added. Stirring was stopped and heating was continued for 3 hours at 95°C. Colourless crystals were obtained during the reaction. Yield; 0.217g (39%) based on $Zn(NO_3)_2\cdot 6H_2O$.

Powder X-ray analysis data matched the theoretical plot simulated from $\{[Zn(tph)(H_2O)]\cdot DMF\}_\infty$ previously reported by Yaghi et *al.*[1]

7.2.2 Synthesis of $\{[Zn_3(tph)_3(H_2O)_3]\cdot 4DMF\}_\infty$ (2) and $\{[Zn(tph)(DMF)]\}_\infty$ (3).

0.500g (1.68 mmol) $Zn(NO_3)_2\cdot 6H_2O$ were dissolved in 10 mL DMF while 0.501g (3.02 mmol) H_2tph were dissolved in 50 mL DMF in a 250 mL round bottomed flask fitted with a condenser and a thermometer. The latter solution was stirred and heated to 115°C and the $Zn(NO_3)_2\cdot 6H_2O$ was then added. Stirring was ceased and the reaction mixture was heated at 115°C for an additional 3 hours. Colourless crystals were obtained, which were

found to be a mixture of **2** and **3**. Crystals of both compounds appeared similar to the naked eye. Combined yield; 0.318g.

7.2.3 Synthesis of $\{[Zn(tph)(DMF)]\}_\infty$ (3).

0.500g (1.68 mmol) of $Zn(NO_3)_2 \cdot 6H_2O$ were dissolved in 10 mL DMF while 0.501g (3.02 mmol) H_2tph were dissolved in 50 mL DMF. The H_2tph solution was put in a pressure cell and heated to 115°C. When the solution reached the desired temperature, the $Zn(NO_3)_2 \cdot 6H_2O$ solution was added, the pressure cell sealed and the mixture pressurised with 3 bars of nitrogen. The reaction was heated for three hours after which colourless crystals were obtained. Yield; 0.311g (61%) based on $Zn(NO_3)_2 \cdot 6H_2O$.

Microanalysis. Calculated for $C_{11}H_{11}NO_5Zn$: C,43.7; H,3.66; N,4.64%. Found C,44.0; H,3.72; N,4.67 %.

Powder X-ray crystallography confirmed that **3** was the only product from the reaction.

7.2.4 Synthesis of $\{(Me_2NH_2)_2[Zn_3(tph)_4] \cdot DMF \cdot H_2O\}_\infty$ (4) and $\{(Me_2NH_2)_2[Zn(DMF)_4(OH_2)_2][Zn_6(tph)_8] \cdot 6DMF\}_\infty$ (5).

0.500g (1.68 mmol) of $Zn(NO_3)_2 \cdot 6H_2O$ and 0.501g (3.02 mmol) H_2tph were dissolved in separate portions of DMF (60 mL in total). The solution containing the ligand was stirred and heated to 115°C in a two necked round bottomed flask fitted with a thermometer and a condenser. The $Zn(NO_3)_2 \cdot 6H_2O$ solution and 0.080g (0.98 mmol) dimethylammonium chloride were added to the reaction mixture. Stirring was continued for 5 minutes and the solution was left standing at 115°C for an additional 3 hours. Colourless crystals formed were found to consist of both **4** and **5**. These two compounds were indistinguishable to the naked eye. Combined yield; 0.20g.

7.2.5 Synthesis of $\{(Et_2NH_2)_2[Zn_3(tph)_4] \cdot 2.5DEF\}_\infty$ (6).

0.083g (0.279 mmol) $Zn(NO_3)_2 \cdot 6H_2O$ and 0.045g (0.271 mmol) H_2tph were dissolved in separate portions of DEF (10 mL in total). The latter solution was stirred and heated to 115°C in a 25 mL two necked round bottomed flask fitted with a condenser and a

thermometer. The $Zn(NO_3)_2 \cdot 6H_2O$ solution was then added, stirring was ceased and the reaction was heated at 115°C for 3 hours. Orange-yellow crystals were formed. Yield; 0.041g (48%) based on H_2tph.

Microanalysis. Calculated for $C_{52.5}H_{67.5}Zn_3N_{4.5}O_{18.5}$: C,50.3; H,5.43; N,5.02%. Found C,49.9; H,5.55; N,5.34 %.

7.2.6 Synthesis of $\{[Zn(bpdc)(DMF)] \cdot 2DMF\}_\infty$ (7) and $\{[Zn_3(bpdc)_3(DMF)_2] \cdot 3DMF \cdot H_2O\}_\infty$ (8).

0.257g (0.86 mmol) $Zn(NO_3)_2 \cdot 6H_2O$ were dissolved in 5 mL DMF while 0.20g (0.83 mmol) 4,4'-biphenyldicarboxylic acid (H_2bpdc) were dissolved in 25 mL DMF. The solution containing the ligand was heated to 95°C in a two necked round bottomed flask fitted with a condensor and a thermometer. The metal solution was added and heating (95°C) was continued for 3 hours. Colourless crystals were obtained. Analysis of the crystals by single crystal X-ray crystallography revealed the presence of **7** and **8**. The crystals of the different compounds were indistinguishable to the eye.
Combined yield; 0.290g.

7.3 Compounds reported in Chapter 3

7.3.1 Synthesis of $\{[Cd(tph)(DMF)]\}_\infty$ (9) and $\{[Cd_3(tph)_4(DMF)_4]\}_\infty$ (10).

0.520g (1.69 mmol) $Cd(NO_3)_2 \cdot 4H_2O$ were dissolved in 10mL DMF while 0.501g (3.02 mmol) H_2tph were dissolved in 50 mL DMF. The H_2tph solution was put in a 250 mL two necked round bottom flask fitted with a thermometer and a condenser. This was stirred and heated to 95°C and the $Cd(NO_3)_2 \cdot 4H_2O$ solution was then added. Stirring was continued for five minutes and the solution was left standing at 95°C for 5 hours. Colourless crystals were obtained. The crystals were found to be a mixture of **9** and **10** and the two compounds were indistinguishable to the eye. Combined yield; 0.415g.

When the reaction described above was carried out at 115°C rather than 95°C, **9** was the only product (confirmed by powder X-ray crystallography and microanalysis). Yield; 0.240g (41%) based on $Cd(NO_3)_2 \cdot 4H_2O$.

Microanalysis. Calculated for $C_{11}H_{11}CdNO_5$: C,37.8; H,3.17; N,4.01%. Found C,37.8; H,3.15; N,4.05 %.

7.3.2 Synthesis of $\{[Cd_3(tph)_3(DMF)_4]\}_\infty$ (11).

0.520g (1.69 mmol) $Cd(NO_3)_2 \cdot 4H_2O$ and 0.501g (3.02 mmol) H_2tph were dissolved in separate portions of DMF (60 mL in total). The ligand solution was put in a pressure cell and heated to 115°C, at which point the $Cd(NO_3)_2 \cdot 4H_2O$ solution was added. The pressure cell was sealed and pressurised with 3 bars of nitrogen. The reaction was heated for 5 hours at 115°C after which colourless crystals were obtained. Yield; 0.515g (81%) based on $Cd(NO_3)_2 \cdot 4H_2O$.

Microanalysis. Calculated for $C_{36}H_{40}Cd_3N_4O_{16}$: C,38.5; H,3.60; N,4.99 %. Found C,38.5; H,3.34; N,4.39 %.

7.3.3 Synthesis of $\{(Me_2NH_2)_2[Cd(tph)_2] \cdot 2DMF\}_\infty$ (12).

0.520g (1.69 mmol) $Cd(NO_3)_2 \cdot 4H_2O$ and 0.501g (3.02 mmol) H_2tph were dissolved in separate portions of DMF (60 mL in total). The H_2tph solution was put in a 250 mL two necked round bottom flask fitted with a thermometer and a condenser. The ligand containing solution was stirred and heated to 115°C. 0.080g (0.98 mmol) dimethylammonium chloride and the $Cd(NO_3)_2 \cdot 4H_2O$ solution were added to the reaction mixture. Stirring was continued for a further five minutes and the reaction was left standing for 5 hours at 115°C. Colourless crystals were obtained. Yield; 0.27g (81%) based on Me_2NH_2Cl.

Microanalysis Calculated for $C_{26}H_{38}CdN_4O_{10}$: C,46.0; H,5.64; N,8.25%. Found C,45.10; H,5.40; N,6.52 %.[I]

[I] Four different samples of **12** were submitted to microanalysis and the % C, H and N found were consistent. These fit with the formula $\{(Me_2NH_2)_2[Cd(tph)_2] \cdot 1DMF\}_\infty$ C,45.59, H,5.16, N,6.93%. The first DMF is lost from **12** at relatively low temperatures as indicated by TGA and this might be the reason for the results obtained.

7.3.4 Synthesis of $\{[Cd_3(tph)_3(DEF)_2]\}_\infty$ (13).

0.086g (0.279 mmol) $Cd(NO_3)_2 \cdot 4H_2O$ were dissolved in 1 mL *N,N'*-diethylformamide (DEF). 0.045g (0.271 mmol) H_2tph were dissolved in 9 mL DEF and placed in a 15mL two neck round bottomed flask fitted with a thermometer and a condenser. The H_2tph solution was stirred and heated at 115°C. The $Cd(NO_3)_2 \cdot 4H_2O$ solution was then added and the reaction mixture was left standing for 5 hours at 115°C. Yellow-orange crystals were obtained. Yield; 0.039g (42%) based on H_2tph.

Microanalysis. Calculated for $C_{34}H_{34}Cd_3N_2O_{14}$: C,39.5; H,3.42; N,2.72 %. Found C,39.2; H,3.52; N,2.98 %.

7.3.5 Synthesis of $\{[Cd_3(bpdc)_3(DMF)_2]\}_\infty$ (14).

0.517g (1.68 mmol) $Cd(NO_3)_2 \cdot 4H_2O$ were dissolved in 10 mL DMF. 0.409g (1.69 mmol) 4,4'-biphenyldicarboxylic acid (H_2bpdc) were dissolved in 50 mL DMF in a two necked round bottomed flask fitted with a thermometer and a condenser. The H_2bpdc solution was heated to 115° C. When the ligand dissolved completely, the $Cd(NO_3)_2 \cdot 4H_2O$ solution was added. Stirring was continued for 5 minutes and then the mixture was left standing for 5 hours at 115°C. Colourless crystals were obtained. Yield; 0.245g (36%) based on $Cd(NO_3)_2 \cdot 4H_2O$.

Microanalysis. Calculated for $C_{48}H_{38}Cd_3N_2O_{14}$: C,47.9; H,3.18; N,2.33 %. Found C,47.5; H,3.40; N,2.86 %.

7.3.6 Lewis-acid catalysed reactions reported in Chapter 3

0.01g (0.0097 mmol) $\{[Cd_3(tph)_3(DEF)_2]\}_\infty$ **(13)**, and 0.013g (0.013 mmol) $\{[Cd(bpdc)_3(DMF)_2]\}_\infty$ **(14)**, were heated at 410° and 400°C respectively for 1 minute under a flow of N_2. The heat treated compounds were transferred to separate schlenks and heated for another hour at 100°C under vacuum. The heat treatment afforded $\{[Cd_3(tph)_3]\}_\infty$ **(13b)** and $\{[Cd(bpdc)_3]\}_\infty$ **(14a)**. 0.564g (6 mmol) phenol and 0.918g (9 mmol) acetic anhydride dissolved in 24 mL dry CH_2Cl_2 were added to the catalysts. The

reactions were stirred at room temperature for 3 days. The solvent volume was reduced and the products were purified on columns using 4:1 hexane/ ethyl acetate as the mobile phase.

Yield for **13b** = 0.141g (17%) based on phenol.
Yield for **14a** = 0.158g (19%) based on phenol.

Phenylacetate
^{1}H NMR ($CDCl_3$) δ 2.19 (s,3H), δ 7.0 (d, 2H *J-J* ^{1}H-^{1}H 8.67Hz), δ 7.10 (t, 1H, *J-J* ^{1}H-^{1}H 8.67 Hz), δ 7.25 (t, 2H *J-J* ^{1}H-^{1}H 8.67Hz).
^{13}C {^{1}H} ($CDCl_3$) δ 22.0 (CH_3), δ 121.9 ($C_{benzene}$), δ 122.4 ($C_{benzene}$), δ 130.5 ($C_{benzene}$), δ 172.2 ($CH_3\underline{C}OO$).

7.4 Gas adsorption properties reported in Chapter 4

Prior to loading onto the ASAP or IGA, the coordinated DMF or DEF molecules were removed from $\{[Cd_3(bpdc)_3(DMF)_2]\}_\infty$ (**14**) and $\{[Cd_3(tph)_3(DEF)_2]\}_\infty$ (**13**). **14** or **13** were heated in the TGA at 400° or 410°C respectively for 1 minute under a flow of N_2 to form $\{[Cd_3(bpdc)_3]\}_\infty$ (**14a**) and $\{[Cd_3(tph)_3]\}_\infty$, (**13b**).

14a was loaded onto the ASAP and heated at 100°C for 4 hours under vacuum. The dry mass was recorded at 0.0891g and the N_2 sorption experiment was carried out at 77 K using a Micromeritics ASAP 2400 apparatus.

Hydrogen adsorption experiments were performed on a Hiden intelligent gravimetric analyser (IGA). A fresh sample of **14a** weighing 0.0891g was loaded onto the IGA and the reaction chamber was sealed. The sample was evacuated to vacuum and heated to 100°C for 4 hours, after which it was cooled to room temperature. A dewar filed with liquid nitrogen was placed round the reaction chamber. Once the temperature reached 178 K, the isothermal analysis was performed in the pressure region of 0.004 to 1.00 P/P_o. (The experiment was all software-controlled, and once completed, the data values of the adsorption, BET surface area and kinetic data of adsorption were available for analysis.)

The same procedure was repeated for **13b**. The dry mass for this compound was recorded at 0.1215g.

7.5 Compounds reported in Chapter 5

7.5.1 Synthesis of 3,4-diacetyl-2,5-dioxohexane (H_2tae)

24.4g (0.20 mol) sodium acetylacetonate were added to 300 mL Et_2O. The suspension was stirred under an atmosphere of N_2. 25.4g (0.10 mol) iodine were dissolved in 300 mL Et_2O. The iodine solution was added dropwise to the stirred sodium acetylacetonate. After the complete addition of iodine, the reaction was stirred for 1 hour and then the solvent was allowed to evaporate overnight under a stream of N_2. The resulting yellow solid was washed with water, dried and recrystallised from hot methanol.[2] Yield; 9.570g (70%) based on I_2.

^{1}H NMR ($CDCl_3$) δ 1.93 (s, 6H), 15.27 (s, 2H). ^{13}C {^{1}H} NMR ($CDCl_3$) δ 24.3(CH_3) , 107.5(C-C(O)CH_3), 193.0(C(O)CH_3).
Microanalysis. Calculated for $C_{10}H_{14}O_4$: C,60.6; H,7.12. Found C,60.40; H,7.13.
Melting point. Reported 191°C,[2] found 192°C.

Mass spectroscopy.
$[M]^+$ *m/z* 198.1. Other fragments observed at *m/z* 181.1 $[M\text{-}CH_3]^+$, 137.1 $[M\text{-}2CH_3]^+$, 67.1 $[M\text{-}(CH_3CO)_3]^+$, 43.0 $[CH_3CO]^+$.

7.5.2 Synthesis of {[Zn(tae)(DMF)]·0.6$CHCl_3$·0.4DMF}$_\infty$ (15).

0.20g (0.672 mmol) $Zn(NO_3)_2{\cdot}6H_2O$ were dissolved in 15 mL DMF while 0.133g (0.671 mmol) 3,4-diacetyl-2,5-dioxohexane (H_2tae) were dissolved in 15 mL $CHCl_3$. The two solutions were mixed together and Et_3N vapour was allowed to diffuse into the mixture. The white powder that precipitated initially was removed by filtration and the supernatant was left to stand. A small quantity of colourless crystals were obtained after 2 months.

X-ray powder diffraction data were obtained for the initially obtained white powder. A comparison of this data with the simulated powder plot for **15** showed no similarities between the two. Microanalysis results for the white powder confirmed that this compound is different from **15** (Microanalysis. Found C,24.7; H,7.48).

7.5.3 Synthesis of $\{[Zn_3(tae)_3(MeOH)(DMSO)_{4.2}]0.8DMSO\}_\infty$ (16).

0.010g (0.0337 mmol) $Zn(NO_3)_2{\cdot}6H_2O$ were dissolved in 2mL DMSO. 0.007g (0.0353 mmol) H_2tae were dissolved in 2mL MeOH. The two solutions were mixed together and Et_3N vapour was allowed to diffuse into this mixture. The white powder that precipitated initially was removed by filtration and the filtrate was left to stand. A small quantity of colourless crystals were obtained after 2 months.

Comparison of experimental X-ray powder plot for the initial white powder to the simulated powder plots for $\{[Zn(tae)(DMF)]{\cdot}0.6CHCl_3{\cdot}0.4DMF\}_\infty$ (**15**) and **16** did not show any matches. This suggested that the powder was a new product.

7.5.4 Synthesis of $\{[Zn_2(\mu\text{-}tae)_2(OH_2)_2]\}_\infty$ (17).

The same experimental procedure as described for the synthesis of **15** and **16** was followed. 0.010g (0.0336 mmol) $Zn(NO_3)_2{\cdot}4H_2O$ and 0.013g (0.0656 mmol) H_2tae were dissolved separately in 2 mL MeOH each. Et_3N was allowed to diffuse into the solution affording colourless crystals. Yield; 0.005g (53%) based on $Zn(NO_3)_2{\cdot}6H_2O$.

Single crystal X-ray data were collected at Daresbury labs. The solution obtained was not good enough to determine the final structure but the heavy atoms and the ligands could be seen. Residual electron density suggests that there might still be atoms that need to be mapped, but data quality prevent obtaining a definitive result.

Microanalysis results suggest that there are two additional water molecules per dimer. Microanalysis. Calculated for $C_{20}H_{28}O_{10}Zn_2$: C,42.9; H,5.05. Found C,42.7; H,5.39.

7.5.5 Synthesis of $\{[Zn_2(\mu\text{-tae})_2(MeOH)_2]\cdot 2MeOH\}_\infty$ (18).

The same experiment described for the preparation of **17** was repeated. After the formation of **17**, the crystals were removed by filtration. Et_3N was left to evaporate into the filtrate and a second compound was formed. Small quantity of crystals were formed.

7.5.6 Synthesis of $\{[Cd_2(\mu\text{-tae})_2(OH_2)_2]\cdot 2.5H_2O\}_\infty$ (19).

0.010g (0.0324 mmol) $Cd(NO_3)_2\cdot 4H_2O$ and 0.013g (0.0656 mmol) H_2tae were dissolved in separate portions of 2 mL MeOH each. Et_3N vapour was allowed to diffuse into the solution. Colourless crystals were obtained after 2 months. Yield; 0.009g (80%) based on $Cd(NO_3)_2\cdot 4H_2O$.

Microanalysis. Calculated for $C_{20}H_{33}Cd_2O_{12.5}$: C,34.4; H,4.76. Found C,34.9; H,4.95.

7.5.7 Synthesis of 3,3'-(1,4-phenylenedimethylene)di-2,4-pentanedione (H_2pdp)

30.0g (0.3 mol) 2,4-pentanedione were added to a stirred refluxed solution of 17.8g (0.159 mol) K-*tert*-butoxide in 200 mL *tert*-butanol. 26.4g (0.100 mol) 1,4-bis(bromomethyl)benzene was added to the solution. After refluxing for 1 hour, 4.0g (0.0241 mol) KI were added to the reaction mixture. After 5 hours the reaction was cooled to room temperature and the solvent was removed under reduced pressure. The resulting solid was washed with water and recrystallised from hot *tert*-butanol.[3]

^1H NMR ($CDCl_3$) δ 2.13 (s, 12H), 3.11 (d, 4H *J-J* ^1H-^1H 7.35Hz), 3.95 (t, 2H *J-J* ^1H-^1H 7.35Hz), 7.05 (s, 4H), 15.30 (s, 2H). ^{13}C $\{^1H\}$ NMR ($CDCl_3$) δ 30.1(CH_3), 35.1(CH_2), 70.3(C-C(O)CH_3), 129.4($C_{benzene}$), 138.0($CH_{benzene}$), 203.8(C(O)CH_3).
Microanalysis. Calculated for $C_{18}H_{22}O_4$: C,71.5; H,7.34. Found C,70.8; H,7.24.

7.5.8 Synthesis of 3,3'-dithio-di-2,4-pentanedione (H_2dtp)

60 mL (58.5g, 0.585 mol) 2,4-pentanedione were cooled at 0°C under an atmosphere of N_2 and 7.5 mL (12.66g, 0.0939 mol) S_2Cl_2 were added dropwise. Excess

cold water was added after the formation of a yellow solid. The solid was separated by filtration, dried in air and recrystallised from hot petroleum ether.[4]

^{1}H NMR ($CDCl_3$) δ 2.30 (s, 12H), 15.26 (s, 2H). ^{13}C {^{1}H} NMR ($CDCl_3$) δ 24.8(CH_3), 107.1(C-C(O)CH_3), 197.6(C(O)CH_3).
Microanalysis. Calculated for $C_{10}H_{14}O_4S_2$: C,45.8; H,5.34. Found C,44.1; H,5.14.

Mass spectroscopy.
$[M]^+$ *m/z* 261.9. Other fragments observed at *m/z* 132.0 $[CH_3COCHSCOCH_3]^+$, 43.0 $[CH_3CO]^+$.

7.5.9 Synthesis of iron-dtp, (20).

0.101g (0.385 mmol) of 3,3'-dithio-di-2,4-pentanedione H_2dtp were dissolved in 20 mL MeOH and 0.11 mL (0.08g, 0.791 mmol) Et_3N. 0.048g (0.120 mmol) $Fe_2(SO_4)_3$ was dissolved in 20 mL H_2O and added to the reaction mixture. Red-brown powder formed instantaneously. Yield; 0.020g.

IR(KBr): υ(O-H)/cm^{-1} 3450(br) υ(C-O)/cm^{-1}1610(br).

Mass spectrometry; EI
$[M]^+$ observed at *m/z* 1133.4. Other peaks observed occurred at *m/z* 948.5 $[Fe_3(dtp)_3]^{3+}$, 894.3 $[Fe_2(dtp)_3]^+$, 632 $[Fe_2(dtp)_2]^{2+}$, 371.8 $[Fe_2(dtp)]^{4+}$, 316.9 $[Fe(dtp)]^+$.

7.6 Compounds reported in Chapter 6

7.6.1 Synthesis of 3-cyano-2, 4-pentanedione (Hcpd)

Following a literature procedure,[5] 27.0 mL of CH_2Cl_2 and 10.0g (0.10 mol) of 2,4-pentanedione were put in a round bottomed flask under an atmosphere of N_2. The solution was stirred vigorously and 4.75 mL (7.72g, 0.055 mol) $ClSO_2NCO$ were added dropwise, followed by 8.40 mL (7.90g, 0.11 mol) DMF. The reaction was stirred for an additional 30 minutes. The organic fraction was washed with water, dried over Na_2SO_4 and the product

was purified by column chromatography using 4:1 hexane–diethyl ether as the mobile phase.

^{1}H NMR ($CDCl_3$) δ 2.32 (s, 6H). ^{13}C {^{1}H} NMR ($CDCl_3$) δ 25.1(CH_3), 91.1(C-C(O)CH_3), 116.9(CN), 197.5(C(O)CH_3).
Microanalysis. Calculated for $C_6H_{7.8}N_1O_{2.4}$ (Hcpd·0.4H_2O): C,54.4; H,5.96; N,10.59 %. Found C,54.7; H,5.32; N,10.59 %.
IR(KBr): ν(CN)/ cm^{-1} at 2218s, ν(CO)/cm^{-1} at 1635(br).

7.6.2 Synthesis of [Cu(cpd)$_2$], (21).

Following a literature procedure,[6] 0.40g (2.35 mmol) $CuCl_2$·2H_2O and 0.521g (3.94 mmol) Hcpd·0.4H_2O were dissolved in 40 mL MeOH in a 100 mL volumetric flask. 4mL of Et_3N were put in a small sample tube which was placed inside the volumetric flask. The flask was covered with parafilm thus allowing the base to diffuse into the solution. Blue crystals were obtained overnight. Yield; 0.093g (15%) based on the ligand.

Microanalysis. Calculated for $C_{12}H_{12}CuN_2O_4$: C,46.2; H,3.88; N,8.99%. Found C,46.2; H,3.88; N,9.02%.
IR(KBr) ν(CN)/cm^{-1} 2194s, ν(CO)/cm^{-1} 1595(br).

7.6.3 Synthesis of [Cu$_6$(μ-OMe)$_2$(μ_3-OMe)$_4$(cpd)$_6$], (22)

This compound was synthesised following the same procedure as for [Cu(cpd)$_2$] but 0.502g (2.08 mmol) $Cu(NO_3)_2$·3H_2O were used instead of $CuCl_2$·2H_2O. Blue crystals of paler colour were formed overnight. Yield; 0.352g (77%) based on $Cu(NO_3)_2$·3H_2O

Microanalysis calculated for $C_{42}H_{54}Cu_6N_6O_{18}$: C,38.4; H,4.14; N,6.40%. Found C,38.2; H,4.16; N,6.20%.
IR(KBr) ν(CN)/cm^{-1} 2213s, ν(CO)/cm^{-1} 1608(br).

7.6.4 Synthesis of [Fe(cpd)$_3$], (23).

0.958g (2.37 mmol) $Fe(NO_3)_3 \cdot 9H_2O$ and 0.902g (6.82 mmol) Hcpd·0.4H_2O were dissolved in 12mL MeOH in a 100mL volumetric flask. 5mL of Et_3N were put in a small sample tube which was inserted in the flask. The flask was covered with parafilm and the base was allowed to diffuse into the solution. Dark-red crystals were obtained after few hours. Yield; 0.192g (20%) based on Hcpd·0.4H_2O.

Microanalysis calculated for $C_{18}H_{18}FeN_3O_6$: C,50.5; H,4.24; N,9.82%. Found C,50.0; H,4.30; N,9.74%.
IR(KBr) ν(CN)/cm^{-1} 2208s, ν(CO)/cm^{-1} 1613(br).

7.6.5 Synthesis of [Al(cpd)$_3$], (24).

0.012g (0.032 mmol) $Al(NO_3)_3 \cdot 9H_2O$ and 0.012g (0.091 mmol) Hcpd·0.4H_2O were dissolved in 4mL 50/50% v/v MeOH/H_2O. 0.20g (2.38mmol) $NaHCO_3$ were dissolved in 4mL 50/50% v/v MeOH/H_2O and added to the mixture. The reaction was stirred for an additional 30 minutes after which a white solid precipitated. The solid was removed by filtration, washed with excess water and dried in air. Yield; 0.010g (67%) based on Hcpd·0.4H_2O.

^{1}H NMR ($CDCl_3$) δ 2.29 (s,18H), ^{13}C {^{1}H} NMR ($CDCl_3$) δ 27.4(CH_3), 92.6(C-C(O)CH_3), 118.7(CN),197.7(C(O)CH_3).
Microanalysis calculated for $C_{18}H_{30}AlN_3O_{12}$([Al(cpd)$_3$]·6H_2O): C,42.6; H,5.96; N,8.28%. Found C, 43.2; H,5.87; N,8.47%.
I.R(KBr) υ(OH)/cm^{-1} 3428(br), ν(CN)/cm^{-1} 2208s, ν(CO)/cm^{-1} 1613(br).

Mass spectrometry
MALDI (mode = PosRef, additive = NaI, matrix = DCTB) $[M+Na]^+$ 422 observed (M = [Al(cpd)$_3$]). Other species observed; 275 $[HAl(cpd)_2]^+$, 158 $[Al(cpd)]^+$ and 124 $[cpd]^+$.

7.6.6 Synthesis of $\{Ag[Cu(cpd)_2]NO_3\}_\infty$, (25).

0.018g (0.058 mmol) of $[Cu(cpd)_2]$ were dissolved in 2mL DMF while 0.029g (0.17 mmol) of $AgNO_3$ was dissolved in 2 mL MeOH. The $AgNO_3$ solution was layered on top of the $[Cu(cpd)_2]$, the sample tube was covered with aluminium foil and placed in the dark. Blue crystals were formed after 1 month. Yield; 0.014g (50%) based on $[Cu(cpd)_2]$.

Microanalysis calculated for $C_{12}H_{12}AgCuN_3O_7$: C,29.9; H,2.51; N,8.72%. Found C, 29.8; H,2.48; N,8.64%.
I.R(KBr) ν(CN)/cm^{-1} 2211s, ν(CO)/cm^{-1} 1602(br).

7.6.7 Synthesis of $\{Ag_2[Fe_2(\mu\text{-}OMe)_2(cpd)_4](NO_3)_2{\cdot}C(CH_3)_2O\}_\infty$ (26) and $\{Ag[Fe_2(\mu\text{-}OMe)_2(cpd)_4]NO_3\}_\infty$, (27).

0.024g (0.056 mmol) $[Fe(cpd)_3]$ were dissolved in 2mL acetone. 0.029g (0.17 mmol) $AgNO_3$ was dissolved in 2mL MeOH. The $AgNO_3$ solution was layered on top of $[Fe(cpd)_3]$ and the sample tube was placed in the dark. Light red crystals were formed after 2 weeks. On analysing the crystals by single crystal and powder X-ray crystallography two networks were discovered. **26** is the major product as no peaks for **27** were observed in the experimental powder X-ray pattern. Yield; 0.003g (10%) based on $[Fe(cpd)_3]$.

Microanalysis calculated for $C_{29}H_{36}Ag_2Fe_2N_6O_{17}$: C,32.6; H,3.40; N,7.87 %. Found C,30.5; H, 3.38; N,7.58%. This suggests loss of acetone guest molecules.
I.R(KBr) ν(CN)/cm^{-1} 2212s, ν(CO)/cm^{-1} 1595(br).

7.6.8 Synthesis of $\{Ag[Fe(cpd)_3]NO_3\}_\infty$, (28).

When the reaction yielding **26** and **27** was repeated but left in contact with the solvent for 1 month, $\{Ag[Fe(cpd)_3]NO_3\}_\infty$, (**28**) was obtained as the major product as demonstrated by powder X-ray crystallography. Minor traces of **27** were also present. The crystals of **28** were darker in colour than the other two iron mixed metal compounds. Yield; 0.009g (27%) based on $[Fe(cpd)_3]$.

Microanalysis calculated for $C_{18}H_{18}AgFeN_4O_9$: C,36.1; H,3.03; N, 9.37%. Found C, 35.7; H, 2.99; N, 8.97%.

I.R(KBr) ν(CN)/cm^{-1} 2212s, ν(CO)/cm^{-1} 1586(br).

7.6.9 Synthesis of $\{Ag[Fe_2(\mu\text{-}OMe)_2(cpd)_4](OH)\cdot 0.4H_2O\}_\infty$, (29).

The same concentrations and conditions as for the reactions yielding **28** were used with the exception that MeOH was used as the only solvent. A mixture of three compounds was obtained, these being **27**, **28** and $\{Ag[Fe_2(\mu\text{-}OMe)_2(cpd)_4](OH)\cdot 0.4H_2O\}_\infty$, (**29**). The latter was obtained as the minor product since no trace of this compound was observed in the powder plot.

7.6.10 Synthesis of $\{[Ag(cpd)]\}_\infty$, (30).

0.023g (0.045 mmol) $[Al(cpd)_3]\cdot 6H_2O$ were dissolved in 2mL DMF. 0.029g (0.17 mmol) $AgNO_3$ were dissolved in 2mL MeOH. The $AgNO_3$ solution was layered on top of $[Al(cpd)_3]\cdot 6H_2O$. The sample tube was covered in foil and left in the dark. Colourless crystals were obtained after 1 month. Yield; 0.006g (19%) based on $[Al(cpd)_3]\cdot 6H_2O$.

Microanalysis calculated for $C_6H_6AgNO_2$: C, 31.0; H, 2.61; N, 6.04. Found C,29.0; H,2.54; N,6.25. (There was a 2nd type of compound in the sample which had black colouration. This might be Ag_2O that forms due to photo induced decomposition of **30**. The mixture could not be separated out. **30** turns black over time and this is suggestive of the network decomposing to Ag_2O).

References:

1. H.Li; M.Eddaoudi; T.L.Groy; O.M.Yaghi, *J.Am.Chem.Soc.* **1998,** 120, 8571.
2. R.G.Charles, *Org. Synth.* **1959**, 38, 61.
3. D.F.Martin; W.C.Fernilius; M.Shamma, *J.Am.Chem.Soc.* **1959**, 81, 130.
4. A.Angeli; A.Mangnani, *Gazz.Chim.Ital.* **1894**, 24, 342.
5. C.M.Silvernail; G.Yap; R.D.Sommer; A.L.Rheingold; V.W.Day; J.A.Belot, *Polyhedron* **2001**, 20, 3113.
6. O.Angelova; G.Petrov; J.Matsichek, *Acta.Crystallogr.* **1989**, C45, 710.